TO THE BOTTOM OF THE STOP

Calibration of bottom-quark jets identification algorithms and search for scalar top-quarks and dark matter with the Run I ATLAS data

Priscilla Pani

TO THE BOTTOM OF THE STOP

Priscilla Pani

To the bottom of the stop

Calibration of bottom-quark jets identification algorithms and search for scalar top-quarks and dark matter with the Run I ATLAS data

Priscilla Pani

To the bottom of the stop

Calibration of bottom-quark jets identification algorithms and search for scalar top-quarks and dark matter with the Run I ATLAS data

ACADEMISCH PROEFSCHRIFT

ter verkrijging van de graad van doctor
aan de Universiteit van Amsterdam
op gezag van de Rector Magnificus
prof. dr. D.C. van den Boom
ten overstaan van een door het college voor promoties ingestelde commissie, in het openbaar te verdedigen in de Aula der Universiteit
op woensdag 10 September 2014, te 11:00 uur

door

Priscilla Pani

geboren te Rome, Italië.

Promotiecommissie:

Promotor:	prof. dr. ir. P.J. de Jong
Co-promotor:	dr. A.P. Colijn
Overige Leden:	prof. dr. W.J.P. Beenakker
	prof. dr. S.C.M. Bentvelsen
	dr. G. Bertone
	prof. dr. J.J. Engelen
	prof. dr. P.M. Kooijman
	prof. dr. P.J.G. Mulders
	dr. S.K. Strandberg

Faculteit der Natuurwetenschappen, Wiskunde en Informatica

This work is part of the research program of the Stichting voor Fundamenteel onderzoek der Materie (FOM), which is part of the Nederlandse organisatie voor Wetenschappelijk Onderzoek (NWO). It was carried out at the Nationaal Instituut voor Subatomaire Fysica (Nikhef) in Amsterdam, the Netherlands. The research has been supported by the VICI grant titled “Between bottom and top: supersymmetry searches with flavour” of prof. dr. ir. P.J. de Jong.

Cover design by Priscilla Pani and Duc Bao Ta © 2014 Typeset by LaTeX. Printed and bound by Gildeprint Drukkerijen.

Contents

Part 1

Experimental and theoretical introduction

Introduction

In the last century high energy physics has made incredible steps forward toward the comprehension of the nature of our universe, its matter content and the interactions of that matter. The Standard Model (SM) [1–4] provides a cogent description of all known subatomic particles and their quantum interactions (strong, weak and electromagnetic). The SM predictive power has been tested to unprecedented precision, with the recent discovery of a Higgs boson by the Large Hadron Collider (LHC) experiments [5, 6] completing the last piece of the particles puzzle. Nevertheless the SM is believed to be an incomplete theory, due to a number of questions that are currently unanswered by the theory.

Dark Matter and Dark Energy represent 96% of the content of the universe and their nature is currently unknown. The remaining four percent is dominated by ordinary (baryonic) matter. The SM is also unable to explain the apparent lack of antimatter in the universe, which should have been made in the Big Bang in equal amount with matter. Furthermore the theory cannot explain neutrino masses and lacks a fundamental explanation for the quarks, leptons and neutrino mass hierarchy and mixing and the existence of three generations of particles. Finally, unification of gravity with the other forces is not possible within the SM theoretical framework.

These and many more open questions about nature call for extensions of the SM. These theories, such as Supersymmetry (SUSY), compositeness and extra dimensions, string theory and multiverses, hidden sectors, extended Higgs sectors and top partners, usually answer some or all of the questions listed above and predict new phenomena, often at the TeV energy scale. Figure 1 gives an schematic representation, presented at the Snowmass 2013 meeting [7], of the different coverage that each type of theory, depicted as *big ideas* in the report, gives to each category of currently open questions. As it stands out, Supersymmetry is one of the most compelling of these ideas and it is one of the main focuses of the research programs at

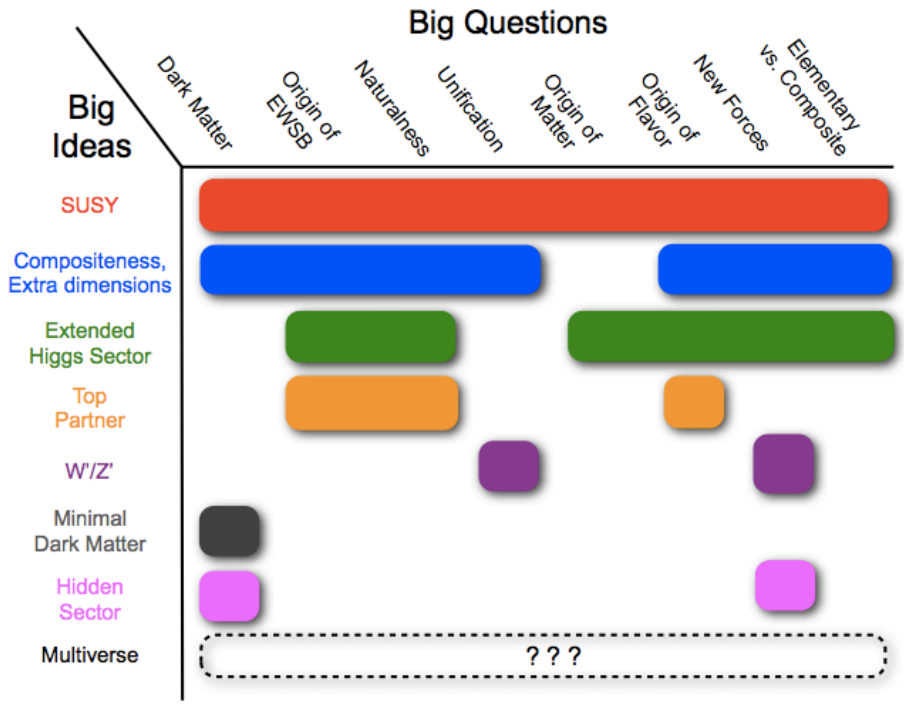

Figure 1: *Representation presented at the Snowmass 2013 meeting [7] of the issues unexplained by the current scientific paradigm (*big questions*) and the theoretical models (*big ideas*) proposed as a solution to them and as an extension of the current theory of particle physics.*

the LHC experiments.

The LHC is currently the most powerful pp collider. The first Run lasted from 2010 to 2012. In this period the accelerator has delivered a total integrated luminosity of pp collisions of 5 and 20 fb^{-1} at a centre-of-mass energy of 7 and 8 TeV, respectively. The A Toroidal LHC ApparatuS (ATLAS) experiment is one of four experiments recording the collisions delivered by the LHC. In these three years, a large crew of physicists and technicians has contributed to the operation of the ATLAS detector, in order to guarantee the highest efficiency in recording the data delivered by the accelerator and the healthy functioning of all sub-detectors.

In 2011, the main focus of the ATLAS experiment has been not only to probe for the first time physics at the energy frontier, but also to improve the understanding and calibration of the detector and the tuning and validation of the Monte Carlo sim-

ulation used to model the SM (and new physics) processes. The analysis presented in Part 2 of this thesis is a study of the reliability of the Monte Carlo simulation of jets originating from bottom quarks (b-jets), the response of the detector to them and the performance of the algorithms used for their identification. The study is based on the 5 fb^{-1} of data collected in 2011 and it was driven by the need of understanding the reasons behind the calibration factors needed to match the simulation to the experimental data.

The dataset collected by ATLAS in 2012 is four times bigger than the one in 2011 and the higher centre-of-mass energy results in a higher production cross section for one of the most intriguing particles predicted by SUSY: scalar top quarks (top squarks). Part 3 presents a search for top squarks in final states with one isolated lepton, b-jets and missing transverse momentum.

Outline of the thesis

This thesis is divided in three Parts. The first one gives a theoretical and experimental introduction to the presented analyses. Chapter 1 is a theoretical introduction to Supersymmetry, mostly focused on the top squark phenomenology, and to the connections between top quarks, neutralinos and Dark Matter. Chapters 2 and 3 introduce the experimental framework: the ATLAS detector and the details about the reconstruction and identification of all the particles used in the presented analyses. Particular attention is devoted in Section 2.3 to performance monitoring and improvement of the ATLAS inner tracking system.

The second Part of this thesis describes a calibration of b-jet identification algorithms, based on a method that exploits fully reconstructed B hadrons that are associated to the b-jets. The main results of this work will be summarised in an ATLAS publication [8], currently in preparation. The strategy of the analysis is introduced in Chapter 4, the validation of the background estimate is given in Chapter 5 and the analysis of the results based on 5 fb^{-1} of data collected at $\sqrt{s}$ = 7 TeV are presented in Chapter 6.

The last part of this thesis is devoted to the description of a search for top squark pairs in final states with one isolated lepton, four jets of which at least one identified as a b-jet and missing transverse momentum. The results of this analysis are part of an ATLAS publication [9]. The search strategy, the backgrounds and the quantities used to discriminate top squark events from the SM processes are introduced in Chapter 7. In Chapter 8 the signal selections are described, with particular attention

to the selection optimisation for top squarks decaying into a chargino and a b-quark ($\tilde{t} \rightarrow b\ \tilde{\chi}^{\pm}$). In the same chapter, the background estimate and validation for all the analysis sections is described. The results of the search are given in the last chapter (Ch. 9). The analysis results are also interpreted, in the same chapter, in terms of upper limits of Dark Matter contact operators in the context of Effective Field Theories. These results will be also part of an ATLAS publication [10], currently in preparation.

1 Physics beyond the Standard Model: SUSY and the top squark

Supersymmetry (SUSY) is one of the most appealing possible extensions of the Standard Model (SM). By introducing an additional symmetry that links fermions and bosons it predicts the existence of a full spectrum of new particles. Among those, a top squark with a mass below 1 *TeV plays a key role for the success of the theory and it is becoming an interesting and challenging signature at the LHC. An introduction to the key ingredients of the minimal supersymmetric extension of the SM (the MSSM) will be given in this chapter, with particular attention to those elements that determine the phenomenology of the top squark or the assumptions that will be imposed in the models considered in this thesis. In addition to this, in the last section Dark Matter (DM) production in* pp *collisions will be described in the effective field theory approximation.*

1.1 Introduction to the Standard Model

The Standard Model (SM) of particle physics [1–4], formulated in the '60s and '70s, describes three natural forces (weak, electromagnetic and strong) and the dynamics of all known subatomic particles in a single model. Its predictive power has been proven in recent decades with unprecedented precision. The SM is a non-abelian gauge theory invariant under the symmetry group

$$SU(3)_C \otimes SU(2)_L \otimes U(1)_Y \tag{1.1}$$

where C, L and Y are the colour charge, the weak isospin and the hypercharge, respectively. The gauge bosons W^i; $i = 1, 2, 3$ and B are the mediators of the elec-

troweak interaction and the gluons g are the carriers of the strong force. The matter sector of the SM is composed of three generations of fermions and anti-fermions. According to their transformation properties under $SU(3)_C$ they are divided into quarks (carrying colour charge) and leptons (colourless). Furthermore, the fermions are divided into left and right handed chirality eigenstates. The former transform as doublets under the weak interaction $SU(2)_L$ and the latter as singlets. In summary, the gauge eigenstates of the SM matter sector are:

$$\underset{u_R,\, d_R}{\begin{pmatrix} u_L \\ d_L \end{pmatrix}} \quad \underset{c_R,\, s_R}{\begin{pmatrix} c_L \\ s_L \end{pmatrix}} \quad \underset{t_R,\, b_R}{\begin{pmatrix} t_L \\ b_L \end{pmatrix}} \qquad \underset{e_R}{\begin{pmatrix} \nu_{eL} \\ e_L \end{pmatrix}} \quad \underset{\mu_R}{\begin{pmatrix} \nu_{\mu L} \\ \mu_L \end{pmatrix}} \quad \underset{\tau_R}{\begin{pmatrix} \nu_{\tau L} \\ \tau_L \end{pmatrix}}$$

In the SM, neutrinos are assumed to be purely left handed and massless. Experimental results have shown that this is not the case and neutrinos have masses. A number of extensions of the SM have been proposed to include right handed neutrinos, although a discussion on these theories is beyond the scope of this introduction.

Any particle mass terms in the SM Lagrangian are forbidden by the gauge symmetry. In 2012 the mechanism that spontaneously breaks the electroweak symmetry in the SM [11–13] giving masses to the particles was experimentally verified with the discovery of the Higgs boson by ATLAS and CMS [5, 6]. After spontaneous symmetry breaking, the electroweak gauge bosons acquire mass. Their mass eigenstates ($W^{\pm}$, Z and γ) are:

$$W^{\pm} = \frac{1}{\sqrt{2}}(W^1 \mp W^2) \qquad \begin{pmatrix} Z \\ \gamma \end{pmatrix} = \begin{pmatrix} \cos\theta_W & -\sin\theta_W \\ \sin\theta_W & \cos\theta_W \end{pmatrix} \begin{pmatrix} W^3 \\ B \end{pmatrix}, \tag{1.2}$$

where the Weinberg angle θ_W is defined by:

$$\sin\theta_W = \frac{e}{g_2}. \tag{1.3}$$

e is the electric charge and, in this notation, it is the coupling of the electromagnetic interaction, while g_2 is the gauge coupling constant for $SU(2)_L$. The core of the Standard Model is characterised by 19 free parameters that have been determined experimentally. In addition there are mass and mixing parameters of the neutrino sector.

The measurement of the Higgs mass fixed the last free parameter of the theory.

Despite its predictive power and success, the SM is an incomplete theory. First of all, it does not include any mechanism that describes the fourth fundamental force,

gravity and it does not include any particle that could account for the non-baryonic content of the universe (Dark Matter). Secondly, the SM is believed to be not *natural*. Some of its parameters, are characterised by large quantum loop corrections that can be cancelled out only by fine-tuned constants. For the Higgs mass they can be expressed for loops involving fermions as [14]:

$$\delta m_H^2 \propto \frac{\lambda_f^2 N_c^f}{8\pi^2}\Lambda^2 \tag{1.4}$$

where λ_f^2 and N_c^f are the Yukawa coupling and the numbers of colours of fermion f. Due to the Yukawa coupling, the dominant term to the correction will be the one coming from the top quark. Λ is the cut-off scale and can be seen as the scale where new physics appears and where the Standard Model is known not to be valid anymore. In the assumption that the SM is valid up to the Grand Unification or the Planck scale, the correction to the Higgs mass is extremely large. To obtain the experimentally measured value of 125.5 ± 0.2 (stat.) $^{+0.5}_{-0.6}$ (syst) GeV [15] a 16 digit fine tuning of these enormous corrections is needed. This is one of the reasons, falling under the name of *naturalness*, that are used to justify the existence of New Physics around the TeV-scale. This would lower the scale at which the SM is valid, fixing $\Lambda \sim$ TeV and reduce the tuning of the Higgs mass. The definition and quantification of this *naturalness* concept is somewhat arbitrary, but it is naively clear that subtracting two numbers at a very high scale to obtain a parameter at the electroweak scale, fine-tuning them by 16 digits has a low degree of *naturalness*. Conversely, a cancellation of divergences arising from a symmetry of the theory is characterised by a high degree of *naturalness*.

1.2 Introduction to Supersymmetry

In the last decades a very large number of extensions of the SM have been proposed in order to solve these shortcomings of the model. Supersymmetry (SUSY) [16–24] is one of the most compelling possible extensions of the Standard Model. This theory is grounded on a generalisation of space-time transformation linking fermions and bosons. It bypasses the Coleman--Mandula theorem, that states the impossibility of combining space-time and internal symmetries in any but a trivial way [25], by introducing fermionic generators of symmetry transformations. In this way it was possible to introduce an additional symmetry, that was shown by Haag, Lopuzansky and Sohnius [26] to be the only possible extension of the known space-

Sparticle	Field content	SM partner	Quantum numbers		
			SU(3)	SU(2)	U(1)
gluino	$\tilde{g}$	g	8	1	0
gauginos	$\tilde{W}^{\pm}$, $\tilde{W}^0$	$W^{\pm}$, W^0	1	3	0
	$\tilde{B}$	B	1	1	0
sleptons	$(\tilde{\nu}, \tilde{\ell}^-)_L$	$(\nu, \ell^-)_L$	1	2	-1
	$\tilde{\ell}_R$	ℓ_R	1	1	-2
squarks	$(\tilde{u}, \tilde{d})_L$	$(u, d)_L$	3	2	1/3
	$\tilde{u}_R$	u_R	3	1	4/3
	$\tilde{d}_R$	d_R	3	1	-2/3
higgsinos	$(\tilde{H}_d^0, \tilde{H}_d^-)$	(H_d^0, H_d^-)	1	2	-1
	$(\tilde{H}_u^+, \tilde{H}_u^0)$	(H_u^+, H_u^0)	1	2	1

Table 1.1: *Fields of the MSSM and their $SU(3) \otimes SU(2) \otimes U(1)$ quantum numbers. Only one generation of quarks and leptons is listed as an example.*

time symmetries of particle interactions. SUSY is an appealing theory that enables to connect the unification of strong, weak and electromagnetic interactions through the high-energy extrapolation of their couplings and it has been widely studied in terms of supersymmetric Grand Unification Theories (GUT) [27–35], linked with gravity [36–41], string theory and cosmology [42, 43].

1.2.1 The Minimal Supersymmetric Standard Model (MSSM)

In this thesis we will refer to the minimal supersymmetric extension of the SM, i.e. the MSSM. A brief overview of the model and the information relevant to the work in this thesis will be given in the following and further details can be found in Refs. [14, 44–47].

In order to supersymmetrize the SM we need to introduce a super-partner for every known particle with half a unit of spin difference, but otherwise with the same properties and quantum numbers (Table 1.1). SM particles and their partners are postulated to have an additional quantum number, the R-parity, that is assumed to be conserved:

$$R = (-1)^{3(B-L)+2S}. \tag{1.5}$$

B and L are the baryon and lepton numbers, respectively and S is the spin. The R-parity allows us to distinguish particles and super-partners and its conservation has important phenomenological consequences:

a) all sparticles are produced in pairs,

b) all decays of SUSY particles involve other SUSY particles in the final state,

c) the lightest SUSY particle is stable and does not decay.

In addition, R-parity conservation allows to eliminate all the lepton and baryon violating terms of the MSSM Lagrangian such that the MSSM obeys to the same conservation rules and symmetries of the SM.

In the SM all matter fields (leptons and quarks) are spin half fermions and the gauge bosons have spin one. The super-partners of the fermions cannot have spin one since the only known consistent relativistic field theories for spin-one particles are those of gauge bosons that are not suitable to describe matter fields [46]. For this reason, the bosonic super-partners of the fermions should be scalars. The fermions and their partners form three generations of six chiral super-multiplets that represent the matter sector content of the MSSM. In contrast to the SM, the Higgs sector of the MSSM contains two chiral super-multiplets with two complex Higgs doublets H_D and H_U and their fermionic counterparts (higgsinos). This is the minimal structure needed to cancel out the gauge anomaly (a requirement of renormalizability of the theory), that arises if

$$\sum_{fermions} Y \neq 0, \tag{1.6}$$

where Y is the hypercharge. Two Higgs doublets is also the minimal structure required to give mass to both up and down type super-multiplets.

Finally the gauge sector consists of the gluons and their *gluino* super-partners and the $SU(2)_L \otimes U(1)_Y$ gauge bosons and their *gaugino* super-partners.

1.2.2 Supersymmetry breaking

The fact that SUSY particles have not yet been observed leads to the conclusion that, if supersymmetry is realised, it is a broken symmetry. The mechanisms by which SUSY is broken is unknown and the Lagrangian is usually split into two components:

$$\mathcal{L}_{MSSM} = \mathcal{L}_{SUSY} + \mathcal{L}_{Soft}, \tag{1.7}$$

where the first term on the right side consists of the dynamics terms of the superfields and their interactions and the second contains the supersymmetry breaking terms. To ensure proper convergence of the theory at high energy, these SUSY-breaking terms have to be *soft*, which means that they must have mass dimension less than four. It can be proven [46] that it is impossible to construct a realistic model of spontaneously broken low-energy SUSY in which the supersymmetry breaking arises only from interactions of the particles of the MSSM. It is therefore assumed that there exists a *hidden sector* consisting of particles that are completely decoupled from the MSSM particles and which is responsible for breaking SUSY. $\mathcal{L}_{Soft}$ is obtained by considering its most general form, without assumptions on the nature of this sector. $\mathcal{L}_{Soft}$ can be written as [46]:

$$\begin{aligned}\mathcal{L}_{Soft} = &- \phi_i^*(m_{ij}^2)\phi_j + \left(\frac{1}{3!}\mathcal{A}_{ijk}\phi_i\phi_j\phi_k - \frac{1}{2}\mathcal{B}_{ij}\phi_i\phi_j + \mathcal{C}_i\phi_i + h.c.\right) \\ &- \frac{1}{2}\sum_{\alpha=1}^{3}\left(M_\alpha\lambda^a\lambda^a + h.c.\right),\end{aligned} \tag{1.8}$$

where ϕ_i is the scalar component of one of the MSSM superfields, with m being interpreted as its mass, and λ^a the gaugino fields, with M their Majorana mass term. $\mathcal{A}, \mathcal{B}$ and $\mathcal{C}$ are the trilinear, bilinear and linear scalar interaction terms.

The MSSM is characterised by 124 independent physical parameters [48] that arise either from the supersymmetric part of the Lagrangian ($\mathcal{L}_{SUSY}$) or from the supersymmetry breaking term ($\mathcal{L}_{Soft}$). The ones that will be relevant to understand the phenomenology and assumptions of the models considered in this thesis are described in the following:

- μ: is the coefficient in the Higgs super-potential $\mathcal{W}$ that gives the mass terms for the Higgs bosons and their partners ($\mathcal{W} \sim \mu H_u H_d$) and is therefore called *the Higgs mass term*. Within the most used convention, the phase of μ is a physical parameter. However, due to possible large CP-violation due to this phase, μ is usually assumed to be real.

- $M_a (a = 1, 2, 3)$: are the soft supersymmetry breaking gaugino mass parameters. Within the most used convention, a redefinition of phases always allows to define these numbers as real and positive.

- $\tan\beta$: is the ratio of the Higgs vacuum expectation values of the two Higgs doublets:

$$\tan\beta = \frac{v_u}{v_d} \tag{1.9}$$

- the squark (and slepton) mass matrices that appear in $\mathcal{L}_{soft}$: $M_{\tilde{q}}$ for the left handed squarks ($M_{\tilde{\ell}}$ for sleptons) and the right handed ones $M_{\tilde{u}}, M_{\tilde{d}}$ ($M_{\tilde{e}}$ for the sleptons).

1.2.3 Gauge eigenstates mixing in SUSY

The breaking mechanism of the Lagrangian causes the presence of mixing between the gauge eigenstates of the SUSY particles. It is important to understand the mass eigenstates of the theory and their gauge eigenstates content because they will characterise its phenomenology.

Each of the SM fermions has two supersymmetric partners $\tilde{f}_L$ and $\tilde{f}_R$ corresponding to the left and right handed fermion. In general, these two sparticles are not mass eigenstates and can mix. The mixing of the two sfermions is proportional to the mass of their fermion partner. In particular for the stop, the squared mass matrix can be approximately written as:

$$M_{\tilde{t}}^2 = \begin{pmatrix} (M_{\tilde{q}}^2)_3 + (1/2 - 2/3 \sin^2\theta_W) M_Z^2 \cos 2\beta + m_t^2 & -m_t(\mathcal{A}^t + \mu \cot\beta) \\ -m_t(\mathcal{A}^t + \mu \cot\beta) & m_{\tilde{t}}^2 + 2/3 M_Z^2 \cos 2\beta \sin^2\theta_W + m_t^2 \end{pmatrix}. \quad (1.10)$$

Here $(M_{\tilde{q}}^2)_3$ is the third component of the left-handed squarks mass matrix and $\mathcal{A}^t$ the matrix of trilinear interaction coefficients of the top squark. Therefore the mixing is expected to be small in general, with the exception of the third generation squarks. Since the off diagonal terms depend on the non negligible masses of their fermion partners, the third generation squarks involve substantial left-right mixing. Especially for the top squark a significant mixing of the left-right gauge eigenstates can occur and determine a large mass splitting between the two mass eigenstates, $\tilde{t}_1$ and $\tilde{t}_2$. In these conditions the lightest of the two, $\tilde{t}_1$, might be considerably lighter than the rest of the squarks.

The charged gauginos and higgsinos mix into four physical states called charginos: $\tilde{\chi}_1^{\pm}, \tilde{\chi}_2^{\pm}$ (where it is assumed $m(\tilde{\chi}_1^{\pm}) < m(\tilde{\chi}_2^{\pm})$). The mixing is described at tree level by a 2×2 complex mass matrix that is a function of M_2, β and μ:

$$\mathcal{M}_{\tilde{\chi}^{\pm}} = \begin{pmatrix} M_2 & \sqrt{2} M_W \sin\beta \\ \sqrt{2} M_W \cos\beta & \mu \end{pmatrix}. \quad (1.11)$$

In the same way the neutral gauginos and higgsinos mix into four physical states called neutralinos: $\tilde{\chi}_1^0, \tilde{\chi}_2^0, \tilde{\chi}_3^0, \tilde{\chi}_4^0$ (index ordered in mass). The mixing is described

at tree level by a 4×4 symmetric complex mass matrix and again depends only on $M_1, M_2, \tan\beta$ and μ:

$$\mathcal{M}_{\tilde{\chi}^0} = \begin{pmatrix} M_1 & 0 & -M_W \tan\theta_W \cos\beta & -M_W \tan\theta_W \sin\beta \\ & M_2 & M_W \cos\beta & M_W \sin\beta \\ & & 0 & -\mu \\ & & & 0 \end{pmatrix}, \tag{1.12}$$

where θ_W is the weak mixing angle. If $\tilde{\chi}_1^0$ is the lightest SUSY particle (as we will assume in this thesis), due to R-parity conservation it is stable. In this scenario, $\tilde{\chi}_1^0$ represents a natural Dark Matter candidate, as further discussed in Section 1.4.

In general the three parameters μ, M_1 and M_2 are completely arbitrary. However, in Grand Unification Theories (GUT) M_1 and M_2 are equal at the high scale (Λ_{GUT}) where the gauge couplings are presumed to unify:

$$M_1(\Lambda_{\text{GUT}}) = M_2(\Lambda_{\text{GUT}}). \tag{1.13}$$

At the scale of the Z mass m_Z we can determine using the renormalisation group equations that:

$$M_1(m_Z) \simeq \frac{1}{2} M_2(m_Z). \tag{1.14}$$

The last condition is also known under the name of *gaugino universality* assumption. Secondly, μ is related to the Z mass by:

$$m_Z^2 = 2\frac{m_{H_d}^2 - m_{H_U}^2 \tan^2\beta}{\tan^2\beta - 1} - 2\mu^2, \tag{1.15}$$

where m_{H_d} and m_{H_u} are couplings of the quadratic terms of H_d and H_u in the SUSY Higgs potential. *Naturalness* arguments require μ to be of the same scale as m_Z in order to have a reasonably little amount of fine-tuning among the parameters.
According to the relative hierarchy between these three parameters μ, M_1 and M_2, the mixture of higgsinos ($\tilde{H}$), winos ($\tilde{W}$) and bino ($\tilde{B}^0$) that contribute to the lightest chargino and neutralino differs. In the phenomenology considered in this thesis the neutralino is considered to be mostly *bino-like* and it is assumed that

$$M_1 < M_2 << |\mu|. \tag{1.16}$$

This condition together with the one in Eq (1.14) implies:

$$m(\tilde{\chi}^{\pm}) \simeq 2\, m(\tilde{\chi}_1^0). \tag{1.17}$$

The afore mentioned hypothesis, however, is not the one favoured by *naturalness* arguments. A natural definition of μ is achieved if $\mu \sim m_Z$, where the hierarchy with the other parameters M_1 and M_2 could be:

$$|\mu| << M_1, M_2. \tag{1.18}$$

This relation implies the lightest neutralino and charginos being higgsino-like and very close in mass:

$$m(\tilde{\chi}^{\pm}) \simeq m(\tilde{\chi}_1^0) \sim |\mu|. \tag{1.19}$$

Otherwise it could be that μ, M_1 and M_2 have similar magnitude, which would lead to a $\tilde{\chi}_1^0$ composed of a equal mixture of higgsinos, winos and bino. Despite its *naturalness*, the condition of Eq. (1.19) is characterised by a phenomenology that is more difficult to detect at the LHC. In this thesis the neutralino is assumed to be bino-like. This does not comply to the most natural definition of the μ parameter but still allows for a natural definition of the Higgs mass.

1.3 The supersymmetric partner of the top quark

1.3.1 Proton-proton collisions at the LHC

The Large Hadron Collider (LHC) accelerates and collides protons at a centre-of-mass of 8 TeV[1)]. The proton constituents (partons) are three valence quarks, two up-type and one down-type, gluons, and the sea quarks and antiquarks, constantly created and annihilated due to quantum fluctuations. The cross section of two protons in an arbitrary final state X ($pp \to X$) can be described in terms of a partonic cross section convoluted with the Parton Distribution Functions (PDFs) of the partons inside the protons:

$$\sigma_{pp\to X} = \sum_{i,j} \int_0^1 \mathrm{d}x_1 \int_0^1 \mathrm{d}x_2 f_i(x_1, \mu_f^2) f_j(x_2, \mu_f^2) \hat{\sigma}_{ij\to X} \left(x_1 p_1, x_2 p_2, \alpha_s(\mu_r^2), \frac{Q^2}{\mu_r^2}, \frac{Q^2}{\mu_f^2} \right). \tag{1.20}$$

The partonic cross section of the hard scattering, $\sigma_{ij\to X}$, describes the production of products X at energy scale Q from the partons i and j with momenta $x_1 p_1$ and

[1)] The centre-of-mass was 7 TeV in 2010-2011.

$x_2 p_2$, p_1 and p_2 being the momenta of the incoming protons. It is typically calculated in perturbation theory, to Leading Order (LO), Next-to-Leading Order (NLO), or even higher orders. The PDFs $f_i(x_1)$ and $f_i(x_2)$ parametrise the probability of having parton i and j from each of the two incoming protons with momentum fraction x_1 and x_2. The shapes of the PDFs are determined by a fit to data from experimental observables in various processes [49–54] and extrapolated using the DGLAP evolution equation [55–59].

The scales μ_r^2 and μ_f^2 are the renormalisation and factorisation scales, respectively. The former indicates the scale at which α_s is evaluated and the latter indicates the scale at which the PDFs are evaluated and at which the long and short distance effects are assumed to factorise.

1.3.2 Motivations for a *light* top squark

If SUSY is realised, the most abundant sparticles produced at the LHC are those with masses accessible to the collider's energy that couple the strongest to the proton constituents. The production cross section for different pairs of sparticles as a function of their mass is shown in Figure 1.1. First and second generation squarks and gluinos are the particles that are produced with the highest cross section at a

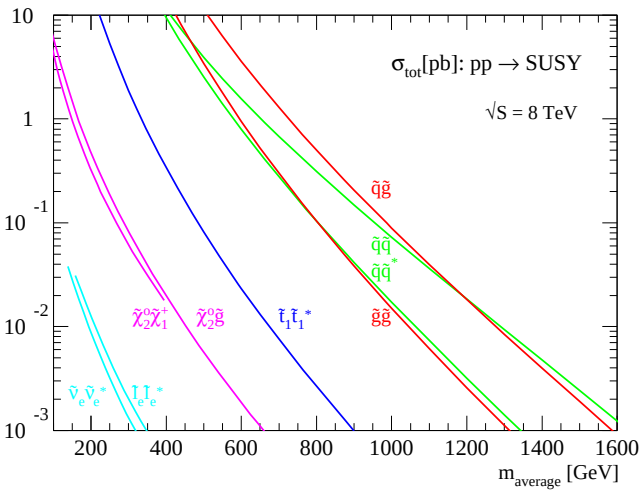

Figure 1.1: *Sparticle production cross section as a function of the average of the masses of the particles produced in the process. The dark blue line describes the cross section for direct production of top squark pairs and it is the relevant cross section for this analysis. The cross sections have been calculated using* Prospino *[60].*

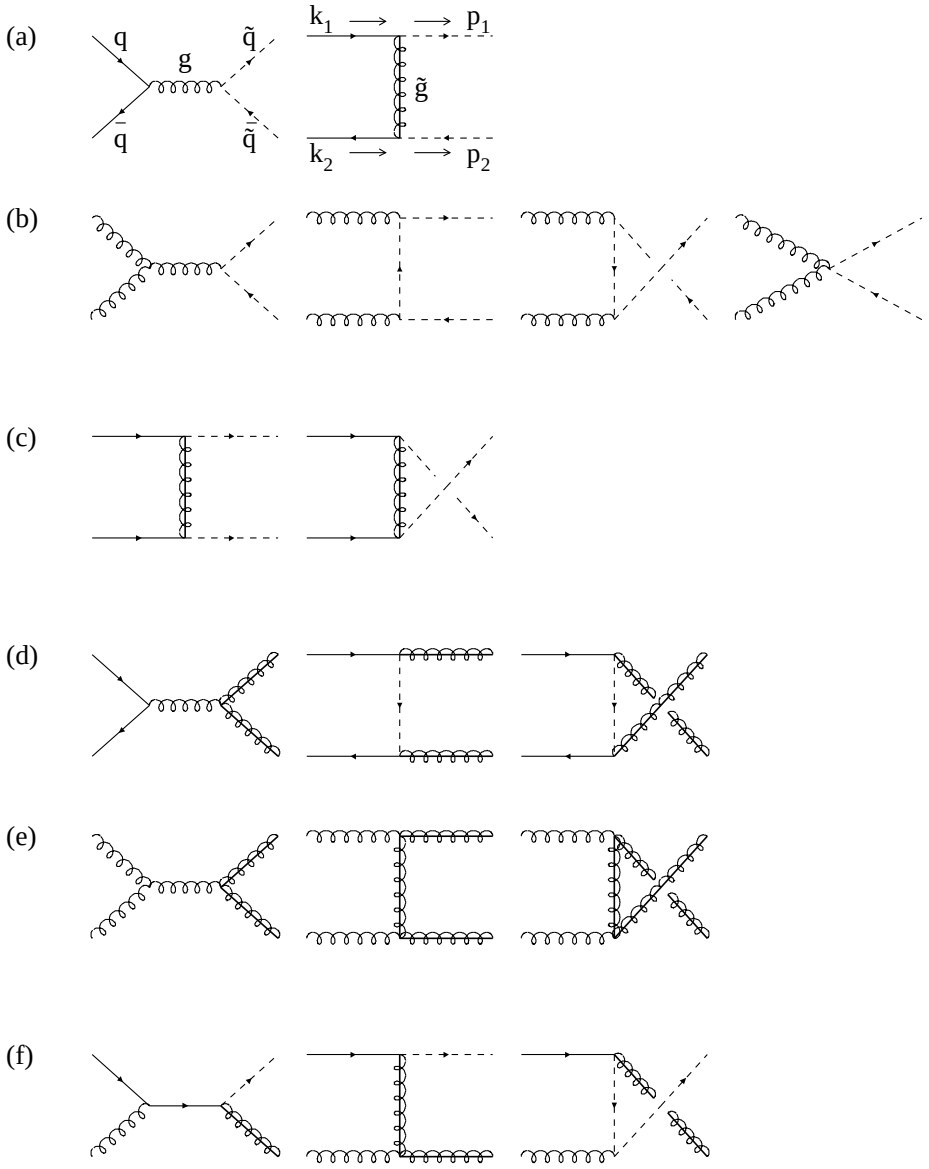

Figure 1.2: *Feynman diagrams for the production of squarks and gluinos in lowest order. The diagrams without and with crossed final-state lines [e.g. in (b)] represent t- and u-channel diagrams, respectively. The diagrams in (c) and the last diagram in (d) are a result of the Majorana nature of gluinos. Note that some of the above diagrams contribute only for specific flavours and chiralities of the squarks [61].*

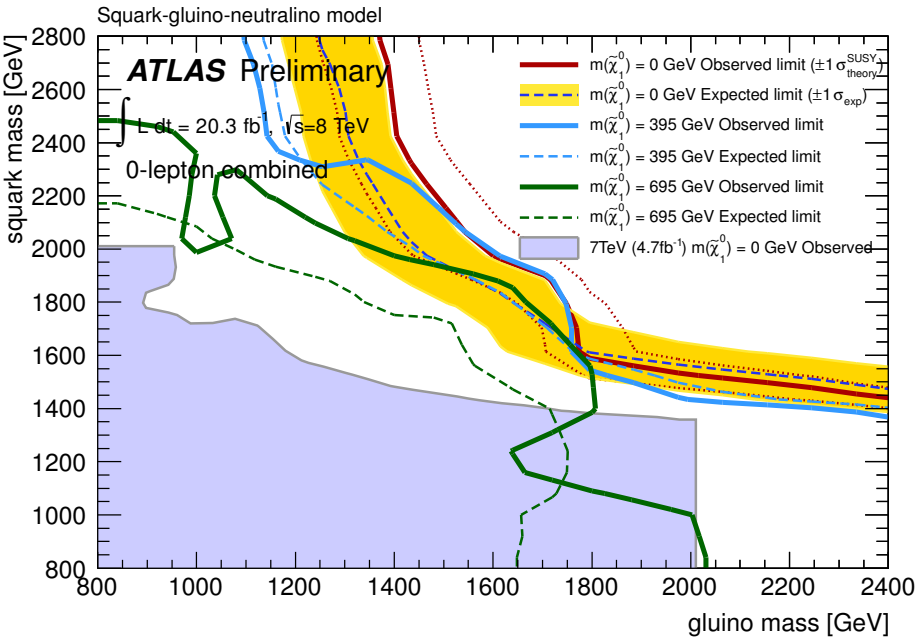

Figure 1.3: *Exclusion limits at 95% confidence level for a simplified phenomenological MSSM scenario where only strong production of gluinos and first- and second-generation squarks is considered. Three values of $\tilde{\chi}_1^0$ masses are considered. The dashed lines show the expected limits with 1σ uncertainty band in yellow on the lowest $\tilde{\chi}_1^0$ mass assumption. Observed limits are indicated by solid curves. Areas to the left and below the curves are excluded. The dotted lines indicate the observed exclusion varying the signal cross section by 1σ uncertainty. Previous results from ATLAS are represented by the shaded light blue area [62].*

given mass; the leading order Feynman diagrams for squark and gluino production at the LHC are shown in Figure 1.2. Searches at 7 and 8 TeV centre-of-mass energy in ATLAS (as well as in CMS) have already excluded a large amount of the parameter space, pushing the lower limits of these particles over the TeV scale[2)] (see Figure 1.3).

Due to these more and more stringent limits on squarks and gluinos, an increasing attention is being devoted to the third generation partners and in particular to

[2)]It is important to realise when speaking about SUSY limits that given the large amount of free parameters of the theory each limit comes with certain assumptions that need to be taken into account when interpreting the results. In addition, there is always a corner of the parameter space where the assumption does not hold and that is not excluded by the most inclusive and powerful search.

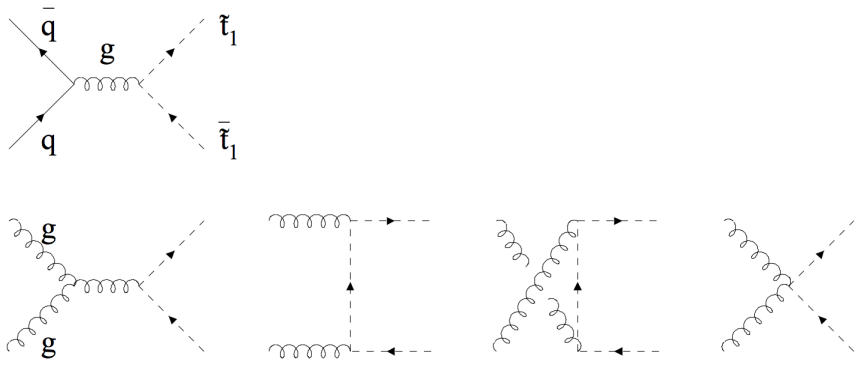

Figure 1.4: *Leading order diagrams for quark–antiquark annihilation and gluon fusion production of pairs of stop particles [63]*

the SUSY partner of the top quark, the stop. Since top quarks are not among the constituents of the proton, the t-channel diagram is not available for scalar top production (Figure 1.4), hence they are produced with a cross section that is a an order of magnitude smaller than that of the first two generation squarks and gluinos. They have a challenging signature due to their similarity to the top quark. Despite the challenge, a number of motivations justify the interest in dedicated searches for top squark direct production.

First of all, the enhanced mixing between the two partners of the right and left handed tops ($\tilde{t}_L$ and $\tilde{t}_R$) might imply a large mass difference between the two physical states $\tilde{t}_1$ and $\tilde{t}_2$. This would lead to a mass hierarchy inversion in the SUSY spectrum, with the $\tilde{t}_1$ as the lightest squark, much lighter than the current limits for the first and second generation squarks.

In addition, top squarks are the main ingredient for the SUSY solution to the *hierarchy problem* of the SM. In fact, each of the supersymmetric partners of the SM particles contribute to δm_H^2 (Eq. 1.4) with opposite sign and cancel the quadratic dependence on Λ. If SUSY masses were equal to SM particle masses, the cancellation would be exact. Otherwise, it is reduced to a logarithmic divergence:

$$\delta m_H^2 \propto \frac{\lambda_f^2 N_c^f}{8\pi^2}(m_{\tilde{f}}^2 - m_f^2)\ln(\Lambda^2/m_{\tilde{f}}^2) \tag{1.21}$$

Following Eq (1.21), the naturalness is re-established by means of an additional symmetry, if the mass difference between the top quark and its partner is between

a few hundred GeV to a few TeV.

1.3.3 Top squark phenomenology

If the top squark exists, and plays a role in solving the hierarchy problem, it can be produced at the LHC and it is not unlikely that ATLAS, with 20 fb^{-1} of data collected at a centre-of-mass energy of 8 TeV, can find it. The top squark production cross section in proton--proton collisions depends on the stop mass as shown in Figure 1.1 [60]. The cross sections for masses between 100 GeV and 700 GeV span five orders of magnitude, varying from 560 pb to 8 fb.

A number of decay modes might be accessible to top squarks of these masses, depending on the masses of the rest of the particles of the SUSY spectrum:

a) $\tilde{t} \to b\,\tilde{\chi}^{\pm} \to b\,W^{\pm}\,\tilde{\chi}^{0}$ (with on/off-shell W)

b) $\tilde{t} \to t\,\tilde{\chi}^{0}$

c) $\tilde{t} \to b\,W^{\pm}\,\tilde{\chi}^{0}$ (via off-shell top)

d) $\tilde{t} \to c\,\tilde{\chi}^{0}$

e) $\tilde{t} \to b\,f\,f'\,\tilde{\chi}^{0}$

A schematic representation of the parameter space $(m_{\tilde{t}}, m_{\tilde{\chi}^0})$ where these five decay modes are accessible is shown in Figure 1.5. All decay modes except the first one are dominating for different regions of the parameter space, while the $\tilde{t} \to b\,\tilde{\chi}^{\pm}$ decay mode is always kinematically allowed if $m(\tilde{\chi}^{0}) < m(\tilde{\chi}^{\pm}) < \big(m(\tilde{t}) - m(b)\big)$.
The last two decays d) and e) have a specific signature that cannot be addressed with the requirements applied in this analysis and have been investigated in other searches exploiting charm and soft lepton identification techniques [9, 64]. Diagrams of the three decay channels considered in this analysis a), b) and c) are presented in Figure 1.6. Signal cross sections are calculated to NLO in the strong coupling constant, adding the resummation of soft gluon emission at Next-to-Leading Logarithm (NLL) accuracy (NLO+NLL) [63, 65–67].

R-parity conservation is the assumption of the MSSM that has the most striking impact on the phenomenology of the stop and its decay. It implies that top squarks are produced in pairs and that the lightest particle of the decay chain (hereby assumed to be the lightest neutralino) is stable.

In order to simplify the treatment of each of the stop decays considered in this thesis an additional constraint is imposed: the so called *simplified model* assumption. This assumption considers each decay mode separately:

I. the decay is assumed to have 100% branching ratio. Since two top squarks are produced in each event due to R-parity conservation, this implies that both squarks decay in the same, symmetric way. When the chargino is involved in the decay chain, also the $\tilde{\chi}^{\pm} \rightarrow W^{\pm}\tilde{\chi}^{0}$ branching ratio is assumed to be 100%. This also means that any interference between the diagrams of the different decay channels is assumed to be zero.

II. All masses of sparticles not involved in the decay chain are assumed to be very high.

III. All masses of the sparticles involved in the decay chain are treated as free parameters. *Signal models* with different parameter assumptions are investigated.

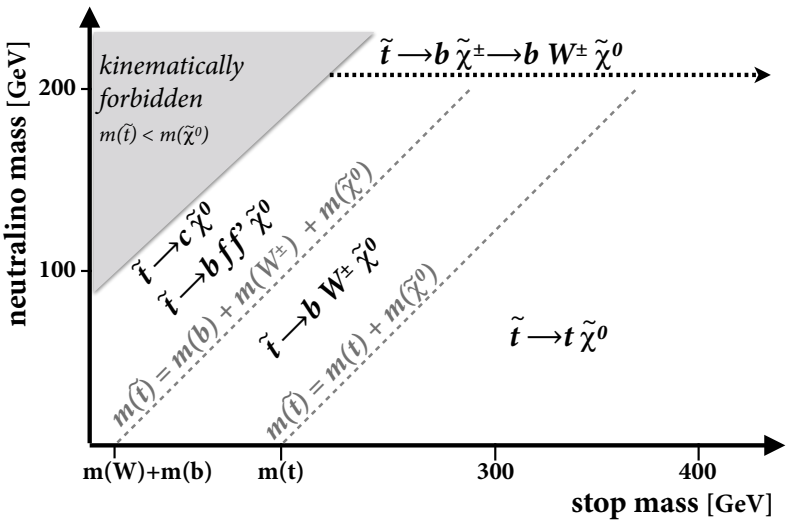

Figure 1.5: *Schematic representation of all possible decays of the top squark. The grey dashed lines indicate the kinematic boundaries for the various decay channels and the region $m(\tilde{t}) < m(\tilde{\chi}^{0})$ is kinematically forbidden. The $\tilde{t} \rightarrow b\ \tilde{\chi}^{\pm} \rightarrow b\ W^{\pm}\ \tilde{\chi}^{0}$ decay is always possible if $m(\tilde{t}) > m(b) + m(\tilde{\chi}^{\pm})$.*

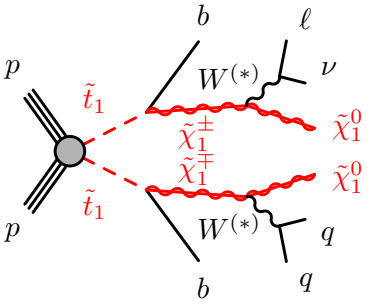

(a) $\tilde{t} \to b\,\tilde{\chi}^{\pm} \to b\,W^{\pm}\,\tilde{\chi}^{0}$

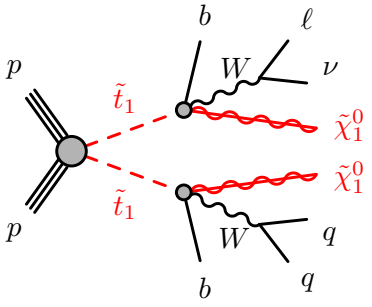

(b) $\tilde{t} \to b\,W^{\pm}\,\tilde{\chi}^{0}$

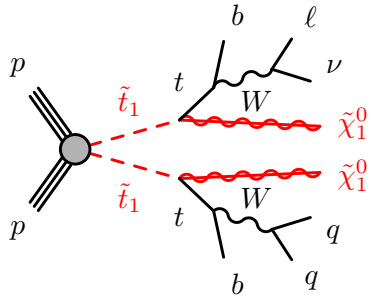

(c) $\tilde{t} \to t\,\tilde{\chi}^{0}$

Figure 1.6: *Diagrams for the three main decay modes of the supersymmetric top, that are addressed with separate selections in this analysis.*

The *simplified model* condition is partially relaxed in one particular set of signal models. As visible in Figure 1.6, $\tilde{t} \to t\,\tilde{\chi}^{0}$ and $\tilde{t} \to b\,\tilde{\chi}^{\pm}$ decay modes overlap in a large portion of parameter space. In this region, there is little justification in imposing 100% branching ratio in either of the decay modes, if the sum of the chargino and the b-quark masses is smaller than the stop mass. Therefore these two decays are both allowed to take place and different branching ratio combinations ($\tilde{t} \to t\,\tilde{\chi}^{0}$,$\tilde{t} \to b\,\tilde{\chi}^{\pm}$) are tested (25--75%, 50--50%, 75--25%). Also in this case, no interference between the diagrams is considered. The final topology will be referred to as *asymmetric* because in a certain fraction of events each of the two top squarks decay in a different mode.

Even under the simplified model assumptions, the $\tilde{t} \to b\,\tilde{\chi}^{\pm}$ decay mode is characterised by a 3-dimensional parameter space determined by the masses of the three particles involved in the chain ($\tilde{t}, \tilde{\chi}^{\pm}, \tilde{\chi}^{0}$). ATLAS has pursued the strategy of cutting this space in bidimensional slices, fixing certain particle masses or relating them according to certain physics-driven motivations:

Gaugino universality: the assumption that gauge couplings unify at the grand unification scale favours the condition (Sec. 1.2.1):

$$m(\tilde{\chi}^{\pm}) \simeq 2\, m(\tilde{\chi}^{0}_{1}). \tag{1.22}$$

The set of models used as a benchmark for $\tilde{t} \to b\, \tilde{\chi}^{\pm}$ selection optimisation span the parameter space of $(m_{\tilde{t}}, m_{\tilde{\chi}^{0}})$ and assume the relation in Eq. (1.22) between the chargino and the neutralino masses.

Mass degeneracy: a particularly challenging scenario is the case in which the top squark and the chargino masses are very similar to each other. This hypothesis is tested considering a set of models that span the $(m_{\tilde{t}}, m_{\tilde{\chi}^{0}})$ parameter space and require $m(\tilde{t}) - m(\tilde{\chi}^{\pm}) = 10$ GeV.

Fixed masses: a convenient approach (orthogonal to the ones listed so far) is fixing one of the sparticle masses to a certain value and vary the other two parameters. This is done with the following assumptions:

a) $m(\tilde{t}) = 300$ GeV

b) $m(\tilde{\chi}^{\pm}) = 106$ or 150 GeV[3)]

c) $m(\tilde{\chi}^{0}) = 0$.

Searches with different final states allow a complementary coverage of these selected models, as summarised in Table 1.2. The models where one lepton final states are expected to have major sensitivity are the ones considered in this thesis.

[3)] The 106 GeV value is chosen just above the LEP chargino mass limit [68]

Assumption	*Motivation*	*Final state*
$m(\tilde{\chi}^{\pm}) = 2m(\tilde{\chi}^0)$	gaugino universality	1/2 lepton
$m(\tilde{t}) - m(\tilde{\chi}^{\pm}) = 10$ GeV	mass degeneracy	2 lepton
$m(\tilde{t}) = 300$ GeV	fixed top mass	0/1/2 lepton
$m(\tilde{\chi}^{\pm}) = 106$ or 150 GeV	fixed chargino mass	0/1/2 lepton
$m(\tilde{\chi}^0) = 0$	massless neutralino	2 lepton

Table 1.2: *Schematic description of the models investigated by ATLAS for the $\tilde{t} \to b\,\tilde{\chi}^{\pm}$ decay mode. In the last column the final state with the major sensitivity in a certain masses assumption is indicated.*

1.4 The connection between top quarks, neutralinos and Dark Matter

Astrophysical observations have provided compelling proof for the existence of a non-baryonic dark component of the universe: Dark Matter (DM). The DM abundance has been precisely measured [69–73] and corresponds to 27% of the total universe content. The nature of DM is not known, but from the theoretical point of view the most studied candidate is represented by a Weakly Interacting Massive Particle (WIMP): a neutral particle with weak-scale mass and weak interactions, whose thermal relic density may naturally fit the observed DM abundance. R-parity conserving SUSY models provide a natural WIMP candidate for DM: the neutralino. In the last chapter of this thesis, the signal selections used to search for $\tilde{t} \to t\,\tilde{\chi}^0$ will be used to interpret the results in terms of DM models.

Searches for DM particles, indicated in the following with the symbol χ, are performed using three orthogonal approaches:

a) Direct detection searches that exploit the high local DM density ($\sim 0.3\,\mathrm{GeV/cm^3}$) to detect WIMP scattering on nuclei: $\chi + N \to \chi + N$, where N is a nucleon.

b) Indirect (astrophysical) searches that look for DM annihilation processes and exploit the Majorana nature of WIMPs: $\chi\chi \to SM\ SM$, where SM represents any SM particle.

c) LHC searches that look for processes where DM is directly produced: $pp \to \chi\chi + X$. Since DM is revealed as missing transverse momentum, X, that might be a quark, a photon or a gauge boson, determines the strategy of the search.

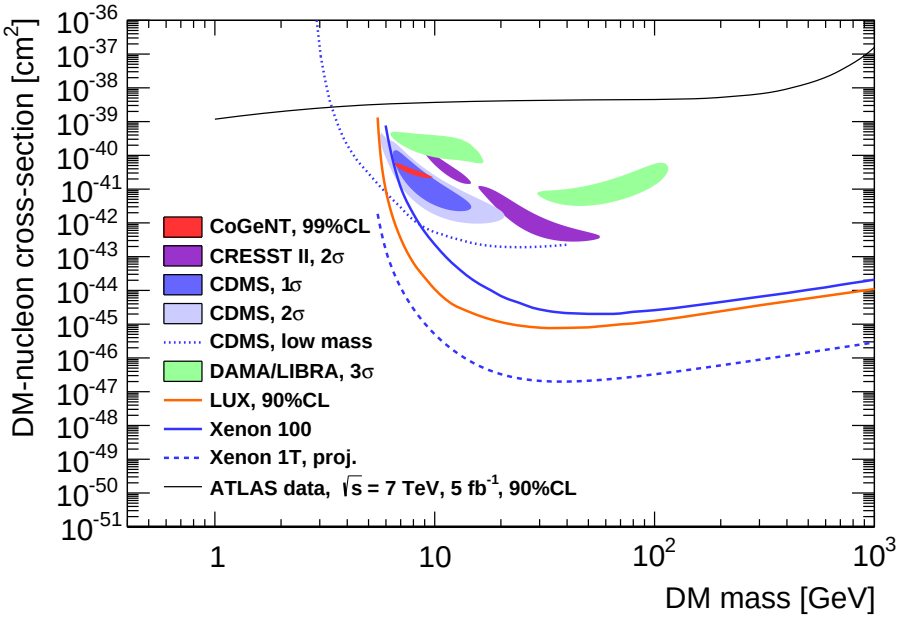

Figure 1.7: *Dotted and solid lines show the most recent upper limits at 90% confidence level (99% for CoGent) on WIMP-nucleon scattering cross section. The most favourable regions for DM candidates reported by DAMA, CRESS and CDMS Collaborations are shown as filled contours. The ATLAS 7 TeV results for contact operator D5 are shown as a black solid line and has a reach to lower DM masses than the direct detection experiments.*

WIMP-DM (χ)	ID	interaction	Operator	G_χ
Dirac scalar	D1	quarks	$\bar{\chi}\chi\bar{q}q$	m_q/M_*^3
Dirac axial	D5	quarks	$\bar{\chi}\gamma^\mu\chi\bar{q}\gamma_\mu q$	$1/M_*^2$
Dirac vector-axial	D9	quarks	$\bar{\chi}\sigma^{\mu\nu}\chi\bar{q}\sigma_{\mu\nu}q$	$1/M_*^2$
Dirac scalar	D11	gluons	$\bar{\chi}\chi G_{\mu\nu}G^{\mu\nu}$	$\alpha_s/4M_*^3$
complex scalar	C1	quarks	$\chi^\dagger\chi\bar{q}q$	m_q/M_*^2
complex scalar	C5	gluons	$\chi^\dagger\chi G_{\mu\nu}G^{\mu\nu}$	$\alpha_s/4M_*^2$

Table 1.3: *Most important contact operators describing the interaction of a Dirac or complex scalar DM particles (χ) with quarks or gluons [76]. G_χ is the coupling of the contact operator and it is defined in Eq.* (1.25)*.*

Tantalising (although controversial) hints of a DM particle with mass of a few GeV are coming from direct detection experiments such as DAMA and CoGent ([74, 75]). The most recent results in terms of WIMP-nucleon scattering cross section upper limits and observations are shown in Figure 1.7. As visible in the plot, LHC searches are most effective for highly boosted, light WIMPs, therefore it is becoming extremely important to probe DM production in order to confirm, or contradict such claims.

Without hints of SUSY, DM searches in pp collisions are performed with a model-independent, Effective Field Theory (EFT) approach. Interactions between DM particles and the SM sector are parametrised by a set of effective (non-renormalizable) operators, generated after integrating out heavy mediators. Dimension six operators

Operator	κ [cm^2]	B [GeV]	C [GeV]	exponent y
D1	1.6×10^{-37}		20	6
D5	1.38×10^{-37}		300	4
D9	9.18×10^{-40}		300	4
D11	3.83×10^{-41}		100	6
C1	2.56×10^{-36}	100	10	4
C5	7.4×10^{-39}	100	60	4

Table 1.4: *Factors used in Eqs.* (1.26) *and* (1.27) *for converting M_* into χ-nucleon cross section [76].*

describe the interactions with quarks and are of the form:

$$\mathcal{L}_{eff} = G_\chi \sum_{quarks} \mathcal{O}(\chi, q), \tag{1.23}$$

while dimension seven operators describe the interaction with gluons (G):

$$\mathcal{L}_{eff} = G_\chi \mathcal{O}(\chi, G). \tag{1.24}$$

$\mathcal{O}$ is one of all possible operators (up to a certain order) that can be considered in the contact interaction of DM with quarks (and gluons) and can be classified in a systematic way [76, 77]. The most important operators for Dirac and complex scalar χ from Ref. [76] are summarised in Table 1.3. The coupling constant, G_χ, is fixed to lead to the correct relic density for WIMPs. This is related to the mass of the mediator of the interaction, M_Ψ, and the couplings of the mediator to χ and quarks, g_q, g_χ:

$$G_\chi = \frac{g_q g_\chi}{M_\Psi^2} \equiv \frac{1}{M_*^2}. \tag{1.25}$$

For each operator the relic abundance, direct detection signal, and collider prediction depend on a single parameter, the *reduced coupling* M_*, through which they can be simply related. This parameter can also be easily compared among the three types of DM searches. For convenience this parameter can be converted into a DM-nucleon scattering cross section. The exact formula will depend on the contact operator that is considered [76]:

$$\sigma^D(\chi, n) = \kappa \mathrm{cm}^2 \left(\frac{\mu_\chi}{1\ \mathrm{GeV}}\right)^2 \left(\frac{C}{M_*}\right)^y \tag{1.26}$$

$$\sigma^C(\chi, n) = \kappa \mathrm{cm}^2 \left(\frac{\mu_\chi}{1\ \mathrm{GeV}}\right)^2 \left(\frac{B}{m_\chi}\right)^2 \left(\frac{C}{M_*}\right)^y. \tag{1.27}$$

The reduced mass μ_χ is defined as:

$$\mu_\chi = \frac{m_\chi \cdot m_n}{m_\chi + m_n}, \tag{1.28}$$

with m_n the nucleon mass and m_χ the DM mass. κ, B, C and the exponent y are listed in Table 1.4 for the most important operators.

It is important to realise that while for direct and astrophysical DM searches the EFT description is completely justified by the energy scales involved, at the LHC the

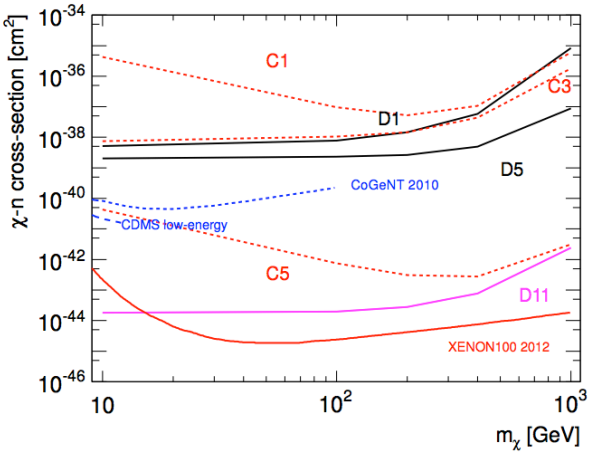

Figure 1.8: *Combination of current collider-based upper limits at 90% confidence level on the spin independent WIMP-nucleon cross section for major contact operators listed in Table 1.3 [78].*

situation is different. In this case the energies can be very high and the processes one wishes to describe in terms of effective operators can actually occur at an energy beyond the validity of the EFT itself. A rough estimate of the EFT validity [78] for s-channel mediator exchange is furnished by $M_\Psi > 2m_\chi$, that accounting for different

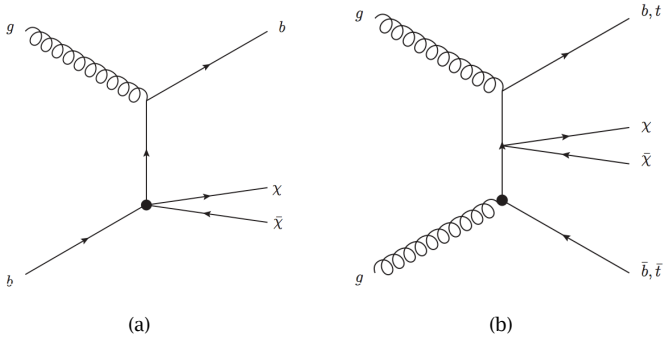

Figure 1.9: *Dominant Feynman diagrams for dark matter production in conjunction with heavy quarks [79].*

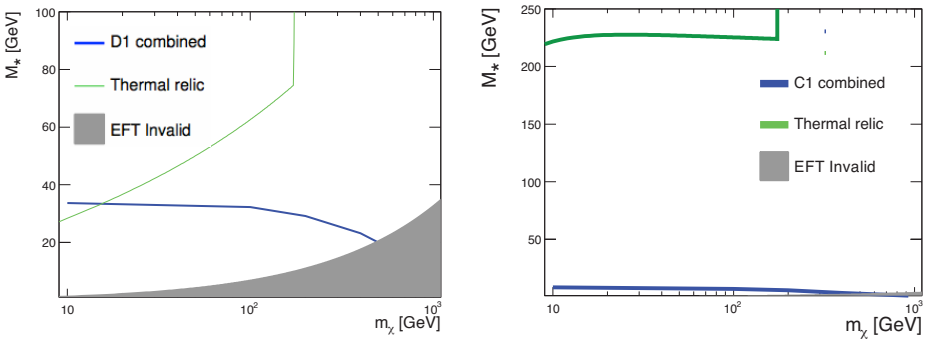

(a) Dirac scalar (b) Complex scalar

Figure 1.10: *Collider based limits at 90% confidence level on M_* from Ref. [78] for scalar interaction of Dirac and complex scalar DM (D1 and C1 operators, respectively) are indicated by the solid blue curve. Values below the line are excluded. The green line indicates the limit on M_* for which WIMPs can couple to quarks or gluons exclusively via the given operator and account entirely for the relic density measured by WMAP.*

factors in the operators translates into the following M_* validity ranges:

$$\sqrt{\frac{M_*^3}{m_q}} > \frac{m_\chi}{2\pi} \qquad (D1) \tag{1.29}$$

$$M_* > \frac{m_\chi}{2\pi} \qquad (D5, D9, D11, C5) \tag{1.30}$$

$$\frac{M_*^2}{m_q} > \frac{m_\chi}{8\pi^2} \qquad (C1). \tag{1.31}$$

A more complete discussion on the limits of EFT at the LHC can be found in Ref. [80].

A summary of the current collider-based limits in the context of effective field theories is given in Figure 1.8 [78]. The results combine the most recent collider upper limits on:

$$pp \to \chi\bar{\chi} + X, \tag{1.32}$$

with X being a gluon, a quark, a photon or a $W^\pm$ or Z boson. The couplings of some of the operators listed in Table 1.3 have a dependence on the quark mass. This implies that the production cross section for $pp \to \chi\chi q$ will be enhanced for heavy flavour quarks (bottom and especially top quarks, Fig. 1.9) and dedicated searches will improve the current limits (Figure 1.10). In Chapter 9 a re-interpretation of the

stop search in the $t\bar{t} + E_{\mathrm{T}}^{\mathrm{miss}}$ final state described in Part 3 of this thesis will be presented in terms of limits for the operators that have a quark mass dependence (D1, C1). DM masses of 10, 50, 100, 200, 400, 700, 1000 GeV, are considered. The highest sensitivity for searches in ATLAS is at low DM masses, i.e. $m_{\chi} < 100$ GeV.

2 The ATLAS experiment

The data analysed in this thesis have been produced during the LHC Run I in the years 2011 and 2012 and collected by the ATLAS experiment. A brief description of the accelerator and a more detailed description of the ATLAS experiment are given in this chapter with attention to the subsystems relevant for the analyses described in this thesis. Then a section is devoted to the description of the data taking operation and monitoring of one of the sub-detectors of the inner tracker and the improvement of the inner tracker performance through the alignment of its components.

2.1 The LHC accelerator and collider

The Large Hadron Collider (LHC) [81, 82] is a proton-proton (pp) accelerator and collider located at CERN in Geneva (Switzerland). The LHC project was first approved in December 1994 and the LHC was built exploiting the already existing tunnel of the LEP collider that was switched off in November 2000 to give way to the LHC. At the time of writing the LHC has successfully operated for three years, from 2010 to 2012, colliding protons at a centre-of-mass energy of 7 and 8 TeV. In addition, the LHC has collided heavy ions (Pb^{82+}) at a centre-of-mass energy of 2.76 TeV and p-Pb at a centre-of-mass energy of 5.02 TeV.

The acceleration cycle for proton collisions starts with the production of protons from ionised hydrogen atoms H^+, which are accelerated to 50 MeV in the Linac-2.

Subsequently, the protons are injected into a chain of injectors, namely the Proton Synchrotron Booster (PSB), the Proton Synchrotron (PS) and the Super Proton Synchrotron (SPS) as represented in Figure 2.1.
The PS+SPS complex accelerates the proton beams up to 450 GeV. The beams are then injected in the LHC and accelerated in both directions in the form of spatially distinct bunches, with an inter-bunch distance of 50 ns[1)] which corresponds to 15 m. The beams are brought to collision in the four interaction points, where the four LHC experiments (ATLAS, CMS, LHCb and ALICE) are situated. They are collided with a small crossing angle between the beams of the order of $150 - 200$ μrad to avoid the occurrence of parasitic bunch crossings.

One of the main goals of the LHC is the discovery of rare processes. The rate R_X at which a certain process X is produced in a collision is given by the product of the luminosity of the beams, $\mathcal{L}$, and the cross section of the process, σ_X, that depends on the centre-of-mass energy of the collider, $\sqrt{s}$:

$$R_x = \mathcal{L}\,\sigma(\sqrt{s}). \tag{2.1}$$

Thus the key performance parameters of the accelerator are:

- $\sqrt{s}$: the centre-of-mass energy, which expresses the energy available in the collision; this parameter defines the accessible phase-space of the final states of the reaction as well the mass of the particles that can be created. The production cross section (σ) of a certain process is a function of this parameter. The centre-of-mass energy reached by the LHC is 7 and 8 TeV for 2011 and 2012 datasets, respectively.

- $\mathcal{L}$: is the delivered instantaneous luminosity. This depends on the number of protons in the bunch, the number of bunches and the configuration of the magnets (quadrupoles) in the proximity of the experiments, which have to focus the beams into the point where the collisions take place. The luminosity can be approximated by:

$$\mathcal{L} = \frac{N_B\, f_{\text{rev}}\, N_p^2}{4\pi\, \sigma_{\text{T}}^2}, \tag{2.2}$$

  where N_B denotes the number of bunches, f_{rev} is the revolution frequency, N_p is the number of protons per bunch, and σ_{T} is the transverse beam size at

[1)] The design distance between the LHC bunches is 25 ns. This has been successfully obtained in a few test fills during operations and will be the operating bunch distance when operations will be resumed after the long shutdown period (2013-2014)

the interaction point. The peak luminosity world record for proton collisions was obtained the 24th of August 2012 with a value of $7.73 \cdot 10^{33}\,\mathrm{cm}^{-2}\mathrm{s}^{-1}$. This instantaneous luminosity is so high that for each bunch crossing many collisions may occur. The average number of additional collisions (or pile-up) was 9 and 21 for 2011 and 2012 respectively and was characterised in both years by a widely spread distribution determined by the improvement in the machine performance throughout the data-taking period.

The amount of data delivered by the LHC and recorded by ATLAS is measured as luminosity integrated over time ($\int \mathcal{L}\, dt$). The recorded data good for physics analyses is $4.7\,\mathrm{fb}^{-1}$ [83] and $20.3\,\mathrm{fb}^{-1}$ [84] for 2011 and 2012, respectively. The delivered and recorded luminosity integrated throughout 2011 and 2012 is shown in Figure 2.2.

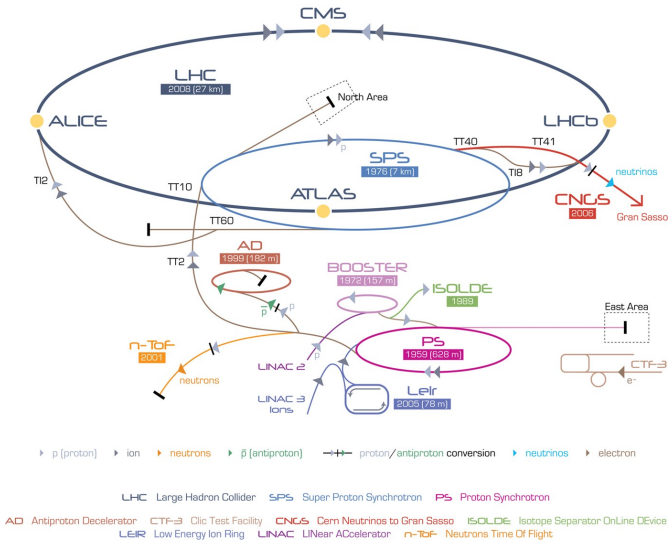

Figure 2.1: *Schematic representation of the LHC accelerator and injection chain. The four LHC experiments are indicated as well.*

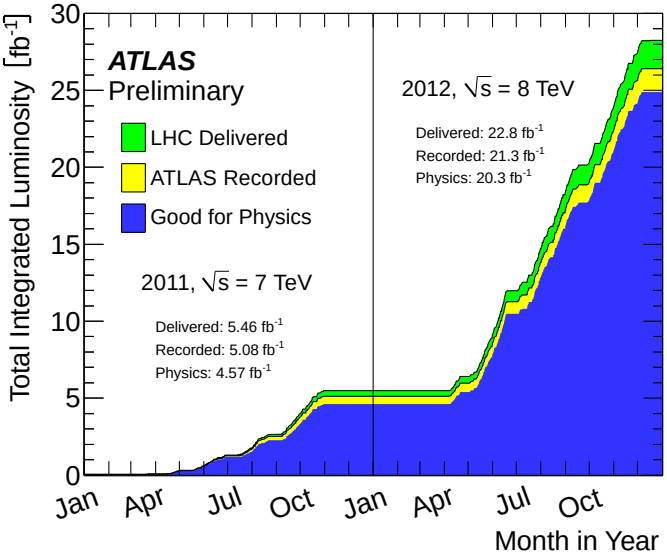

Figure 2.2: *Cumulative luminosity versus time, delivered by the LHC (green), recorded by ATLAS (yellow), and certified to be good quality data (blue) during stable beams and for pp collisions at 7 and 8 TeV centre-of-mass energy in 2011 and 2012.*

2.2 The ATLAS experiment: detector

The ATLAS detector is a general-purpose experiment that detects and records collisions produced at the LHC. A comprehensive description can be found in Ref. [85]. In this chapter we present a summary of its structure and sub-detectors, in order to introduce the detection systems and mechanisms of relevance for the presented analyses.

The ATLAS geometry can be best described in cylindrical coordinates, since they reflect the detector geometry. The azimuthal angle ϕ ($\phi = 0$ on the x direction) and the polar angle θ ($\theta = 0$ along the positive z axis) are used as default in ATLAS. In addition to those, a z-boost invariant variable, the pseudorapidity, is commonly used:

$$\eta = -\ln\left(\tan\frac{\theta}{2}\right). \tag{2.3}$$

The ATLAS detector is nominally forward-backward symmetric with respect to the interaction point. The products of the interaction are detected, measured and identified in different layers of the detector elements. The detector structure (as well as each sub-detector) can be divided into three parts:

Barrel The *Barrel* is the cylindrically symmetrical central part of the detector and covers a pseudorapidity range of approximately $|\eta| < 1.4$.

End-caps The longitudinal hermeticity of the detector is guaranteed by two circular structures that close off the two sides of the *Barrel*. These structures are called *End-caps* and extend into a pseudorapidity range of $1.5 < |\eta| < 5$, with some overlap with the *Barrel* coverage.

A cut-out view of the ATLAS detector is shown in Figure 2.3. The magnet configuration comprises a thin superconducting solenoid surrounding the Inner Detector (ID) creating a magnetic field of 2 T, and three large superconducting toroids (one *Barrel* and two *End-caps*) of which the coils are arranged with an eight-fold azimuthal symmetry around the calorimeters. These strong magnetic fields bend the trajectories of the charged particles allowing for a precise momentum measurement.
From small to large radii around the interaction point, ATLAS is composed of an:

Inner Tracker Tracking of charged particles and vertex reconstruction are achieved with a combination of high-resolution semiconductor pixel and strip detectors in the inner part of the tracking volume, and straw-tube tracking detectors with the capability to generate and detect transition radiation in its outer

part. The pseudorapidity coverage provided by this ID is $|\eta| < 2.5$. The resolution achieved by the tracking system momentum measurement is $\sigma_{p_T}/p_T = 0.05\% p_T(\text{GeV}) \oplus 1\%$.

Calorimetry The calorimeter is placed outside the solenoid covers $|\eta| < 4.9$ and is composed of sampling electromagnetic and hadronic calorimeters with either liquid Argon (LAr) or scintillating tiles as the active media. Its main goal is the absorption of electrons, photons and hadrons and the measurement of their energy.

The resolution of the calorimeters is given by $\sigma_E/E = 10\%/\sqrt{E(\text{GeV})} \oplus 0.7$ for the electromagnetic calorimeter and $\sigma_E/E = 100\%/\sqrt{E(\text{GeV})} \oplus 10\%$ for the hadronic one.

Muon system The Muon Spectrometer (MS) surrounds the calorimeter. A muon momentum resolution of $\sigma_p/p = 25\%/p_T(\text{TeV}) \oplus 17\% p_T(\text{TeV}) \oplus 3\%$ [86, 87] is achieved in 2011 in the barrel region with three layers of high precision tracking chambers and fast triggering chambers. The air-core toroid system generates strong bending power (1-7 Tm) in a large volume within a light and open structure and minimises multiple-scattering effects.

As previously mentioned, the LHC provides a bunch crossing every 50 ns, which converts into a bunch crossing rate of 20 MHz, impossible to entirely record. For this reason, an online event selection, called *trigger* system, is employed in ATLAS in order to select only the most interesting collisions, where a hard scattering has occurred between the partons inside the protons, from the *Minimum Bias* background[2)]. The decision chain is divided into three different stages. The *Level-1* trigger is a hardware implemented, fast triggering system. This trigger uses reduced granularity information from the muon system and the calorimeters and it is able to handle the incoming bunch crossing rate, reducing it to 75 kHz. The following stages of triggering, the *Level-2* and the *Event Filter* are high level filters that use all detector information and reduce the total rate incoming to the 400 Hz that is possible to write on disk. With an average event size of 1.5 MB this converts to a data storage rate of 600 MB/s. The *Level-2* decision is seeded by regions of interest of the detector based on the objects identified by the *Level-1*. For these regions, the *Level-2* trigger accesses the full granularity information for all sub-detectors and has a processing

[2)] Typically, interaction with low momentum transfer between the protons.

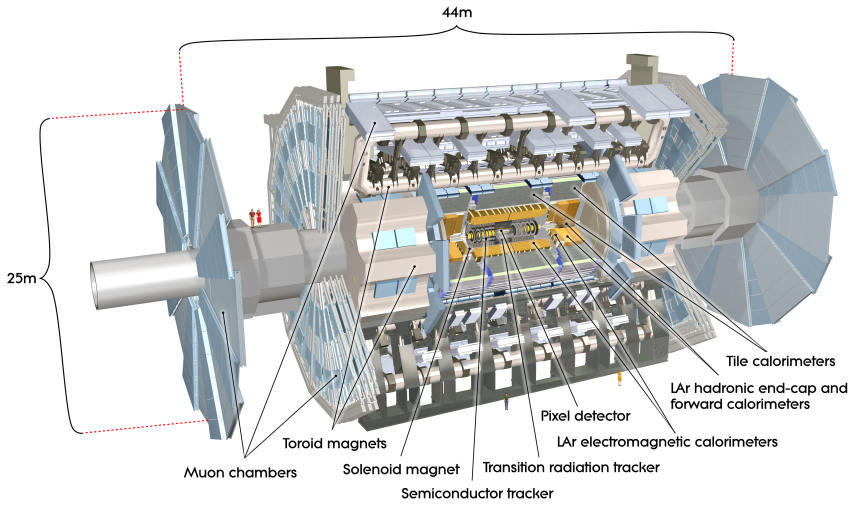

Figure 2.3: *A cut-out view of the ATLAS detector with the innermost tracking detectors, followed by the calorimeters and enclosed by the largest system, the muon spectrometer. The magnet toroid structures in the* Barrel *can be seen between the muon chambers.*

time of approximately 40 ms. Finally, the *Event Filter* rebuilds the full event using the standard ATLAS event reconstruction. The event processing time is about 4 s and the total data taking rate is achieved by parallelisation of the reconstruction on a farm of 1500 CPUs.

2.2.1 The Inner Detector (ID)

In order to reconstruct the trajectories of the charged particles produced in the collisions, ATLAS is equipped with a tracking system built on two different technologies: silicon planar sensors (pixel and micro-strip) and drift-tube based detectors.

The innermost silicon based detector is the *Pixel* detector. In the *Barrel* region it consists of three concentric cylinders around the beam axis at average radii of 5.05, 8.85 and 12.2 cm (1456 modules), and three disks on each *End-cap* side, between radii of 9 and 15 cm (288 modules), respectively. The first of these layers is the closest to the interaction region, and its radial distance to it drives the impact parameter resolution; since this is extremely important for an efficient b-jet identification, the first layer is usually called the B-Layer.

The pixel sensors are made of oxygenated $250\,\mu$m thick n-type wafers with readout pixels on the n+ implanted side of the detector. Each pixel has a size of $50 \times 400\,\mu\text{m}^2$ which determines the intrinsic resolution of the detector and is limited by the size of the corresponding readout cell on the readout chip. The high granularity of the innermost tracking system is the crucial element to achieve a robust pattern recognition in the high occupancy and pile-up environment of ATLAS. It results in an intrinsic accuracy of $10\,\mu$m in $(r-\phi)$ and $115\,\mu$m in z.

Outside the *Pixel* detector there is a second silicon based sub-detector, called the SCT. It comprises 15392 silicon sensors assembled into 4088 independently powered and operated modules of silicon-strip detectors arranged in four concentric layers in the *Barrel* region of the detector (pseudorapidity range extends to $|\eta| < 1.4$) and in 9 disks for each of the two *End-caps* (pseudorapidity range $1.1 < |\eta| < 2.5$). The *Barrel* modules are of uniform design, with strips approximately parallel to the magnetic field and the beam axis. The *End-cap* consists of up to three rings of modules with trapezoidal sensors and the strip direction is radial with constant azimuthal angle. Each module is designed, constructed and tested to operate as a stand-alone unit, mechanically, electrically, optically and thermally. The modules consist of up to four silicon strip sensors of size $6\,\text{cm} \times 6\,\text{cm}$ with a strip pitch of $80\ \mu$m. Two sensors on each side are chained together and a second pair is glued back-to-back with the first at a stereo angle of 40 mrad, in order to provide three dimensional information.

The outermost element of the Inner Detector (ID) is the TRT. It uses a gas-filled polyamide drift straw tubes technology and allows for pion versus electron separation by absorbing and measuring transition-radiation photons. The TRT provides only (r, ϕ) information, for which it has an intrinsic accuracy of $130\,\mu$m per straw. In the *Barrel* region, the straws are parallel to the beam axis and are $144\,\text{cm}$ long. In the *End-cap* region the $37\,\text{cm}$ long straws are arranged radially in wheels. Despite the fact that the TRT intrinsic resolution cannot compete with the resolution of the silicon technology, the straw-tube based detectors allow for a high number of samplings (on average 36 per track) and a long lever arm that significantly contribute to the momentum resolution of the tracks.

2.2.2 The calorimetry system

The ATLAS detector is equipped with a hermetic calorimetry system that is extensively described in Refs. [88] and [89]. It employs different technologies across the different regions in pseudorapidity and in different sub-detectors and guarantees

a large pseudorapidity coverage (up to $|\eta| = 4.9$) as well as a good energy measurement of hadrons, photons and electrons. A cut-away view of the calorimetry system is shown in Figure 2.5.

Both the electromagnetic and the hadronic calorimeters are designed to contain showers of particles up to the TeV scale, since energy escaping from the calorimeter results in reduced energy resolution and in punch throughs into the muon system. For this reason, the electromagnetic calorimeter thickness is 22 and 24 radiation lengths (X_0), for *Barrel* and *End-caps*, respectively, and the hadronic calorimeter is 11 interaction lengths (λ) deep.

The electromagnetic calorimeter is a liquid-Argon sampling detector with accordion-shaped electrodes and lead absorber plates over its full coverage. The accordion geometry provides complete ϕ symmetry without azimuthal cracks. The thickness of the lead absorber plates has been optimised in order to compromise costs, full coverage and high energy resolution in the regions devoted to precision physics.

In the region of $|\eta| < 1.8$, a pre-sampler detector is used to correct for the energy lost by electrons and photons between the interaction point and the calorimeter. The pre-sampler consists of an active LAr layer of thickness 1.1 cm (0.5 cm) in the *Barrel* (*End-cap*) region.

The outer hadronic calorimeter employs scintillator tiles as sampling medium and steel as absorber medium. The tile calorimeter covers the range $0 < |\eta| < 1.7$. The hadronic calorimetry is extended to larger pseudorapidities by the Hadronic End-cap Calorimeter (HEC), a copper/liquid-Argon detector composed of two wheels per *End-cap* and located directly behind the *End-cap* electromagnetic calorimeter.

The Forward Calorimeter (FCal), a copper-tungsten/liquid-Argon detector, provides calorimetry coverage for the pseudorapidity range of $3 < |\eta| < 4.9$. The FCal is approximately 10 interaction lengths thick and consists of three modules in each *End-cap*: the first, made of copper, is optimised for electromagnetic measurements, while the other two, made of tungsten, measure predominantly the energy of hadronic interactions.

2.2.3 The muon spectrometer

The ATLAS muon spectrometer [90], shown in Figure 2.6, is designed to provide precision muon momentum measurements and a stand-alone trigger subsystem. The muon momentum measurement relies on the magnetic deflection of muon tracks in the large superconducting air-core toroid magnets. Over the range $|\eta| < 1.4$,

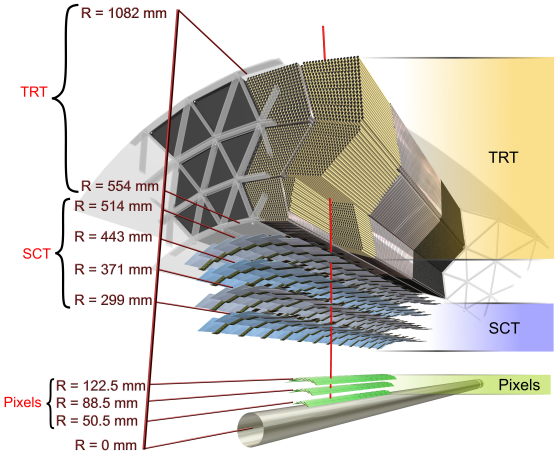

Figure 2.4: *Drawing of the sensors and structural elements traversed by a charged track of* 10 GeV p_T *in the* Barrel *Inner Detector. The track traverses successively the beryllium beampipe, the three cylindrical silicon-pixel layers (Pixel detector), the four cylindrical double layers of* Barrel *silicon-microstrip sensors (SCT), and approximately 36 axial straws contained in the* Barrel *transition-radiation tracker modules (TRT).*

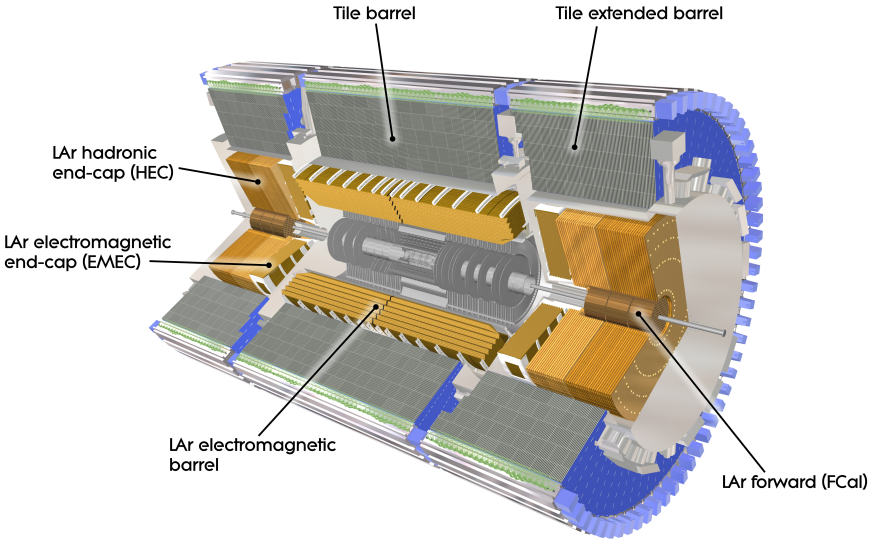

Figure 2.5: *A cut-out view of the ATLAS calorimetry system.*

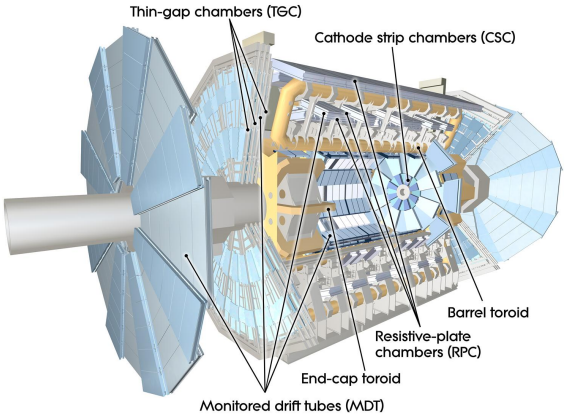

Figure 2.6: *Cut-away view of the ATLAS muon spectrometer*

magnetic bending is provided by the large *Barrel* toroid. For $1.6 < |\eta| < 2.7$, muon tracks are bent by two smaller *End-cap* magnets inserted into both ends of the *Barrel* toroid. Over $1.4 < |\eta| < 1.6$, usually referred to as the transition region, magnetic deflection is provided by a combination of *Barrel* and *End-cap* fields. This magnet configuration provides a field which is mostly orthogonal to the muon trajectories, while minimising the degradation of resolution due to multiple scattering.

The precision chambers are made of Monitored Drift Tubes (MDTs) and of Cathode Strip Chambers (CSCs), while the trigger is provided by Resistive Plate Chambers (RPCs) and Thin Gap Chambers (TGCs). The muon spectrometer is the largest detector system and extends up to a radius of $\sim 10\,\text{m}$ and a z-position of $21.5\,\text{m}$ with respect to the centre of the ATLAS reference frame. The trigger chambers provide the trigger system with the information about the multiplicity and transverse momentum of muons. It also complements the precision chambers with additional information about the track position in the non-bending plane (ϕ coordinate).

2.3 The ATLAS experiment: performance monitoring and improvement

The ATLAS detector is often denoted as a *general purpose* experiment, with the aim to express that behind its design lies the purpose of performing a large variety of very different measurements with the data collected in the next twenty years of

data taking.

For this reason, it is of utmost importance to ensure that the detector reaches, and if possible outperforms, its design requirements.
This can be summarised in three different key points of action:

(a) Guarantee that the detector efficiently records high quality data. This is ensured by a constant monitoring of the collected data.

(b) Increase the understanding of the detector in order to improve the performance and achieve a precise simulation description;

(c) Evaluate the time evolution of the detector's performance, both in the long and in the short term, to ensure the detector's health throughout the experiment lifetime.

The number of tasks, sub-groups and manpower employed to achieve these results in a complex detector such as ATLAS is enormous. In this section we will outline two examples of performance monitoring and improvement, namely the alignment of the Inner Detector and the monitoring of the acquired data of the SCT.

The former is very important in any physics analysis involving b-jets or isolated charged particles such as electrons and muons. The knowledge of the position of each single module of the tracking system, down to the micrometer precision, has an impact on both the momentum resolution of tracks and the track impact parameter that are used as input in the b-tagging algorithms introduced in Sec 3.2.2.

The second example will outline the various observables on which the SCT monitoring is based, since the assessment of the quality of the data recorded by the silicon tracker is of obvious importance for all analyses relying on tracks.

2.3.1 Alignment of the Inner Detector: performance improvement

The precise knowledge of the position of the different modules, layers, disks and wheels of the sub-detectors that compose the Inner Detector (ID) is of utmost importance for physics analyses relying on b-jets tagging and or isolated charged particles.

The main goal of the ID alignment is to ensure that at high transverse momentum the degradation of momentum resolution due to non perfect alignment does not exceed 20% of the momentum resolution of a perfectly aligned detector.

The current achieved precision in term of position alignment is shown in Table 2.1.

sub-detector		Module Resolution $x \times y$ [μm]	Alignable Objs
Pixel	*Barrel*	10×115	1744
	End-caps	16×140	
SCT	*Barrel*	17×580	4088
	End-caps	30	
TRT		130	350848

Table 2.1: *Module resolution and number of alignable objects of the ID components. x and y are the two cartesian coordinates in the plane of the silicon module with x in the most sensitive direction, or x perpendicular to the TRT straw.*

Alignment procedure and track based algorithms

The ID alignment is performed at three different levels of granularity, where collections of detector elements (modules, wires), corresponding to substructures of various sizes, are treated as rigid bodies with three translational and three rotational degrees of freedom each (2 DoFs for TRT single straws).

At the first level, the sub-detector structures are aligned: all Pixel detectors are treated as a single unit and SCT and TRT are composed of 3 structures each (*Barrel* plus 2 *End-caps*). At the second level, silicon *Barrels* and *End-cap* disks, TRT *Barrel* modules and *End-cap* wheels are considered. The number of degrees of freedom that are aligned at this level is 1260. At the third level the single modules and wires are aligned, for a total degrees of freedom of 726800.

To this purpose, two main track-based algorithms have been developed and used in ATLAS:

a) *Global* χ^2 (Baseline) [91]

b) *Local* χ^2 [92]

The *Global* and *Local* alignment algorithms rely on the minimisation of a χ^2 constructed on track-hit residuals. The alignment χ^2 is defined as [93]:

$$\chi^2 = \sum_{tracks} \left[\vec{r}(a,\tau)\right]^T V^{-1} \left[\vec{r}(a,\tau)\right] \tag{2.4}$$

where V is the individual hit covariance matrix; the vector of the residual parameters $\vec{r}(a,\tau)$ is defined as the distance between the measured hit position and the

extrapolated track intersection in the module plane and it depends on the track parameters $\tau = (d_0, z_0, \phi_0, \theta, q/p)$ and the alignment parameters a. The latter are determined from:

$$\frac{\mathrm{d}\chi^2}{\mathrm{da}} = 0 \qquad \Rightarrow \qquad \sum\left[\left(\frac{d\vec{r}}{da}\right)^T V^{-1}\left(\frac{d\vec{r}}{da}\right)\right]\delta a + \sum\left(\frac{d\vec{r}}{da}\right)^T V^{-1}\vec{r_0} = 0, \tag{2.5}$$

where $\vec{r_0}$ refers to the vector of residuals calculated for the initial track parameters. This requires solving a linear system with a number of equations equal to the number Degrees of Freedom (DoF).

The individual hit covariance matrix (V) does not have any correlations, i.e. all measurements including scatterings are assumed to be independent. On the other hand, correlations between the alignment parameters are considered in Equation (2.4). The *Global* χ^2 approach is used for systems of equations that involve up to the entire silicon tracking system (35000 DoFs). However, it is practically impossible to solve the $\sim 7 \cdot 10^5$ DoF set of linear equations of the third level alignment without a dedicated computing hardware. For problems of this size, the *Local* χ^2 algorithm is used, which neglects correlations between the alignment parameters, and allows to solve for such a high number of DoFs at the third level of granularity.

The implementation of the track-based alignment within the ATLAS software framework unifies different alignment approaches and allows the alignment of all tracking subsystems together. The alignment-specific classes derive from the track reconstruction software and provide tools for computation of necessary quantities (residuals, pulls, track derivatives, covariance matrices). Solving the *Global* χ^2 problem poses a computational challenge as it involves inversion of a large matrix that may be not sparse and not diagonal. Fast solving algorithms as well as full diagonalization have been implemented.

The alignment software also has the ability to introduce constraints on track parameters (beam spot, primary vertex, momentum from the ATLAS muon system, momentum charge asymmetry from calorimeter information) or on the alignment parameters, in order to help control "weak modes" of the solution, which are due to distortions of the detector.

Monitoring and performance of the detector alignment

The detector alignment is monitored by means of a python-based monitoring infrastructure that collects properties of individual tracks, the beam spot, well known resonances such as K^0_s, J/Ψ, Υ, Z for each run recorded by ATLAS. Both the produc-

tion and the validation of alignment constants are done using the LHC Computing Grid (LCG), allowing access to all datasets, usage of thousands of CPUs and virtually unlimited disk storage.

The track residual distributions are also used to monitor and validate the alignment sets and to decide whether updates are needed due to considerable detector movements. Since 2012, whenever detector movements are identified (for example in case of change of the cooling or the magnetic field conditions), a new set of alignment constants is produced on the fly and applied to the data reconstruction algorithms. In addition, alignment constants are re-computed before each data reprocessing campaign, approximately two or three times per year.

Residual distributions The performance of the alignment is visible in Figure 2.7, where residual distributions for Pixel and SCT *Barrels* in 2011 proton-proton collisions are presented. The distributions are centred at zero and the resolution, indicated in the legend of the plots, approaches that of a perfectly aligned Monte Carlo simulation.

Correcting weak modes The track-based algorithms guarantee that the various components of the detector are aligned in order to provide an efficient and good-quality track fit. A number of detector distortions, that leave the track residuals unaffected and are not corrected by the track-based algorithm, can still largely bias the track reconstructed parameters. Such distortions are referred to as "weak modes". Especially dangerous are misalignments affecting the particle momentum and impact parameters which are key ingredients for physics measurements.

In order to remove weak modes, one needs to rely on additional information, such as vertex constraints, well-known resonances and calorimeter information.

Large charge-antisymmetric momentum biases, measured in terms of variation of the sagitta of the track δ_{sagitta}, have been removed in the 2011 data using the difference of energy of electrons and positrons measured in the calorimeters. This type of weak mode affects the reconstructed momentum as shown in Equation 2.6:

$$q/p \to q/p(1 + qp_T\delta_{\text{sagitta}}). \tag{2.6}$$

In the equation q is the electron charge and p_T its transverse momentum. δ_{sagitta} is the bias on the track transverse momentum induced by alignment distortions in units of TeV^{-1} and it is independently measured using the dependence of the reconstructed $Z \to \mu^+\mu^-$ invariant mass on the $\mu^+\mu^-$ kinematics. Figure 2.8(a) shows

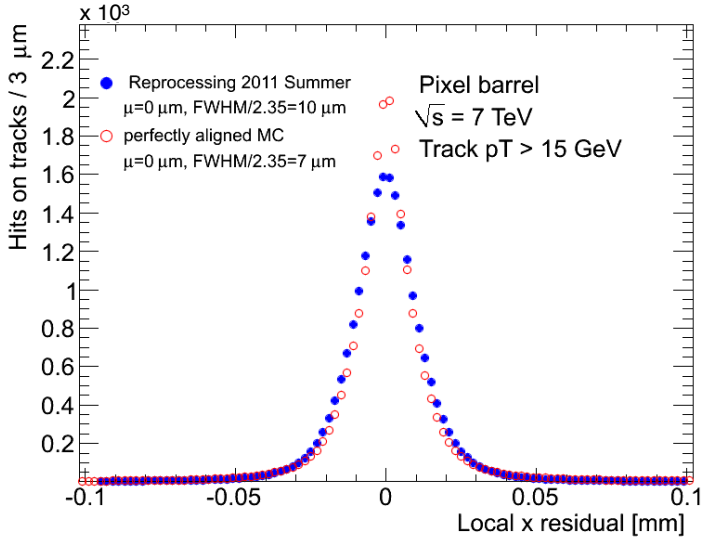

(a) Pixel *Barrel*

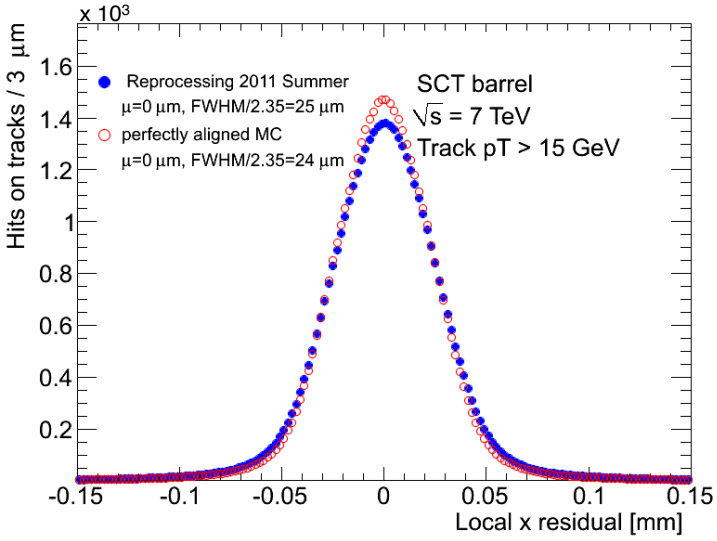

(b) SCT *Barrel*

Figure 2.7: *Residual distribution in Pixel and SCT* Barrel. *2011 proton-proton collisions are compared to perfectly aligned Monte Carlo and the width of each distribution is shown in the legend.*

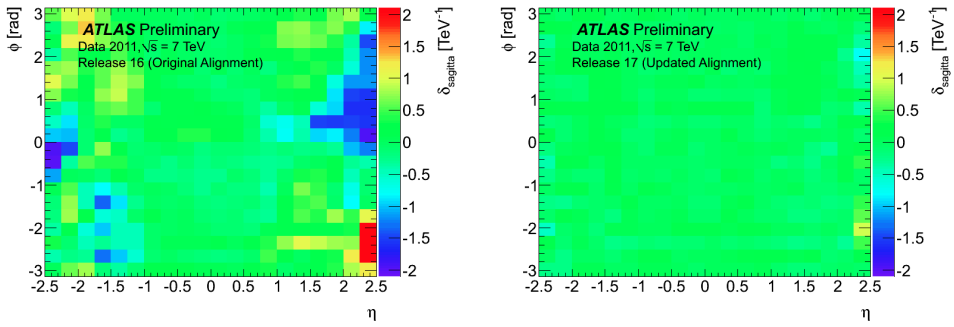

(a) Original Alignment

(b) Updated Alignment

Figure 2.8: *Weak-mode bias in 2011 proton-proton collisions [94]. In the plots η is a function of the polar angle θ (pseudorapidity $\eta = -\ln\tan(\theta/2)$) and phi the azimuthal angle. δ_{sagitta} is bias on the track momentum introduced by the distortion and measured using $Z \to \mu\mu$ events.*

a momentum bias (δ_{sagitta}) before the alignment correction. Local biases up to 8% can be observed.

The results after momentum-constrained alignment of the detector are shown in Figure 2.8(b). Charge-antisymmetric momentum biases have been reduced by an order of magnitude resulting in a uniform detector response for the momentum measurement.

2.3.2 SCT monitoring: 2011-2012 detector operations

Ensuring the health and performance of the ATLAS detector as well as the quality of the recorded data at all times is an important challenge to be faced when doing physics analyses at the LHC.

Each of the sub-detectors is a complicated system by itself, run, maintained and operated by a separate team of shifters and experts. In this section we will give an overview of the performance of one sub-detector, the SCT in the period 2010-2013 during which the sub-detector has been fully operational and more than 99% efficient [95].

The quality of the data taking has been constantly monitored both online and offline, taking into account information from a wide amount of sources to assess the status of the detector and the quality of the data taking. In addition, these

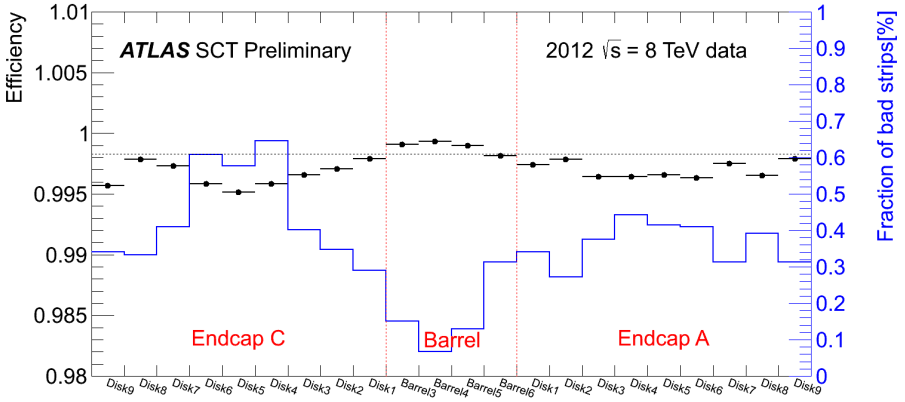

Figure 2.9: *The mean intrinsic hit efficiency for each layer of the SCT measured in* 8 *TeV proton-proton collisions is shown. The continuous line and right-hand axis indicate the fraction of disabled strips in each layer. [96]*

observables have been studied on a longer time scale in order to asses the health of the detector.

The SCT was fully operational throughout all data taking periods and achieved data taking efficiencies of 99.9%, 99.6% and 99.1% in 2010, 2011 and 2012 respectively [95]. During the three years of data taking, 99% of strips were active and available for tracking at all times. The SCT was always powered on. The bias voltage was maintained at 50 V outside of LHC stable beam conditions (*Standby*) and at 150 V during stable beams. Using an evaporative cooling system, it was operated cold in order to mitigate the effects of radiation damage. Calibrations were performed regularly. In order to optimise the data taking configuration, a common 1 fC hit threshold was applied across the SCT, which ensured a low occupancy ($< 5 \cdot 10^{-4}$) and high hit efficiency ($> 99\%$) for all strips.

Online and offline monitoring of the SCT

It is important to assess the quality of the data within 24 hours after being recorded, and propagate this information to the physics analysis teams in terms of a *good run list* where defects in the data are indicated. A number of defects that might occur in the SCT data taking and performance can be defined as *intolerable* for the physics analyses, marking the afflicted data as not usable for these purposes.

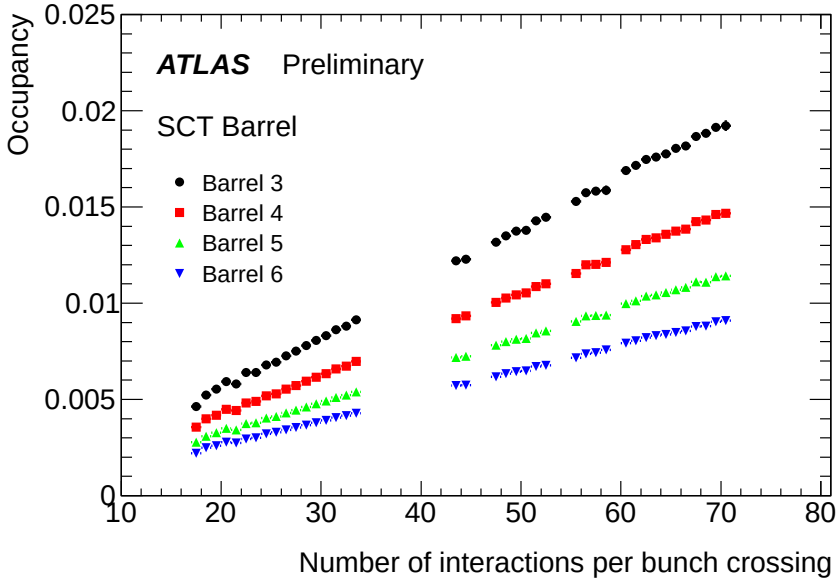

Figure 2.10: *Mean occupancy of each layer of the SCT* Barrel *as a function of the number of interactions per bunch crossing in minimum bias pp data. Values for less than 40 interactions per bunch crossing are from* 7 *TeV collisions; those for higher values correspond to special test runs at* 8 *TeV with fewer bunches of protons and higher number of protons per bunch [96].*

This quality control process is generally referred to as *offline monitoring*.

In the *online monitoring* instead, *during* the data acquisition, a certain number of events, taken from different data streams, are processed on the fly from the online monitoring infrastructure. This information is used to asses immediately any lack of quality in the data taking and to promptly instigate further investigation. The quantities that are monitored are briefly described in the following.

Intrinsic hit efficiency The intrinsic hit efficiency is defined as the probability of a hit being registered in an operational detector element when a charged particle traverses the sensitive part of the element. It is defined as the ratio of the numbers of recorded hits on a track with $p_T > 1$ GeV ($\mathcal{N}_{hits}$) to the total expected number of hits, given by the number of hits plus the number of misses ($\mathcal{N}_{holes}$).

$$\varepsilon = \frac{\mathcal{N}_{hits}}{\mathcal{N}_{hits} + \mathcal{N}_{holes}} \tag{2.7}$$

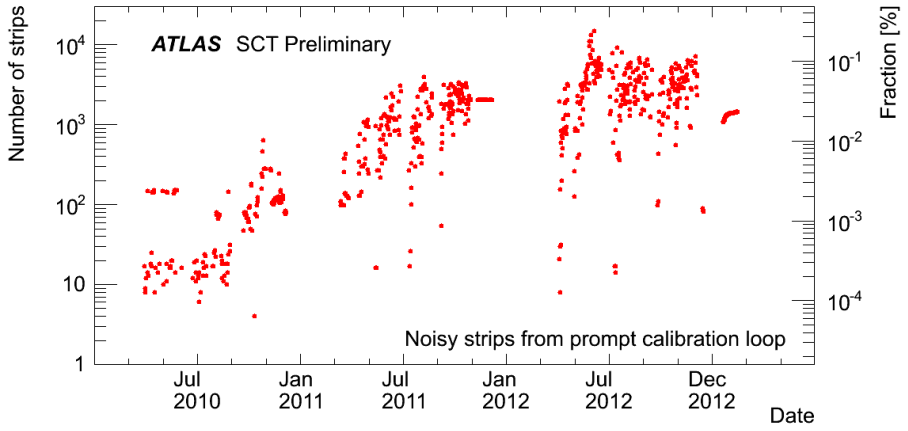

Figure 2.11: *Number of noisy strips determined offline in the prompt calibration loop as a function of time from the start of data-taking in 2010 to the end of data-taking in 2013. The left-hand axis shows the number of strips, and the right-hand axis the fraction of the total number of working strips in the SCT. [96]*

Dead modules and chips are omitted in the efficiency evaluation.

The hit efficiency for each of the SCT layers and disks is shown in Figure 2.9, together with the fraction of non-working strips in that layer. The figure shows that the hit efficiency is $> 99.5\%$ for all layers and that the inefficiency is correlated with the number of bad strips, as expected.

Detector occupancy The detector track occupancy is defined as the ratio of the number of strips giving hits in a given event to the total number of strips. The SCT design was optimised to minimise the detector occupancy, hence reducing the confusion in pattern recognition that arises from the high track multiplicity environment. The 1% mean strip occupancy design threshold has been reached and, in 2012, exceeded, with no significant loss in tracking efficiency. The detector occupancy has been studied in dedicated runs as a function of the number of interactions per bunch crossing delivered in the collision and its trend has been found to show a good linearity (Figure 2.10) and a value smaller than 2% for the *Barrel* region up to 70 interactions per bunch crossing.

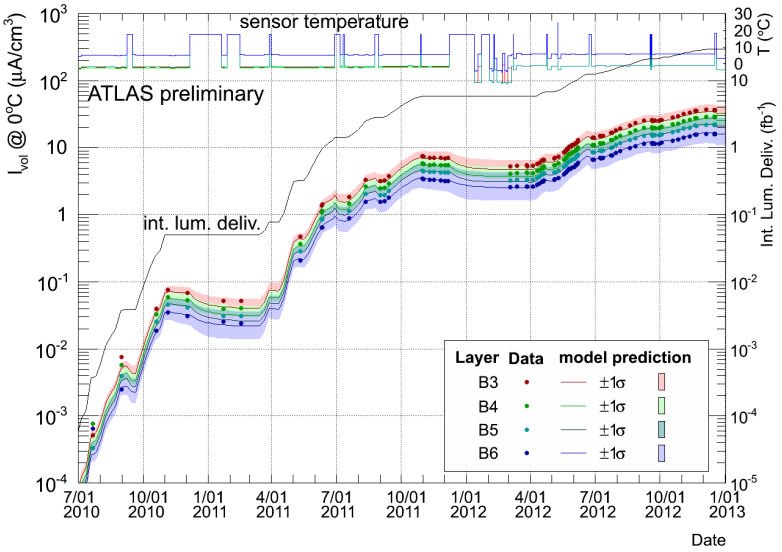

Figure 2.12: *In this plot, the HV current measured in the HV power supply of the ATLAS SCT* Barrel *modules are shown by points at four SCT* Barrel *layers (B3 to B6) . The data were taken when the LHC beams were off and are compared with the predicted leakage currents by the Hamburg /Dortmund model. See text for references and details. [96]*

Noise occupancy The probability to record a hit due only to noise is measured in *collisions* with empty bunch trains. A noisy strip is defined as one with an average occupancy of more than 1.5% in such empty bunch-crossings. Noisy strips are identified and monitored, since maintaining a low noise is of crucial importance in order to maintain high tracking efficiency in the detector. Strips that were noisy, or showed other problems in previous online calibration runs are excluded. The rate of noisy strips is observed to rise with luminosity, as radiation provokes *single event upsets*, i.e. bit flips in the chip register, that affects the effective readout thresholds. This is observed in Figure 2.11 where the number of noisy strips determined offline in the prompt calibration loop are shown as a function of time from the start of data-taking in 2010 to the end of data-taking in 2013. Often whole chips are affected, leading to large run-to-run fluctuations in the number of noisy strips. The number is relatively stable during the periods of heavy-ion running at the end of 2011 and in 2013, when the luminosity was relatively low.

Radiation Damage Irradiation of silicon sensors results in damage in the bulk silicon and the dielectric layers, with main effects being the increase in leakage current of the sensor, the change in the effective doping concentration and a change in the inter-strip capacitance. A measurement of leakage current during off beam periods was made and converted to those at a temperature of $0°C$, assuming that all HV currents are due to generation current in the silicon bulk [97].
The experimental measurement was found to be in agreement with the Hamburg--Dortmund model simulated using FLUKA [98]. The increase in the Leakage Current is shown in Figure 2.12. Coloured bands indicate $1\ \sigma$ uncertainty, which is obtained by quadratically summing up all uncertainties of the model parameters as well as the temperature measurements. The prediction takes into account the self-annealing effects using the measured sensor temperatures shown at the top of plots and is based on the total 7 and 8 TeV collision luminosities delivered to ATLAS, shown by the black solid line.

The leakage current was observed to be correlated with the increase in integrated luminosity as expected and excellent agreement between data and predictions is observed over the three years of operations. This indicates that the observed HV currents are mostly due to bulk generation current and also that the leakage current modelling incorporating self-annealing effects are well applicable. Although a significant increase in leakage current is observed the change in depletion voltage so far is negligible and the SCT remains far from the type inversion.

3 Object reconstruction

For each collision at the LHC, the information of the various ATLAS sub-detectors is combined and processed (the event is "reconstructed") in order to identify the particles produced in the pp interaction and to measure their properties. The definition of these objects and their identification criteria are presented in this chapter. Leptons, particle jets originating from the production of quarks and missing transverse momentum resulting from escaping particles will be described.

The particles directly produced in the collision or in the decays of other particles are not directly "seen". Each particle is reconstructed according to electric signals acquired in the various ATLAS sub-detectors. The combined information collected from all or some of the sub-detectors allows the identification of the various particles that traverse the detector, and the precise measurement of their properties. This procedure is commonly referred to as *event reconstruction*. Hence an electron is a calorimetric deposit matched to a track and a muon is a sequence of hits in the muon chambers. The aim of this chapter is to provide an introduction of the physical objects that are used in both of the two analyses described in this thesis, giving an overview of the algorithms used for the definition of these objects and their identification criteria. The objects that will be described in this section are: leptons (electrons and muons[1)]), jets from light quarks as well as from bottom quarks and,

[1)]Due to their very different behaviour, we do not aim to select taus in any of the analyses presented in this thesis and we will usually refer only to muons and electrons when using the word leptons.

finally, missing transverse momentum.

3.1 Leptons: electrons and muons

3.1.1 Electrons

Electrons and photons are both stopped inside the electromagnetic calorimeter and produce similarly shaped depositions. Their identification steps are very similar and mainly deviate after the matching of the electromagnetic cluster to a track [99].

Electrons are identified as clusters in the electromagnetic calorimeter by means of a sliding window algorithm [100]. The algorithm divides the electromagnetic calorimeter into a grid of elements of size $\Delta\eta \times \Delta\phi = 0.025 \times 0.025$ and slides a window of 5×5 of these elements across all layers of the calorimeter calculating the sum of the transverse energy of these cells building up the clusters. The total energy of the cluster is a linear, η dependent, weighted sum of the contribution of the pre-sampler and the three calorimeter layers.

Subsequently, tracking informations are extensively used, in order to increase the electron identification efficiency and limit the bremsstrahlung impact on the electron trajectory.

For electron Particle Identification (PID) three working points are defined: *Loose, Medium* and *Tight*. They are characterised by requirements of increasing tightness on the quality of the electron identification and are based on the following criteria:

(a) The extension and shape of the electromagnetic shower in the calorimeter and the fraction of the hadronic component of the energy deposit.

(b) Quality requirements on the matched Inner Detector track (the most important of which being the requirement of at least two hits in the Pixel detector of which one in the B-Layer), are tightened for the *Medium* and *Tight* working points.

(c) Matching requirements between the ID track and the calorimeter cluster, such as the calorimeter energy to track momentum ratio E/p and the track-cluster $\Delta\phi$ (*Tight* working point).

The efficiency of the electron reconstruction and identification is measured in

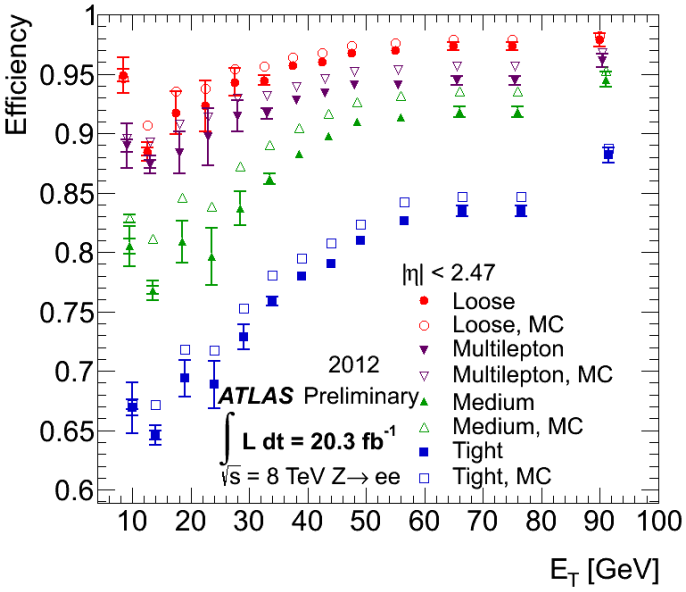

(a)

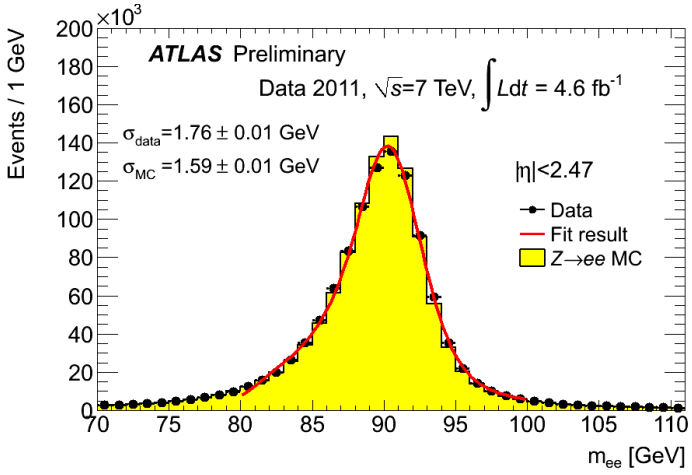

(b)

Figure 3.1: *Electron identification efficiency for the different PID working points (a) and calibrated $Z \to ee$ invariant mass distribution in data and Monte Carlo (b). Loose, medium and tight PID definitions are given in the text. The multi-lepton working point accounts for multiple leptons selections.*

data using a *tag and probe*[2)]method using $Z \to ee$ events and compared to the one obtained in the Monte Carlo simulation. The electron reconstruction efficiency increases with the electron transverse momentum and decreases with the tightness of the requirements (Figure 3.1). It varies between 70% and 80% for the one used in the analysis presented in Part 3. The Z peak mass resolution and scale is compared as well in the same figure.

Energy smearing and correction factors are derived in such studies and applied in the physics analyses in order to improve the agreement between the simulation and the experimental data.

3.1.2 Muons

The muon detection in the ATLAS detector relies on the two high precision tracking systems, namely the Inner Detector and the Muon Spectrometer (MS). In addition the calorimeter ensures efficient hadron filtering with high purity for muons of momentum with a minimum of 3 GeV, least they are stopped in the calorimeter system.

The combination of measurements made in the muon system with the ones from the Inner Detector improves the momentum resolution in the momentum range 6 GeV $< p_{\mathrm{T}} <$ 100 GeV, in which the Inner Detector momentum performance is better than one of the the Muon Spectrometer. In addition, the matching of the two independently reconstructed tracks allows the rejection of muons from secondary interactions as well as the ones from kaon decays in flight.

Four different categories of muons are available, that can be obtained with two different reconstruction algorithms, one of which - *Chain 1*[101] - is used in this thesis.

Combined (CB) muons are based on a fully reconstructed track in the muon spectrometer that is matched to an Inner Detector track (pseudorapidity coverage $|\eta| < 2.5$, driven by the ID).

Segment Tagged (ST) muons are a combination of an ID track with a Muon Spectrometer segment. They are particularly efficient to recover low momentum

[2)] The tag and probe method identifies one of the two electrons (the tag) from the Z decay using tight identification criteria. The second electron (the probe) is selected by means of an orthogonal method (i.e. a track in the ID) and its invariant mass with the tag electron is required to match the Z invariant mass. The electron reconstruction and identification efficiency can then be calculated from the probe electron.

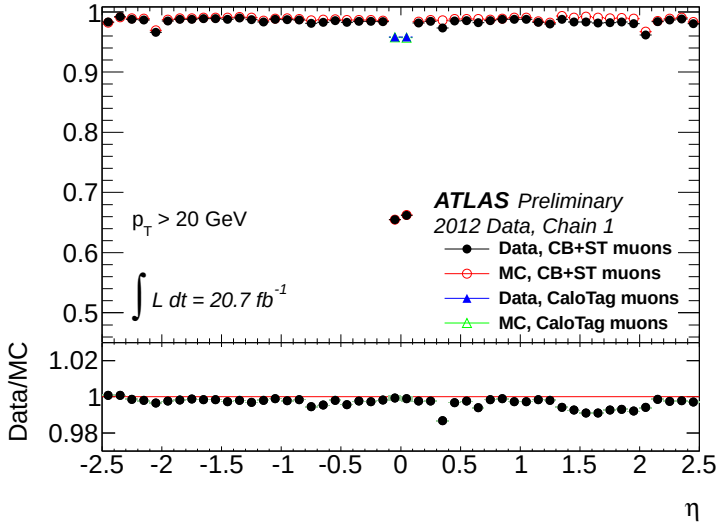

Figure 3.2: *Muon reconstruction efficiency as a function of the muon η for muons with $p_{\mathrm{T}} > 20$ GeV, for different muon categories. The panel at the bottom shows the ratio between the measured and predicted efficiencies [102].*

muons that after loosing energy in the calorimeter, do not have enough momentum to traverse the whole spectrometer.

Calorimeter Tagged (CaloTag) muons are a combination of an ID track and a calorimeter energy deposit. This type of muons allows to recover efficiency at $\eta \sim 0$, which is uncovered by the Muon Spectrometer.

Stand-alone muon track reconstruction based solely on the MS measurements. The MS acceptance determines $|\eta| < 2.7$ for this category of muons.

The efficiency of the muon reconstruction is measured in data using a *tag and probe* method using $Z \to \mu\mu$ events and found to be always above 95%. It is compared to the one obtained in the Monte Carlo simulation and differs from it by at most 2% (Figure 3.2). In addition the Z peak resolution and scale is compared between data and Monte Carloin Figure 3.3(a). By means of these studies, energy smearing and correction factors to the Monte Carlo simulation are derived. These corrections, shown in Figure 3.3(b), are then applied in the physics analyses in order to improve the agreement between the simulation and the experimental data.

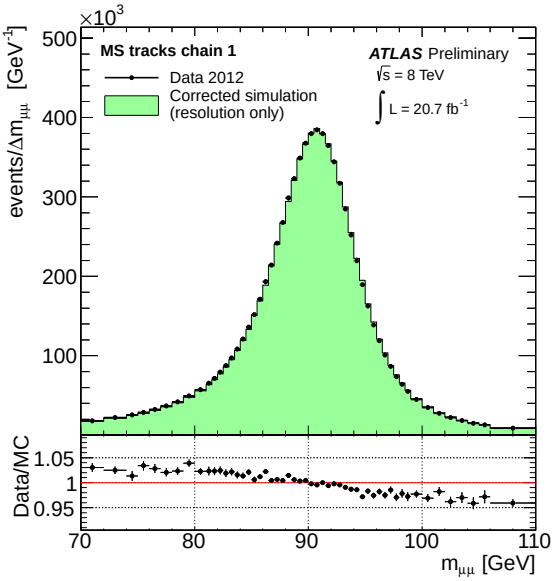

(a)

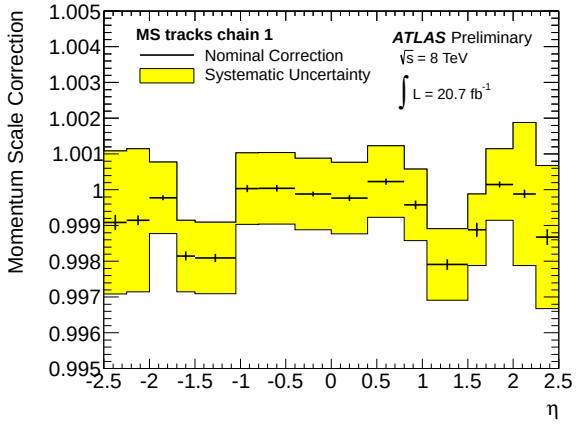

(b)

Figure 3.3: *(a) dimuon invariant mass for Combined* Chain 1 *muons, isolated and with* $p_{\mathrm{T}} > 25$ *GeV. The plot shows the invariant mass for 2012 data and corrected* POWHEG *simulation of* $Z \to \mu\mu$ *events. Smearing and scale corrections derived from the full 2012 dataset are applied. (b) Muon Spectrometer momentum scale correction for Monte Carlo, derived from* $Z \to \mu\mu$ *data for the* Chain 1 *reconstruction [102]*

3.1.3 Selected leptons

Both analyses of this thesis rely on muon reconstruction. However, the muons selected by each analysis are of completely different nature, to the level that what is considered a good candidate for one analysis is background for the other.

The top squark search (Part 3) targets muons coming directly from the primary interaction, *primary muons*, mainly of high transverse momentum. These muons are required to be *geometrically* isolated from the other objects in the event, in particular jets, by means of an angular separation requirement:

$$\Delta R(\mu, jet) = \sqrt{(\phi_\mu - \phi_j)^2 + (\eta_\mu - \eta_j)^2} \tag{3.1}$$

An additional *activity* isolation requirement is applied to the *isolated muons*, for which the sum of the momentum of all tracks in the vicinity of the muon must be small:

$$\sum_{\Delta R<0.2} p_{\mathrm{T}} < 1.8 \text{ GeV}. \tag{3.2}$$

Conversely, the b-tagging analysis (Part 2) aims to identify *secondary muons* coming from a B hadron decay. They are characterised by a large surrounding activity, due to the fact that the decay happens usually inside a jet, and has a lower transverse momentum. Although no effort is made to reject *primary muons* in the analysis, they contribute to the background in this case. The summary of all requirements for the three muon categories are summarised in Table 3.1.

Electrons are of interest only for the top squark search (Part 3). Also in this case the interesting electrons are the ones coming directly from the interaction vertex. Similarly to the muon case, a geometrical isolation is applied to the *primary electrons*, with respect to either jets or b-tagged jets (see following section for details). *Isolated electrons* fulfil the additional activity isolation:

$$\frac{\sum_{\Delta R<0.2} p_{\mathrm{T}}}{p_{\mathrm{T}}^{ele}} < 0.1. \tag{3.3}$$

The summary of all requirements for the electron categories are summarised in Table 3.2.

Secondary muons		
Reconstruction	Muon category	CB
p_{T}	Momentum from the ID-MS combined track	> 4 GeV
$\lvert\eta\rvert$	pseudorapidity of the combined track	< 2.4
ID track quality	requirements on the number of hits in the Pixels N_{pix}, in the SCT N_{SCT} and the number of combined hits in the silicon detectors N_{sil}.	$N_{pix} \geqslant 0$, $N_{SCT} \geqslant 5$, $N_{sil} \geqslant 8$
Primary muons		
Reconstruction	Muon category	CB or ST
p_{T}	Momentum from the ID-MS combined track	> 10 GeV
$\lvert\eta\rvert$	pseudorapidity of the combined track[3)]	< 2.4
ID track quality	requirements on the number of hits in the Pixels N_{pix}, in the SCT N_{SCT} and the number of missed hits in both silicon detectors N_{miss}. If $1.0 < \lvert\eta\rvert < 1.9$ an additional req. is applied for the number of TRT hits N_{TRT}	$N_{pix} \geqslant 1$, $N_{SCT} \geqslant 5$, $N_{miss} \leqslant 3$, $N_{TRT} \geqslant 6$
Geometrical Isolation	$\Delta R(\mu, jet)$	> 0.4
Isolated muons		
Reconstruction	Muon category	CB or ST
p_{T}	Momentum from the ID-MS combined track	> 25 GeV
$\lvert\eta\rvert$	pseudorapidity of the combined track	< 2.4
ID track quality	same requirement as for *Primary Muons* and impact parameter (z_0, d_0) requirements with respect to the primary vertex	$\lvert z_0\rvert < 1\,\mathrm{mm}$, $\lvert d_0\rvert < 0.2\,\mathrm{mm}$
Geometrical Isolation	$\Delta R(\mu, jet)$	> 0.4
Activity Isolation	Sum of the momentum of all the tracks (except the muon) within a cone of $\Delta R < 0.2$	1.8 GeV

Table 3.1: *Summary of the selection requirements of all muon categories used in the two analyses presented in this thesis.* Secondary muons *are used in the b-tagging calibration presented in Part 2 and* Primary *and* Isolated muons *are used in the search in Part 3. See text for details.*

Primary electrons		
PID	Electron identification requirements	Loose
EMF	Fraction of energy deposited in the electromagnetic calorimeter	> 0.8
p_{T}	Calculated from the cluster energy and projected in the transverse plane using the matched track η	> 10 GeV
$\lvert\eta\rvert$	pseudorapidity of the electromagnetic cluster	< 2.47
Geometrical Isolation from b-jet	$\Delta R(e, b-jet)$	> 0.2
Geometrical Isolation from jet	$\Delta R(e, jet)$	> 0.4
Isolated electrons		
PID	Electron identification requirements	Tight
p_{T}	Calculated from the cluster energy and projected in the transverse plane using the matched track η	> 25 GeV
Geometrical Isolation from b-jet	$\Delta R(e, b-jet)$	> 0.2
Geometrical Isolation from jet	$\Delta R(e, jet)$	> 0.4
Activity Isolation ($\sum_{\Delta R<0.2} p_{\mathrm{T}}/p_{\mathrm{T}}^{track}$)	Fraction of the momentum of the matched track with respect to all other tracks within a cone of $\Delta R < 0.2$	< 0.1

Table 3.2: *Summary of the selection requirements of the two categories of electrons used in the top squark search (Part 3). See text for details.*

3.2 Jets and b-tagging

Each parton generated in the interaction goes through a hadronization process, generating a collimated spray of hadrons with null colour charge approximately in the direction of the original parton. This *jet* of particles is what is observed in the detector. Since jets are features of the final state, they cannot be uniquely mapped on to partons.
Nevertheless, jets are designed such that their gross properties (energy, momentum, etc) should reflect as closely as possible the short distance dynamics of the collision in which they are produced. Many jets of high transverse momentum (p_{T}) may be present in a single event, and each jet has a high chance of evolving a complex substructure. For much of the region of interest, jet multiplicities and structure can be described by a combination of fixed-order matrix elements and leading-logarithmic parton showering or resummation. An approximate representation of jet production is given in Figure 3.4.

3.2.1 Jets identification, reconstruction and calibration

Jets must be defined by clustering algorithms, and the algorithms are designed such that the jets clustered from the complex structure of objects in each event accurately represent the physical properties of the partons originated in the hard scattering. It is important to underline that the algorithm does not find jets, but *defines* them, such that jets do not exist independently of the algorithm. Consequently, in order to guarantee the ATLAS measurements to be connected with the fundamental degrees of freedom of the SM such as quarks and gluons, it needs to be possible to meaningfully compare the jet reconstruction algorithm definition to the theoretical calculations and the algorithm needs to be unambiguously communicable between experiments. For this to be possible, the jet reconstruction algorithm has to comply a number of properties. Above all it is important that the algorithm is *collinear and infrared safe*, which means that the algorithm should not be sensitive to collinear splitting of the input object (partons) and to the extra radiation of arbitrarily soft particles.

A number of algorithms have been developed and studied in the last decades. The jet finding algorithm most commonly used in ATLAS and in the analyses presented in this thesis belongs to the collection of sequential clustering algorithms, namely the anti-kT algorithm [103]. These iterative algorithms group objects based

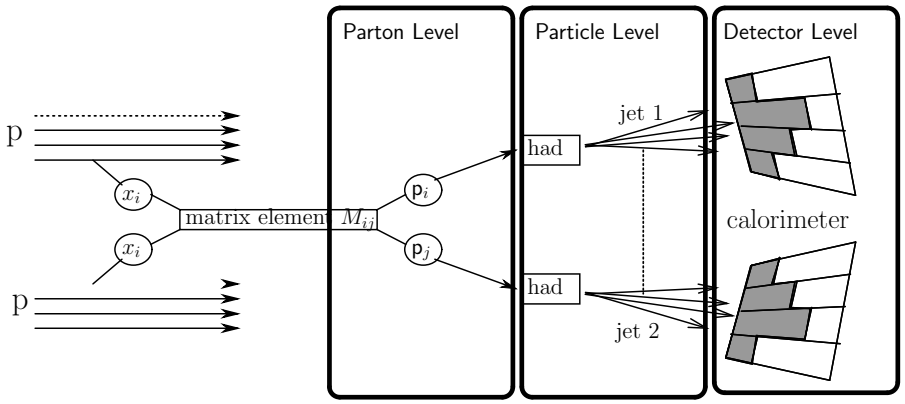

Figure 3.4: *The production of quarks in a hard scattering interaction and their detection as jets*

on their respective distance, defined as:

$$d_{ij} = \min\left(k_{Ti}^{2p}, k_{Tj}^{2p}\right)\frac{\Delta R_{ij}}{D}, \tag{3.4}$$

and their distance to the beam axis:

$$d_{iB} = k_{Ti}^{2p}, \tag{3.5}$$

where $\Delta R_{ij}^2 = (\eta_i - \eta_j)^2 + (\phi_i - \phi_j)^2$ and k_{Ti}, η_i and ϕ_i are respectively the transverse momentum, the pseudorapidity and the azimuth angle of particle i. p and D are constants that define the type of algorithm. The (inclusive) clustering proceeds by identifying the smallest of the distances between d_{ij} and d_{iB}. If it is a d_{ij}, it recombines entities i and j, otherwise it calls i a jet and removes it from the list of entities. The distances are recalculated and the procedure repeated until no entities are left.

Specifically, the anti-kT(0.4) algorithm uses

- $p = -1$. In the vicinity $\Delta R < D$ of a hard object, all softer objects will be merged with the harder object in order of their closeness in ΔR.
- $D = 0.4$, scale of the jet structure with respect to the event structure, such that any pair of jets are at least separated by $\Delta R = D$

The jet energy calibration relates the jet energy measured with the ATLAS calorimeter to the true energy of the corresponding jet of stable particles entering the ATLAS detector. Thus calibration corrects for a number of detector effects that affect the jet energy measurement: calorimeter non-compensation, energy losses in the uninstrumented material, calorimeter hermeticity imperfections, out-of-jet-cone particles, noise and particle reconstruction efficiency.

ATLAS has developed several calibration schemes, fully documented in Refs. [104, 105], that will briefly be summarised in the following. Each calibration scheme starts from the measured calorimeter energy at the Electromagnetic (EM) energy scale, which correctly measures the energy deposited by electromagnetic showers. The simple Electromagnetic + Jet Energy Scale (EM+JES) calibration scheme applies corrections as a function of the jet energy and pseudorapidity to jets reconstructed at the electromagnetic scale and for its simplicity was widely used in the 2011 dataset and consequently in the b-tagging analysis presented in Part 2. The EM+JES calibration scheme consists of three subsequent steps as outlined below:

I. pile-up correction: The average additional energy due to additional proton-proton interactions in each collision is subtracted from the energy measured in the calorimeters using correction constants obtained from in situ measurements.

II. Vertex correction: The direction of the jet is corrected such that the jet originates from the primary vertex of the interaction instead of the geometrical centre of the detector. This is a small correction to the jet transverse momentum ($\sim 1\%$) and does not affect its energy.

III. Jet energy and direction correction: The jet energy and direction as reconstructed in the calorimeters are corrected using constants derived from the comparison of the kinematic observables of reconstructed jets and those from truth jets in Monte Carlo simulation.

A second, more sophisticated method was used for the jet calibration for the analyses using the 2012 dataset, namely the Local Calibration Weighting + Jet Energy Scale (LCW+JES) calibration scheme. This involves an additional calibration step between the EM level and the Jet Energy Scale (JES) calibration, namely the Local Calibration Weighting (LCW). The LCW calibration method first clusters together topologically connected calorimeter cells and classifies these clusters as either electromagnetic or hadronic. Based on this classification energy corrections are derived from

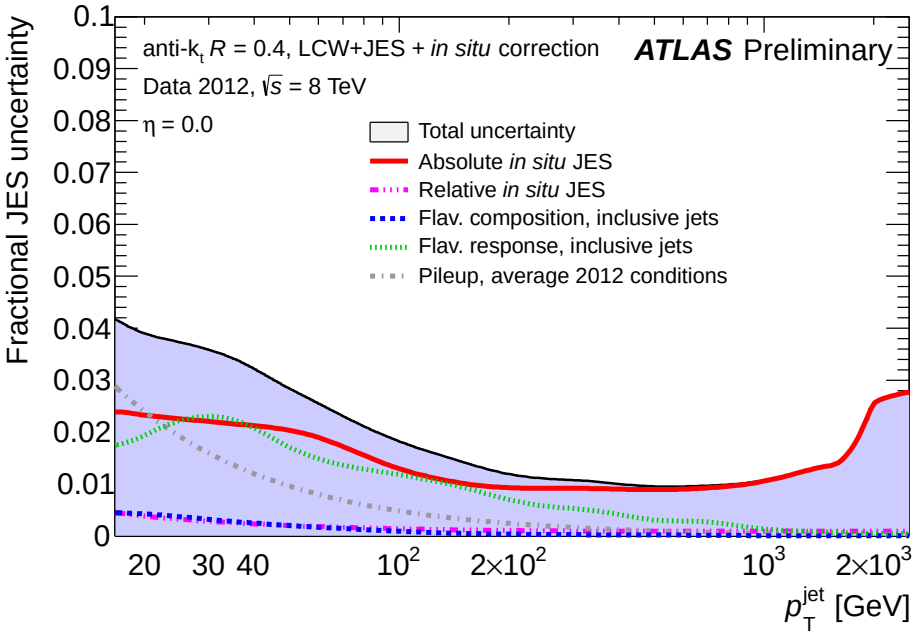

Figure 3.5: *Fractional jet energy scale systematic uncertainty as a function of the jet p_T for central jets calibrated with the LCW+JES scheme [106].*

single-pion Monte Carlo simulations. In this case, the energy corrections are applied directly to calorimeter clusters and are defined without reference to a jet definition and are therefore called *local* corrections. This calibration scheme was used in the 2012 dataset and in the search presented in Part 3.

A number of methods are used to assign a systematic uncertainty to the jet calibrations, ranging from p_T balance measurements in Z/γ+jet events to comparisons of jets reconstructed from calorimetric information and jets reconstructed from tracking information. The total uncertainty in 2012 as a function of the jet transverse momentum for central jets is shown in Figure 3.5 for the LCW+JES calibration scheme. It amounts to roughly 2-3% uncertainty per jet and it is one of the most important uncertainties for the stop search (see Part 3).

3.2.2 b-tagging algorithms in ATLAS

The lifetime-based bottom quark identification ("b-tagging") algorithms take advantage of the relatively long lifetime of hadrons containing a b quark, of the order

of 1.5 ps ($c\tau \simeq 450\,\mu$m). A B-hadron therefore has a significant flight path length, travelling on average about 2-3 mm in the transverse plane (for a hadron with momentum of 30 GeV) before decaying. They are therefore characterised by topologies with at least one displaced vertex with respect to the point where the hard-scatter collision occurred.

Three classes of algorithms [107] aim at identifying such topologies and are summarised in the following.

Impact parameter-based taggers A rather inclusive approach consists of using the impact parameters of the charged-particle tracks in a jet. The transverse impact parameter, d_0, is the distance of closest approach of the track to the primary vertex point, in the $r\phi$ projection. The longitudinal impact parameter, z_0, is the difference between the z coordinates of the primary vertex position and of the track at this point of closest approach in $r\phi$. The tracks from b-hadron decay products tend to have rather large impact parameters which can be distinguished from tracks stemming from the primary vertex. Two tagging algorithms exploiting these properties have been developed in ATLAS: JetProb, used mostly for early data and for the online trigger b-tagging, and IP3D for high-performance tagging.

Vertex-based algorithms The second approach, more demanding, is to reconstruct explicitly the displaced vertices. Two main algorithms are used to this effect: the Secondary Vertex (SV) algorithm, which comes in two versions, SV0 and SV1, attempts to reconstruct an inclusive secondary vertex. A very different algorithm of this category, the JetFitter algorithm, aims at reconstructing the complete B hadron decay chain.

Combined tagging algorithms The vertex-based algorithms exhibit much lower fake (*mistag*) rates than the impact parameter-based ones, but their efficiency for actual b-jets is limited by the secondary vertex finding efficiency. Both approaches are therefore combined to define versatile and powerful tagging algorithms. The IP3D and SV1 algorithms are combined in a straightforward manner by summing their respective weights: this is the so-called IP3D+SV1 algorithm. An alternative combination technique is the use of an artificial neural network, which can take advantage of complex correlations between the input values. Two tagging algorithms are defined in this way. IP3D+JetFitter is a combination of the two algorithms IP3D and JetFitter, while the MV1 algorithm is a neural network-based combination of the results of the

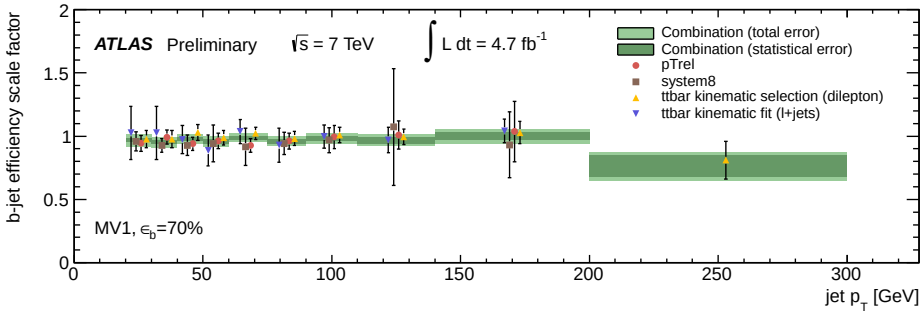

(a) *b*-jet efficiency scale factors in 2011 data

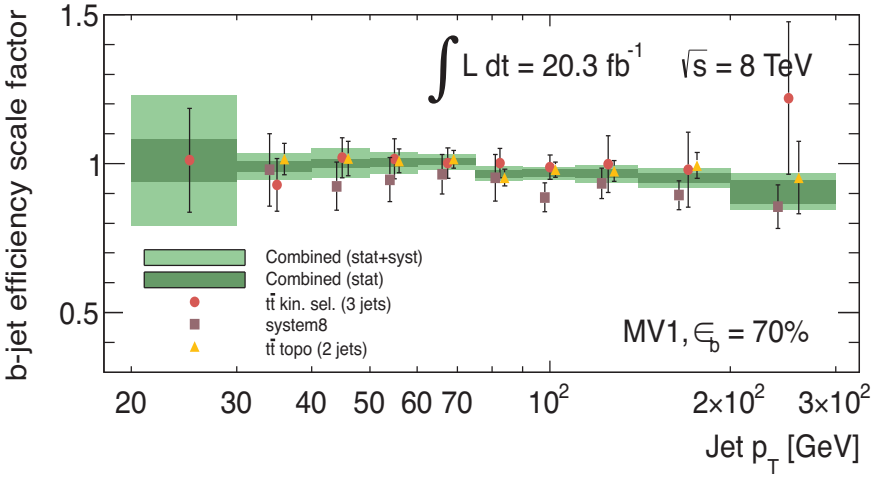

(b) *b*-jet efficiency scale factors in 2012 data

Figure 3.6: *Data over Monte Carlo scale factors for the probability of tagging a b-jet as such. Each marker indicates a different calibration methods that exploit a $t\bar{t}$ dileptonic or semileptonic sample, a sample of b-jets containing a muon (pTrel), and a method based on a system of independent equations to extract the number of b-jets in the sample (system8).*

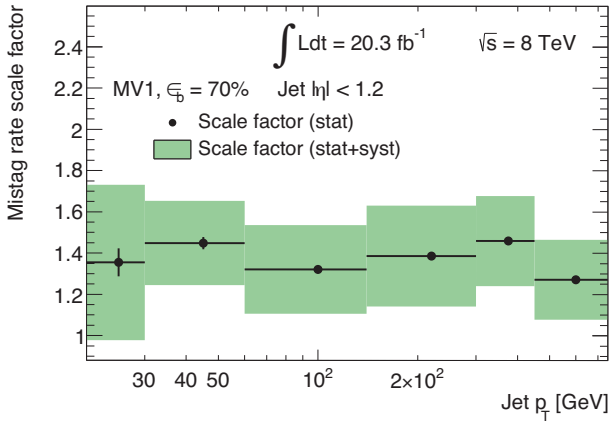

Figure 3.7: *Data over Monte Carlo scale factor for the probability of mis-tagging a light flavour jet as a b-jet.*

IP3D, SV1 and IP3D+JetFitter algorithms. In 2012, the MV1 has become the default tagger for many physics analyses, including the search presented in Part 3 of this thesis. The calibration of the various b-taggers [108, 109], including MV1, is performed using a number of different techniques that vary from muon enriched samples to samples that exploit dileptonic $t\bar{t}$ events, that allow to directly measure the b-jets tagging efficiency. Results in terms of data over Monte Carlo ratios for both 2011 and 2012 datasets are shown in Figure 3.6. The c-jet efficiency is measured in an inclusive sample of jets associated to D^0 mesons. The mistag rate due to resolution effects is measured in an inclusive jet sample by reversing the impact parameter significance sign of tracks for impact parameter based tagging algorithms (such as IP3D), or reversing the decay length significance sign of secondary vertices for secondary vertex based tagging algorithms (SV). An example of mistag rate scale factors for the MV1 tagger in the 2012 dataset is given in Figure 3.7.

3.2.3 Selected jets and b-jets

The jets used in this thesis are reconstructed with the anti-kT(0.4) ([103]) jet finding algorithm. The jets used in Part 2 of this thesis have been calibrated according to the EM+JES [104] calibration scheme, while the ones in Part 3 use the LCW+JES [104] one. All jets are required to have $p_{\mathrm{T}} > 25$ GeV and $|\eta| < 2.5$. Since all electrons are also reconstructed as jets, all jets within $\Delta R < 0.2$ from a primary electron (before the jet-geometrical isolation requirement) are rejected. The b-jets have to fulfil the same requirements and be *tagged* as originating from a b quark from one of the

available taggers. In the analysis presented in Part 2 the performance of almost all available taggers has been investigated. Instead, in the search presented in Part 3 MV1 has been used to identify b-jets at a *loose* and *tight* working point according to the final investigated selection.

3.3 Missing transverse momentum

The interesting events in hadron colliders are the ones that involve hard scattering of the partons inside the protons. These events are characterised by a high momentum component in the transverse plane, unlike the more common scattering events (i.e. *Minimum Bias*) that involve a small transfer of momentum.

Usually the events are energy-balanced in the transverse plane and not along the beam direction, due to the unknown component along the beam axis of the centre-of-mass frame of the hard interaction. However, events with weakly interacting particles that escape the detector undetected such as neutrinos in the SM, have a large amount of imbalance in the transverse plane (missing transverse momentum), that

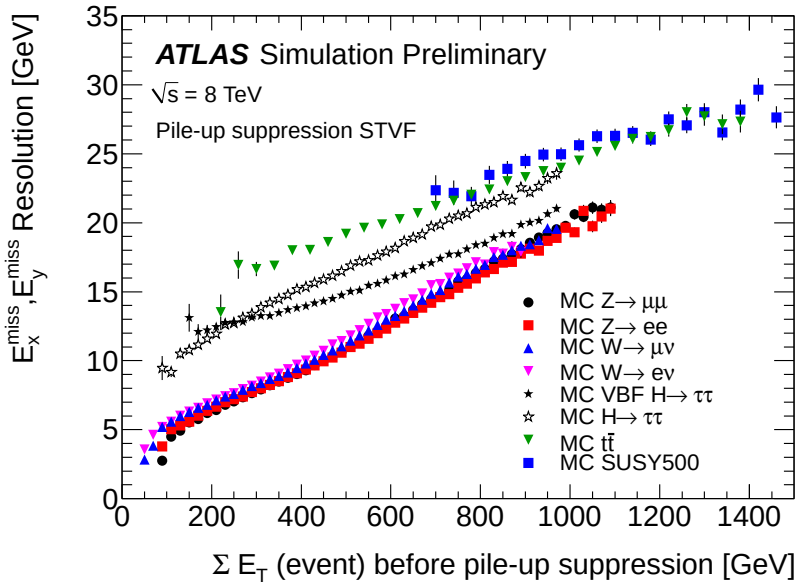

Figure 3.8: *Summary of the resolution of the x and y components of the missing transverse momentum for various simulated processes.*

is proportional to the escaping particle energy. It is straightforward to understand that any mis-measurement of the energies of the particles in the event (and in particular jets) would result in an imbalance in the transverse momentum, mimicking an escaping particle.

The missing transverse momentum ($E_{\mathrm{T}}^{\mathrm{miss}}$) calculation uses reconstructed and calibrated physics objects. Calorimeter energy deposits are associated with a reconstructed and identified high-p_{T} parent object in a specific order: electrons, photons, hadronically decaying τ-leptons, jets and finally muons. In the specific $E_{\mathrm{T}}^{\mathrm{miss}}$ definition used in this thesis jets are required to fulfil $p_{\mathrm{T}} > 20$ GeV and $\eta < 4.9$ and are calibrated at the LCW+JES energy scale, electrons have $p_{\mathrm{T}} > 10$ GeV and fulfil *medium* PID criteria and muons are reconstructed using the *Chain 1* algorithm and are required to have a geometrical isolation from the jets with $\Delta R > 0.3$. Deposits not associated with any such objects are also taken into account in the calculation; these form the so called *soft term* of the $E_{\mathrm{T}}^{\mathrm{miss}}$ and are taken from topological calorimeter clusters at the LCW energy scale which are not included in any reconstructed object. The resolution of the missing transverse momentum in Monte Carlo is shown in Figure 3.8 for different simulated processes and it is found to be between 5 and 30 GeV depending on the total energy in the event.

Part 2

B-Tagging calibration with the 7 TeV dataset

4 Selecting b-jets through fully reconstructed B-hadrons

A large number of measurements and new physics searches performed in ATLAS *rely on the identification of jets originating from* b*-quarks. The aim of the study introduced in this chapter is to investigate the reliability of the Monte Carlo simulation in describing the quantities exploited directly and indirectly by these* b*-tagging algorithms. This is achieved by studying a* b*-jet enriched sample from fully reconstructed* $B^{\pm} \to J/\psi\, K^{\pm}$ *decays and geometrically associating them to their jet. The study was performed using the data collected by* ATLAS *in 2011 at* $\sqrt{s}$ = 7 TeV*. An introduction of the selection strategy, the investigated quantities and the Monte Carlo treatment are presented.*

4.1 Introduction and motivations

The identification of jets originating from b-quarks plays a key role in the physics programme of ATLAS. Many searches for physics Beyond the Standard Model (BSM) and SM measurements performed with the ATLAS detector investigate signatures that involve b-jets in the final state and rely on b-tagging techniques. Several algorithms to identify b-jets that make use of the relatively long lifetime of B mesons have been developed in ATLAS: (i) those based on the reconstruction of an inclusive secondary vertex or (ii) those that require the presence of tracks with large impact parameters and (iii) the combined tagging algorithms that make use of multi-variate discriminants. They have all been introduced in Section 3.2.2.

It is important that the Monte Carlo simulation is able to reproduce the response to b-jets of the tagging algorithms. For example, many BSM searches, included the one presented in Part 3 of this thesis, extrapolate background estimates from b-jet-veto selections to selections involving one or more b-jets entirely relying on the Monte Carlo simulation. In this context, it is then important to accurately model the simulation of the b-jets and the b-tagging performance. In addition, the calibration results discussed in Chapter 3 (Fig. 3.6) show that a correction factor is needed to match the performance of the taggers in Monte Carlo with the experimental data. This hints at the fact that some variables, on which taggers rely, might not be well described in the simulation.

The accurate modelling of b-jets and b-taggers is mostly based on a correct description of the underlying quantities, such as the reconstruction efficiency and fake rate of tracks and vertices, and the properties of the reconstructed objects on which the identification algorithms rely. Ultimately, the outcome of this study could drive a re-tuning of the simulation to improve the agreement with data.

The basic idea of this work is to exploit fully reconstructed B hadrons in an exclusive decay channel to select a b-jet enriched sample both in data and Monte Carlo. First a B hadron is fully reconstructed from its decay products and then geometrically associated to its jet. As a second step, a requirement on the invariant mass distribution of the B hadron candidate is applied to select a sample enriched of true b-jets. The residual contamination is treated by means of a background subtraction procedure (see Section 4), in order to obtain a pure b-jet sample that is totally independent from the b-taggers and that is used for the comparison of data and Monte Carlo

4.2 Reconstruction and selection procedure

The $B^{\pm}$ meson (or hadron) is a bound state of a quark and an antiquark (up-type and bottom-type). It has a mass of 5279.26 ± 0.17 MeV and a long lifetime (compared to other mesons and baryons) of $(1.641 \pm 0.008) \cdot 10^{-12}$ s [44]. The lifetime allows an energetic B hadron to travel a few millimetres before decaying at a secondary vertex. $B^{\pm}$ mesons decay into D mesons with a branching ratio of 97%. However, in this analysis it was chosen to study a decay mode characterised by a clear signature that would provide an efficient reconstruction and a small background. Although there are a reasonable number of decay channels of the $B^{\pm}$ that would be suitable for the selection of the b-jet-enriched sample, in practice only one decay mode is

chosen for this analysis:

$$B^{\pm} \to J/\psi K^{\pm} \to \mu^{+}\mu^{-}K^{\pm} \tag{4.1}$$

The J/ψ - a $c\bar{c}$ quarks bound state - decaying into two muons with a branching ratio of $(5.93 \pm 0.06) \cdot 10^{-2}$ [44] provides the required clear signature. In addition this decay mode is characterised by a high branching ratio of $(1.028 \pm 0.031) \cdot 10^{-3}$ [44], compared to other B-decays involving a J/ψ. Finally, the presence of only one additional track to the μ^{+} and μ^{-} increases the reconstruction efficiency, though at the expense of a lower purity.

The study presented in this part of the thesis is based on 4.7 fb^{-1}collected by ATLAS during the year 2011 at a centre-of-mass energy of 7 TeV. The data were triggered requiring two muons originating from the decay of a J/ψ. The data were then selected according to a standard *good run list*, that guarantees a good functioning of all sub-detectors during data acquisition. Due to the high luminosity, multiple interactions can occur in a single bunch crossing. Only the Primary Vertex (PV) of the event is considered and it is defined as the one reconstructed by tracks with the highest squared transverse momentum sum ($\sum_{tracks} p_{\mathrm{T}}^2$). If this vertex is reconstructed by less than four tracks, the event is rejected.

The J/ψ candidate is selected requiring two muons with $p_{\mathrm{T}} > 4$ GeV and an invariant mass within 200 MeV from the J/ψ mass of (3096.916 ± 0.011) MeV [44]. The muons fulfil the *Secondary muons* momentum and pseudorapidity requirements listed in Table 3.1 in Ch. 3. The two muon tracks are fitted together assuming they come from a common vertex and their invariant mass is re-calculated according to the re-fitted parameters.

Secondly, a fully reconstructed $B^{\pm}$ candidate is selected following the scheme shown in Fig. 4.1(a). All tracks that fulfil minimal quality requirements, and have a transverse momentum greater than 2.5 GeV are refitted to a common vertex together with the selected muons. The p_{T} requirement has been chosen in order to reduce the combinatorial background. Any triplet whose re-fit has converged is considered a B candidate. If more than one candidate is found in the event, the one with the lowest vertex fit χ^2 is selected.

Finally, the $B^{\pm}$ candidate is matched to a jet satisfying the basic selection criteria described in Chapter 3 ($p_{\mathrm{T}} > 20$ GeV, $|\eta| < 2.5$) by means of angular matching. It is required to have $\Delta R(B, \mathrm{jet}) < 0.4$[1)], where the candidate $B^{\pm}$ direction is estimated

[1)] $\Delta R = \sqrt{(\phi_B - \phi_{\mathrm{jet}})^2 - (\eta_B - \eta_{\mathrm{jet}})^2}$

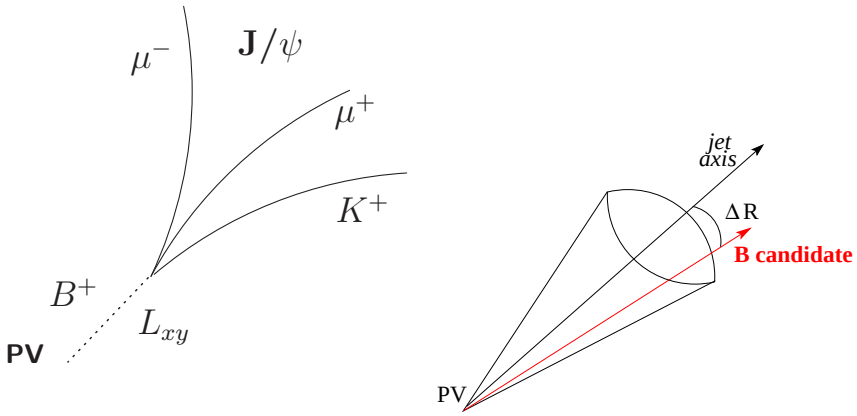

(a) $B^{\pm} \to J/\psi\ K^{\pm}$ candidate (b) jet matching

Figure 4.1: *Schematic view of a $B^{\pm} \to J/\psi\ K^{\pm}$ decay (left) and matching of the* B *hadron to the jet (right).*

by summing the momenta of the muons and the third track. This cut does not introduce any bias, since the bulk ΔR distribution for b-jets is within the requirement, as it will be shown in Ch. 6. If more than one jet is found compatible with the $B^{\pm}$ candidate, only the jet having the smallest ΔR is considered.

It immediately stands out that we are not applying a number of conventional selections for B hadron identification, usually used to enhance the purity of B-resonances sets, such as requirements on the hadron L_{xy} (displacement in the transverse plane) and on the χ^2 of the fit of the displaced vertex.

Making use of these criteria would introduce an obvious bias in our study, since the taggers we are aiming to investigate make use of the same information for the tagging algorithm. However, these relaxed criteria come at the price of higher combinatorial contamination in the B-resonance region of the mass spectrum. The contamination is of the order of 40%, which corresponds to $4 \cdot 10^4$ events within $\pm 2\sigma$ of the B-resonance in the invariant mass distribution, where σ is the resolution of the resonance. This contamination is accounted for by means of a sideband background subtraction procedure described in detail in the following chapter (Ch. 5).

4.3 Definition of the variables under study

As previously mentioned, the aim of this study is to evaluate the reliability of the Monte Carlo description of the most important quantities that characterise the physics and topology of b-jets. These quantities might directly or indirectly influence the behaviour and performance of the b-taggers. For sake of clarity we divide all investigated variables into three groups, although this procedure is not perfectly rigorous, since these categories do not simply factorise.

In the following, we list and describe each variable of each category, as a reference for the rest of the thesis.

Detector specific variables are those variables, that are mostly related to detector reconstruction effects. They are evaluated on each track associated to the jet matched to the B hadron:

- The number of hits in the Pixel detector, in the SCT and in the TRT. For the Pixel detector, the innermost layer (the B-Layer) is studied separately for its importance to the vertex resolution.
- The number of shared hits per track, which are those hits that are associated to multiple tracks by the tracking reconstruction algorithm.
- The impact parameter in the xy plane (d_0) and along the longitudinal axis (z_0) with respect to the Primary Vertex of the interaction and their errors.

Each track entering this study must fulfil the loose requirements as listed in the first column of Table 4.1. Tracks that fulfil stricter requirements are also investigated. These requirement are applied to all tracks used as an input from the b-taggers and will be referred as Btag-Quality criteria.

Physics variables are correlated to the hadronization physics and the topology of the b-jets. In this study we have considered:

- The angular distance of each track to the jet axis ($\Delta R(\text{jet, track}) = \sqrt{(\phi_j - \phi_t)^2 - (\eta_j - \eta_t)^2}$)
- The number of tracks in the jet.
- The number of tracks in a jet that fulfil Btag-Quality requirements (see Table 4.1).

Variable	Standard	Btag-Quality
p_{T} > [GeV]	0.4	1
IP d_0 < [mm]	2	1
IP z_0 < [mm]	10	1.5
SCT hits $\geqslant$	0	5
Silicon hits $\geqslant$	8	8
Pixel hits $\geqslant$	0	3
B-Layer hits $\geqslant$	0	1

Table 4.1: *Requirements for standard and Btag-Quality selected tracks.*

- The track multiplicities as a function of jet p_{T}.

b-tagging algorithm performances The last group of variables aims to investigate the accuracy of the Monte Carlo simulation in describing the behaviour of the taggers and their performance:

- The association efficiency of the B decay products to a displaced vertex for each tagger. For the IP3D tagger we instead evaluate how often the decay tracks enter the pool of tracks used for the probability calculation.
- The association efficiencies as a function of the working points of the taggers.

In Section 3.2.2 the b-tagging algorithms were divided into three categories: the impact parameter based taggers, the vertex based ones and the combined taggers. In this study, a representative tagger for each category was chosen and investigated: IP3D for the first category, SV1 for the second, and JetFitter for the third.

The fact that the B hadron decay in the selected b-jets is fully reconstructed and the B decay products are identified, allows to divide the tracks associated to the b-jet into two categories and separately compare the investigated quantities:

I. the B decay products (muons and kaons);

II. the hadronization tracks, defined as those tracks associated to the selected jet and not identified as the kaon or the muons.

As described in the following section, the different nature of these categories will be taken into account also in calculating corrective weights for the Monte Carlo simulation.

4.4 The Monte Carlo simulation

The Monte Carlo simulation used for the comparison with the experimental data in this analysis is enriched in $B^{\pm} \to J/\psi\, K^{\pm}$ decays. At the generator level, the ATLAS specific PYTHIA implementation for the generation of B decays was used, which provides an interface to PYTHIA (version 6.4) [110]. The detector simulation was performed using the ATLFAST-II package [111], which performs a simulation of the ATLAS detector geometry based on the Geant4 toolkit [112]. In this package a *fast* simulation of the ATLAS calorimeter is implemented, which relies on the parameterisations of the longitudinal and lateral energy profiles. The rest of the detector, including the tracking system is fully simulated. In this way the simulation time is reduced by one order of magnitude. All distributions of this Monte Carlo sample have been compared with a smaller sample based on a full Geant4 simulation of the entire ATLAS detector, including the calorimeters, and found to be in very good agreement.

The signal events in the Monte Carlo simulation have been further selected requiring a true $B^{\pm} \to J/\psi\, K^{\pm}$ decay within geometrical acceptance associated in ΔR to the reconstructed candidate.

As mentioned in Sec. 2.1, the high luminosity conditions of the LHC come at the price of a high average number of interactions (pile-up) occurring at each bunch crossing. This is not perfectly reproduced in the Monte Carlo simulation and a corrective weight needs to be applied to each event to improve the simulation modelling of the pile-up. In addition, the momentum and pseudorapidity distributions of the matched jets, and, as a consequence, of the jet tracks differ between the data and the simulation. This might introduce a distortion in some distributions. In order to disentangle p_{T} and η effects in the comparisons, it was decided to apply an additional reweighting of these distributions, on top of the afore mentioned pile-up correction.

In summary, the following corrective weights have been applied to the quantities investigated in this study:

(a) A weight has been calculated for each *track category* - muons, kaons and hadronization tracks - in order to match the η and p_{T} distributions of each category between data and the Monte Carlo simulation.

(b) All variables that do not belong to any specific *track category*, have been reweighted according to the η and p_{T} distributions of the matched jet.

(c) From the average number of interactions per event (pile-up) an overall weight was derived that has been applied to every object in the event.

The distributions of the momenta of the matched jet and of the hadronization tracks of the jet are shown in Figures 4.2. The good agreement of such distributions after re-weighting assure that any p_{T}-effect is disentangled and removed from the other more interesting sources of discrepancies in the investigated variables.

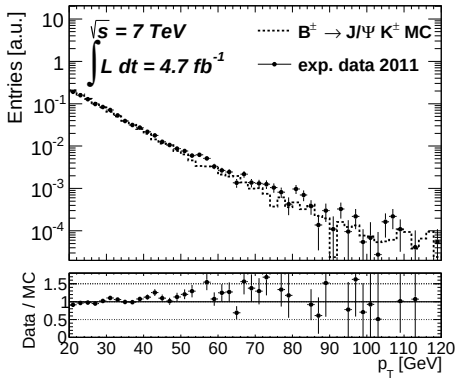

(a) matched jet p_{T} before reweighting

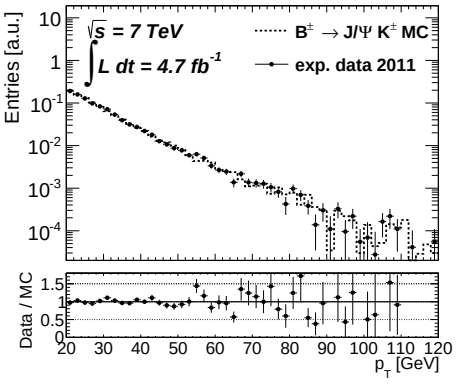

(b) matched jet p_{T} after reweighting

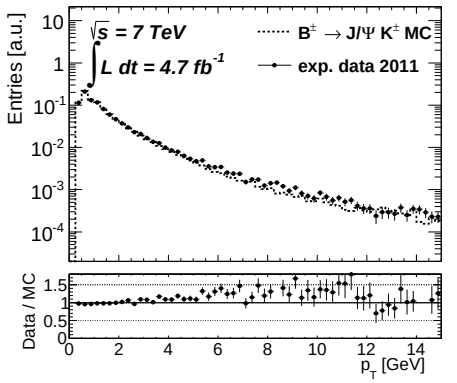

(c) hadronization tracks p_{T} before reweighting

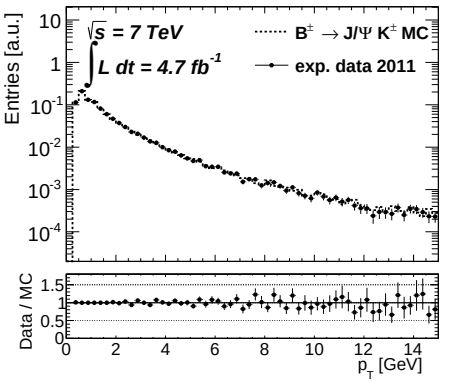

(d) hadronization tracks p_{T} after reweighting

Figure 4.2: *Transverse momentum distributions of the jet associated to the* B *hadron and of the hadronization tracks associated to this jet, before and after $eta - p_{\mathrm{T}}$ reweighting.*

5 The sideband background subtraction procedure

The selection of an unbiased sample of $B^{\pm} \to J/\psi\, K^{\pm}$ *decays and their associated b-jets comes at the price of a relatively high contamination of combinatorial background. This problem is addressed by means of a sideband background subtraction procedure. The number of* $B^{\pm} \to J/\psi\, K^{\pm}$ *candidates and the combinatorial background is obtained by fitting the invariant mass distribution of the* $\mu^+\mu^- K^{\pm}$ *tracks. In this section, the background subtraction procedure and the invariant mass fit are presented. The assumptions of the method are verified by three different consistency tests directly in the experimental data and in a Monte Carlo simulation that consists of* $B^{\pm} \to J/\psi\, K^{\pm}$ *events and injected background.*

5.1 Background subtraction procedure

The mass spectrum of all $B^{\pm}$ candidates selected according to the procedure described in Chapter 4 is shown in Figure 5.1. In order to separate the signal from the combinatorial background, a sideband-based background subtraction procedure has been adopted. The main assumption of this procedure is that it is possible to define a background enriched region in the invariant mass spectrum, the *sideband region*, that can be extrapolated to the region around the $B^{\pm}$ resonance peak, the *peak region*. The *sideband region* is defined as the mass region between $m_B + 3\sigma$ and 6.6 GeV, with m_B the $B^{\pm}$ mass and σ the variance of the fitted peak. The *peak region* is defined by a 2σ window around the $B^{\pm}$ mass. A simultaneous fit is performed in

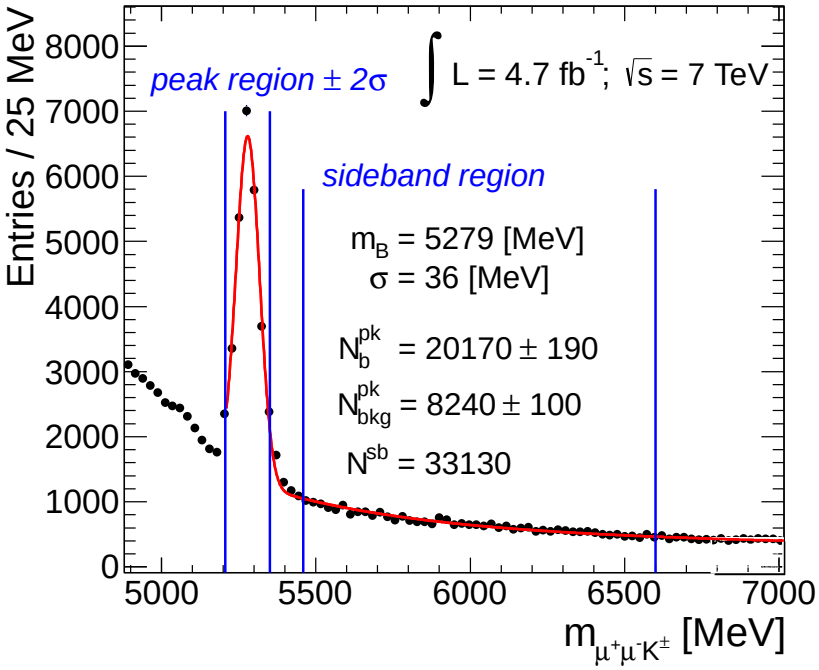

Figure 5.1: *Invariant mass distribution of* $B^{\pm}$ *hadron candidates in the full 2011 dataset (*4.7 fb^{-1}*). The curve in the plot shows the result of the fit (gaussian plus two exponential distributions) used to estimate the background normalisation in the resonance region. The integral of the gaussian and the exponential distributions resulting from the fit are shown in the plot (*N_b^{pk} *and* N_{bkg}^{pk} *respectively).* N^{sb} *is the number of events in the high invariant mass sideband.*

these two regions of invariant mass in order to estimate the background and signal normalisations.

It is assumed that the distribution of a certain variable $\mathcal{X}$, that is our object of study, in the background is the same for the events in the sideband region $\mathcal{X}^{sb}$ and under the resonance peak $\mathcal{X}^{pk}$. Under this assumption, the background distribution of this quantity is obtained from the *sideband region* and statistically subtracted from the *peak region* events in order to obtain the distribution of $\mathcal{X}$ for the $B^{\pm} \to J/\psi\, K^{\pm}$ events:

$$\mathcal{X}^{sig} = \mathcal{X}^{pk} - \kappa_{fit}\mathcal{X}^{sb} \tag{5.1}$$

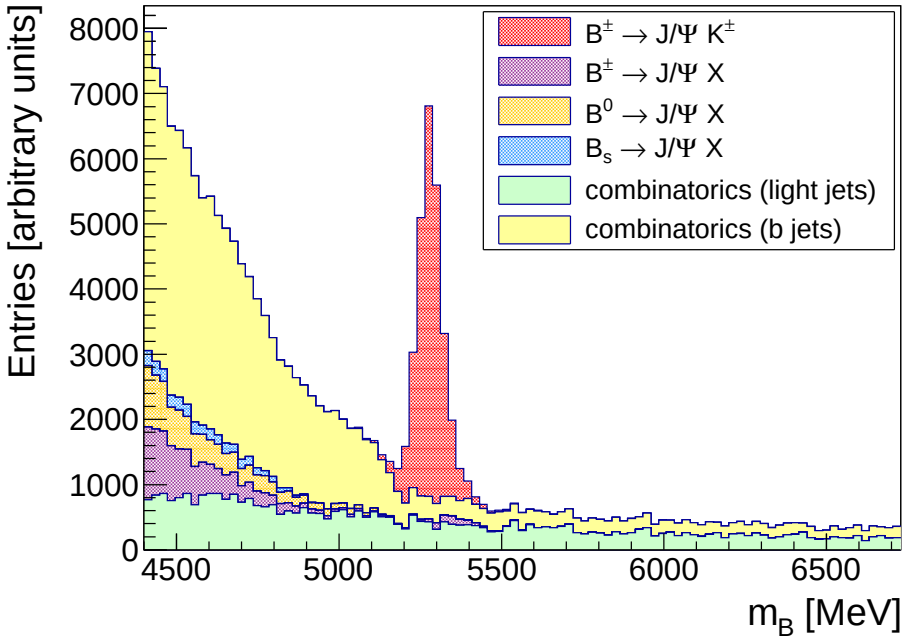

Figure 5.2: *Invariant mass distribution of* $B^{\pm}$ *hadron candidates in the Monte Carlo simulation. The* $B^{\pm} \rightarrow J/\psi\ X$ *events and combinatorial background are plotted in different colours to highlight the high and low mass* sidebands *compositions with respect to the* peak region.

where κ_{fit} is the ratio of the number of background events in the *peak region* estimated by the fit over the number of events in the *sideband region*. After the background subtraction, $\mathcal{X}^{\text{sig}}$ is compared with the distribution of true $B^{\pm} \rightarrow J/\psi\ K^{\pm}$ events obtained from the Monte Carlo simulation ($\mathcal{X}^{\text{true}}$).

Two *sidebands*, on each side of the resonance peak, are commonly used for the background estimate and subtraction. However, studies based on Monte Carlo simulation have shown that masses lower than the $B^{\pm}$ resonance peak are not enriched by the same background (combinatorics and jets from light flavour quarks) that we find in both the *peak region* and the high mass *sideband*. Figure 5.2 shows that the low invariant mass region has a large contribution from partially reconstructed B-hadron decays, other than $B^{\pm} \rightarrow J/\psi\ K^{\pm}$ ones, and therefore differs in composition from the rest of the spectrum, mainly contaminated by combinatorics.

	Peak window	Fit range bounds		$B^{\pm} \to J/\psi\, K^{\pm}$ events	
		Low	High	fitted	true
Test 1	$mB \pm 2\sigma$	$mB - 2\sigma$	6.0 GeV	1219 ± 30	1238
Test 2	$mB \pm 2\sigma$	$mB - 2\sigma$	6.5 GeV	1375 ± 29	1267
Test 3	$mB \pm 2\sigma$	$mB - 5\sigma$	8.0 GeV	1156 ± 65	1223
Test 4	$mB \pm 5\sigma$	$mB - 5\sigma$	6.5 GeV	1601 ± 35	1406
Test 5	$mB \pm 5\sigma$	$mB - 5\sigma$	8.0 GeV	1600 ± 55	1406
Nominal	$mB \pm 2\sigma$	$mB - 2\sigma$	8.0 GeV	1246 ± 61	1242
1 exponential	$mB \pm 2\sigma$	$mB - 2\sigma$	8.0 GeV	1327 ± 61	1242

Table 5.1: *Various tests in which different fit boundaries and peak windows are used. The number of* $B^{\pm} \to J/\psi\, K^{\pm}$ *events estimated by the fit are compared with the true value in order to estimate the goodness of the fit. Unless otherwise stated all tests assume bi-exponential background description.*

5.2 Details on the background normalisation estimate

The background normalisation in the peak region is evaluated by a simultaneous fit of the invariant mass distribution both in the *peak* and in the *sideband regions*.

A double exponential function is used to describe the background and a Gaussian is used for the signal. The double exponential is justified by the presence of two kinds of combinatorial backgrounds, one mainly composed of J/ψ mesons produced at the primary vertex (*prompt* J/ψ) and associated with light flavour or charm jets and one composed of $B^{\pm}$ hadron decays without a J/ψ.

The fitting procedure, the background fitting function and the stability of the fit against a variation of its boundaries have been tested on a Monte Carlo sample. The results have been summarised in Table 5.1. The configuration that estimated best the true number of $B^{\pm} \to J/\psi\, K^{\pm}$ in the resonance peak is found to be the one with a 2σ window around the $B^{\pm}$ mass and fit boundaries of $m_B - 2\sigma < m_{\mu\mu K} < 8$ GeV.

Applied in data, this fit procedure results in an estimate of $(8.2 \pm 0.1) \cdot 10^3$ background events and $(20.2 \pm 0.2) \cdot 10^3$ $B^{\pm} \to J/\psi\, K^{\pm}$ candidates in the *peak region*. The fit uncertainty on the total number of background events has been propagated into the background subtraction procedure and it gives rise to a systematic uncertainty of 1.2% on the normalisation of the background distributions. This uncertainty is

subdominant with respect to the statistical uncertainty of the Monte Carlo sample.

5.3 Consistency tests of the procedure

From the breakdown of the invariant mass distribution into the various contributions from background and signal processes in Figure 5.2 it was deduced that the high invariant mass sideband has a background composition that is more similar to the peak region than the low mass sideband. In addition it was stated that the basic assumption of the background subtraction procedure is that for each variable $\mathcal{X}$ considered:

$$\mathcal{X}^{\mathrm{pk}}(\mathrm{bkg}) = \mathcal{X}^{\mathrm{sb}}, \tag{5.2}$$

where $\mathcal{X}^{\mathrm{pk}}(\mathrm{bkg})$ is the distribution of the background in the *peak region* and $\mathcal{X}^{\mathrm{sb}}$ is the background distribution in the *sideband region*. For each distribution considered in this analysis, this assumption has been verified by means of three different tests in order to eliminate the background subtraction procedure as a source of residual disagreement between data and Monte Carlo.

The first test (background injection test) consists of a validation of the background subtraction procedure with a Monte Carlo sample that is composed of true $b\bar{b}$ events (including $\mathrm{B}^{\pm} \to \mathrm{J}/\psi\,\mathrm{K}^{\pm}$ events) and a fixed contamination of prompt J/ψ. The latter has been normalised such that the total number of events in the high sideband region was matching the number of events in data. Distributions obtained from this $b\bar{b}$+prompt J/ψ Monte Carlo sample according to the background subtraction procedure described in Sec. 5.1 have been compared with the true $\mathrm{B}^{\pm} \to \mathrm{J}/\psi\,\mathrm{K}^{\pm}$ events of the same sample. The same closure test has been performed by also injecting different amounts of background and varying the width of the peak region. All different variations of this test have proved that it is always possible to separate the background component of the sample from the true signal events.

Another way to formulate the assumption in Equation (5.2) is that for background events the variables under investigation are independent of the $\mathrm{B}^{\pm}$ reconstructed invariant mass. The second test aims to verify this main hypothesis directly on data. Two intervals have been defined in the invariant mass region of the sideband and compared to identify possible distribution dependences on the $\mathrm{B}^{\pm}$ invariant mass. The first is defined in the range $[5.5-6.0]$ GeV and the second is defined in the range $[6.0-7.5]$ GeV.

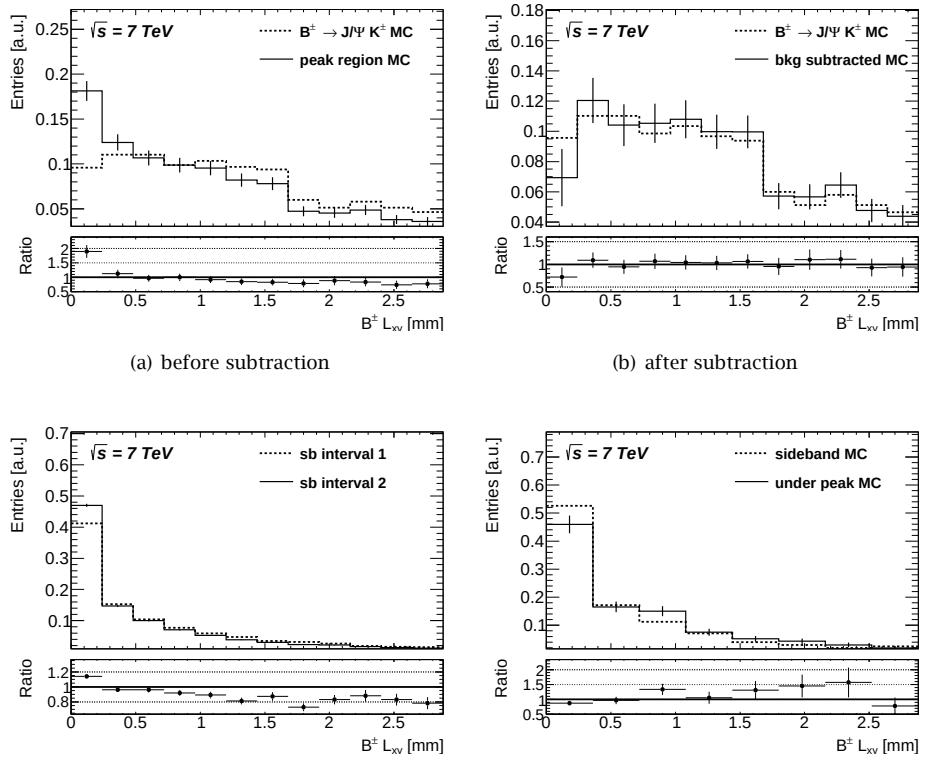

(a) before subtraction

(b) after subtraction

(c) mass dependence test on data

(d) mass dependence test on Monte Carlo

Figure 5.3: *Displacement in the transverse plane of the* $B^{\pm}$ *secondary vertex with respect to the Primary Vertex of the event (L_{xy}). The distribution before and after background subtraction are shown in subfigures (a) and (b). The mass dependence tests, where background from either data or Monte Carlo is compared in two different invariant mass regions, are presented in subfigures (c) and (d).*

Finally, the third test makes use of a pure background sample, with the same composition used for the background injection test, and compares the various distributions between the sideband and the peak region.

The first important proof of the fact that the background subtraction is really addressing the contamination of the distribution is given by the $B^{\pm}$ displacement in the transverse plane, L_{xy}, shown in Figure 5.3. The events labelled $B^{\pm} \to J/\psi\, K^{\pm}$ MC are the signal events selected using the true Monte Carlo information. In the first two subfigures the comparison of the distributions in the background injection test

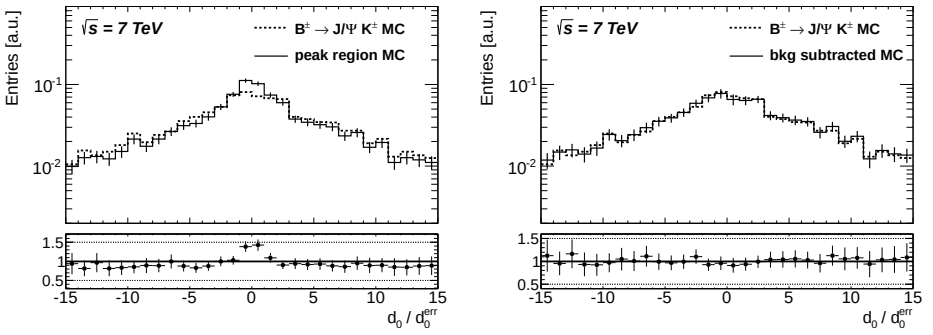

(a) before subtraction (b) after subtraction

Figure 5.4: *Distribution of the transverse impact parameter significance (d_0/d_0^{err}) of muons produced in the* $\mathrm{B}^{\pm}$ *decay. The contamination of background muons with small impact parameter significance can be seen in the distribution before background subtraction (left). This contamination is removed after the background subtraction (right).*

before and after the true signal event extraction using the background subtraction procedure is shown. After the subtraction there is good agreement between the two distributions. In the other two subfigures the result of the invariant mass dependence tests performed in data and using the Monte Carlo simulation are displayed. In Figure 5.3(c) the shape of the L_{xy} distribution in two different sideband intervals is compared. In Figure 5.3(d) the distribution of L_{xy} in the sideband region is compared to the distribution in the peak region using a pure background Monte Carlo sample. In both cases, no dependence of the distribution on the invariant mass of the B candidate is observed, proving that the assumptions made for using the background subtraction procedure hold for this distribution.

Figure 5.4 shows the significance of the transverse impact parameter of the tracks with respect to the primary vertex (i.e. the ratio of the impact parameter d_0 over its uncertainty). This example shows again how a mixed composition of events (b-jets and light flavour jets) that enter in the resonance region of the $\mathrm{B}^{\pm}$ candidate invariant mass distribution, can be corrected for background contamination through the subtraction procedure. All impact parameter related distributions and their uncertainties, for both muons and kaons have been investigated and show the same characteristics of the afore mentioned Fig. 5.4.

A number of distributions show only a very small influence from the combinatorial contamination, such as the number of hits in the inner detector subsystems,

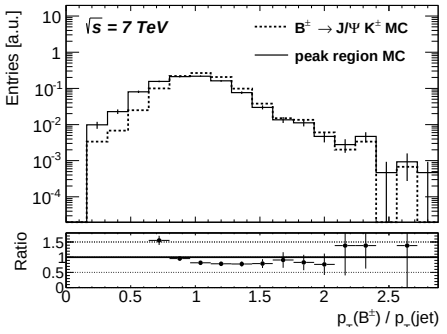

(a) before subtraction

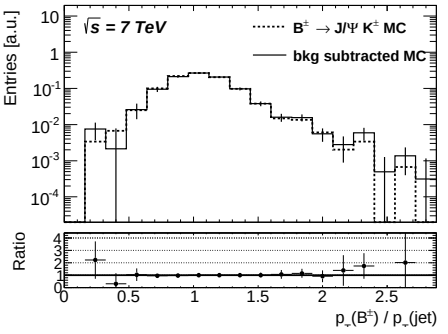

(b) after subtraction

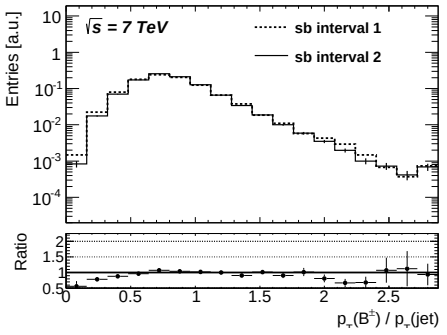

(c) mass dependence test on data

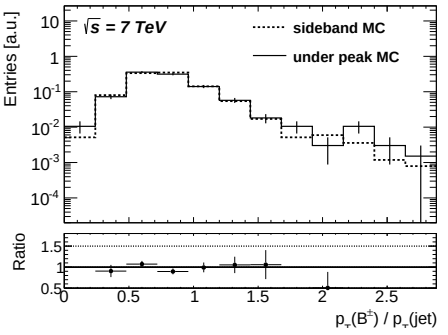

(d) mass dependence test on Monte Carlo

Figure 5.5: *Ratio of the transverse momenta of the* $B^{\pm}$ *candidate and the jet associated to it* ($\frac{p_T(B^{\pm})}{p_T(jet)}$)*. The distribution before and after background subtraction, and the mass dependence tests are presented in the four subfigures.*

the hadronization tracks multiplicity, and the $B^{\pm}$ candidates multiplicity. For these distributions the hypothesis of the background subtraction procedure is proven to be valid.

The transverse momentum of the $B^{\pm}$ hadron and its decay products seems instead sensitive to the contamination. Figure 5.5 shows the ratio of the transverse momenta of the $B^{\pm}$ and the jet matched to it. Since the muons are not included in the jet energy measurement, except for the small amount of energy they loose in the calorimeter, the distribution can assume values above one. The validation plots show that before the correction, there is a shoulder in the low edge of the distribution. This feature is removed in the background subtraction procedure and (almost) completely corrected. The invariant mass dependence tests on data and Monte Carlo confirm the independence of this observable from the $B^{\pm}$ invariant mass and verify the main assumption of the procedure.

In the selections only the direction of the reconstructed B hadron is matched to the jet, hence the tracks from its decay products might not all be associated to the jet. The distribution in Figure 5.6(a) shows the number of B decay products that are associated to the jet in each event. It represents a clear example of quantities for which the background subtraction assumption does not hold since it shows a strong invariant mass dependence. Further considerations on this quantity in Section 6.4 will lead us to restrict the analysed sample to those events in which all three decay tracks of the $B^{\pm}$ end up in the matched jet.

Additional examples of distributions for which the background subtraction procedure might introduce a bias are shown in the other subfigures of Figure 5.6. The angular distance (ΔR) between each of the $B^{\pm}$ decay products (muons and kaons) and the $B^{\pm}$ flight direction is presented. The kaons show a strong invariant mass dependence that might lead to the introduction of biases in the procedure. The muons show a similar behaviour, though with a smaller dependence of the observable to the $B^{\pm}$ invariant mass and no dependence at all if the ΔR with respect to the jet axis is considered.

Also the ratio between the kaon momentum and the jet p_{T} and the ΔR between the kaon and the jet axis fall in the same category of suspicious variables.

In conclusion, the majority of the quantities that this analysis aims to investigate has been proved to be unbiased by the background subtraction procedure needed to deal with the combinatorial contamination. For a limited group of quantities, however, the assumption of this procedure does not hold and they will be either excluded from the study or interpreted with additional caution in the comparisons

presented in the next chapter.

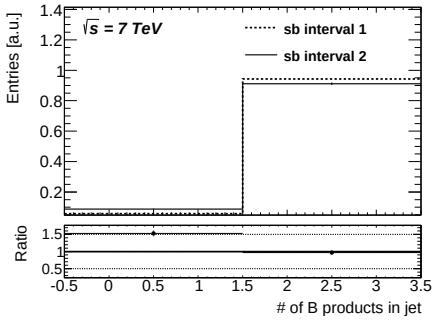

(a) Number of $B^{\pm} \to J/\psi\, K^{\pm}$ decay products that are associated with the matched jet

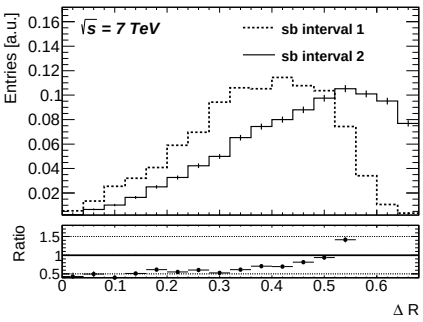

(b) Angular distance (ΔR) between the kaon track and the B hadron direction of flight

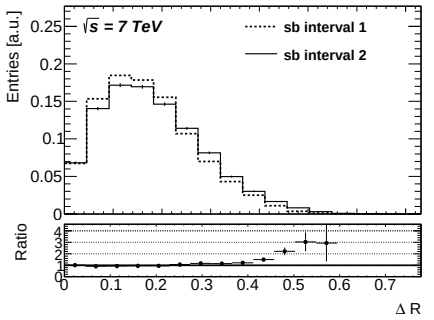

(c) Angular distance (ΔR) between the muon track and the B hadron direction of flight

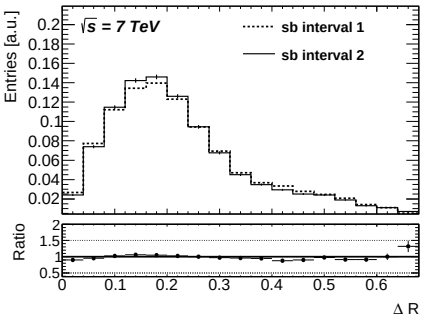

(d) Angular distance (ΔR) between the muon track and the matched jet axis

Figure 5.6: *Mass dependence test performed on data. All distributions show a different shape in the two sidebands intervals that corresponds to an invariant mass dependence of the quantity. This makes the background subtraction procedure not applicable for all these distributions.*

6 Analysis of b-jets properties in $5\,\text{fb}^{-1}$ of data at $\sqrt{s}$ = 7 TeV

B-jets properties and the performance of the tagging algorithms are studied in data and compared to the Monte Carlo simulation. The majority of the observables are found to be well described by the simulation, in particular the modelling of the hadronization track properties and their angular distribution with respect to the jet. A few variables have been found to be sensitive to contamination and not included in the comparison. Finally the b-tagging performance has been found to be in agreement to the Monte Carlo at the few percent level.

In this chapter, a number of properties of b-jets will be evaluated in the data sample collected with the ATLAS detector at $\sqrt{s}$ = 7 TeV during the year 2011 and compared to the Monte Carlo simulation. In each of the Figures, the bottom panel indicates the ratio between the two distributions shown in the plot. For sake of clarity the investigated variables are divided into three categories: detector specific quantities, observables sensitive to the hadronization physics, and tagging algorithm performance. All distributions are reweighted according to the procedure in Section 4.4 and the background contamination has been subtracted according to the sideband subtraction method detailed in Chapter 5.

6.1 Evaluation of the detector reconstruction simulation

The *detector specific* variables describe a class of observables that are strongly influenced by the detector reconstruction. The accuracy of the description in the Monte Carlo simulation is evaluated in the following.

The number of innermost Pixel layer (the B-Layer) and other Pixel detector hits for hadronization and B decay products are compared in Figure 6.1. They are of utmost importance for the tagger performance since they determine both the primary and the secondary vertices reconstruction efficiency and resolution. The distribution of the number of B-Layer hits and number of total Pixel detector hits is well reproduced by the Monte Carlo, with a small shift toward higher multiplicity values of approximately 10%. The number of hits associated to the SCT and TRT sub-detectors for the hadronization and the $B^{\pm}$ decay products have also been studied and show a similar behaviour, but with a smaller discrepancy of approximately 5%.

The second comparison for the detector simulation concerns the impact parameters of the hadronization tracks of the jet in the transverse plane (d_0) and along the beam axis (z_0), calculated with respect to the primary vertex of the interaction. They are shown in Figure 6.2 and they are characterised by a wider distribution in data compared to the Monte Carlo simulation, with a 20% discrepancy in the tails of the distribution. This underestimation of the spread of the distribution in Monte Carlo was confirmed by orthogonal studies [8] and it is likely to have an impact on the different performance of the b-taggers in data and Monte Carlo, since they exploit or rely on this information for the b-jets identification. It would be realistic to assume that this mismodelling contributes to the deviation from one of the b-tagging calibration scale factors. The distributions of the uncertainty associated to the impact parameters and the impact parameter distributions of the $B^{\pm}$ decay products have been also investigated and in this case they are found to be in very good agreement between data and Monte Carlo.

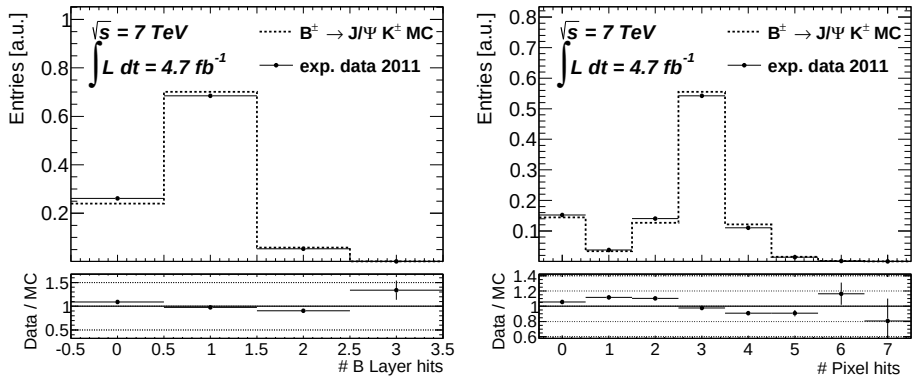

(a) Innermost Pixel layer (B-Layer) (b) all Pixel detector hits

Figure 6.1: *The multiplicity distributions of B-Layer and other Pixel detector hits are presented. Tracks used to evaluate the multiplicity distributions are identified as hadronization products, which means that they have been associated to the jet and are not identified as* $B^{\pm}$ *decay products.*

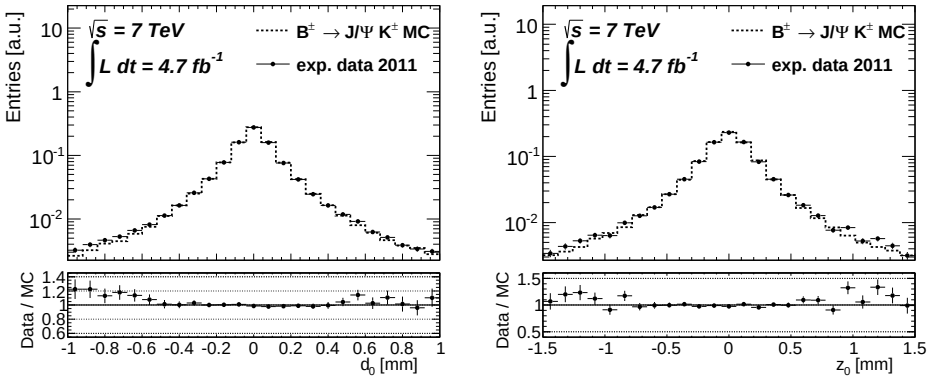

(a) transverse impact parameter (b) longitudinal impact parameter

Figure 6.2: *Transverse and longitudinal impact parameters of the hadronization tracks calculated with respect to the primary vertex of the interaction.*

6.2 Comparison of hadronization physics observables

The reliability of the description of the hadronization process in simulated events is verified by means of the second group of quantities. These so called *physics variables* are connected directly with the physics involved in the simulation, such as the spatial distribution of hadronization products, the track multiplicity and the structure of the b-jet as well as the topological distribution of the B decay products and their orientation with respect to the jet axis. A number of these variables were proven in Chapter 5 to have a dependence on the B candidate invariant mass, such that the background subtraction procedure would introduce a bias. Among these are quantities like the probability of the B decay products to be associated to the jet by angular matching and the angular separation (ΔR) between the kaon track and either the jet axis or the B direction of flight. For this reason, the angular distributions of tracks with respect to the jet presented in this section have been evaluated only on muon and hadronization tracks. In addition, all distributions aiming to evaluate the b-tagging algorithms performance in the following section were obtained by requiring that all the three decay products of the $B^{\pm}$ were associated to the jet, in order to remove possible disagreements raising from events in which not all the B decay products were among the sample of tracks used by the tagging algorithms.

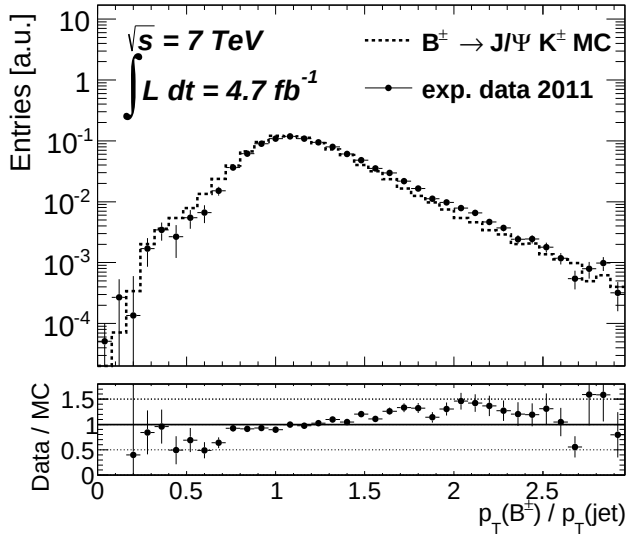

Figure 6.3: *Fraction of momentum carried by the $B^{\pm}$ with respect to the jet.*

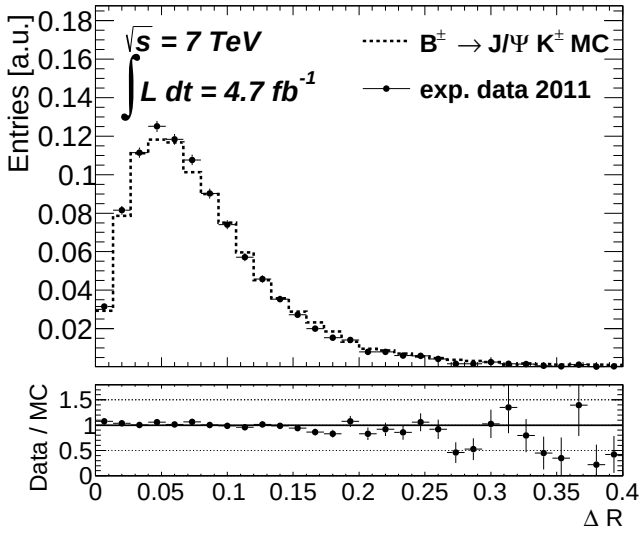

Figure 6.4: *Angular distance between the reconstructed* B *hadron and the matched jet axis.*

6.2.1 B hadron and jet correlations

The first comparison that is presented aims to investigate the correlations between the B hadron and the associated jet. Figure 6.3 shows the fraction of momentum carried by the $B^{\pm}$ with respect to the jet, an observable that is correlated with the B fragmentation function of the jet showering process. The bulk of the distribution is well described by the simulation. However, a larger tail in data can be observed for events in which the B hadron momentum is more than one and a half times larger than the one of the associated jet, which hints to a deficiency of the simulation in modelling soft hadronization processes. The discrepancy seems to be more prominent, although with lower statistical significance, in the *Barrel* region and at low hadron momentum.

In order to complete the overview on the correlations between the B hadron and its associated jet, the distribution of the angular distance (ΔR) of the B hadron to the jet axis is shown in Figure 6.4. It shows a good agreement with data that reflects the quality of the Monte Carlo generator tuning and the good description the *b*-quark and its hadronization process.

6.2.2 Jet topology

The general topology of the b-jet is studied through the multiplicity of the tracks in the jet and the angular distance between these tracks and the jet axis.

A first evaluation of the reliability of the Monte Carlo simulation is obtained by studying the multiplicity of the hadronization tracks of the jet. A different density of tracks in the jet environment might highlight a simulation inaccuracy that causes different performance of the b-taggers in data and in Monte Carlo. The plots in Figure 6.5 show a good agreement of the hadronization track multiplicity and its p_{T} profile, with a very small tendency of the simulation to underestimate the multiplicity.

As the jet-track association is mostly based on angular matching, the ΔR of the hadronization tracks with respect to the jet axis has also been considered. As shown in Figure 6.6(a) it is extremely well described by the simulation. Furthermore, the distribution of the maximum of this ΔR for each jet, representing the most "far-away" hadronization product, is presented in Figure 6.6(b). Also this distribution is well modelled by the simulation, including the bin at zero that represent those events in which no other charged particles in addition to the $\mathrm{B}^{\pm}$ decay products have been associated to the matched jet.

The muon angular distance with respect to the B direction of flight is shown in Figure 6.7. There is a reasonable agreement, up to $\Delta R = 0.4$, between the data and the simulation. Above $\Delta R = 0.4$, the hypothesis of the background subtraction was proven not to hold (see Chapter 5) and a bias from the procedure was expected. However, the ΔR between the muon tracks and the jet axis, for which no bias was expected from the background subtraction, shows a consistent disagreement between the data and the simulation. It was not possible to unambiguously determine whether this effect is a real mismodelling of the simulation or it is caused by a not understood correlation effect between the B invariant mass and the ΔR between the muon tracks and the jet axis.

In summary it is safe to state that the simulation of the hadronization physics, once disentangled from the rest of the event (background contamination effects, B decay, etc.), is in very good agreement with the experimental data.

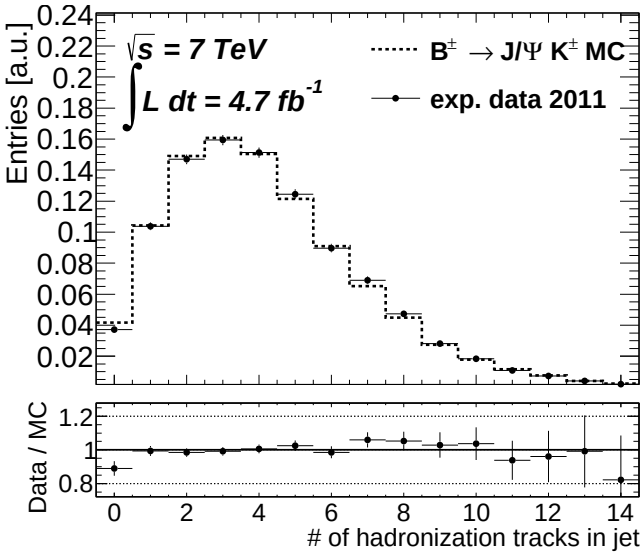

(a) multiplicity distribution

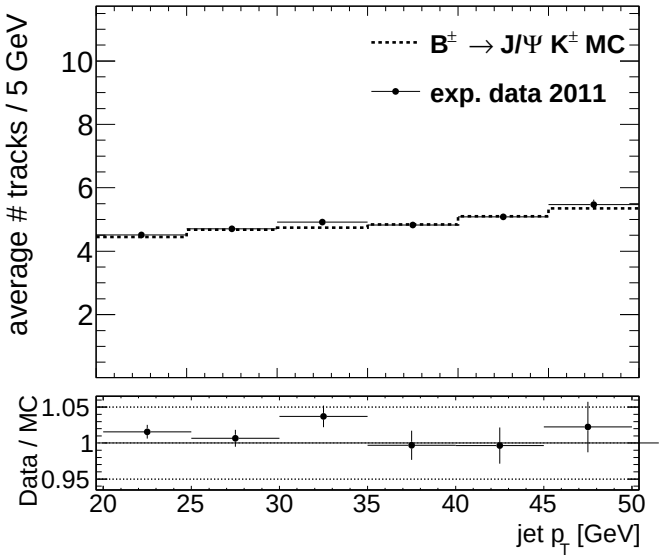

(b) p_{T} profile

Figure 6.5: *Number of hadronization tracks in the b-jet. The hadronization tracks are identified as all the tracks associated to the jet except the* $\mathrm{B}^{\pm}$ *decay products. The multiplicity is also shown as a function of the jet* p_{T}*.*

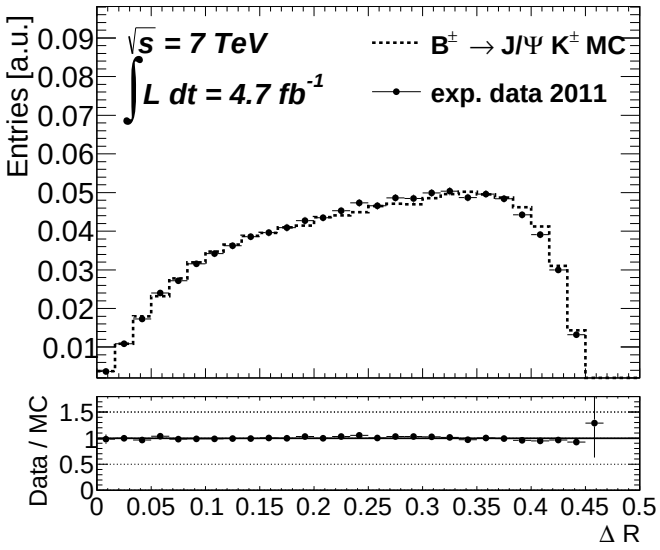

(a) ΔR track - jet axis

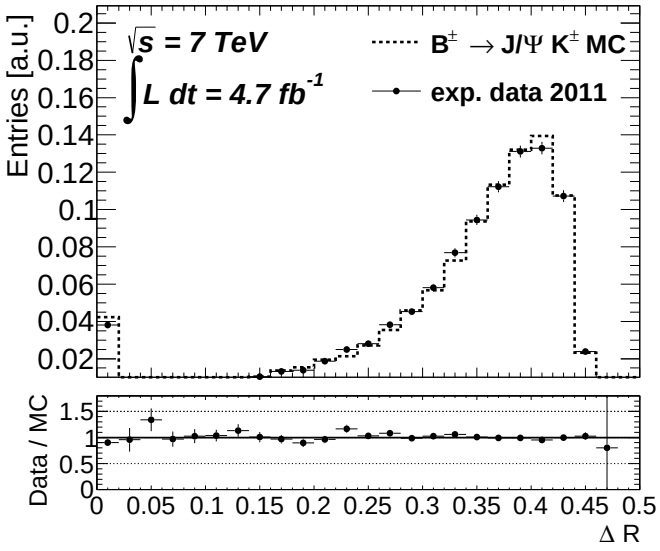

(b) maximum of ΔR track - jet axis

Figure 6.6: *Angular distance between the hadronization tracks of the jet and the jet axis and distribution of the maximum value per each jet.*

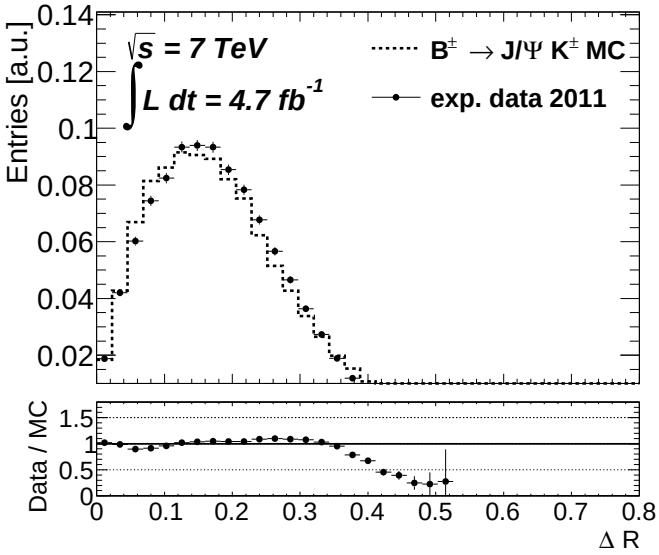

(a) ΔR muon track - B hadron

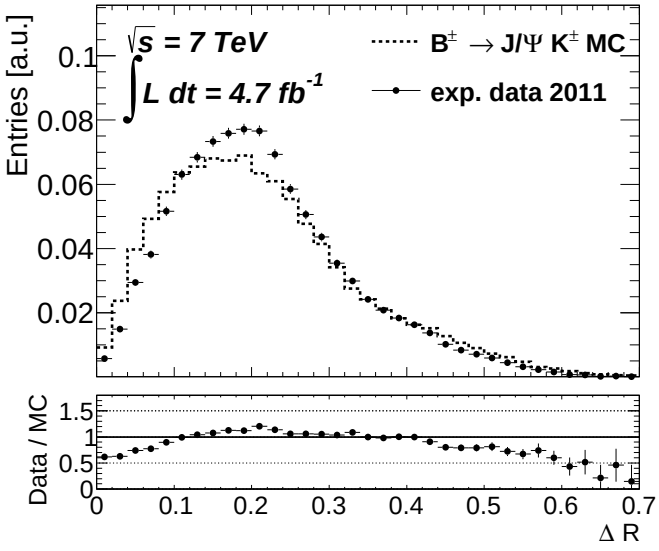

(b) ΔR muon track - jet axis

Figure 6.7: *Angular distance between the muon tracks from the* B *decay and the* B *hadron direction of flight or the distance between the muon tracks and the jet axis.*

6.3 Intermezzo: detector effects on hadronization physics

The tracks used by the b-taggers have to fulfil stricter quality requirements than the tracks investigated in the previous sections. These requirements have been introduced in Chapter 4.3, Table 4.1 and involve higher cuts on the number of hits on tracks in the Inner Detector and a minimum track transverse momentum of 1 GeV. Consequently, once the good description of the detector is verified, it is interesting to investigate the ability of the Monte Carlo simulation to describe the jet physics if only these "high quality" (Btag-Quality) tracks are considered. The number of inner detector hits and the impact parameters have been studied for this additional track category. As before, these show a good agreement in the shapes with the same tendency of the Monte Carlo simulation of overestimating the number of hits on a track.

Secondly, the angular distribution of the hadronization tracks that fulfil Btag-Quality requirements with respect to the jet axis was investigated. Both the distribution of ΔR between each track and the jet axis and the maximum ΔR for each jet are presented in Figures 6.8(a) and 6.8(b) and found to be in excellent agreement with the data.

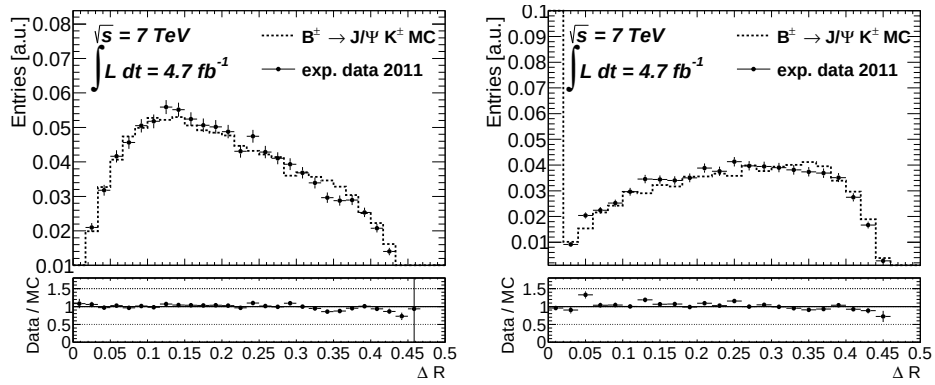

(a) ΔR (b) ΔR max

Figure 6.8: *Angular distance between the hadronization tracks of the jet and the jet axis and the maximum value for each jet for tracks of Btag-Quality.*

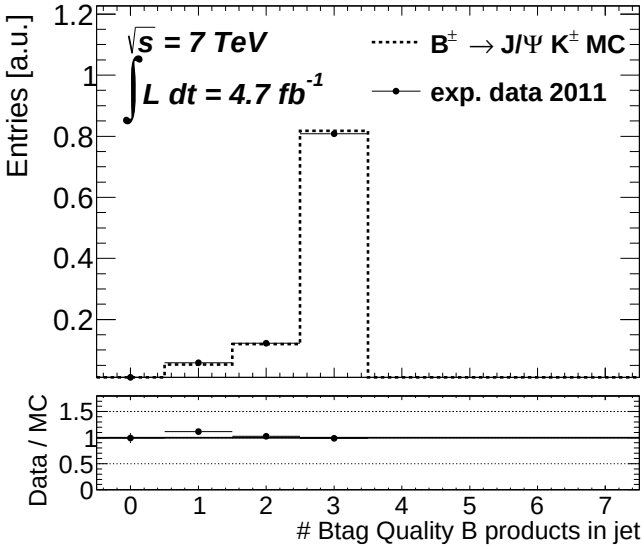

Figure 6.9: *Distribution of the number of* B *decay products associated to the matched jet that that fulfil Btag-Quality requirement.*

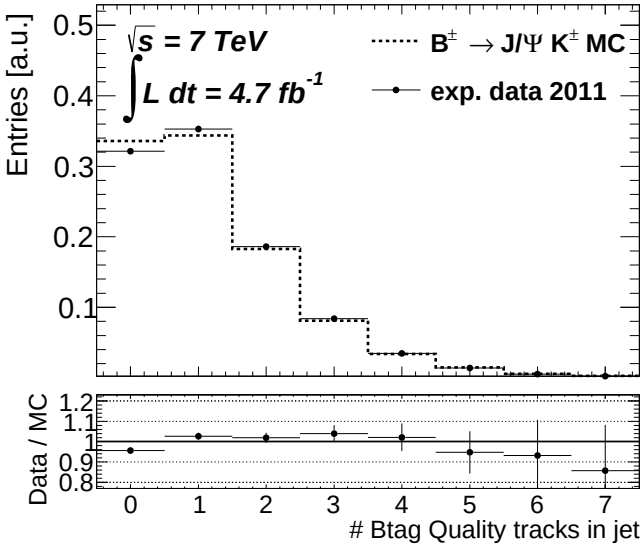

Figure 6.10: *Distribution of the number of hadronization tracks in a jet that fulfil Btag-Quality requirement.*

Subsequently, the distribution of the number of B decay products in the jet that fulfil the Btag-Quality criteria is presented in Figure 6.9 and it is also found to be well modelled.

Finally, the multiplicity of hadronization tracks that fulfil these Btag-Quality requirements is presented in Figure 6.10, with the purpose of probing the response to these selection criteria of the jet hadronization products. There is a good agreement between the data and the Monte Carlo simulation, with a small tendency from the latter in underestimating the reconstruction performance by 5%, estimating a lower number of Btag-Quality tracks with respect to the data. In order to further investigate this effect, an additional set of requirements has been defined, each obtained by removing one of the requirements that define the Btag-Quality tracks criteria. Each of these sets of requirements was separately investigated, in the attempt to identify which of the Btag-Quality requirement(s) is mainly responsible for the disagreement.

All distributions have shown a very good agreement between the Monte Carlo simulation and the data, which leads us to the conclusion that the 5% disagreement on the inclusive distribution is originating from the combination of many small effects (<1%) in each of the variables used to define the Btag-Quality requirements and not from a single mismodelled distribution.

6.4 Tagging algorithms performance studies

The last comparison aims to evaluate the simulation of the the performance of the *b*-tagging algorithms. Given that the $B^{\pm}$ decay is completely reconstructed, it is possible to investigate the performance of the taggers under study evaluating their ability to correctly identify the tracks from the decay. In order to disentangle the jet association efficiency from the performance evaluation, only events in which the B decay products have been associated to the matched jet are considered.

In such a clear topology as the $B^{\pm}$ decay we consider, it would prove particularly interesting to identify differences between data and Monte Carlo. This decay is characterised by little impact of track reconstruction efficiency effects, due to the fact that in all events it has already been possible to reconstruct the $B^{\pm}$. Therefore this study allows to disentangle this effect from any other possible source of disagreement. On the other hand, it is important to highlight that any conclusions about a good modelling of the performance in these events cannot be easily extrapolated to an inclusive *b*-jets sample.

First of all, Figures 6.11(a) and 6.11(b) show the number of tracks associated by

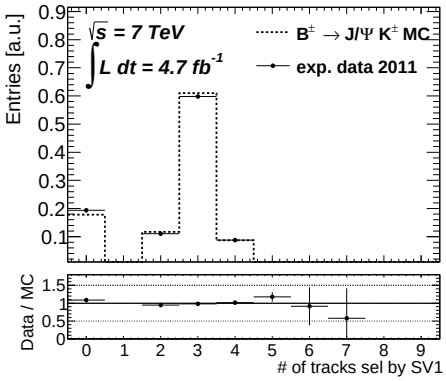

(a) SV1 associated tracks

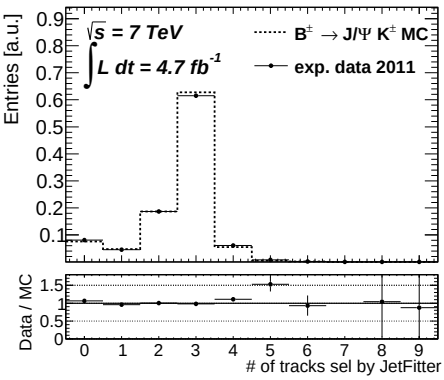

(b) JetFitter associated tracks

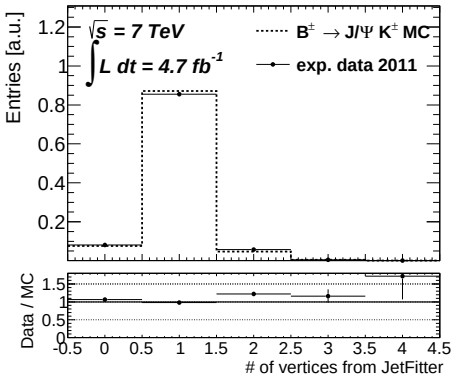

(c) JetFitter vertices

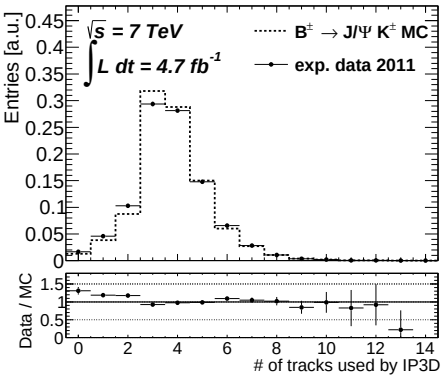

(d) IP3D associated tracks

Figure 6.11: *Number of tracks associated with the displaced vertices reconstructed by the SV1 (a) and JetFitter (b) algorithms. Zero associated tracks means that no displaced vertex was reconstructed. (c) Number of reconstructed vertices for JetFitter. (d) Number of tracks used by the IP3D tagger for the weight evaluation. Only events where all the* B *decay products have been associated to the jet are considered.*

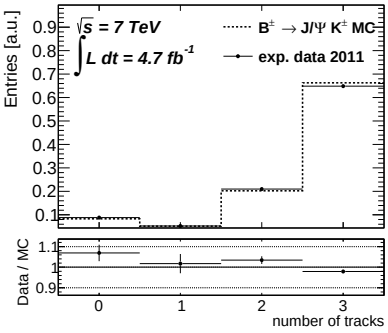

(a) JetFitter - B products association

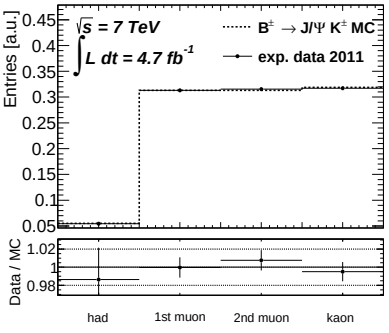

(b) JetFitter - nature of associated tracks

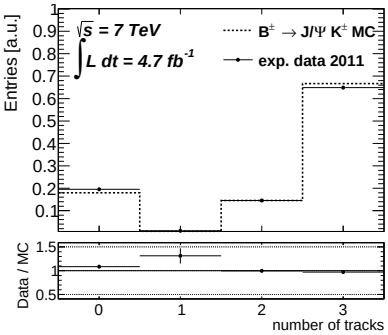

(c) SV1 - B products association

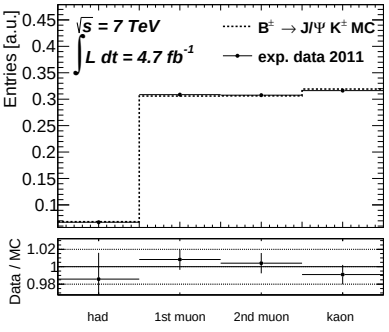

(d) SV1 - nature of associated tracks

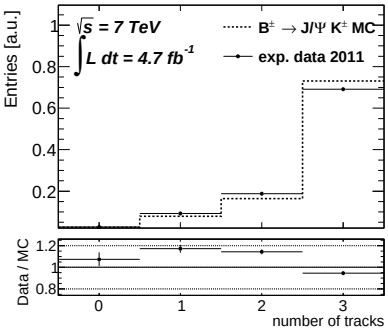

(e) IP3D - B products association

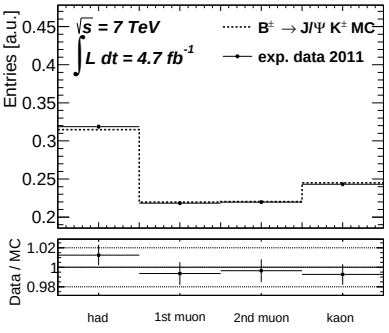

(f) IP3D - nature of selected tracks

Figure 6.12: *SV1 and JetFitter performance in associating the* B *decay products to the displaced vertex (top and middle left) and frequency of kaons, muons and hadronization tracks association to the displaced vertex (vertices) (top and middle right). Cross check for evaluating whether the* B *decay products are included in the set of tracks used by the IP3D tagging algorithm for the weight evaluation (bottom left and right).*

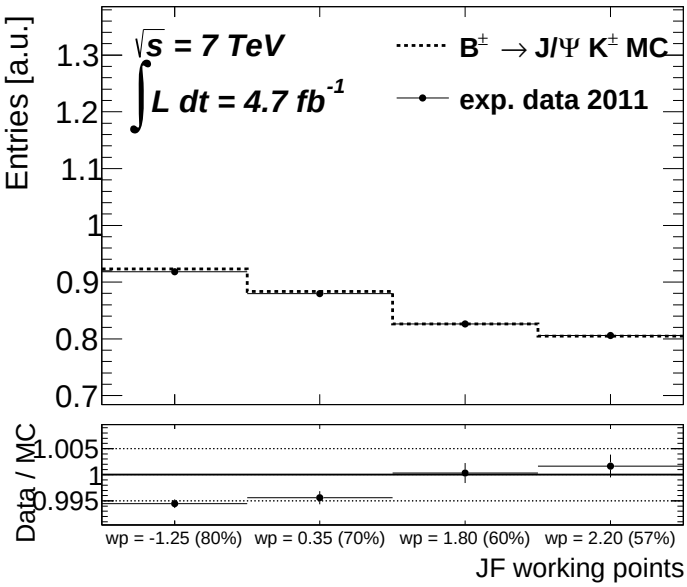

Figure 6.13: *Tagging efficiency as a function of the tagging working point for the JetFitter tagging algorithm.*

the vertex finding taggers SV1 and JetFitter to the displaced vertex. Due to the B decay topology under investigation the expected average number of tracks is three. As visible in the figure, the Monte Carlo simulation describes the outliers of this distribution with an agreement better than 10%. In Figure 6.11(c) the number of vertices reconstructed by the JetFitter tagger is shown. Also in this case the average value is compatible with the decay topology and the outliers are described by the simulation with an accuracy between 10 and 20%. Finally, Figure 6.11(d) shows the total number of tracks used by the Impact Parameter (IP) tagger. This tagger performs the b-jet identification based on the impact parameter significance of all Btag-Quality tracks in the jet, so in this case, the expected average number of tracks is higher because the total number of tracks used in the evaluation is shown. The Monte Carlo simulation is characterised by a narrower distribution than the distribution in data, with a discrepancy up to 25% for the very particular case in which no tracks associated to the jet fulfil Btag-Quality requirements.

The performance of the b-taggers are evaluated by the efficiency with which they associate the B decay products to the reconstructed, displaced vertex (vertices) as shown in Figure 6.12. As a cross check, also the IP tagger is analysed (Figures 6.12(e)-6.12(f)), in order to verify whether the B decay products are selected among the tracks used for the weight evaluation. The same information is shown in the plots

in the right column of these two Figures, where the probability with which one of the muons, the kaon or an hadronization track are associated to the displaced vertex is shown. Again, In the case of the IP tagger, a higher number of hadronization tracks is expected.

Finally the tagging efficiency is studied as a function of the working points for the JetFitter tagger (Figure 6.13). Each bin of the distribution corresponds to a working point of the algorithm and the efficiency of each working point in selecting b-jets from an inclusive sample is also indicated. The efficiency measured in this sample is higher than the nominal one for all working points due to the clear signature of the B decay used to select the b-jets. The agreement between the experimental data and the Monte Carlo simulation is excellent ($\leqslant 0.5\%$), also expected for this clean B decay topology.

6.5 Conclusions

The study presented in this part of the thesis gives an overview of a number of observables that characterise the properties of b-jets and their modelling by the available Monte Carlo simulation.

Three different categories of quantities have been investigated: the ones related to detector reconstruction effects, the ones related to the hadronization physics of the b-jets and the performance of the b-taggers. Except for a limited number of cases for which no clear conclusion could be drawn, the Monte Carlo simulation showed a reliable modelling of all these quantities and of the response of the b-taggers to the b-jets selected by this analysis.

In the short term, this study provides confidence in the Monte Carlo tunings and modelling of the fragmentation function of B hadrons, of the hadronization process in the jet and of the jet universality assumption on which the modern Monte Carlo tuning methods rely. In fact, tunings [113] rely on information based on many different experiments and assume for example that particles fragment in the same way at a hadron collider as they did at the Large Electron-Positron (LEP) collider.
Since the infrared environment in hadron collisions is characterised by a different (hadronic) initial-state vacuum by a larger final-state gluon component, and also by simply having a lot more colour flowing around in general, it is important to check to what precision this assumption holds explicitly, e.g., by measuring multiplicity and p_{T} spectra of identified particles, particle-particle correlations, and particle production ratios in situ at hadron colliders. The hadronization track investigation in this

analysis represents a first, preliminary attempt to validate the modelling of the behaviour of particles in the specific environment of b-jets and showed very positive results.

In the long term, it would be interesting to improve the analysis strategy in order to allow the investigation of the properties of a more inclusive sample of B decays, considering also B^0 and B_s hadrons and considering charm decays as well. Exploiting a more representative sample of the majority of b-jets in ATLAS it will be possible to draw more impelling conclusions on the modelling of the taggers performance and improve even more their simulation.

Part 3

Search for top squarks with the 8 TeV dataset

7 Stop: searching for it

This part of the thesis describes a search for a heavy scalar supersymmetric partner of the top quark in the data collected by ATLAS in 2012 at $\sqrt{s} = 8$ TeV. We investigate final states containing one isolated lepton, at least four jets, of which one or two are identified as b-jets, and missing transverse momentum. In this chapter we introduce the search strategy and the backgrounds, that are mainly top pair production and production of vector bosons in association with jets. In addition, the kinematic observables exploited to discriminate the signal from the main background are presented.

7.1 The top squark (stop) signal

The top squark (or stop) plays a fundamental role in the SUSY solution to the hierarchy problem if it has a mass smaller than a few TeV. If the stop exists, it could therefore be produced at the LHC and it is not unlikely that ATLAS, with 20 fb^{-1} of data collected at a centre-of-mass energy of 8 TeV, can find it.

The top squark production cross section in proton-proton collisions depends on the stop mass as shown in Figure 1.1 in Ch. 1. Of all the possible top squark decay modes, three will be considered in this search:

a) $\tilde{t} \to t\,\tilde{\chi}^0$ (with subsequent decay $t \to W\,b$)

b) $\tilde{t} \to b\,\tilde{\chi}^{\pm} \to b\,W^{\pm}\,\tilde{\chi}^0$ (with on/off-shell W)

c) $\tilde{t} \to b\, W^{\pm}\, \tilde{\chi}^0$ (via off-shell top)

R-parity is assumed to be conserved in the models addressed in this search. This implies that the top squarks have to be produced in pairs and that the neutralino produced in the last step of the decay chain is stable and escapes the detector without interaction. The main handle used for the signal selection in this search is the presence of exactly one lepton in the final state, either an isolated electron or a muon that fulfils the requirement described in Chapter 3. Events with extra primary electrons or muons are rejected. With this requirement we implicitly select events where one of the W bosons decays leptonically and the other hadronically. Complementary searches with either two or no leptons in the final state are performed in ATLAS as well ([114, 115]) and will be compared with the results of this work in Chapter 9 of this thesis. Given the topology of the decay, the final state is required to be characterised by at least four jets that fulfil the minimal requirements introduced in Ch. 3, of which at least one b-tagged, and an amount of missing transverse momentum of at least 100 GeV.

The three stop decay modes are addressed using the approach introduced in Ch. 1. Each stop decay mode and each mass hypothesis of the stop and the other particles in the decay chain are considered a different *signal model*. These signal models are described using a Monte Carlo simulation generated with MADGRAPH 1.5.4 [116] and showered with PYTHIA (6.426) [110] using the CTEQ6L1 [117] PDF set. The $\tilde{t} \to t\, \tilde{\chi}^0$ decay is instead generated using (HERWIG)++ [118]. The detector simulation in these Monte Carlo samples was performed using ATLFAST-II.

7.2 Background processes

The main purpose of this analysis is to investigate whether the top squark exists and decays into one of the final states listed in the previous section. A large number of SM processes produce a similar final state and thus are a background to this search. These processes are mostly top quark pair and single top quark production in association with extra jets or vector bosons, production of vector bosons ($W^{\pm}$ and Z) in association with jets and two or more vector bosons associate production. A summary of the cross sections for these processes as measured by ATLAS is shown in Figure 7.1. The pure multi-jet production, despite its high cross section, is easily rejected by the one isolated lepton and $E_{\mathrm{T}}^{\mathrm{miss}}$ requirements of this analysis and its contribution is found to be negligible. Each SM process is modelled by a Monte Carlo

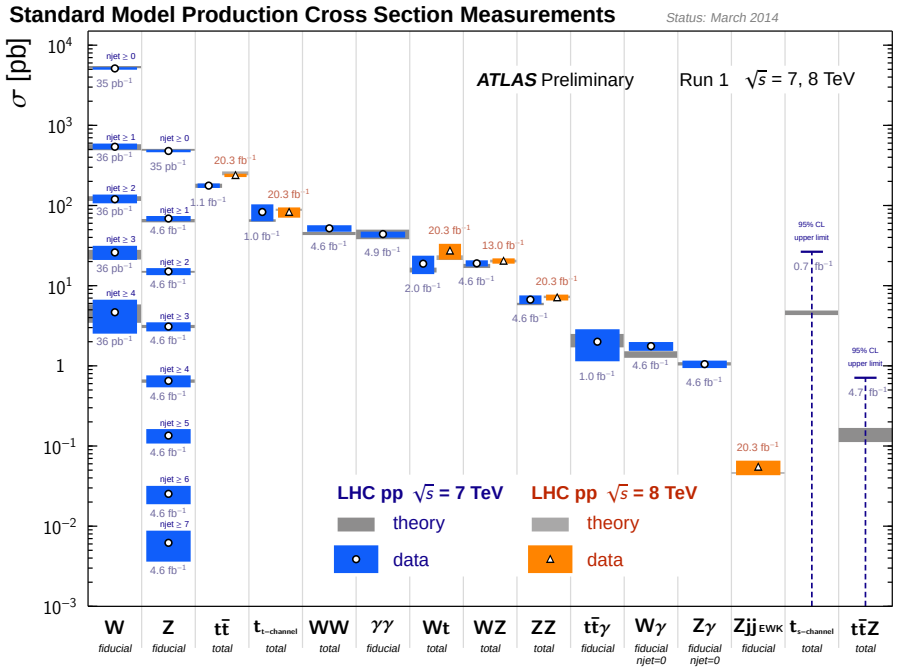

Figure 7.1: *Standard Model total and fiducial production cross section measurements performed by ATLAS, corrected for leptonic branching fractions, compared to the corresponding theoretical expectations. All theoretical expectations were calculated at NLO or higher. [119].*

simulation. A summary of the details on the Monte Carlo generators, shower tunes and PDF sets used for each background process (and the top squark signal described in the previous section) is given in Table 7.1.

7.2.1 Top quark production

The top quark is the heaviest of all quarks and has a mass of 173.3 ± 0.8 GeV [120]. At hadron colliders, top quarks are produced either in pairs, predominantly through the strong interaction, or singly through the weak interaction. The former mode is the dominant production mechanism for top quarks at the LHC and the cross section is 253^{+13}_{-15} pb [121–123] at a centre-of-mass energy of 8 TeV. Due to its mass, the top quark decays in a two body decay $t \to Wb$ before hadronising. Hence, $t\bar{t}$ events can

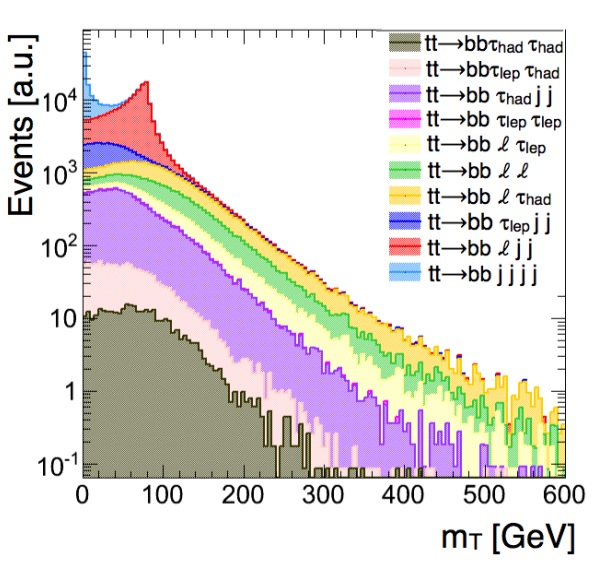

Figure 7.2: *Transverse mass distribution for $t\bar{t}$ processes requiring exactly one isolated lepton in the final state, split in all possible final states (neutrinos are not shown in the legend). The semileptonic component of $t\bar{t}$ peaks at the $W^{\pm}$ mass and dileptonic and hadronic tau $t\bar{t}$ decays become dominant for $m_T > 120$ GeV.*

be classified according to the decay modes of the W bosons produced by the top decay. Roughly 33% of the W bosons decay in a lepton-neutrino pair (where lepton is either an electron, a muon or a tau) and the remaining 68% in a quark pair (30% in a $c\bar{s}$ pair). Therefore, to highlight the different $t\bar{t}$ decay modes that contribute to the background, we classify the $t\bar{t}$ decays as in the following:

(a) hadronic modes (44%): $t\bar{t} \to b\bar{b}\, q\bar{q}'\, q''\bar{q}'''$ where $q, q', q'', q''' = c, s, u, d$

(b) single lepton modes (30%): $t\bar{t} \to b\bar{b}\, \ell\nu_\ell\, q\bar{q}'$ where $\ell = e, \mu$ and $q, q' = c, s, u, d$

(c) hadronic or leptonic tau modes (20%): $t\bar{t} \to b\bar{b}\, \tau\nu_\tau + X$, where X can be either a lepton-neutrino or a quark pair. The lepton-neutrino mode has the highest chance to pass the selections of this analysis. The adjective (hadronic or leptonic) refers to the subsequent tau decay.

(d) dileptonic modes (4%): $t\bar{t} \to b\bar{b}\, \ell\bar{\ell}'\, \nu_\ell\nu_{\ell'}$ where $\ell, \ell' = e, \mu$

The obvious background to this stop search is the single lepton mode. However, the transverse mass of the $E_{\mathrm{T}}^{\mathrm{miss}}$ and the lepton in the event can be used to reconstruct the mass of the leptonic $W^{\pm}$ in this topology (see Sec. 7.4 for details), as represented in Figure 7.2. The semileptonic component of $t\bar{t}$ peaks at the $W^{\pm}$ mass of 80 GeV. A simple transverse mass requirement of about 120 GeV efficiently removes this type of events (without affecting the signal acceptance) and the dileptonic and tau modes will assume a dominant role as backgrounds. Variables dedicated to reconstruct the kinematics of these $t\bar{t}$ modes and to veto taus and not identified leptons in the event are exploited in the signal selections and introduced in Section 7.4. The most selective are the stransverse mass, the topness and the isolated track and tau vetoes.

Top quarks can also be produced alone, through the weak interaction, hence with a lower cross section. The dominant production mode is through a t-channel ($87.8^{+3.4}_{-1.9}$ pb [124]), followed by the associate production with a $W^{\pm}$ (22.4 ± 1.5 pb [125]) and finally through the s-channel (5.61 ± 0.22 pb [126]). Considering the lower intrinsic jet multiplicity of this process, the single top represents a subdominant, yet not negligible, background to this analysis.

Monte Carlo simulation of the top processes

The Monte Carlo simulation for the top pair processes uses, as a default in ATLAS, POWHEG (version 1.0) [127, 128] for the matrix element generation, interfaced to PYTHIA (version 6.427) [110] for the parton showering and fragmentation using the NLO PDF CT10 [129] and the tune Perugia 2011(C) [113].

process	Generator	Showering	PDF set	tune	Detector Rec.
$t\bar{t}$	POWHEG (1.0)	PYTHIA (6.427)	CT10	P2011(C)	ATLFAST-II
single top (Wt/s)	POWHEG (1.0)	PYTHIA (6.426)	CTEQ6L1	P2011(C)	ATLFAST-II
single top (t)	AcerMC (3.8)	PYTHIA (6.426)	CTEQ6L1	P2011(C)	Full Sim.
W + jets	SHERPA (1.4.1)		CT10	-	ATLFAST-II
Dibosons	SHERPA (1.4.1)		CT10	-	Full Sim.
$t\bar{t}$+V	MADGRAPH (5-1.3.33)	PYTHIA (6.426)	CTEQ6L1	-	Full Sim.
$\tilde{t} \to t\,\tilde{\chi}^0$ signal	HERWIG++	PYTHIA	CTEQ6L1	-	ATLFAST-II
other signals	MADGRAPH (5-1.5.4)	PYTHIA	CTEQ6L1	AUET2B	ATLFAST-II

Table 7.1: *Summary of the Monte Carlo generators, PDF sets and tunes used for each simulated SM background and signal model.*

As far as single top production is concerned, the Wt and s-channels are generated using POWHEG (version 1.0) [127, 128] for the matrix element generation interfaced to PYTHIA (version 6.426) with tune Perugia 2011(C) [113], similarly to $t\bar{t}$ processes. The t channel instead is generated with AcerMC (version 3.8) [130] interfaced to PYTHIA (version 6.426), that had proved to give a better description of this process. All three channels are generated with the CTEQ6L1 [117] PDF set.

7.2.2 Reweighting of the top pair production process

In a recent ATLAS measurement of the differential cross-section of top pair quark production [131], it was discovered that the default Monte Carlo generator used for the simulation of the $t\bar{t}$ processes (POWHEG+PYTHIA) overestimates the transverse momentum of the top pair system with respect to the data.

$t\bar{t}$-system p_{T}[GeV]	Event weight
$p_{\mathrm{T}} < 40$	0.97
$40 < p_{\mathrm{T}} < 170$	0.95
$170 < p_{\mathrm{T}} < 340$	0.83
$p_{\mathrm{T}} > 340$	0.73

Table 7.2: *Weight applied to the Monte Carlo simulation to correct the mis-modelling of the top pair system transverse momentum.*

This disagreement is propagated to all distributions that are not invariant under Lorentz boosts, resulting in a overestimation of the Monte Carlo simulation of the tails of such distributions. An example of such a mis-modelled distribution is the transverse momentum of the leading (i.e. highest p_{T}) jet shown in Figure 7.3(a)
The general analysis strategy, that relies on data-driven estimation of the $t\bar{t}$ normalisation, was proved to be unaffected by this mis-modelling. Nevertheless, in order to improve the reliability of the Monte Carlo estimates a corrective weight was applied to every Monte Carlo event.
The weight, derived from the afore mentioned cross section result from ATLAS [131], depends on the transverse momentum of the $t\bar{t}$-system and is independent of the flavour of the selected lepton. The weight values are reported in Table 7.2 and the corrected p_{T} distribution for the leading jet[1)] is shown in Figure 7.3(b).

[1)] which is the jet characterised by the highest transverse momentum in the event

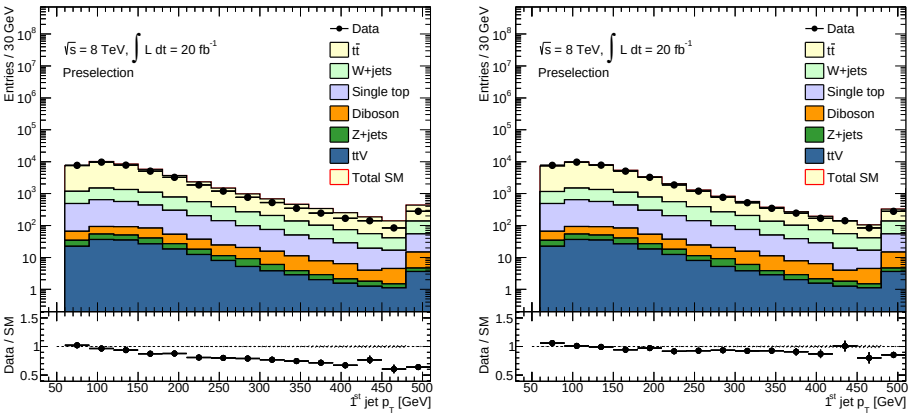

(a) no weight (b) reweighted

Figure 7.3: *Comparison between data and the Monte Carlo simulation of the leading jet p_{T} distribution before and after the reweighting of the $t\bar{t}$ background. Only statistical uncertainties are included in the bands.*

7.2.3 Vector bosons produced in association with jets

The production of a $W^{\pm}$ boson in association with jets is the second dominant background of the stop search. The so-called W+jets process is understood in terms of the radiation of additional gluons and quarks in association with the vector boson. For each extra radiated jet, the production cross section decreases by roughly half an order of magnitude and the total cross section is 12 nb [132, 133].

The jets produced in association with the $W^{\pm}$ boson are predominantly originating from gluons and light quarks. However, $W^{\pm}$ bosons can also be produced in association with heavy flavour jets (b, c, $b\bar{b}$, $c\bar{c}$), with a cross section between 0.1 and 15 pb [134, 135] (depending on the jets flavour and transverse momentum). The contribution of heavy flavour and mis-identified light flavour jets both contribute to the processes that represent a background to this search.

The Z+jets process instead is easy to reject due to the presence of either two or no isolated leptons in the final state. The case in which one of the leptons from the Z decay is not reconstructed or outside of the detector acceptance gives a negligible contribution to the background.

Monte Carlo simulation of the W + jets processes

The Monte Carlo simulation for W + jets was generated and showered using SHERPA (version 1.4.1) [136] with the NLO PDF set CT10 [129]. Up to four additional partons were generated from the matrix element and charm and bottom quarks were treated as massive. Additional samples that required $W^{\pm}$ bosons with high transverse momentum ($p_{\mathrm{T}}^{W} > 200$ GeV) were generated in order to increase the Monte Carlo statistics in the kinematic region selected in the analysis. The low momentum samples were simulated using the ATLFAST-II simulation of the detector, while the high momentum samples were simulated using the Full-Geant4 simulation [112].

7.2.4 Gauge boson pair production

Pairs of vector bosons are produced in the SM through the electroweak interaction. The dominant processes, in terms of cross sections are [133]:

I. WW with a NLO cross section of 66.1 pb,

II. WZ with a NLO cross section of 38.5 pb,

III. ZZ with a NLO cross section of 13.1 pb.

A few decay modes of the two vector bosons produced in this type of processes are characterised by a final state that enters the selections of this analysis. However, these processes always represent a subdominant background due to the extra initial or final state radiation of quarks and gluons needed for these events to fulfil the four jets requirement of the selections.

Monte Carlo simulation of the diboson processes

The Monte Carlo simulation for the afore mentioned diboson associate production was generated using SHERPA (version 2.1) [136] with the NLO PDF set CT10 [129] and up to three jets generated from the matrix element, with charm and bottom quarks treated as massive.

7.2.5 Tops and vector bosons associate production

A quite rare process is the electroweak mediated associate production of a top quark pair and a vector boson, either a W or a Z. These processes are characterised by a small cross section of 0.232 pb and 0.206 pb for $t\bar{t} + W^{\pm}$ and $t\bar{t} + Z$,

respectively [137]. Despite their small cross section, they do represent one of the most thorny backgrounds for searches. These processes are not experimentally well studied since the LHC experiments are just now starting to become sensitive to them. However, the cross section of these processes is in some cases comparable or higher than the stop signal and their final state even more similar than the top quark pair production, since for example invisible decays of the vector boson might mimic the kinematics of neutralinos in the event.

The even smaller contribution of single top associated production with the Z boson was investigated and included in the simulation of the $t\bar{t}$+V background processes.

Monte Carlo simulation of the $t\bar{t}$+V processes

The Monte Carlo simulations for the $t\bar{t}$+V processes was generated using MADGRAPH (version 5-1.3.33) [138] for the matrix element generation interfaced to PYTHIA (version 6.426) for the showering and CTEQ6L1 [117] as PDF set.

7.3 Strategy of the top squark search

The analysis is based on 20 fb^{-1} of pp collision data collected by ATLAS during the year 2012 at a centre of mass energy of 8 TeV. The data were triggered requiring either one electron or muon in the event or a missing transverse momentum of 80 GeV.

The general strategy of this analysis can be summarised in a few steps that are common to the majority of the ATLAS SUSY searches:

I. First of all a set of signal enhanced regions is defined (signal regions). The choice of the selection criteria for these regions is based on Monte Carlo simulation only and aims to extend the reach of the analysis to the largest number of signal models with the minimum number of signal selections. Experimental data are kept blinded until the analysis is fully defined.

II. The background contamination of the signal regions is estimated by Monte Carlo simulation for the minor backgrounds and by a data-driven approach for the two major backgrounds: $t\bar{t}$ and W+jets. In the latter case, two background enriched selections (control regions), one for each background, are defined. They are required to be kinematically as close as possible to events passing

the signal selections, but orthogonal to them. They have a high purity with respect to the background process under study and have low top squark signal contamination. They are used to derive the background normalisation directly from data and extrapolate it into the signal regions, therefore increasing the reliability of the background estimation. The background enriched regions are described in Sec. 8.3.

III. The quality of the background estimate and the reliability of the extrapolation of the background normalisation from the background enriched regions to the signal selections is probed by the use of validation regions (Sec. 8.4).

IV. Finally, the results are obtained by a likelihood fit to the number of observed events in each signal region and the two background enriched regions. The SM hypothesis is assessed by a discovery test and if no excess of the data with respect to the expected SM background is observed the results are interpreted in terms of exclusion limits on signal models using the *CLs* method [139].

7.3.1 Top squark signal and selection strategy

In order to achieve a good sensitivity for the three top squark decay modes ($\tilde{t} \to b\,\tilde{\chi}^{\pm}$, $\tilde{t} \to t\,\tilde{\chi}^{0}$,$\tilde{t} \to b\,W^{\pm}\,\tilde{\chi}^{0}$) and the widest range of assumptions for $m_{\tilde{t}}, m_{\tilde{\chi}^{\pm}}, m_{\tilde{\chi}^{0}}$ we exploit two different strategies to define the signal enriched regions:

- Selections defined by requirements on a number of quantities with high discrimination power between signal and background. The final discrimination is achieved by counting and comparing the number of signal and background events passing all requirements, and therefore these selections are called *cut-and-count* selections.

- A simultaneous fit of multi-bin selections referred to in the following as *shape fits*. The binning is defined in the two most discriminating quantities and allows to exploit the difference in shape between the background and the signal in order to increase the discriminating potential.

A total of six *cut-and-count* selections and four *shape fit* selections are defined for this analysis, the details of which are are presented in Chapter 8.

7.3.2 Statistical treatment of the data

The results of this analysis will be extracted by a hypothesis test based on a likelihood function:

$$L(\mu, \boldsymbol{\theta}) = \mathcal{P}(\mathcal{N}_{\text{SR}}(data)|\mu\, s + \mu_b b, \boldsymbol{\theta}) \cdot \tag{7.1a}$$

$$\prod_{j=1}^{\mathcal{N}_{\text{CR}}} \mathcal{P}(\mathcal{N}_{\text{CR}j}(data)|\mu_b b_j, \boldsymbol{\theta}) \cdot \tag{7.1b}$$

$$\mathcal{A}(\tilde{\boldsymbol{\theta}}, \boldsymbol{\theta}). \tag{7.1c}$$

$\mathcal{P}$ is Poisson probability, s is the expected number of top squark events in the signal selection for the considered model and b the total SM background. j represents the identifier of the two background enriched regions, $\mathcal{N}_{\text{SR}}(data)$ and $\mathcal{N}_{\text{CR}j}(data)$ are the number of experimental event counts in the different regions (either a signal selection or a background control region), b_j is the number of background events that fulfil such selections and μ_b is the background normalisation. The likelihood function depends on the top squark signal strength, μ, in our experimental dataset. This dependence is contained in the signal-rich components of the likelihood, which in Eq. (7.1a) is specified for a *cut-and-count* selection. The likelihood is maximised over a number of parameters: $\boldsymbol{\theta}$, μ_b and μ. The values of these parameters that maximise the likelihood are conventionally indicated with a hat superimposed on the symbol, i.e. $\hat{\mu}$.

$\boldsymbol{\theta}$ is a vector of nuisance parameters that represent the systematic uncertainties arising from the detector response simulation and the event generation. $\mathcal{A}(\tilde{\boldsymbol{\theta}}, \boldsymbol{\theta})$ represents the auxiliary constraints on these uncertainties which are imposed as Gaussians, except for statistical uncertainties that are treated with Poisson distributions. The width of the constraint of each uncertainty considered in the analysis will be discussed in Section 9.2.2.

The signal and background expectations (s and b) are functions of the nuisance parameters $\boldsymbol{\theta}$. These functions are parametrised, such that the response of s and b to each θ is factorised from the nominal value of the expected rate. That is, $s = s_{Nom} \times \prod \nu(\boldsymbol{\theta})$, where the form of $\nu(\boldsymbol{\theta})$ depends on the systematic source. The systematic variation might affect the event rate or might affect the shapes of the distributions. When a systematic variation affects the shape of the distribution it is first separated into a rate component and a pure shape component, such that varying the pure shape component of s or b has no effect on the expected rate, and the two components are treated separately.

The normalisation of the two major backgrounds of the analysis (top pairs and W + jets) are estimated from data in two background enriched selections. They are treated as nuisance parameters and left to float in the fit. Therefore Eq. (7.1b) can be expanded as:

$$\prod_{j=1}^{N_{\text{CR}}} \mathcal{P}(\mathcal{N}_{\text{CR}j}(data) \,|\, \mu_b^{top} b_j^{top} + \mu_b^W b_j^W + b_j^{other}, \boldsymbol{\theta}), \tag{7.2}$$

where μ_b^{top} and μ_b^W are also nuisance parameters for the top and the W + jets background normalisations and the normalisation of the minor backgrounds, b_j^{other}, is taken directly from the simulation.

For the shape fits the separation between the bins that constrain the background normalisation and the signal-rich components is less obvious and it is more clear to merge the two subequations (7.1a) and (7.1b) into a single product. The likelihood can be expressed as:

$$L(\mu, \boldsymbol{\theta}) = \prod_{i=1}^{\mathcal{N}_{bins}} \mathcal{P}(\mathcal{N}_i(data) |\, \mu s_i + \sum_{k=1,2} \mu_b^k b_i^k + b_i^{other}, \boldsymbol{\theta}) \;\cdot \mathcal{A}(\tilde{\boldsymbol{\theta}}, \boldsymbol{\theta}), \tag{7.3}$$

where $k = 1, 2$ refers to $t\bar{t}$ and W + jets backgrounds and i runs over all the shape fit bins. In addition, two of the shape fits (tN_diag and bC_bulk) use three sets of μ_b^{top}, μ_b^W, one for each slice in the first fit variable (x) and keeping the parameter correlated across the second variable (y). This strategy allows to rely less on the Monte Carlo simulation of one of the variables used in the shape fit. This comes at the price of higher impact of the statistical uncertainties on the background estimate and therefore is used only in the two shape fits with high background yield. The full likelihood becomes:

$$L(\mu, \boldsymbol{\theta}) = \prod_{i=1}^{\mathcal{N}^x_{bins}} \prod_{j=1}^{\mathcal{N}^y_{bins}} \mathcal{P}(\mathcal{N}_{ij}(data) |\, \mu s_{ij} + \sum_{k=1,2} \mu_b^{jk} b_{ij}^k + b_{ij}^{other}, \boldsymbol{\theta}) \;\cdot \mathcal{A}(\tilde{\boldsymbol{\theta}}, \boldsymbol{\theta}), \tag{7.4}$$

with $\mathcal{N}^x_{bins}$ and $\mathcal{N}^y_{bins}$ spanning over all the shape fit bins and x and y being the two variables used to define the shape fit binning.

Discovery and exclusion hypothesis tests

For the purpose of discovering a new signal process in a search for a new phenomenon one can define the null hypothesis, $\mathcal{H}_0$, as describing only known processes, i.e the SM backgrounds. This is to be tested against the alternative hypothesis, $\mathcal{H}_1$, which includes both background as well as the sought after signal, in this

case the top squark. The formalism of a discovery test and exclusion of a certain signal hypothesis is briefly summarised in this section. A more complete discussion can be found in Ref. [140].

To test a hypothesised value of signal strength μ we consider the profile likelihood ratio:

$$\lambda(\mu) = \frac{L(\mu, \hat{\hat{\boldsymbol{\theta}}})}{L(\hat{\mu}, \hat{\boldsymbol{\theta}})} \tag{7.5}$$

Here $\hat{\hat{\boldsymbol{\theta}}}$ in the numerator denotes the value of $\boldsymbol{\theta}$ that maximises L for the specified μ. The denominator is the maximised (unconditional) likelihood function. In this analysis we choose to quantify the level of agreement of the observed data with a given hypothesis $\mathcal{H}$ by using the profile likelihood ratio as a test statistic:

$$t_\mu = \begin{cases} -2ln\lambda(\mu) & \hat{\mu} \geqslant \mu \\ 0 & \hat{\mu} < \mu \end{cases} \tag{7.6}$$

The discovery of a positive signal against the background only hypothesis, $\mathcal{H}_0$, is tested by fixing $\mu = 0$ in Eq. (7.6) and computing a p-value:

$$p_\mu = \int_{q_0^{data}}^{\infty} f(t_\mu|\mu) dt_\mu. \tag{7.7}$$

$f(t_0|\mu)$ denotes the probability density function of the test statistic. Conventionally, the data are considered incompatible with the SM-only hypothesis if

$$p_0 \leqslant 2.87 \cdot 10^{-7}, \tag{7.8}$$

corresponding to the 5σ tail of a Gaussian.

If the SM-only hypothesis cannot be excluded it is important to interpret the results in terms of an upper limit on the strength parameter μ. In particular we are interested in excluding the case $\mu = 1$ for a given signal model (Eq. (7.6)). This is obtained by computing the CL_S [139]:

$$CL_S = \frac{p_1}{1 - p_0} \tag{7.9}$$

where p_1 and p_0 are the p-values calculated in Eq (7.7) for $\mu = 0$ and $\mu = 1$, respectively. A signal model with strength $\mu = 1$ is excluded at 95% Confidence Level (CL) if

$$CL_S \leqslant 0.05. \tag{7.10}$$

7.4 How to select the top squark: discriminating quantities

Many parameters determine the kinematics of the signal models targeted in this analysis, in particular the assumed masses of $m_{\tilde{t}}$, $m_{\tilde{\chi}^{\pm}}$, $m_{\tilde{\chi}^{0}}$ and their corresponding mass differences $\Delta m(\tilde{\chi}^{\pm}, \tilde{\chi}^{0})$ and $\Delta m(\tilde{t}, \tilde{\chi}^{\pm}/\tilde{\chi}^{0})$.

A number of variables that aim to describe or reconstruct the kinematics of the events are exploited in order to obtain discrimination power between the signal and the SM backgrounds. In the following, we will try to give an overview of the mathematical definition of all discriminating variables used in this analysis and an explanation of the type of backgrounds they help to reject. In addition, to provide the reader with a preliminary impression of the discriminating power of these observables and the ability of the Monte Carlo simulation to model their shapes, a characteristic distribution for each quantity will be shown in the following. These distributions were obtained after the selections presented in the following.

- exactly one isolated lepton (e or μ) with $p_{\mathrm{T}} > 25$ GeV;
- at least four jets of which at least one b-tagged. The leading jet, which is the jet characterised by the highest transverse momentum, is required to have $p_{\mathrm{T}} > 60$ GeV and the other jets have a minimum p_{T} of 25 GeV;
- $E_{\mathrm{T}}^{\mathrm{miss}} > 100$ GeV;
- $E_{\mathrm{T}}^{\mathrm{miss}}/\sqrt{H_{\mathrm{T}}} > 5\sqrt{\mathrm{GeV}}$ (see Sec. 7.4.1 for the variable definition)
- $m_{\mathrm{T}} > 60$ GeV where m_{T} is transverse mass of the lepton and the $E_{\mathrm{T}}^{\mathrm{miss}}$(see Sec. 7.4.3 for details).

These selections were chosen to reject part of the backgrounds while retaining almost 100% signal efficiency and are applied to all distribution plots shown in the rest of this chapter. The shaded area in each of these plots include the statistical and major systematic uncertainties on each distribution and the last bin includes the overflow. One or more top squark signal models are superimposed in each plot in order to highlight the shape difference between background and signal in each distribution. For visualisation purposes, the signal normalisation is enhanced and the scaling factor κ is indicated as $\sigma \times \kappa$ in the plot.

7.4.1 Invisible particles: $E_{\mathrm{T}}^{\mathrm{miss}}$ and its significance

Missing transverse momentum

The topologies of the top squark decay modes targeted in this search are characterised by three weakly interacting particles, a neutrino and two neutralinos ($\tilde{\chi}^0$) that escape the detector without interacting. For this reason, the presence of a large quantity of $E_{\mathrm{T}}^{\mathrm{miss}}$ will be one of the fundamental requirements for selecting the signal. The distribution of this quantity in data is compared with the Monte Carlo simulation in Figure 7.4(a) and found to be in very good agreement. Furthermore, the distribution shows a good discrimination power between to top squark signal and the background.

$E_{\mathrm{T}}^{\mathrm{miss}}$ significance: $\not{E}_{\mathrm{T}}^{\mathrm{sig}}$

The significance of the missing transverse momentum is defined as the ratio between the $E_{\mathrm{T}}^{\mathrm{miss}}$ and the square root of the total hadronic energy in the event ($\mathrm{H_T}$):

$$\not{E}_{\mathrm{T}}^{\mathrm{sig}} = E_{\mathrm{T}}^{\mathrm{miss}} / \sqrt{\mathrm{H_T}}. \tag{7.11}$$

The $E_{\mathrm{T}}^{\mathrm{miss}}$ significance (Figure 7.4(b)) quantifies how likely the measured missing momentum is entirely an effect of mis-measurement of highly energetic jets in the event, where $\sqrt{\mathrm{H_T}}$ represents the resolution of the hadronic energy measurement. In this analysis $\mathrm{H_T}$ is calculated only on the leading four jets of the event for sake of robustness against extra jets in the event:

$$\mathrm{H_T} = \sum_{i=1}^{4} p_{\mathrm{T}}^{i}(\mathrm{jet}). \tag{7.12}$$

$\mathrm{H}_{\mathrm{T}}^{\mathrm{miss}}$ significance: $\not{H}_{\mathrm{T}}^{\mathrm{sig}}$

The $\not{H}_{\mathrm{T}}^{\mathrm{sig}}$ variable is an alternative observable that quantifies the significance of the missing transverse momentum. Its design was inspired by Ref. [141], it is a scalar and it is defined as:

$$\not{H}_{\mathrm{T}}^{\mathrm{sig}} = \frac{\langle \mathrm{H}_{\mathrm{T}}^{\mathrm{miss}} \rangle_{\sigma} - \kappa}{\mathrm{RMS}_{\langle \mathrm{H}_{\mathrm{T}}^{\mathrm{miss}} \rangle}}. \tag{7.13}$$

$\mathrm{H}_{\mathrm{T}}^{\mathrm{miss}}$ is the absolute value of the vector sum of all leptons and jets in the event with $p_{\mathrm{T}} > 25$ GeV. $\langle \mathrm{H}_{\mathrm{T}}^{\mathrm{miss}} \rangle$ is the mean of the $\mathrm{H}_{\mathrm{T}}^{\mathrm{miss}}$ distribution obtained by smearing

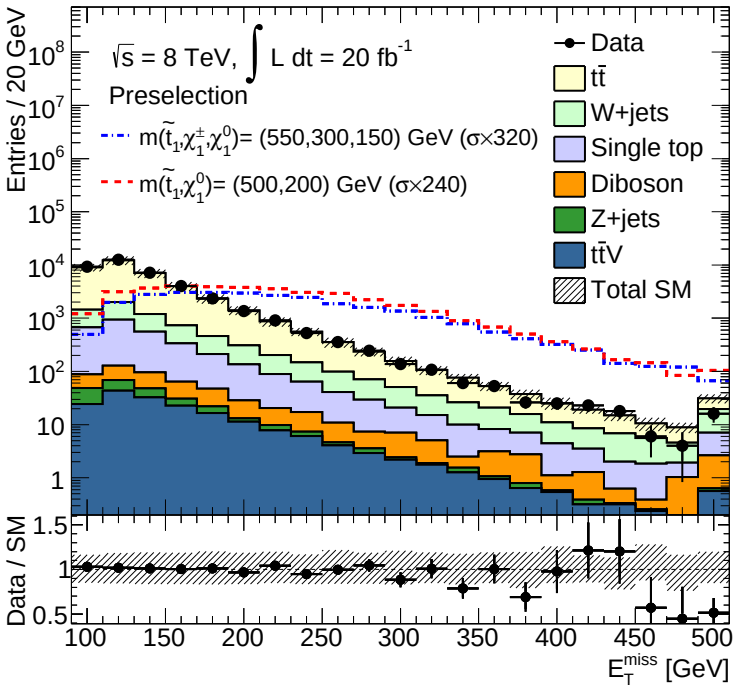

(a) Missing transverse momentum ($E_{\mathrm{T}}^{\mathrm{miss}}$)

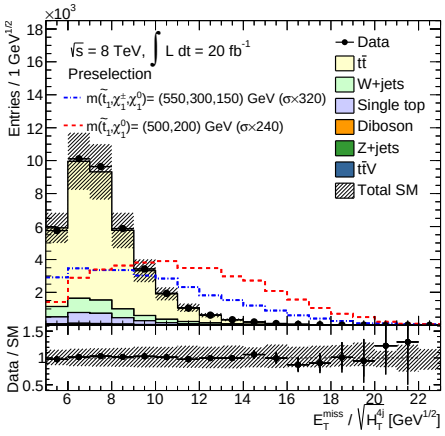

(b) missing transverse momentum significance ($\not{E}_{\mathrm{T}}^{\mathrm{sig}}$)

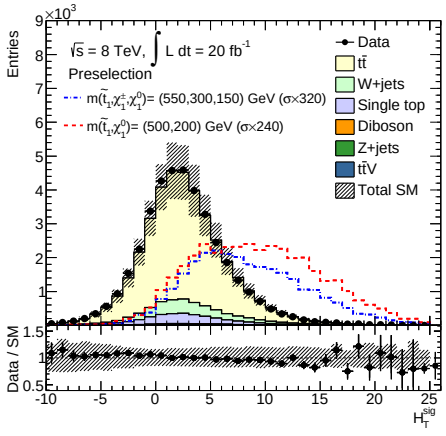

(c) $\mathrm{H}_{\mathrm{T}}^{\mathrm{miss}}$ significance ($\not{H}_{\mathrm{T}}^{\mathrm{sig}}$)

Figure 7.4: *Missing transverse momentum and significance distributions in data and in the Monte Carlo simulation. The band includes statistical and systematic uncertainties.*

the jet energies by a gaussian with central value equal to their measured energy and width equal to the ATLAS jet energy resolution. The denominator of Eq. 7.13 is the width of this H_T^{miss} distribution.

Finally, the constant κ represents a characteristic scale of the background, and is fixed at 100 GeV in this analysis based on optimisation studies[141] with simulated signal and background samples. The distribution is shown in Figure 7.4(c). It shows a small shift in the distribution in the Monte Carlo with respect to the data that is however well covered by the systematic uncertainty band.

7.4.2 Correlation between particles in the final state

The angular distance between certain particles in the final state was found to be a useful quantity to discriminate the background from the top squark signal. The angular distance between two objects a, b is defined as:

$$\Delta R(a,b) = \sqrt{(\phi_a - \phi_b)^2 + (\eta_a - \eta_b)^2}. \tag{7.14}$$

In addition, if the z component of the object is not available, as in case of E_T^{miss}, only the difference between the azimuthal angle ϕ is considered and the angular distance is indicated with $\Delta\phi$. The afore mentioned angular separation between

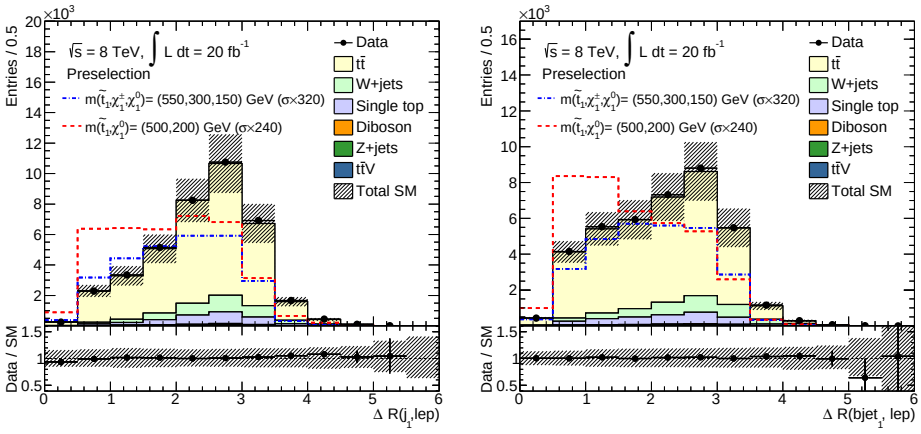

(a) $\Delta R(lep, j_1)$ (b) $\Delta R(lep, b-jet)$

Figure 7.5: *$\Delta R(b-jet, \ell)$ and $\Delta R(j_1, \ell)$ distributions in data and in the Monte Carlo simulation. The band includes statistical and systematic uncertainties.*

jets and $E_{\mathrm{T}}^{\mathrm{miss}}$ is one example of such case.
In the final signal selection of this analysis the angular distance between the following objects will be considered:

a) the leading jet and the lepton ($\Delta R(j_1, \ell)$), shown in Figure 7.5(a);

b) the leading b-jet and the lepton ($\Delta R(b-jet, \ell)$), shown in Figure 7.5(b);

c) the lepton and the $E_{\mathrm{T}}^{\mathrm{miss}}$ ($\Delta\phi(\vec{p}_{\mathrm{T}}^{\mathrm{miss}}, \ell)$);

d) the two most energetic jets and the $E_{\mathrm{T}}^{\mathrm{miss}}$ ($\Delta\phi(j_i, \vec{p}_{\mathrm{T}}^{\mathrm{miss}})$ $i = 1, 2$). This variable is extremely useful to suppress multi-jet events where *fake* $E_{\mathrm{T}}^{\mathrm{miss}}$ is originating from a mis-measurement of the jet energy and is therefore aligned with one of the jets.

7.4.3 Masses of particles: top, $W^{\pm}$, and effective masses

Top mass: m_{top}

The reconstruction of the top mass from a trijet system is very useful to select those top squark decays that involve an on-shell top in the final state.
This observable was obtained by means of a chi-square distribution minimisation, for each possible assignment of the two leading light flavour jets (j_1, j_2) and the two b-jets (b_i):

$$\chi^2 = \frac{(m_{j_1 j_2 b_i} - m_t)^2}{\sigma^2_{j_1 j_2 b_i}} + \frac{(m_{j_1 j_2} - m_W)^2}{\sigma^2_{j_1 j_2}}, \tag{7.15}$$

where m_{abc} is the invariant mass of the three objects a, b and c, m_t and m_W are the top and the $W^{\pm}$ masses respectively, and σ_{abc} is given by:

$$\sigma^2_{abc} = m^2_{abc} \cdot (r_a^2 + r_b^2 + r_c^2). \tag{7.16}$$

r_a, r_b and r_c are the fractional jet energy resolution uncertainties for the objects a, b and c. The invariant mass of the jet triplet in each event that minimises the χ^2 distribution is used as estimate of the top mass. The distribution of this quantity is shown in Figure 7.6(a). Events in a window around the top mass are selected in this analysis. The width of the window is optimised for each selection and introduced in the next chapter.

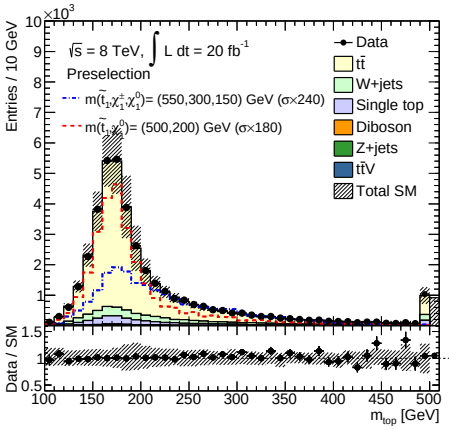

(a) Top mass (m_{top})

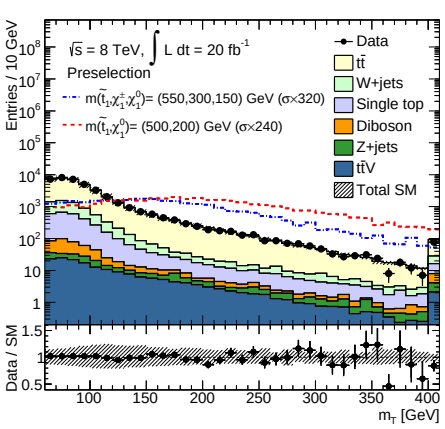

(b) Transverse mass (m_{T}) of lepton and $E_{\text{T}}^{\text{miss}}$

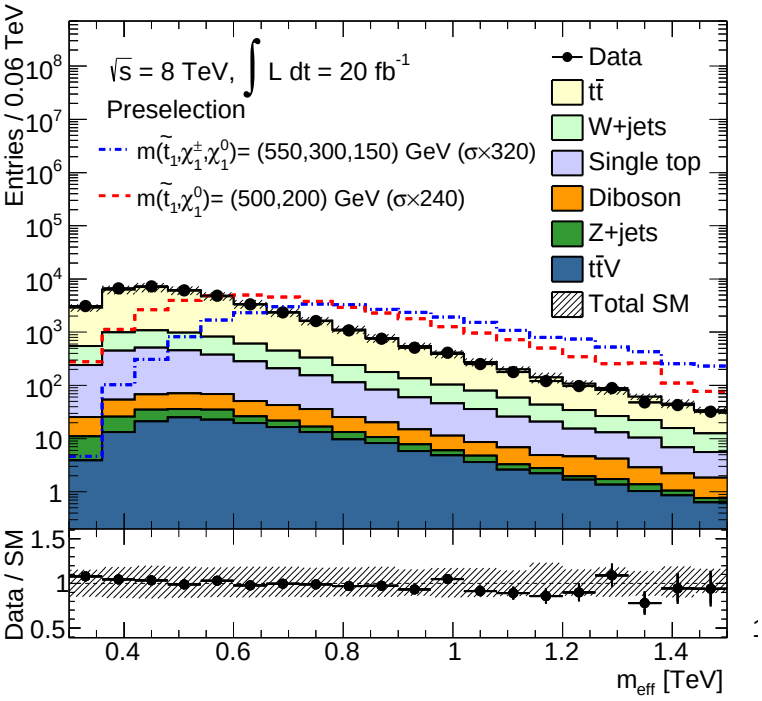

(c) Effective mass (m_{eff})

Figure 7.6: *Top mass, m_{T} and m_{eff} distributions in data and in the Monte Carlo simulation. The band includes statistical and systematic uncertainties.*

Trijet invariant mass: m_{jjj}

The trijet invariant mass m_{jjj} is obtained by first selecting the jet-jet pair among the four leading jets with an invariant mass above 60 GeV which has the smallest ΔR to form the hadronic W boson. Then m_{jjj} is reconstructed including the third jet closest in ΔR to the hadronic W boson momentum vector. This reconstructed mass of the hadronic top is required to have > 130 GeV. It is characterised by a lower resolution with respect to the top mass described in the previous subsection. However, it was found to be useful for rejecting vector boson associate production background.

Transverse mass: m_{T}

The transverse mass (Figure 7.6(b)) is calculated from the lepton and the missing transverse momentum:

$$m_{\mathrm{T}} = \sqrt{2\, E_{\mathrm{T}}^{\mathrm{miss}}\, \mathrm{E}_{\mathrm{T}}^{\mathrm{lep}} (1 - \cos\phi)}, \tag{7.17}$$

where $\mathrm{E}_{\mathrm{T}}^{\mathrm{lep}}$ is the transverse momentum of the lepton, which is assumed to be massless, and ϕ is the angle in the transverse plane between the $E_{\mathrm{T}}^{\mathrm{miss}}$ and the lepton vectors. If calculated between the lepton and the neutrino produced in the decay of a $W^{\pm}$ boson, this variable manifests an end-point at m_W. However, the presence of multiple invisible particles as in the case of the top squark signal, the distribution will have a large tail for values $m_{\mathrm{T}} > m_W$. As mentioned in the previous chapter, a requirement of $m_{\mathrm{T}} > 120$ GeV is very powerful to reject most of the semileptonic $t\bar{t}$ background.

Effective mass: m_{eff}

The effective mass of the event is the scalar sum of the transverse momenta of all the objects in the final state: the jets, the lepton p_{T} and the $E_{\mathrm{T}}^{\mathrm{miss}}$.

$$m_{\mathrm{eff}} = \sum_{i=1}^{\mathcal{N}_{jets}} p_{\mathrm{T}}^{i} + p_{\mathrm{T}}^{lep} + E_{\mathrm{T}}^{\mathrm{miss}}. \tag{7.18}$$

The sum over the jets considers only those fulfilling the requirement $p_{\mathrm{T}} > 30$ GeV. The distribution is shown in Figure 7.6(c). This quantity is very useful to select signal models characterised by a high top squark mass.

Working point	BDT value (>)	τ-rejection in $t\bar{t}$[%]	τ mis-identification [%]
Loose 1 prong	0.654	30.2	3.6
Loose 3 prong	0.563	12.3	2.0
Tight 1 prong	0.733	22.3	2.2
Tight 3 prong	0.617	7.9	1.0
Combined Loose	-	36.3	4.9
Combined Tight	-	23.9	1.4

Table 7.3: *Specifics of the τ veto working points for tau decays involving one (1 prong) or three (3 prong) charged particles in the final state. The efficiency for tau removal (τ-rejection) and the τ mis-identification rate are presented.*

7.4.4 Rejecting dileptonic and hadronic tau $t\bar{t}$ events

Taus (and extra leptons) rejection

Top events decaying into τ leptons represent a source of background for this search. Therefore an explicit identification of tau candidates was performed in this analysis. Tau leptons are the heaviest known leptons, with a mass of (1.7768 ± 0.0002) GeV [44], and a proper lifetime of $c\tau = 87\,\mu$m. They decay before reaching the detector and can only be identified through the reconstruction of their decay products. Due to their high mass, τ leptons are the only leptons for which decay modes involving hadrons are allowed. This unique property leads to the division of the tau decay modes into two categories: leptonic and hadronic. The leptonic mode ($\tau_{\text{lep}} : \tau \to \ell\bar{\nu}_\ell\nu_\tau$) in which the tau decays into two neutrinos and either a muon or an electron represents 35% of all tau decays.

Events with more than one isolated track[2)], in addition to the track associated to the selected lepton ($\mathcal{N}^{\text{iso}}_{\text{trk}}$), were rejected. For the rejection only tracks are considered that have opposite charge with respect to the selected lepton in order to identify and suppress dileptonic and leptonic tau $t\bar{t}$ decays. The distribution of track multiplicity is shown in Figure 7.7(a).

The hadronic mode (τ_{had}) represents the remaining 65% of all tau decays. In this

[2)]Isolated tracks are required to have $p_{\text{T}} > 10$ GeV and $|\eta| < 2.5$, at least five hits in the ID and no additional tracks with $p_{\text{T}} > 3$ GeV in a cone of $\Delta R = 0.4$ around it.

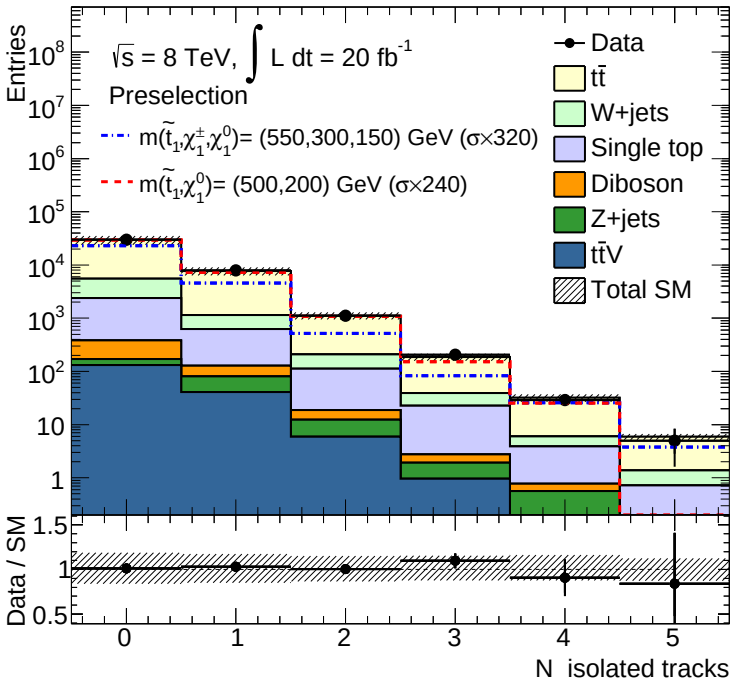

(a) $\mathcal{N}_{\text{trk}}^{\text{iso}}$

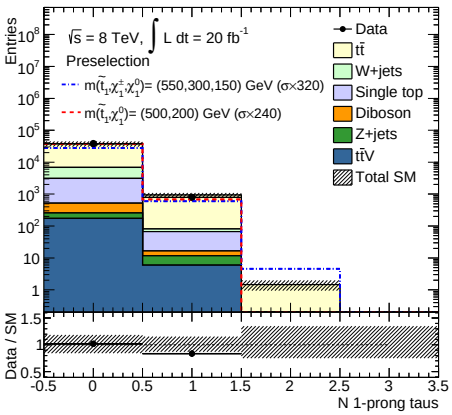

(b) $\mathcal{N}_{\tau}$ (1 prong tight)

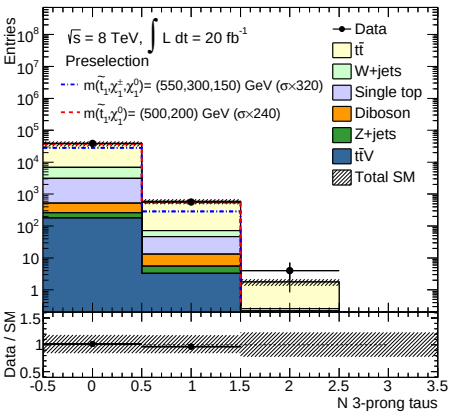

(c) $\mathcal{N}_{\tau}$ (3 prong tight)

Figure 7.7: *Distributions of the number of isolated tracks (top) and the number of 1 prong (left) and 3 prong (right) tau candidates.*

mode, the tau decays into a tau neutrino, accompanied predominantly by charged and neutral pions, and rarely by kaons. The two dominant cases are the *one prong* and *three prong* decays in which the number of charged particles produced in the final state is one and three, respectively. Hadronically decaying τ leptons are distinguished in ATLAS from jets on the basis of the calorimetric shower shape and a collimated track structure that neither match track segments in the muon spectrometer nor reveal features (such as high transition radiation in the TRT) characteristic of an electron track. All information is combined into a multi-variate discrimination technique, a Boosted Decision Tree (BDT), that is used as final discriminating variable for τ-tagging. More information about the algorithm and the calibration can be found in Ref. [142]. The BDT selection working points for τ identification were re-optimised for this analysis, in order to achieve a very low mis-identification rate ($< 3\%$), needed to guarantee a high selection efficiency on the top squark signal. The τ candidate is therefore identified by a requirement on the BDT values, a minimal transverse momentum of 15 GeV and opposite charge with respect to the selected lepton of the event.

Two working points for each tau decay topology (one and three tracks in the final state) have been defined and are listed in Table 7.3, together with the associated efficiency in removing $t\bar{t}$ decays with τ-leptons (τ-rejection) and τ mis-identification rate.

The distributions of the number of tau candidates for the tight working point are shown in Figures 7.7(b) and 7.7(c).

Stransverse masses: am_{T2} and m^{τ}_{T2}

The stransverse mass is an extension of the transverse mass to a more general case where more than one invisible particle is produced in the final state. The definition of the stransverse mass [143] is:

$$m_{\mathrm{T2}} \equiv \min_{\vec{q}_T + \vec{r}_T = \vec{p}_{\mathrm{T}}^{\mathrm{miss}}} \{\max[m_{\mathrm{T}}(\vec{p}_{\mathrm{a}}, \vec{q}_{\mathrm{T}}), m_T(\vec{p}_{\mathrm{b}}, \vec{r}_{\mathrm{T}})]\}, \tag{7.19}$$

The variable is calculated by minimisation over all the possible decompositions of p_T^{miss} into the vectors $\vec{q}_{\mathrm{T}}$ and $\vec{r}_{\mathrm{T}}$. The choice of a and b defines the characteristic of the event the variable is aiming to reconstruct. According to the choice, and as in the case of the transverse mass, this distribution will present an end-point at the mass of the particle that decays into a and b.

In this search two different implementations of stransverse mass were exploited,

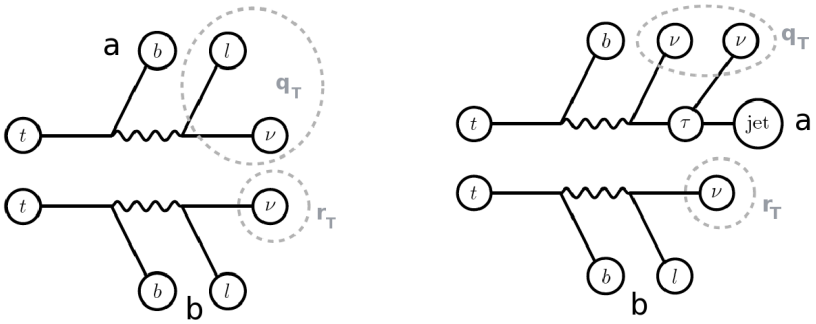

(a) Schematic representation of am_{T2}

(b) Schematic representation of m^{τ}_{T2}

Figure 7.8: *Schematic representation of the assignment of the final state objects in the stransverse mass calculation, for the asymmetric (left) and the tau (right) variations.*

both targeting specific decays of top pairs. The first one, the asymmetric stransverse mass am_{T2}, aims to reconstruct dileptonic $t\bar{t}$ decays where a lepton is not reconstructed or is outside the acceptance (and therefore adds to the $E_{\mathrm{T}}^{\mathrm{miss}}$ of the event). a is chosen as the system between the lepton and one b-jet, and b is the other b-jet in the event (Fig 7.8(a)). In this way one of the missing particles ($\vec{q_T}$) is assumed to have the $W^{\pm}$ mass, so that the distribution presents an endpoint at the top mass and, by construction, has a lower bound at the $W^{\pm}$ mass. In case of signal, the two jets coming from the hadronic $W^{\pm}$ decay will never be considered in the calculation, such that the distribution will not show the endpoint at the top mass, as can be seen in Figure 7.9. Three signal models are shown in this figure, one for each stop decay mode addressed in this analysis. The three body decay ($\tilde{t} \rightarrow b\ W^{\pm}\ \tilde{\chi}^0$) is characterised in this case by a different distribution with respect to the other decay modes and shows a peak at $\sim m_W + m_b$. Nevertheless, the stransverse mass is as powerful as for the other signal models to discriminate top squark events from background events. The large discrimination power of this variable will be widely used in most of the signal selections presented in the next chapter.

The second implementation of this variable, the tau stransverse mass m^{τ}_{T2}, targets hadronic τ $t\bar{t}$ decays, in which one top decays leptonically and the other top decays into a tau that subsequently decays hadronically. In this case a, b are chosen to be the leading light-flavour jet, which is likely to originate from the τ lepton decay, and the lepton and in this case the distribution presents an endpoint at the W mass (Fig 7.8(b)). As in the previous case, the signal distribution of this quantity is

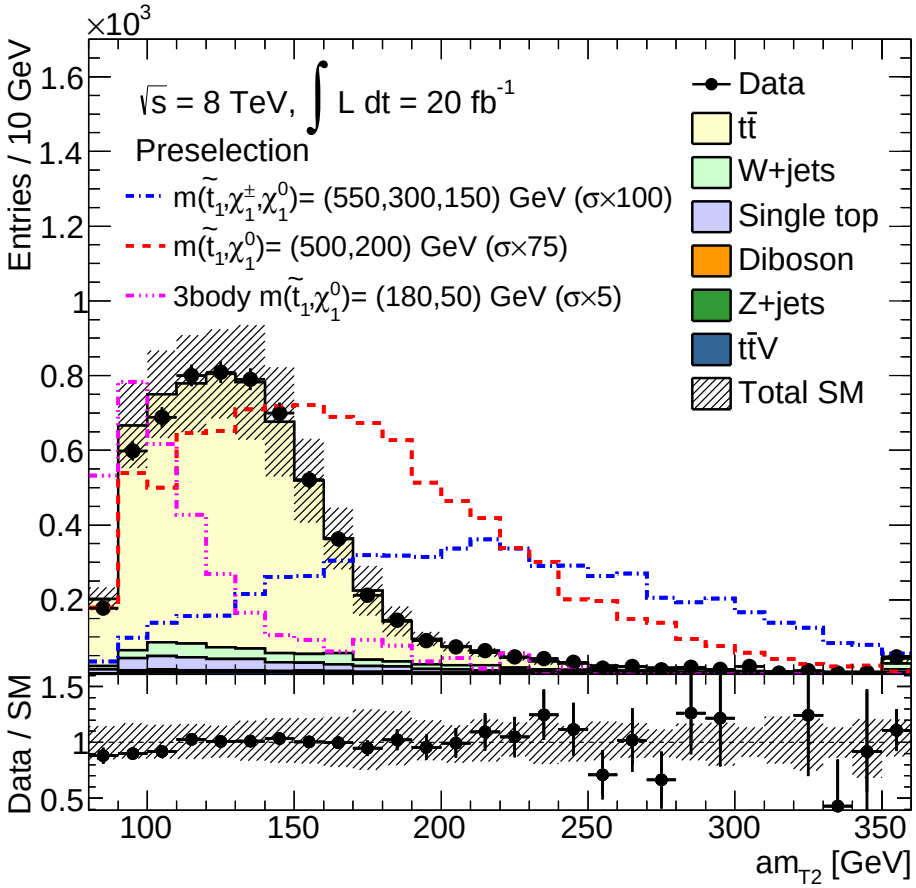

Figure 7.9: *Distributions of the asymmetric stransverse mass am_{T2}. An additional requirement of $m_{\mathrm{T}} > 120$ GeV is applied to enhance the dileptonic component of $t\bar{t}$ background.*

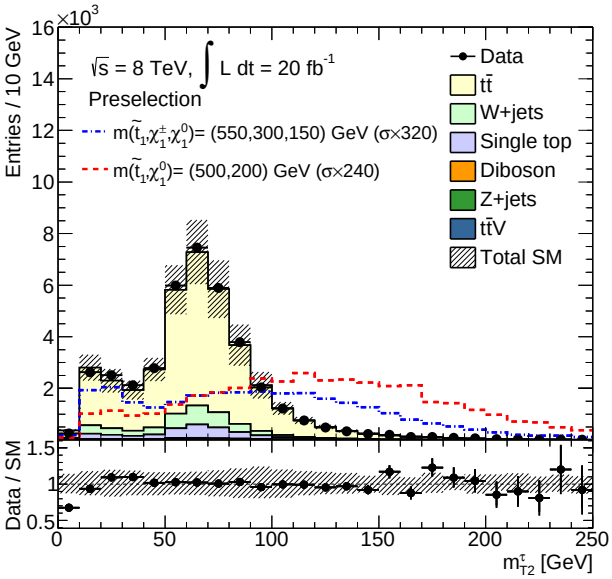

Figure 7.10: *Distributions of the tau stransverse mass m_{T2}^{τ}. An additional requirement of $m_{\mathrm{T}} > 120$ GeV is applied to enhance the dileptonic component of $t\bar{t}$ background.*

characterised by a larger tail (Figure 7.10)

Topness

The topness is an observable for reconstructing, identifying and rejecting partially reconstructed dileptonic $t\bar{t}$ events [144]. The topness distribution for background and signal is shown in Figure 7.11 and defined as

$$t = \ln(\min S), \tag{7.20}$$

where S is defined as:

$$S(p_{W,x}, p_{W,y}, p_{W,z}, p_{\nu,z}) = \frac{\left(m_W^2 - (p_\ell + p_\nu)^2\right)^2}{a_W^4} + \frac{\left(m_t^2 - (p_{b_1} + p_\ell + p_\nu)^2\right)^2}{a_t^4} + \tag{7.21}$$

$$\frac{\left(m_t^2 - (p_{b_2} + p_W)^2\right)^2}{a_t^4} + \frac{\left(4\,m_t^2 - (\Sigma p)^2\right)^2}{a_{CM}^4}, \tag{7.22}$$

where p_b, p_ℓ, p_ν, p_W are the b-jets, lepton, neutrino and $W^\pm$ momenta respectively, m_t and m_W are the top and the $W^\pm$ masses and the denominators a_K determine the weighting of the mass shell conditions and are used to model the detector resolution. They are set to the following values (from [144]): $a_W = 5$ GeV,

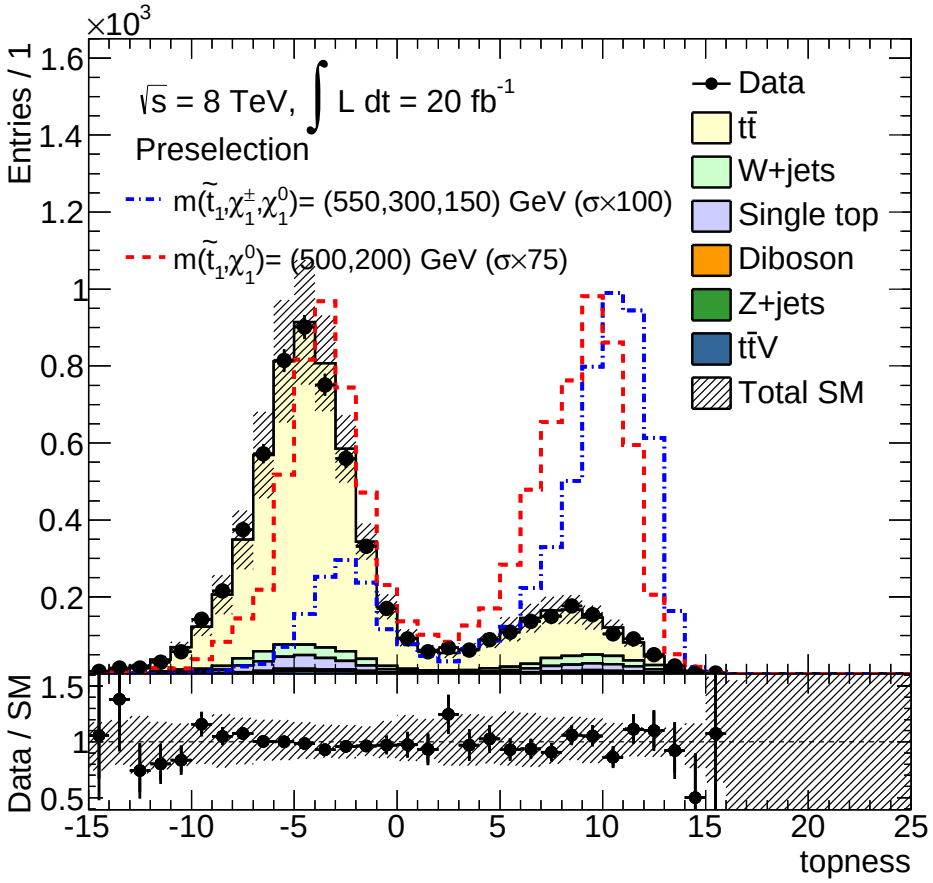

Figure 7.11: *Topness distribution in data and in the Monte Carlo simulation. An additional requirement of* $m_{\mathrm{T}} > 120$ GeV *is applied to enhance the dileptonic component of* $t\bar{t}$ *background. The band includes statistical and systematic uncertainties.*

a_t = 15 GeV, a_{CM} = 1 TeV. S aims to reconstruct $t\bar{t}$ event kinematics in the assumption that both $W^{\pm}$ decay leptonically and one of the leptons is unaccounted for due to limited acceptance or identification inefficiency. It therefore assumes small values for top events and high values for other processes, including the signal. In such events the $E_{\mathrm{T}}^{\mathrm{miss}}$ is artificially high due to the missed lepton.
The momentum vector of the non-reconstructed $W^{\pm}$ boson and the z-component of the neutrino produced in the decay of the other $W^{\pm}$ boson decay of the top pair are undetermined. These four variables are varied to find the minimum of S. Four constrains are applied in order to derive the four unknowns of the equation. These constrains are the on-shell requirements for the masses of the two tops (m_t), the mass of the reconstructed $W^{\pm}$ (m_W) and it is required that the reconstructed centre-of-mass energy of the event is minimised. As consequence of the Parton Distribution Function (PDF), $\sqrt{s}$ is a steeply falling distribution, therefore the centre-of-mass minimisation provides a good approximation to the true event kinematics.

To fully unravel the construction of this variable the b-jets in Eq. 7.21 have to be assigned to one of the top quarks. Both possible combinations for b_1 and b_2 are evaluated during the minimisation; if only one b-tagged jet is present, it is used together with the leading or sub-leading jet (a total of four possible jet assignments are evaluated in this case).

b-jet multiplicity and b-tagging working points

The signal is characterised by two b-jets in the final state, with the exception of the compressed $\tilde{t} \to b\,\tilde{\chi}^{\pm}$ scenario ($m_{\tilde{t}} \sim m_{\tilde{\chi}^{\pm}}$) in which the mass difference between the top squark and the chargino is so small that the b-jets in the final state will be too soft to be identified.

The MV1 tagging algorithm, introduced in Chapter 3.2.2, was used for this analysis at *loose* and *tight* working points, in order to tune the b-jet efficiency versus the purity according to the needs of the final state. In particular, all selections requiring at least one b-tagged jet in the final state have used the *tight* working point, that has 70% efficiency of tagging a b-jet. In case of events with two real b-jets, as in the case of $t\bar{t}$ background or stop signal, this results in a selection efficiency of 87.2% for a benchmark top squark signal model and of 83.8% for $t\bar{t}$ events. The selections requiring at least two b-jets use the *loose* working point, that has 80% b-tagging efficiency, in order to increase the signal acceptance. The efficiency for tagging both b-jets in the event is 59.8% for signal and 51.8% for $t\bar{t}$ events. Finally,

the selections that veto the presence of b-jets in the final state use the tight working point. The modelling of the jet and tight b-jet multiplicities is shown in Figure 7.12. In the same figure the momenta of the leading and the sub-leading b-jet in the event is compared between background and top squark signal, in order to highlight the harder spectrum of the latter, a characteristic that will be largely exploited in the signal selections.

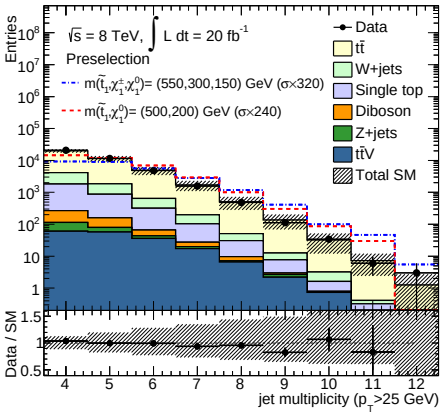

(a) jet multiplicity

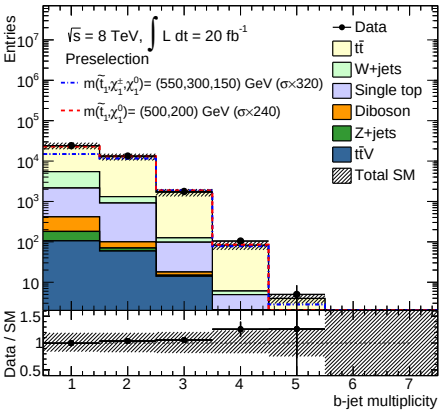

(b) tight b-jet multiplicity

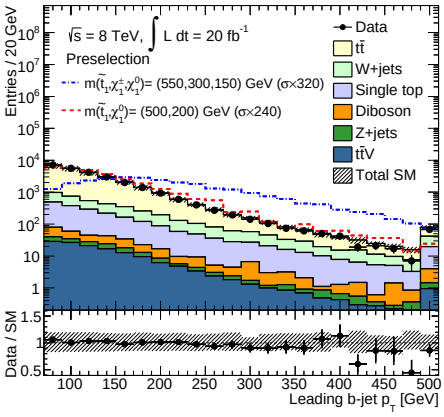

(c) leading b-jet p_{T}

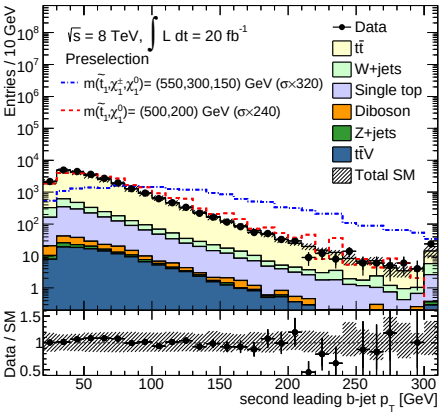

(d) sub-leading b-jet p_{T}

Figure 7.12: *Jet and tight b-jet multiplicity distributions and b-jet momenta in data and in the Monte Carlo simulation. The band includes statistical and systematic uncertainties.*

8 Signal selections and background estimate

Three decay modes of the top squark are considered in this search. They depend on the mass assumption of the stop and the other SUSY particles in the decay chain. The optimisation strategy followed to design the final signal selections for the $\tilde{t} \to b\,\tilde{\chi}^{\pm}$ decay mode are presented in this chapter. In addition, an overview of the selections dedicated to the other two decay modes is given. Finally, the strategy to estimate a data-driven background normalisation and its validation is presented in the last two sections of this chapter.

The selections of this analysis have been optimised for three decay modes of the top squark (see Section 7.1). For each of these decays, different mass assumptions for the SUSY particles in the decay chain have been considered. All the selections dedicated to the different signal models and decay channels have been optimised exploiting a similar strategy. The optimisation of the selections was based only on the Monte Carlo simulation and the experimental data were kept *blinded*. This means that the region of the phase space that is most sensitive to the stop signal (data events with $m_{\mathrm{T}} > 120\,\mathrm{GeV}$ and $E_{\mathrm{T}}^{\mathrm{miss}} > 250\,\mathrm{GeV}$) was omitted from the comparisons with the Monte Carlo until the analysis was considered finalised.

The figure of merit used for the optimisation is the CL_S hypothesis test introduced in Sec. 7.3.2. An approximate systematic uncertainty of 20% on the background estimate was considered in the optimisation. When faster processing was required, an alternative figure of merit was used:

$$\mathcal{S} = \frac{\mathcal{N}_{\mathrm{sig}}}{\sqrt{\mathcal{N}_{\mathrm{sig}} + \mathcal{N}_{\mathrm{bkg}} + (\mathrm{sys} * \mathcal{N}_{\mathrm{bkg}})^2}}, \tag{8.1}$$

where $\mathcal{N}_{sig}$ and $\mathcal{N}_{bkg}$ are the number of selected signal and total background events and sys represent an approximate estimate of flat (kinematical independent) systematic uncertainty of 20%.

The quantities used in the selection optimisation have been chosen according to their shape separation power between the signal models and the top pair background. Additional considerations, such as correlations among variables and statistical uncertainties on the Monte Carlo samples were considered. The variables were used to define sets of cuts (order 10^5), the best of which were chosen to maximise the sensitivity $\mathcal{S}$ defined in Eq. (8.1) across the maximum number of signal models. The procedure was iterated multiple times and the final best selections were compared using the CLs figure of merit.

Signal models characterised by a final-topology kinematics very similar to the background were addressed by shape fits. In this case the bin with the lowest statistics of the shape fit was optimised with the same strategy of a *cut-and-count* selection and then a binning in the two most powerful variables was designed according to the criteria described in the next section.

In all selections, except the one addressing the $\tilde{t} \to b\,\tilde{\chi}^{\pm}$ compressed scenario, bC_diag, the requirements listed in Section 7.4 are applied, that suppress part of the background while retaining almost 100% signal efficiency.

8.1 $\tilde{t} \to b\,\tilde{\chi}^{\pm}$ selection optimisation

The optimisation of the selections dedicated to the $\tilde{t} \to b\,\tilde{\chi}^{\pm}$ decay mode is presented in this section as an example for the optimisation that has been performed for all selections targeting the many signal models of this analysis. The $\tilde{t} \to b\,\tilde{\chi}^{\pm}$ decay is characterised by a three dimensional phase space, determined by the three unknown masses of SUSY particle in the decay chain ($\tilde{t}$, $\tilde{\chi}^{\pm}$, $\tilde{\chi}^{0}$). We obviously assume that $m(\tilde{\chi}^{0}) < m(\tilde{\chi}^{\pm}) < \big(m(\tilde{t}) - m(b)\big)$. In order to reduce the plethora of models that arise from the combination of all possible masses of these three particles, one of the most common phenomenological constraint is imposed: the gaugino universality (See Chapter 1 for the details). This constraint implies:

$$m(\tilde{\chi}^{\pm}) = 2m(\tilde{\chi}^{0}) \tag{8.2}$$

and it is used for the models used in the signal selection optimisation.

Obviously this assumption, despite its theoretical motivation, is somehow arbitrary. However, it has the practical advantage that this particular relation between

Region	Scenario		Technique	Table
bC_diag	I	$m_{\tilde{t}} \gtrsim m_{\tilde{\chi}^{\pm}}$	*cut-and-count*	8.4
bC_bulk	II and IV	$m_{\tilde{t}} \lesssim 300\,\text{GeV}$	shape fit (am_{T2} and m_{T})	8.5
bC_med	III and IV	$m_{\tilde{t}} < 600\,\text{GeV}$	shape fit (am_{T2} and m_{T})	8.5
bC_high1	III	$m_{\tilde{t}} \gtrsim 500\,\text{GeV}$	*cut-and-count*	8.3
bC_high2	III	$m_{\tilde{t}} \gtrsim 500\,\text{GeV}$	*cut-and-count*	8.3

Table 8.1: *Summary of the signal regions targeting $\tilde{t} \to b\,\tilde{\chi}^{\pm}$ decay mode. The scenario that is addressed by each region, the table where the selections are listed and the technique used to extract the results are listed in the last three columns.*

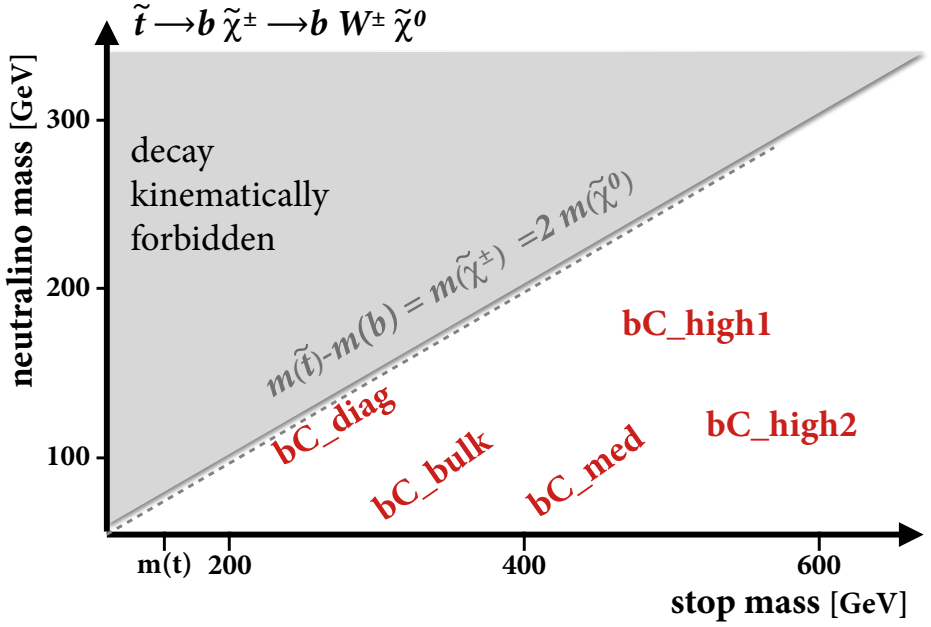

Figure 8.1: *Schematic representation of the grouping scheme of different top squark models according to the top squark and the neutralino mass assumptions for the $\tilde{t} \to b\,\tilde{\chi}^{\pm}$ decay mode. A selection was designed for each of these regions. $m_{\tilde{\chi}^{\pm}} = 2m_{\tilde{\chi}^{0}}$ is assumed.*

the neutralino and the chargino mass includes models with very different final state kinematics and allows to design selections that are powerful also in selecting signal models with very different chargino and neutralino masses.

This set of models can be divided into four scenarios characterised by different phenomenology and are addressed with five signal selections summarised in Figure 8.1 and Table 8.1:

I. $m(\tilde{\chi}_1^{\pm}) \sim m(\tilde{t})$: in this scenario the two bottom quarks tend to have too low momenta to be reconstructed or identified. The signal selection strategy is therefore to veto events with b-tagged jets. The event selection (labelled **bC_diag**) for this *diagonal* (or *compressed*) scenario is described in Section 8.1.3.

II. $m(\tilde{\chi}_1^0) < m(\tilde{\chi}_1^{\pm}) < m(\tilde{t})$: in this group of signal models the bottom quarks tend to have medium momenta, while the W bosons and two $\tilde{\chi}_1^0$ have medium to large momenta. The signal selection strategy is to find events with $\geq 1b$-tagged jets. Details for this event selection optimisation (labelled **bC_bulk**) are given in Section 8.1.4.

III. $m(\tilde{\chi}_1^0) < m(\tilde{\chi}_1^{\pm}) << m(\tilde{t})$, high $m(\tilde{t})$: in this scenario the bottom quarks tend to have very large momenta, the W bosons and two $\tilde{\chi}_1^0$ have medium to large momenta. The signal selection strategy is to require events with $\geq 2b$-tagged jets with large p_{T} thresholds. Details for this selection optimisation (labelled **bC_high1** and **bC_high2**) are given in Section 8.1.2 and **bC_med** is described in Section 8.1.4.

IV. $m(\tilde{\chi}_1^{\pm}) - m(\tilde{\chi}_1^0) < m(W)$: an off-shell W boson is produced in this decay but the mass splitting is enough to boost the charged lepton to pass the 25 GeV threshold. This selection was addressed using a shape fit strategy and requiring at least one or two b-jets. Details for this selection optimisation (**bC_bulk** and **bC_med**) are given in Section 8.1.4.

8.1.1 Variable ranking in terms of separation power for scenarios II, III and IV

The most powerful quantities that discriminate $\tilde{t} \to b\,\tilde{\chi}^{\pm}$ signal from the background (see Section 7.4 for details) are:

- transverse momenta, $E_{\mathrm{T}}^{\mathrm{miss}}$, sum of the total transverse energy in the event ($\mathrm{H_T}$, m_{eff}) and the transverse mass (m_{T}) that reject semileptonic $t\bar{t}$ and W + jets.

Variable	$\langle S \rangle$ for signal model m($\tilde{t}$)-m($\tilde{\chi}^{\pm}$)-m($\tilde{\chi}^{0}$) [GeV]				
	medium mass	virtual W		high mass	
	275-150-75	300-100-50	400-100-50	500-300-150	600-200-100
1st b-jet p_{T}	0.04	0.14	0.31	0.21	0.47
2nd b-jet p_{T}	0.03	0.11	0.25	0.18	0.37
1st jet p_{T}	0.01	0.08	0.26	0.15	0.47
2nd jet p_{T}	0.01	0.07	0.24	0.19	0.45
3rd jet p_{T}	0	0.02	0.10	0.12	0.26
4th jet p_{T}	0	0.01	0.04	0.07	0.14
m_{T}	0.05	0.05	0.06	0.23	0.11
$E_{\mathrm{T}}^{\mathrm{miss}}$	0.03	0.08	0.24	0.26	0.47
$E_{\mathrm{T}}^{\mathrm{miss}}/\sqrt{H_{\mathrm{T}}}$	0.01	0.02	0.06	0.11	0.15
$\mathrm{H_T}$	0.01	0.08	0.29	0.22	0.55
m_{eff}	0.01	0.08	0.30	0.30	0.56
am_{T2}	0.07	0.22	0.39	0.31	0.50
m_{T2}^{τ}	0.03	0.06	0.04	0.15	0.07
topness	0.09	0.20	0.34	0.32	0.42

Table 8.2: *Shape separation power of the most discriminating variables for representative benchmark point of the various groups of signal models considered in the optimisation.*

- asymmetric stransverse mass and topness to reject dileptonic $t\bar{t}$ decays.
- isolated tracks and τ leptons veto to reject $t\bar{t}$ tau decays.

The ranking was based on the separation power of each of these quantities. The separation power for an observable y is defined as:

$$\langle S \rangle = \frac{1}{2} \int \frac{\left(f_s(y) - f_B(y)\right)^2}{f_s(y) + f_B(y)} dy, \tag{8.3}$$

where $f_B(y)$ and $f_S(y)$ are respectively the background and signal probability distribution functions of y. Since top pair production is the dominant background, $f_B(y)$ was evaluated only on $t\bar{t}$. $\langle S \rangle = 0$ means that the two distributions completely overlap, while $\langle S \rangle = 1$ is obtained for distributions that are completely separated.

A summary of the most discriminant variables and their separation power value for the benchmark models used in the optimisation are given in Table 8.2. This rank-

ing has been used as an indication to identify the powerful variables to be tested. In this preliminary procedure the relative normalisation between signal and background and correlations between variables are neglected. In Table 8.2, it can be noticed that the medium mass signal models are not characterised by energetic jets or b-jets. The most effective selection was found to be the one based on the requirement of at least one b-tagged jet in the final state and minimal jet momentum requirement to reduce subdominant background such as W-jets and Pile-Up. On the other hand, the b-jets momenta represent a powerful quantity to discriminate for high mass top squark signal models. $\mathrm{H_T}$ and m_{eff} are correlated at 80%, so that despite they both show high shape discrimination power for high top squark masses, effectively only one at a time was tested in the selection. The same considerations apply for m^{τ}_{T2}, since it is correlated to m_{T} at 65%. Finally topness is correlated by 55% to am_{T2}, which justifies why it proved to be a useful variable only in certain selections. It is also important to notice that m_{T} and am_{T2} are in all presented cases among the highest variables in ranking. In addition they are not correlated among each others and only mildly correlated with all the other powerful variables used in the selections. These motivation will bring us to design a bidimensional shape fit in Section 8.1.4 based on these two observables.

8.1.2 Cut-and-count selections for high top squark masses: bC_high1 and bC_high2

In order to address the models with high stop masses, we designed two *cut-and-count* selections (bC_high1 and bC_high2), that are summarised in Table 8.3. These selections require at least two b-tagged jets selected with the *loose* (highly efficient) working point. $|\Delta\phi(\mathrm{jet}_{1,2}, E^{\mathrm{miss}}_{\mathrm{T}})| > 0.8$ was fixed a priori in the optimisation procedure because it guarantees a negligible impact from events with fake $E^{\mathrm{miss}}_{\mathrm{T}}$ in the selection. For the same reason the $E^{\mathrm{miss}}_{\mathrm{T}}/\sqrt{H_{\mathrm{T}}}$ requirement was bound to be greater than 5 in the optimisation. Figures 8.2 and 8.3 show the comparison between the data and the SM background. The latter is modelled by Monte Carlo simulation and normalised from the likelihood fit as described in Section 8.3. All requirements are applied, except the one on the shown distribution. The requirement on the distribution that is shown is indicated instead with an arrow. Two signal models are superimposed in the plot in order to highlight the discrimination power of the requirement. bC_high2 is characterised by tighter selection with respect to bC_high1, in the attempt to push the sensitivity of our selections to very high top

squark masses.

8.1.3 Cut-and-count selection for compressed scenario: bC_diag

In this scenario the bottom quarks produced in the decay of the top squark have too low momenta to be reconstructed or identified. For this reason bC_diag was designed to require at least three jets in the final state (instead of the four jets required in all the other selections targeting the same decay channel) and vetoes the presence of b-tagged jets. Differently from all the other selections presented in this analysis, the dominant background of this selection is dominated by W + jets processes, and $t\bar{t}$ represents the second dominant contribution. All the requirements of bC_diag are listed in Table 8.4. The requirements on the $E_{\mathrm{T}}^{\mathrm{miss}}/\sqrt{H_{\mathrm{T}}}$ and the $|\Delta\phi(\mathrm{jet}_i, \vec{p}_{\mathrm{T}}^{\mathrm{miss}})|$ $(i = 1, 2)$ reduce the contamination from multi-jet background to a negligible amount. In addition to the b-jets veto, the requirements on the lepton pseudorapidity and its angular distance from the leading jet were found to be powerful in rejecting the background.

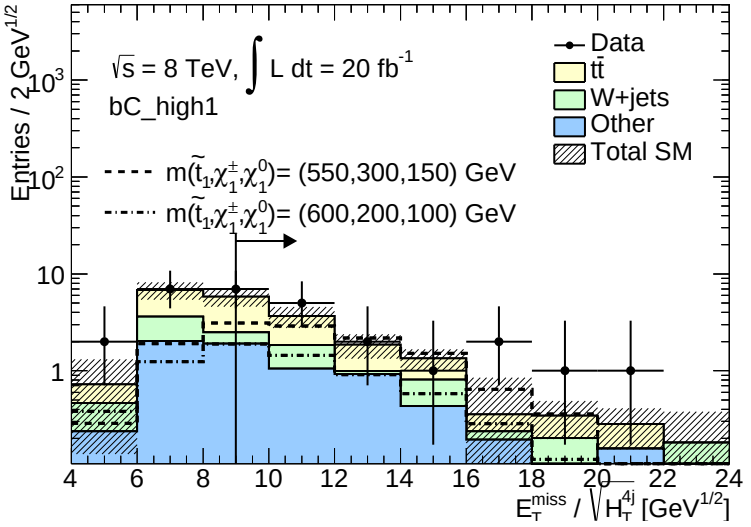

(a)

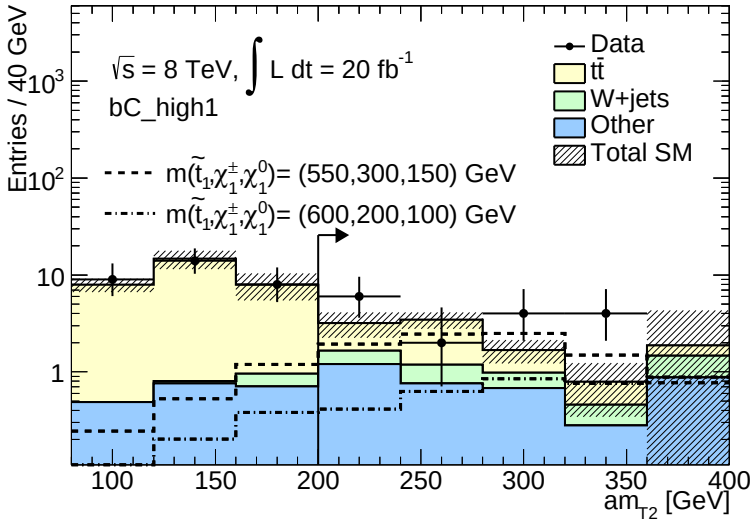

(b)

Figure 8.2: *Distributions of the two most discriminating variables used for the bC_high1 selection. All requirements except the one on the distribution showed are applied, that is indicated by the arrow instead. The background estimate is normalised to the fit results and both statistical and systematic uncertainties are included in the shaded band.*

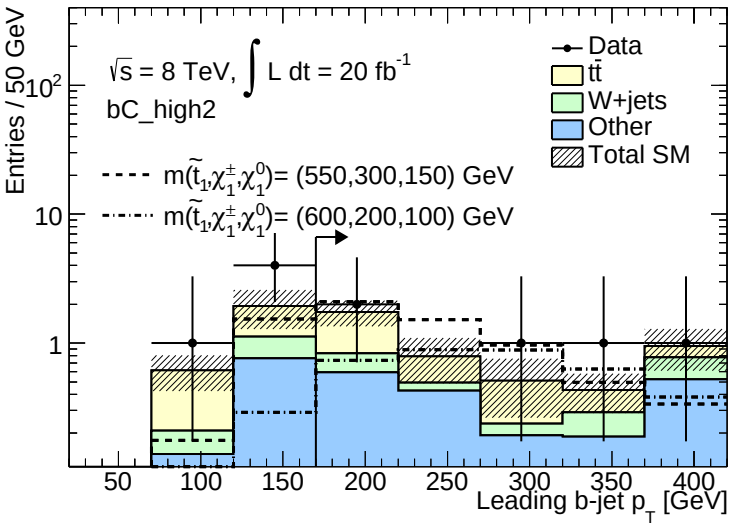

(a)

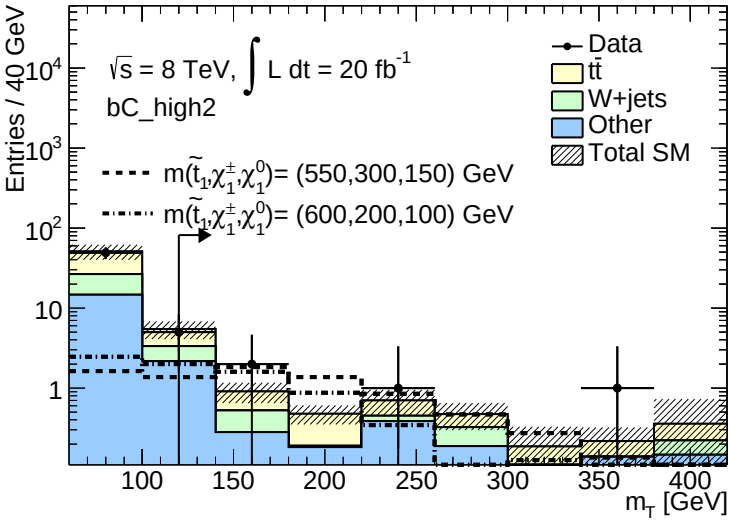

(b)

Figure 8.3: *Distributions of the two most discriminating variables used for the bC_high2 selection. All requirements except the one on the distribution showed are applied, that is indicated by the arrow instead. The background estimate is normalised to the fit results and both statistic and systematic uncertainties are included in the shaded band.*

Requirement	bC_high1	bC_high2
Number of loose b-jets $\geq$	2	2
$E_{\mathrm{T}}^{\mathrm{miss}}/\sqrt{H_T}$ [GeV$^{1/2}$] >	9	8
$\lvert\Delta\phi(\mathrm{jet}_{1,2}, E_{\mathrm{T}}^{\mathrm{miss}})\rvert$ >	0.8	0.8
p_{T} (b-jets) [GeV] >	75-75	170-80
p_{T} (jets) [GeV] >	80-60-40-25	80-80-40-25
$E_{\mathrm{T}}^{\mathrm{miss}}$ [GeV] >	150	160
m_{T} [GeV] >	120	120
m_{eff} [GeV] >	600	-
am_{T2} [GeV] >	200	250
$\mathcal{N}_{\mathrm{trk}}^{\mathrm{iso}} = 0$	Yes	Yes
Tight tau veto	Yes	Yes

Table 8.3: cut-and-count *signal regions targeting the high mass region of the $\tilde{t} \to b\,\tilde{\chi}^{\pm}$ grid: bC_high1 and bC_high2.*

Requirement	bC_diag
$N_{\mathrm{jets}}^{\mathrm{signal}} \geq$	3
jet p_{T}s [GeV] >	80, 40, 30
Number of tight b-jets ($p_{\mathrm{T}} > 25$ GeV) =	0
$E_{\mathrm{T}}^{\mathrm{miss}}/\sqrt{H_{\mathrm{T}}}$ [GeV$^{1/2}$] >	5
$E_{\mathrm{T}}^{\mathrm{miss}}$ [GeV] >	140
m_{T} [GeV] >	120
$\lvert\eta(\ell)\rvert$ <	1.2
$\Delta R(j_1, \ell) \in$	[0.8:2.4]
$\lvert\Delta\phi(\mathrm{jet}_i, \vec{p}_{\mathrm{T}}^{\mathrm{miss}})\rvert$ >	2.0 (i=1), 0.8 (i=2)

Table 8.4: cut-and-count *signal region targeting the compressed region of the $\tilde{t} \to b\,\tilde{\chi}^{\pm}$ grid (bC_diag).*

8.1.4 Shape fits for intermediate top squark masses and off-shell $W^{\pm}$: bC_bulk and bC_med

The selection of signal models with intermediate top squark masses and or with the $W^{\pm}$ emitted off-shell represent a somewhat more difficult situation than the selection of very high stop mass models. *cut-and-count* selection strategies have been studied and presented in previous results of this analysis in ATLAS [145]. Such approaches tend to converge into signal selections that achieve a reasonable sensitivity only to a restricted number of models. This implies that a large number of different selections are needed to extend the analysis coverage to all models we aim to optimise for and the analysis will not be powerful for additional re-interpretations of the results in terms of different signal models.

For this reason it was decided to exploit a shape fit in the variable that provides the highest shape separation power between signal and background: namely the asymmetric stransverse mass am_{T2}. A binned fit in the am_{T2} has not only the advantage of increasing the separation with the background, but allows to be simultaneously more efficient in selecting a large number of signal models, that depending on the top squark mass assumption tend to peak at different values of this distribution, as can be observed in Figure 8.4(a). In the same figure, the red dashed lines indicate the boundaries used in the fit. The first bin edge is in correspondence of the top mass (175 GeV) and was chosen such that the first bin is highly enriched in background and can be used to control its normalisation. The other two boundaries are the result of a compromise between an high sensitivity to the largest number of stop models and a low impact of the Monte Carlo statistical uncertainties in the bins.

The distribution of the transverse mass of the $E_{\mathrm{T}}^{\mathrm{miss}}$ and the lepton is shown in Figure 8.4(b) for $t\bar{t}$ background and few signal models. It is possible to notice that there is a smaller shape separation power of this observable for signal models in which the W is emitted off-shell and there is a considerable amount of signal in the region $60 < m_{\mathrm{T}} < 90\,\mathrm{GeV}$. The combination of this variable with the am_{T2} in a bidimensional shape fit allowed to powerfully discriminate between signal and background and efficiently recover signal events that would be suppressed by a requirement on the transverse mass. The addition of the events with $30 < m_{\mathrm{T}} < 60\,\mathrm{GeV}$ was tested and did not provide a significant improvement of the sensitivity and was therefore not included in the shape fit.

It was decided to implement a loose and a tight version of the shape fit, so that

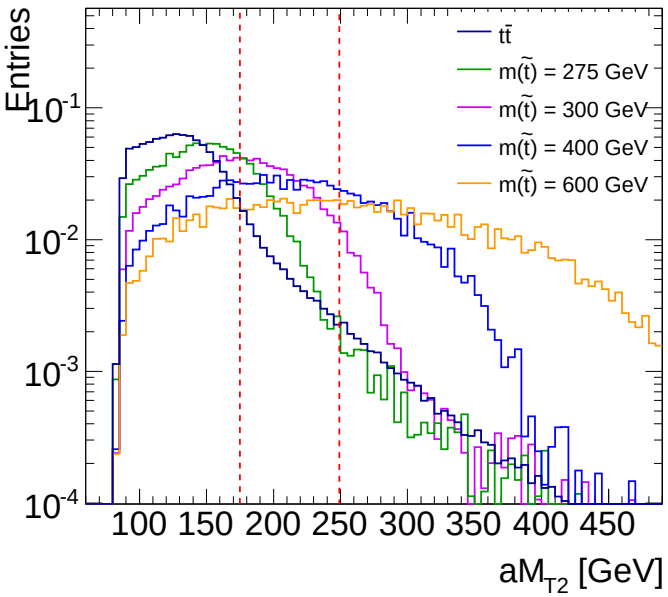

(a) am_{T2}

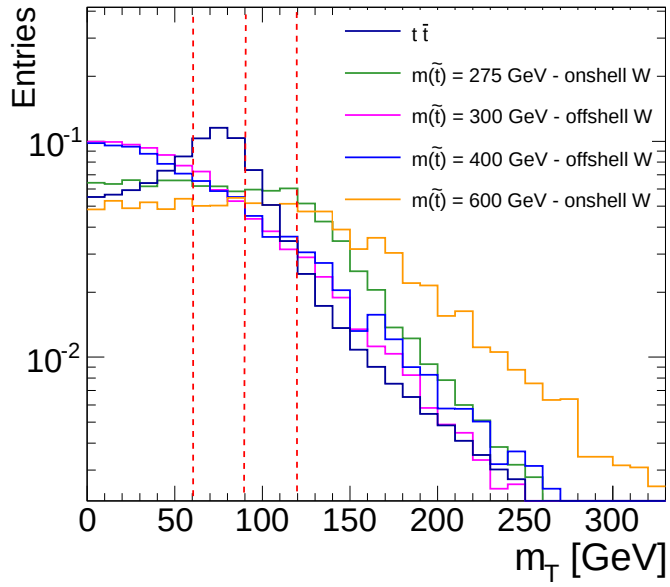

(b) m_{T}

Figure 8.4: *Shape comparison between $t\bar{t}$ background and different signal models for the two variables used in the shape fit. Distributions are normalised to the same area. The red dashed lines in the plot indicate the boundary of the binning used in the fit*

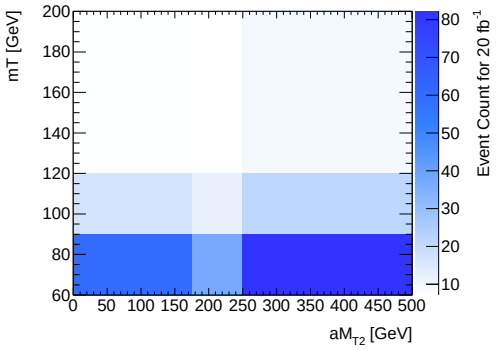

(a) background

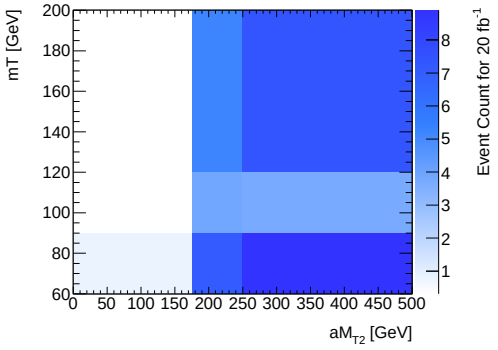

(b) $m(\tilde{t}) = 350$ GeV, $m(\tilde{\chi}^{\pm}) = 100$ GeV, $m(\tilde{\chi}^{0}) = 50$ GeV

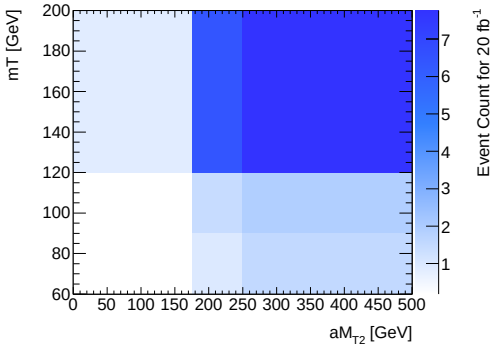

(c) $m(\tilde{t}) = 500$ GeV, $m(\tilde{\chi}^{\pm}) = 300$ GeV, $m(\tilde{\chi}^{0}) = 150$ GeV

Figure 8.5: *Visual representation of the shape and normalisation difference between the background and two signal models in the shape fit 2D plane. The yields are normalised to 20 fb^{-1}.*

the two signal selections exploit the same fitting strategy (variables and binning) meanwhile they are characterised by very different final yields. bC_bulk, that is the loosest of the two, aims to select top squark signal models with intermediate or low masses. The requirements applied to the events used in the shape fit are only the minimal requirement to suppress backgrounds other than $t\bar{t}$ and are summarised in Table 8.5. At least one tight b-tagged jet is required in this selection in order to maximise the signal efficiency. The τ and isolated tracks veto was found to improve the signal over background ratio and was added to the requirements.

The selections for the tight shape fit, bC_med, are also listed in Table 8.5. In this case the purpose of the selections was to reduce the $t\bar{t}$ background in addition to the other backgrounds exploiting the variables that provide discrimination power for intermediate and high stop masses. The selections were optimised using the same strategy as for the *cut-and-count* selections in the tightest bin of the shape fit ($am_{\mathrm{T2}} > 250\,\mathrm{GeV}, m_{\mathrm{T}} > 120\,\mathrm{GeV}$). Variables correlated with am_{T2} and m_{T} were not included, with the exception of topness. Despite topness being correlated at 55% with am_{T2}, it was proven to be very useful to decrease the background events in the most powerful bins of the shape fit while retaining a reasonable efficiency for top pair production in the background enriched bins used to constrain the $t\bar{t}$ normalisation.

The choice of the same binning in both the loose and the tight versions of the shape fit is not fully optimal, since lower bin boundaries might have been beneficial for the loose selection that aims to be sensitive to intermediate and low top squark masses. On the other hand, separate fit boundaries would have increased even more the complexity without introducing a real improvement due to the risk of fine tuning.

The shape power of the tight version of the fit (bC_med) is visualised as an example in Figure 8.5, where the background and two signal model distributions in the $(am_{\mathrm{T2}}, m_{\mathrm{T}})$ plane are represented. Certain signal models such as $m(\tilde{t})$ = 500 GeV, $m(\tilde{\chi}^{\pm})$ = 300 GeV, $m(\tilde{\chi}^{0})$ = 150 GeV dominate in the high-$m_{\mathrm{T}}$and high-am_{T2}bins of the bidimensional plane and are obviously different in shape from the background. However, the real strength of this bidimensional fit stands out investigating the distribution in the $(m_{\mathrm{T}}, am_{\mathrm{T2}})$ plane of signal models characterised by an off-shell $W^{\pm}$ such as $m(\tilde{t})$ = 350 GeV, $m(\tilde{\chi}^{\pm})$ = 100 GeV, $m(\tilde{\chi}^{0})$ = 50 GeV. For these models, the binning in m_{T} allows for a great recovery in signal selection efficiency, compared to an hypothetical requirement of $m_{\mathrm{T}} > 120\,\mathrm{GeV}$ as implemented in the single bin selections. The combination between m_{T} and am_{T2} provides a discriminating shape difference with respect to the background and it is the reason

for which, it was possible for the first time in ATLAS to extend the sensitivity of this analysis to this category of top squark signal models.

Requirement	bC_bulk	bC_med
Number of loose b-jets $\geq$	-	2
Number of tight b-jets $\geq$	1	-
$E_{\mathrm{T}}^{\mathrm{miss}}/\sqrt{H_T}$ [GeV$^{1/2}$] >	7	6
$\Delta\phi(\mathrm{jet}_{1,2}, E_{\mathrm{T}}^{\mathrm{miss}})$ >	0.8	0.8
p_{T} (leading b-jet) [GeV] >	25	140
p_{T} (second b-jet) [GeV] >	-	75
p_{T} (leading jet) [GeV] >	80	140
p_{T} (2nd leading jet) [GeV] >	60	75
p_{T} (3rd jet) [GeV] >	40	40
p_{T} (4th jet) [GeV] >	25	25
$E_{\mathrm{T}}^{\mathrm{miss}}$ [GeV] >	150	170
topness >	-	7.5
$\mathcal{N}_{\mathrm{trk}}^{\mathrm{iso}} = 0$	Yes	Yes
Tight tau veto	Yes	Yes
Binned variables		
m_{T} [GeV] $\in$	[60-90], [90-120], [120-∞]	
am_{T2} [GeV] $\in$	[80-175], [175-250], [250-∞]	

Table 8.5: *Shape fit selections targeting the intermediate masses and the virtual W regions of the $\tilde{t} \to b\,\tilde{\chi}^{\pm}$ grid.*

8.2 Selections for other top squark decays

The other two stop decay modes considered in this analysis ($\tilde{t} \to t\,\tilde{\chi}^0$ and $\tilde{t} \to b\,W^{\pm}\,\tilde{\chi}^0$) are addressed with three *cut-and-count* selections and two shape fits, as summarised in Figure 8.6 and Table 8.6.

One of the *cut-and-count* selections exploits dedicated techniques to identify highly energetic tops in the final state whose decay products are not fully resolvable with the standard jet identification algorithms. This specific region, tN_boost, is described in Ref. [9] and will not be detailed in this thesis. The results will however be presented together with all selections in Chapter 9.

8.2.1 $\tilde{t} \to t\,\tilde{\chi}^0$ selections: tN_diag, tN_med and tN_high

Two *cut-and-count* regions (tN_med and tN_high) are used to select $\tilde{t} \to t\,\tilde{\chi}^0$ signal models where $m_{\tilde{t}} >> m_t$. An overview of all selections applied in these two signal regions is shown in the first two columns of Table 8.7 and the most discriminating distribution for each region is shown in Figure 8.7. A shape fit strategy was implemented for $m_{\tilde{\chi}^0} \sim m_{\tilde{t}} - m_t$ (tN_diag). In this case the two discriminating variables used in the fit are the transverse mass and the missing transverse momentum. The summary of the selections applied to the events used in the fit is given in the second column of Table 8.8.

8.2.2 Selection for asymmetric decays of the top squark: SR_mix

One signal selection has been optimised for signal models where two decay modes are allowed at the same time:

$$\tilde{t} \to t\,\tilde{\chi}^0$$
$$\tilde{t} \to b\,\tilde{\chi}^{\pm} \to b\,W^{\pm}\,\tilde{\chi}^0.$$

For the optimisation of the selections the two decays were both assumed to have 50% branching ratio. The requirements for this signal selection are summarised in the last column of Table 8.7. One of the most discriminating variable, $E_{\mathrm{T}}^{\mathrm{miss}}$ is shown in Figure 8.8.

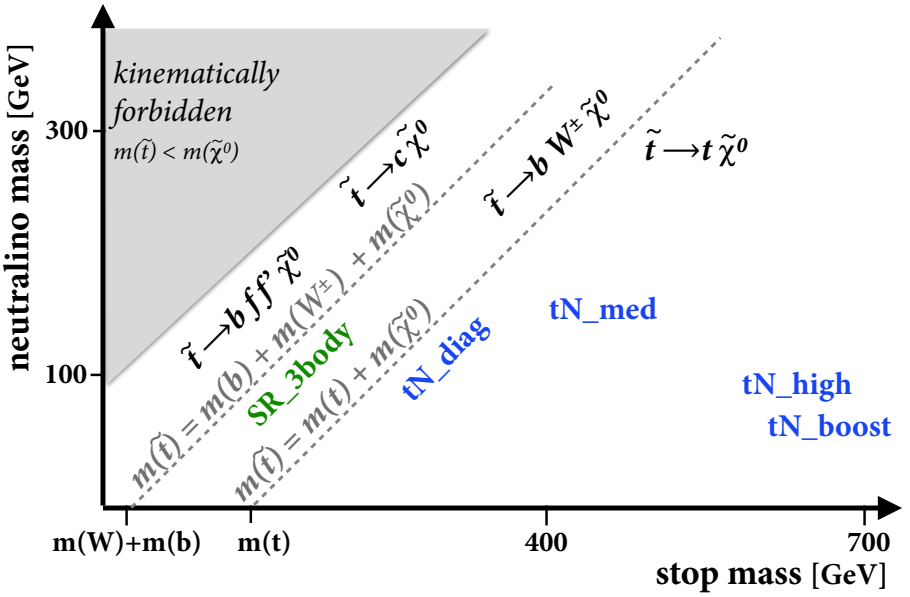

Figure 8.6: *Schematic representation of the grouping scheme of different top squark models according to the top squark and the neutralino mass assumption. A selection was designed for each of these regions*

Region	Scenario	Technique	Table
tN_diag	$\tilde{t} \to t\,\tilde{\chi}^0 m_{\tilde{t}} \gtrsim m_t + m_{\tilde{\chi}_1^0}$	shape fit ($E_{\mathrm{T}}^{\mathrm{miss}}$ vs m_{T})	8.8
tN_med	$\tilde{t} \to t\,\tilde{\chi}^0 m_{\tilde{t}} \sim 550\,\mathrm{GeV}$, $m_{\tilde{\chi}_1^0} \lesssim 225\,\mathrm{GeV}$	*cut-and-count*	8.7
tN_high	$\tilde{t} \to t\,\tilde{\chi}^0 m_{\tilde{t}} \gtrsim 600\,\mathrm{GeV}$	*cut-and-count*	8.7
tN_boost	$\tilde{t} \to t\,\tilde{\chi}^0 m_{\tilde{t}} \gtrsim 600\,\mathrm{GeV}$	*cut-and-count*	Ref. [9]
SR_3body	$\tilde{t} \to b\,W^{\pm}\,\tilde{\chi}^0 m_{\tilde{t}} \lesssim 300\,\mathrm{GeV}$	shape fit (am_{T2} vs m_{T})	8.8
SR_mix	$\mathcal{BR}(\tilde{t} \to t\,\tilde{\chi}^0, \tilde{t} \to b\,\tilde{\chi}^{\pm}) = (50\%,50\%)$	*cut-and-count*	8.7

Table 8.6: *Summary of the signal regions targeting $\tilde{t} \to t\,\tilde{\chi}^0$ and $\tilde{t} \to b\,W^{\pm}\,\tilde{\chi}^0$ and asymmetric decay modes. The scenario that is addressed by each region, the table where the selections are listed and the technique used to extract the results are listed in the last three columns.*

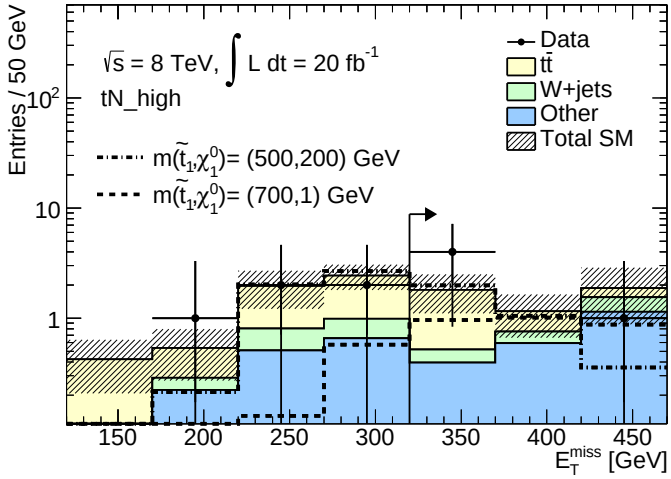

(a) tN_high

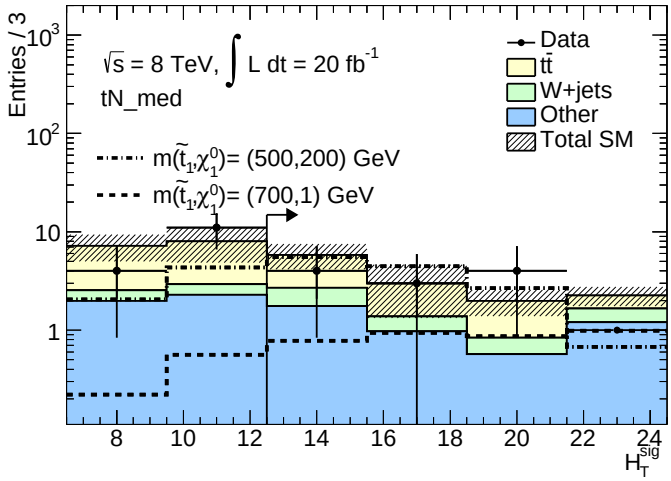

(b) tN_med

Figure 8.7: *Distributions of the most discriminating variables for tN_med and tN_high* cut-and-count *selections. All requirements except the one on the distribution showed are applied, that is indicated by the arrow instead. The background estimate is normalised to the fit results and both statistic and systematic uncertainties are included in the shaded band.*

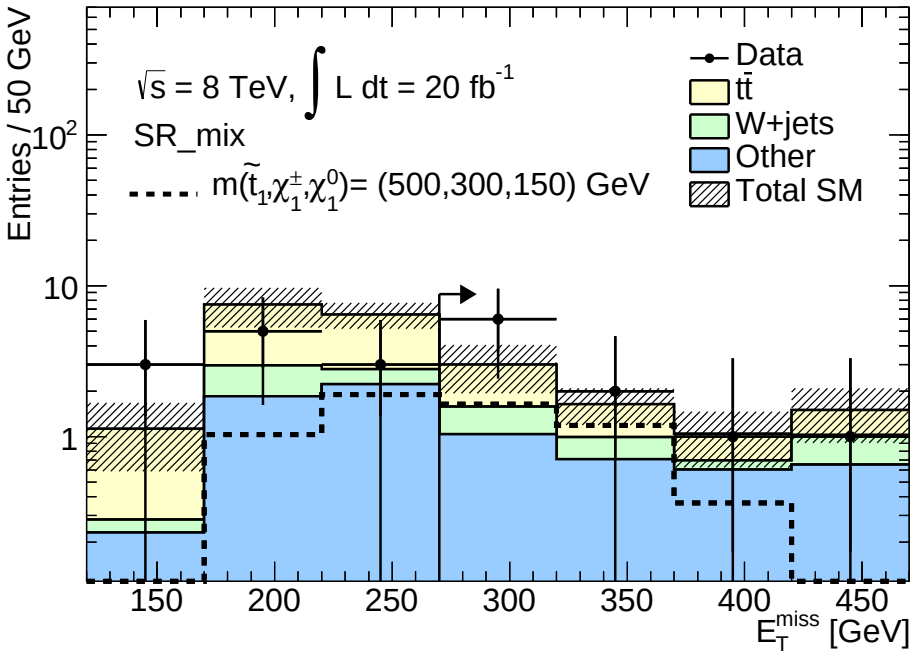

Figure 8.8: *Distributions of the most discriminating variable for SR_mix. All requirements except the one on the distribution showed are applied, that is indicated by the arrow instead. The background estimate is normalised to the fit results and the shaded band includes statistic and systematic uncertainties.*

Requirement	tN_med	tN_high	SR_mix
jet p_{T}s [GeV] >	80-60-40-25	100-80-40-25	80-70-50-25
Number of tight b-jets $\geqslant$	1	1	1
1st b-jet p_{T} [GeV] >	25	25	60
$E_{\mathrm{T}}^{\mathrm{miss}}/\sqrt{H_{\mathrm{T}}}$ [GeV$^{1/2}$] >	-	-	9
$\not{H}_{\mathrm{T}}^{\mathrm{sig}}$ >	12.5	12.5	-
$E_{\mathrm{T}}^{\mathrm{miss}}$ [GeV] >	200	320	270
m_{T} [GeV] >	140	200	130
am_{T2} [GeV] >	170	170	190
m_{T2}^{τ} [GeV] >	-	120	-
$m_{\mathrm{had-top}} \in$	[130,195]	[130,250]	-
topness >	-	-	2
τ-veto	no	no	tight
m_{jjj} <	-	-	360
$\Delta R(j_1, \ell)$ <	-	-	2.75
$\Delta R(b-jet, \ell)$ <	-	3	3
$\lvert\Delta\phi(\mathrm{jet}_i, \vec{p}_{\mathrm{T}}^{\mathrm{miss}})\rvert$ >	0.8 (i=1,2)	-	0.6 (i=1,2)
$\lvert\Delta\phi(\ell, \vec{p}_{\mathrm{T}}^{\mathrm{miss}})\rvert$ >	-	-	0.6

Table 8.7: *Requirement for the* cut-and-count *signal selections tN_med, tN_high and SR_mix. The first two selections target high mass stops decaying into $\tilde{t} \to t\ \tilde{\chi}^0$ mode and the last one selects events where the stop can decay either into $\tilde{t} \to t\ \tilde{\chi}^0$ and $\tilde{t} \to b\ \tilde{\chi}^{\pm}$ with 50% branching ratio.*

8.2.3 Selection for $\tilde{t} \to b\ W^{\pm}\ \tilde{\chi}^0$: SR_3body

The last selection exploiting a shape fit is the one designed for $\tilde{t} \to b\ W^{\pm}\ \tilde{\chi}^0$ decays (SR_3body). Similarly to the $\tilde{t} \to b\ \tilde{\chi}^{\pm}$ signature, it exploits a bidimensional fit in the $(m_{\mathrm{T}}, am_{\mathrm{T2}})$ plane. In this case however, the binning was chosen differently since the three body decay topology is such that am_{T2} peaks around $m_W + m_b$, therefore the lowest am_{T2} bin is the one with the highest signal yield. The selections and the shape fit bins are given in the first column of Table 8.8.

Requirement	SR_3body	tN_diag
$N_{\text{jets}}^{\text{signal}} \geqslant$	4	4
N_{bjets} tight $\geqslant$	1	1
$E_{\text{T}}^{\text{miss}}/\sqrt{H_T}$ [GeV$^{1/2}$] >	5	5
$\Delta\phi(\text{jet}_{1,2}, E_{\text{T}}^{\text{miss}})$ >	0.2	0.8
p_{T} (1st b-jet) [GeV] >	25	25
jet p_{T}s (1st jet) [GeV] >	80-25-25-25	60-60-40-40
$E_{\text{T}}^{\text{miss}}$ [GeV] >	150	fitted
$\mathcal{N}_{\text{trk}}^{\text{iso}} = 0$	no	no
τ-veto	tight	loose
Binned variables		
m_{T} [GeV] $\in$	[60,90,120,∞]	[60,90,120,140,∞]
am_{T2} [GeV] $\in$	[80,90,100,120,∞]	-
$E_{\text{T}}^{\text{miss}}$ [GeV] $\in$	-	[100,125,150,∞]

Table 8.8: *Shape fit selections targeting the compressed scenario of $\tilde{t} \to t\,\tilde{\chi}^0$ (tN_diag) and the stop 3-body decay $\tilde{t} \to b\,W^{\pm}\,\tilde{\chi}^0$ (SR_3body).*

8.3 Data driven estimate of the background normalisation

The Monte Carlo simulation is used for the optimisation of the signal selection and for the estimate of the contamination of all SM background processes. However, the analysis strategy is designed such that the normalisation of the dominant processes is directly derived from data. For this purpose we use selections that are highly enriched in one of the two major backgrounds of the analysis: top pair production and W + jets. There are two background enriched selections (or background control regions) for each *cut-and-count* signal selection overviewed in the previous sections, which provide a robust strategy against mismodelling of the simulation. In the case of the shape fits, the $t\bar{t}$ enriched region is already embedded in the binning strategy described in Section 8.1, where a few bins are background dominated and only an additional W + jets background enriched region is defined.

The normalisation of the two dominant backgrounds is derived from the background enriched regions and extrapolated to the signal region by means of an extrapolation factor (ε):

$$\mathcal{N}_{\mathrm{SR}}^{\mathrm{bkg}} = \varepsilon_1 \, \mathcal{N}_{\mathrm{CR1}}(\mathrm{data}) + \varepsilon_2 \, \mathcal{N}_{\mathrm{CR2}}(\mathrm{data}) \tag{8.4}$$

$$\varepsilon_{\mathrm{i}} = \frac{\mathcal{N}_{\mathrm{SR}}^{\mathrm{bkg1}}(\mathrm{MC})}{\mathcal{N}_{\mathrm{CRi}}(\mathrm{MC})} \tag{8.5}$$

Where *SR* refers to one of the final signal selections, *CR1* (or *TCR*) refers to the top control region and and *CR2* (or *WCR*) to the W + jets enriched region. *MC* refers to the estimate of the event counts as predicted by the Monte Carlo simulation and *data* refers to the event counts measured in the experimental dataset. Equation (8.5) is a simplification of the full likelihood fit described in Sec. 7.3.2 and neglects contaminations of the two main backgrounds in the two control regions. This cross contamination varies between 5% and 30% and is accounted for in the final analysis fit. Equation (8.5) implies that the uncertainty on the background normalisation will directly depend on the uncertainty on the extrapolation factor from the background control region to the signal region. If the control region is carefully designed, the impact of some kinds of uncertainties on this extrapolation factor can be greatly reduced. This is achieved if the selections of the background control region are sufficiently close to the signal selections and the requirement that guarantees the orthogonality between the two does not have a direct dependence on the uncertainty

that we aim to absorb in the extrapolation factor. The control regions allow to absorb a number of systematics that arise from the detector response simulation and also some arising from the event simulation modelling. However, it is important always to guarantee a good statistical constraining power of the control region, such that the estimate of the normalisation is not dominated by statistical uncertainties. This means that the criteria that define the background control regions are a compromise between statistics and reduced impact of the systematics. Particular care is taken to guarantee a negligible contamination ($< 5\%$) of all signal models in these background enriched selections. In summary a good background control region:

(a) contains different events with respect to the signal region;

(b) has good statistical power to estimate the yield of a certain SM background process in the signal selection;

(c) has a low contamination of other SM processes and of signal;

(d) has good absorption power of systematic uncertainties achieved by selections that are as close as possible to the ones of the corresponding signal region.

8.3.1 $t\bar{t}$ enriched selections for the *cut-and-count* regions

A sample enriched in top pair production events was selected for each of the six *cut-and-count* selections. Although only the normalisation of the $t\bar{t}$ background is obtained in these regions, am_{T2} and $E_{\mathrm{T}}^{\mathrm{miss}}$ distributions are shown in Figure 8.9 for bC_high1 and SR_mix in order to visually verify the Monte Carlo modelling of these events. Each of these regions require the same b-jets multiplicity as the signal selection they correspond to. Orthogonality and low signal contamination is guaranteed requiring the transverse mass compatible with the W mass:

$$60 \text{ GeV} < m_{\mathrm{T}} < 90 \text{ GeV} \tag{8.6}$$

In the tight selections a few requirements are relaxed in order to maximise the statistical constraining power of the control region. For bC_high1, bC_high2 and tN_med it was chosen to reduce the requirement on the am_{T2} to 120 GeV. This is justified by the fact that am_{T2} is well modelled by the Monte Carlo simulation. Furthermore all other requirements that could be relaxed such as jets and b-jets transverse momentum and m_{eff} depend on the Jet Energy Scale (JES) and Jet Energy Resolution (JER).

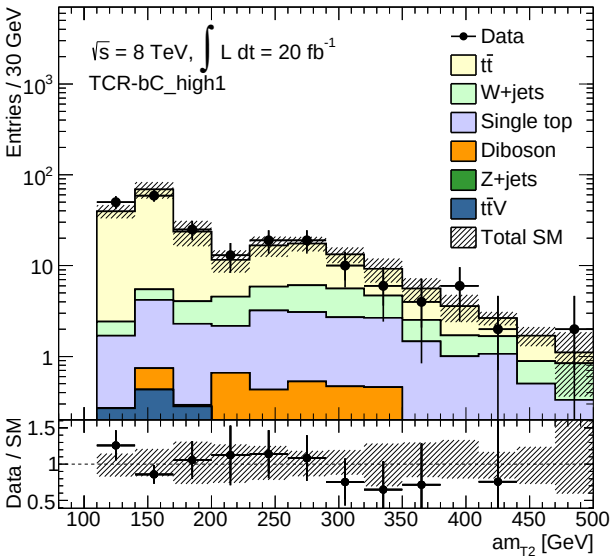

(a) $t\bar{t}$ enriched region for bC_high1

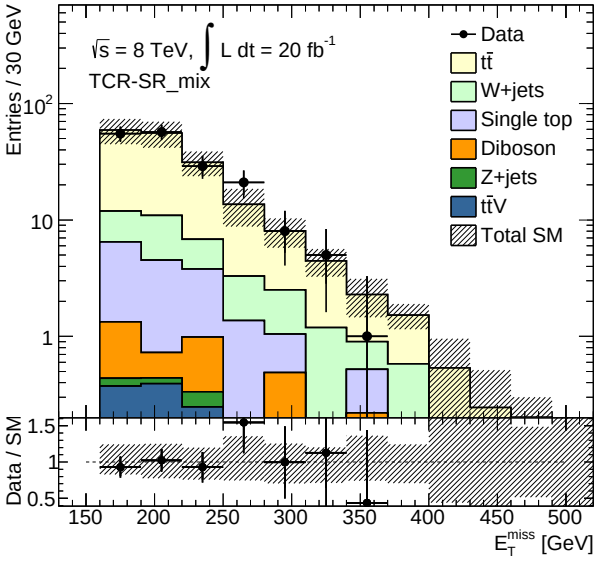

(b) $t\bar{t}$ enriched region for SR_mix

Figure 8.9: *Distributions of $E_{\mathrm{T}}^{\mathrm{miss}}$ and am_{T2} in the for the $t\bar{t}$ enriched selections of bC_high1 and SR_mix. The $t\bar{t}$ and W + jets processes are scaled by the factors resulting from the fit for each region.*

These are the dominant systematic uncertainties in this analysis where a high number of jets is selected in the final state. Maintaining the same requirements on these variables in the background enriched regions was proven to increase the systematic absorption power of the extrapolation factor and reduce the impact of JES and JER in the final result. tN_high was designed to be a very tight selection. For this reason, to guarantee a reasonable $t\bar{t}$ statistics in this background control region, the am_{T2} requirement was completely removed and the following cuts were relaxed: the $E_{\mathrm{T}}^{\mathrm{miss}}$ from 320 GeV to 225 GeV, the $\not{H}_{\mathrm{T}}^{\mathrm{sig}}$ was loosened by 30% and finally the m_{T2}^{τ} requirement was removed. The $t\bar{t}$ control region for asymmetric decays dedicated selection, SR_mix, is characterised by a relaxed am_{T2} requirement (reduced to 120 GeV). In addition, the $E_{\mathrm{T}}^{\mathrm{miss}}$ requirement was reduced from 270 GeV to 170 GeV and the $E_{\mathrm{T}}^{\mathrm{miss}}/\sqrt{H_{\mathrm{T}}}$ was required to be at least $5\,\mathrm{GeV}^{1/2}$ instead of $9\,\mathrm{GeV}^{1/2}$. The relative contributions to the top enriched region of all SM processed and the yield obtained by fitting the control region to the observed data are summarised in Table 8.9. The scale factor of the $t\bar{t}$ process obtained by the fit is also shown.

8.3.2 W + jets enriched selections for the *cut-and-count* regions

The W + jets background yield is derived by selections that are enriched in this SM process. One W + jets enriched region was defined for each signal selection.

The orthogonality with respect to the signal selection is obtained, as in the case of the $t\bar{t}$ background, requiring the transverse mass loosely compatible with the W

Process	bC_diag	bC_high1	bC_high2	tN_med	tN_high	SR_mix
ttbar	74%	75%	71%	69%	76%	74%
W + jets	16%	13%	15%	20%	15%	15%
other bkgs	10%	12%	14%	10%	9%	10%
top squark	< 1%	< 2%	< 2%	< 2%	< 1%	< 2%
observed data	1650	218	129	159	359	177
$t\bar{t}$ scale factor	0.98	0.99	0.83	1.15	1.08	1.11

Table 8.9: *Relative contribution of the different background processes to the $t\bar{t}$ control regions. Yields are normalised to 20 fb^{-1} and uncertainties include both systematics and statistics and are estimated by likelihood fit.*

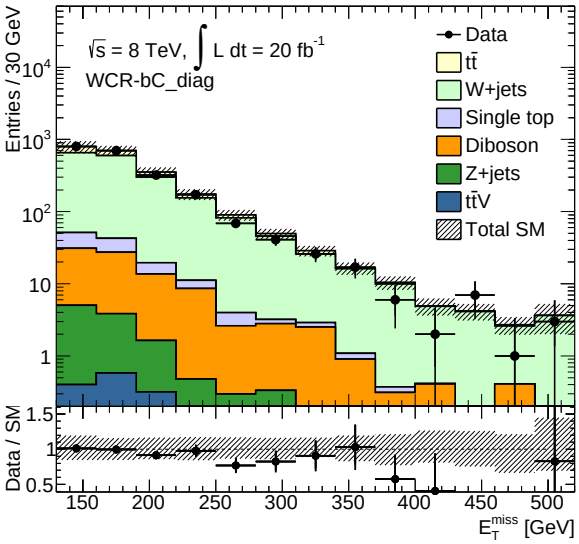

(a) W + jets enriched region for bC_diag

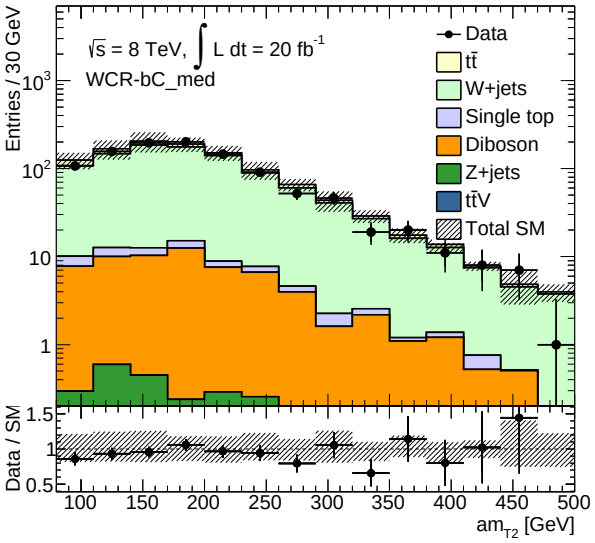

(b) W + jets enriched region for bC_med

Figure 8.10: *Distributions of $E_{\mathrm{T}}^{\mathrm{miss}}$ and am_{T2} for the W +* jets *enriched selections of bC_diag and the shape fit bC_med, for which one of the fitted distribution is shown. The $t\bar{t}$ and W +* jets *processes are scaled by the factors resulting from the fit for each region.*

mass:

$$60\,\text{GeV} < m_{\text{T}} < 90\,\text{GeV} \tag{8.7}$$

In order to have a larger content of W + jets with respect to $t\bar{t}$ a b-jet veto is also imposed. The b-tagging working point of the veto is kept consistent with respect to the signal selection the W + jets control region is dedicated to.

Three selections (bC_high1, bC_high2 and bC_med) are characterised by leading and second leading b-jet p_{T} requirement higher than the one imposed to the untagged jets in the event. Despite all jets being untagged in the W + jets control regions, these requirements on the leading jet transverse momenta are maintained in order to provide a better systematic absorption of the JES systematic for the W + jets process.

A few tight selections (tN_med, tN_high and SR_mix) pursue the strategy of maximising the statistical constraining power of their corresponding W + jets control region and relax the same requirement listed in the previous section for the $t\bar{t}$ enriched region. This strategy was not implemented for bC_diag, bC_high1, bC_high2 and the shape fits, where it was attempted to achieve a higher systematic absorption potential and a lower $t\bar{t}$ contamination relaxing no requirement with respect to the corresponding signal region.

In the case of the loose shape fits selections, tN_diag and bC_bulk, three additional bins are added to the fit plane and three different W + jets normalisation parameters were estimated by the fit, one for each am_{T2} or $E_{\text{T}}^{\text{miss}}$ slice. In the bC_med shape fit only one additional bin was added for the W + jets normalisation estimate and no requirement was applied on asymmetric stransverse mass am_{T2}. Finally for SR_3body the single normalisation parameter for the W + jets background was estimated in four bins in am_{T2}, with the bin requiring $am_{\text{T2}} > 120\,\text{GeV}$ providing the largest constraining power.

A summary of the composition of the W + jets enriched regions for all selections is given in Table 8.10. In the same tables the data yield observed in each control region and the Monte Carlo normalisation scale factors resulting from the likelihood fit are also shown. The signal contamination was always found to be much smaller than 1% due to the combined effect of the b-jet veto and the m_{T} window required in this selections and it therefore not shown in the Table. The modelling of $E_{\text{T}}^{\text{miss}}$ and am_{T2} distributions of W + jets events in the control regions is shown in Figure 8.10.

Process	bC_diag	bC_high1	bC_high2	tN_med	tN_high	SR_mix
W + jets	80%	86%	87%	80%	77%	78%
ttbar	14%	9%	7%	13%	16%	16%
other bkgs	6%	5%	6%	7%	7%	6%
observed data	2162	757	654	161	483	387
W+jets scale fac.	0.93	0.72	0.69	0.59	0.57	0.82

Table 8.10: *Relative contribution of the different background processes to the W + jets control regions. See text for details on the selection requirements. Signal contamination is always smaller than < 1%. Yields are normalised to 20 fb^{-1} and uncertainties include both systematics and statistics and are estimated by likelihood fit.*

8.3.3 Background normalisation in shape fit signal regions

The $t\bar{t}$ control regions are already embedded in the shape fit strategy, since in order to obtain shape discrimination a number of bins are enriched in background and the rest are enriched in signal. As described in Section 7.3.2, Eq. 7.3 the $t\bar{t}$ and W + jets normalisations μ_b^{top} and μ_b^W are nuisance parameters of the likelihood fit. Hence, additional bins are included in the fit to constrain μ_b^W, exploiting the same selection strategy of the *cut-and-count* W + jets control regions: a b-jet veto and m_{T} loosely compatible with the $W^{\pm}$ mass.

Two slightly different approaches were used for the four shape fits. Since tN_diag and bC_bulk are characterised by high expected yields in all bins, it was possible to decorrelate the two background normalisations across $E_{\mathrm{T}}^{\mathrm{miss}}$ and am_{T2}, respectively. Three sets of μ_b^{top} and μ_b^W were used, one for each $E_{\mathrm{T}}^{\mathrm{miss}}$ or am_{T2} slice as in Eq. (7.4). This strategy allows to rely less on the Monte Carlo simulation of one of the variables used in the shape fit. Three bins in each of the shape fits are characterised by high $t\bar{t}$ yield and low signal contamination (Table 8.11). In order to constrain μ_b^W in each of the slices, three b-veto bins were included with the same m_{T} requirement as the $t\bar{t}$ enriched bins (Table 8.12). The observed data and SM expected background yields after the fit in all bins for tN_diag and bC_bulk shape fits are shown in Figure 8.11.

The approach used for tN_diag and bC_bulk increases the impact of statistical uncertainties in the fit while reducing the impact of systematic uncertainties, since the strategy relies less on the modelling of one of the fitting variables.

A different strategy was used for bC_med and SR_3body shape fits. These sig-

tN_diag - 60 GeV < m_{T} < 90 GeV			
Process	$E_{\mathrm{T}}^{\mathrm{miss}} \in [100, 125]$GeV	$E_{\mathrm{T}}^{\mathrm{miss}} \in [125, 150]$GeV	$E_{\mathrm{T}}^{\mathrm{miss}} > 150$GeV
ttbar	88%	87%	82%
W + jets	6%	7%	11%
other bkgs	5%	6%	7%
top squark	$< 0.5\%$	$< 0.5\%$	$< 0.5\%$
$t\bar{t}$ scale factor	1.02	1.01	1.01
bC_bulk - 60 GeV < m_{T} < 90 GeV			
Process	$am_{\mathrm{T2}} < 175$GeV	$am_{\mathrm{T2}} \in [175, 250]$GeV	$am_{\mathrm{T2}} > 250$GeV
ttbar	83%	60%	48%
W + jets	10%	28%	36%
other bkgs	7%	12%	16%
top squark	$< 2\%$	$< 5\%$	$< 2\%$
$t\bar{t}$ scale factor	1.00	0.78	0.75

Table 8.11: *Relative contribution of the different background processes in the $t\bar{t}$ enriched bins of the shape fits. for tN_diag and bC_bulk. Three background enriched bins per shape fit are considered. Yields are normalised to 20 fb^{-1} and uncertainties include both systematics and statistics and are estimated by likelihood fit.*

tN_diag - b-veto and 60 GeV < m_{T} < 90 GeV			
Process	$E_{\mathrm{T}}^{\mathrm{miss}} \in [100, 125]$GeV	$E_{\mathrm{T}}^{\mathrm{miss}} \in [125, 150]$GeV	$E_{\mathrm{T}}^{\mathrm{miss}} > 150$GeV
W + jets	61%	64%	70%
ttbar	33%	30%	24%
other bkgs	6%	6%	6%
W+jets scale fac.	0.78	0.75	0.72
bC_bulk - b-veto and 60 GeV < m_{T} < 90 GeV			
Process	$am_{\mathrm{T2}} < 175$ GeV	$am_{\mathrm{T2}} \in [175, 250]$ GeV	$am_{\mathrm{T2}} > 250$ GeV
W + jets	80%	87%	88%
ttbar	15%	8%	6%
other bkgs	5%	5%	6%
W+jets scale fac.	0.74	0.81	0.74

Table 8.12: *Relative contribution of the different background processes in the bins of the bC_bulk and tN_diag shape fits with b-veto requirement. Yields are normalised to 20 fb^{-1} and uncertainties include both systematics and statistics and are estimated by likelihood fit.*

bC_med and SR3body - 60 GeV < m_{T} < 90 GeV		
Process	bC_med $am_{\mathrm{T2}} < 175$ GeV	SR_3body $am_{\mathrm{T2}} > 120$ GeV
ttbar	92%	74%
W + jets	2%	18%
other bkgs	6%	7%
top squark	< 1%	< 1%
$t\bar{t}$ scale factor	1.02	1.06
bC_med and SR_3body - b-veto and 60 GeV < m_{T} < 90 GeV		
Process	bC_med	SR_3body $am_{\mathrm{T2}} > 120$ GeV
ttbar	7%	11%
W + jets	87%	83%
other bkgs	6%	6%
W + jets scale factor	0.77	1.11

Table 8.13: *Relative contribution of the different background processes in the background enriched bins of the shape fits bC_med and SR_3body. $t\bar{t}$ enriched bins are shown at the top and W+jets enriched bins at the bottom. Yields are normalised to 20 fb^{-1} and uncertainties include both systematics and statistics and are estimated by likelihood fit.*

nal regions are characterised by lower event yield per bin with respect to the other shape fits and therefore the statistical component of the uncertainty dominates with respect to the systematic one. For this reason, these two shape fits have been fitted with only one nuisance parameter per background normalisation as shown in Eq. (7.3). In this setup each background normalisation is fully correlated across all bins of the fit. The $t\bar{t}$ background enriched bin is the one that requires $60\,\text{GeV} < m_{\text{T}} < 90\,\text{GeV}$ and $am_{\text{T2}} < 175\,\text{GeV}$ or $am_{\text{T2}} > 120\,\text{GeV}$ for bC_med and SR_3body shape fits, respectively (Table 8.11). To understand these requirements it is important to remember that due to the different phenomenology of the stop three body decay, the bin with the highest signal yield is the one with $am_{\text{T2}} < 90\,\text{GeV}$ and $m_{\text{T}} > 120\,\text{GeV}$ (see Fig. 7.8(a) in Ch. 7.4).

The W+jets normalisation parameter is constrained simultaneously in four bins with b-veto requirements for SR_3body. Due to the fact that one of the bins is characterised by a much higher yield with respect to the others, this will not result in over constrain. Conversely, in bC_med only one bin with no am_{T2} requirement is defined, in order to avoid the risk of over constraining the W + jets normalisation and to reduce the impact of statistical uncertainties with higher bin yield. The composition of the highest statistic W + jets enriched bins for bC_med and SR_3body are shown in Table 8.13.

The background estimates after fit and data are compared for all bins in Figure 8.12. All background processes are considered in the comparison and yields are normalised to 20 fb^{-1}.

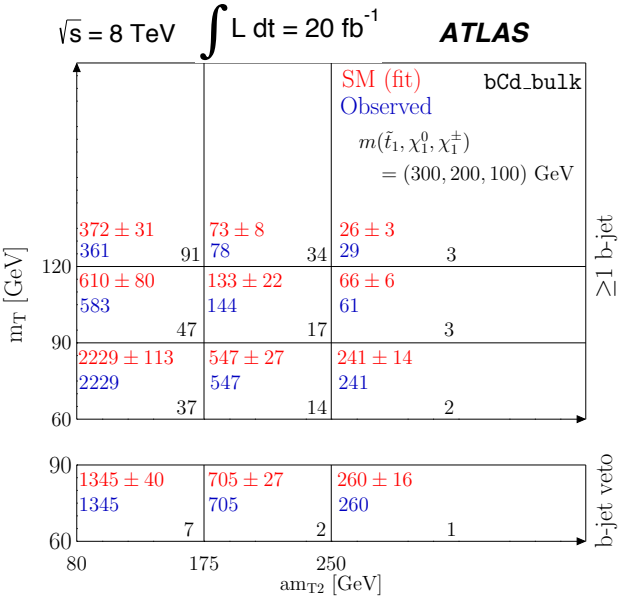

(a) bC_bulk

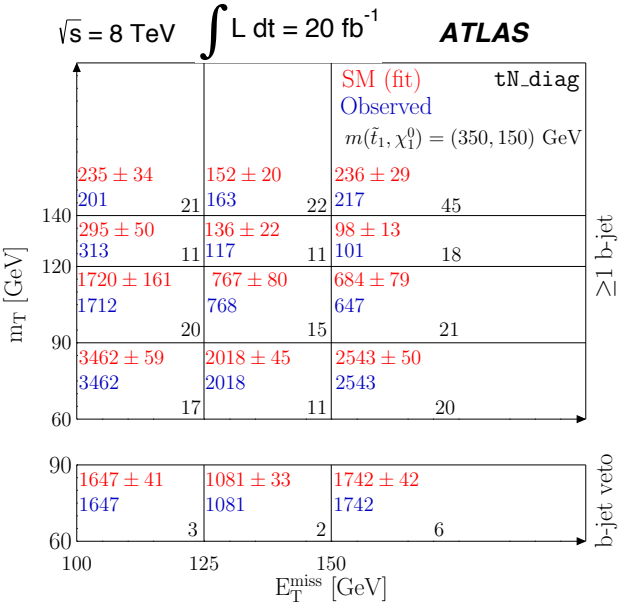

(b) tN_diag

Figure 8.11: *Schematic illustration of the bC_bulk and tN_diag shape fits binning. The m_{T} and am_{T2} (top) or $E_{\mathrm{T}}^{\mathrm{miss}}$ (bottom) variables are used to define a matrix of 3 × 3 bins (top) or 4 × 3 bins (bottom) in the top part of the scheme. Some of these bins are enriched in $t\bar{t}$ and constrain three sets of normalisation parameters for this background (one for each $E_{\mathrm{T}}^{\mathrm{miss}}$ or am_{T2} slice); the bins at the bottom of the scheme invert the b-jet requirement into a veto, and serve to constrain the three W + jets normalisations parameters. Yields are normalised to 20 fb^{-1} and both statistic and systematic uncertainties are included.*

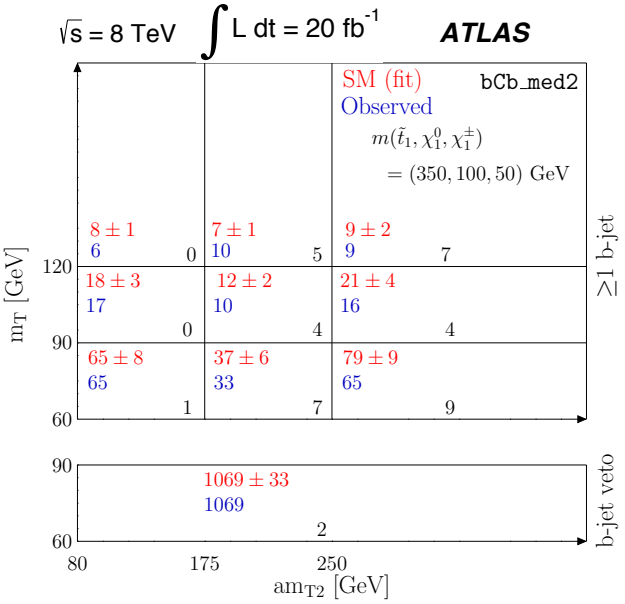

(a) bC_med

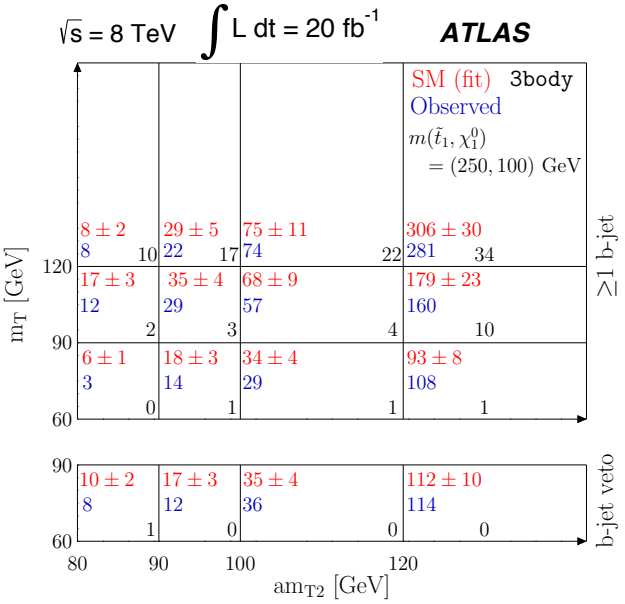

(b) SR_3body

Figure 8.12: *Schematic illustration of the bC_med and SR_3body shape fits binning. The m_{T} and am_{T2} variables are used to define a matrix of 3 × 3 bins (top) or 4 × 4 bins (bottom) in the top part of the scheme. Some of these bins are enriched in $t\bar{t}$ and constrain the normalisation of this background; the bins at the bottom of the scheme invert the b-jet requirement into a veto, and serve to normalise the W + jets background. One nuisance parameter per background is used in these selections. Yields are normalised to 20 fb^{-1} and both statistic and systematic uncertainties are included.*

8.4 Validation of the background estimate

As introduced in Section 7.3.2, the normalisation of the two major background processes of this analysis are estimated by a likelihood fit to the data (Eq. 7.3) and constrained in two regions enriched in each of the two backgrounds. These estimates are based on a number of assumptions, such as the possibility of relying on the Monte Carlo modelling of the quantities we extrapolate on (m_{T} and b-jets multiplicity). In the next sections we will first validate the m_{T} extrapolation assumption for both the top and the W+jets backgrounds testing the compatibility of the background normalisation in the control and in the validation regions. The m_{T} extrapolation also implies that we derive the normalisation of dileptonically decaying tops produced in association with two extra jets (required to fulfil our four jets requirement) from semileptonic $t\bar{t}$ decays. The modelling of initial and final state radiation for dileptonic $t\bar{t}$ decays is therefore investigated in Section 8.4.2. The W+jets events in the dedicated background enriched region are mostly W events produced in association with light flavour jets. Conversely in our signal selection this background is represented by 60% of Ws produced in association with heavy flavour jets. The reliability of the flavour extrapolation is studied in Section 8.4.3.

8.4.1 Validation of the extrapolation factors

The extrapolation of the normalisation factor from events characterised by $60\,\mathrm{GeV} < m_{\mathrm{T}} < 90\,\mathrm{GeV}$ to events characterised by high transverse mass ($> 120/140\,\mathrm{GeV}$) is verified by means of additional validation selections that require:

$$90\,\mathrm{GeV} < m_{\mathrm{T}} < 120\,\mathrm{GeV} \tag{8.8}$$

These selections are defined for both the $t\bar{t}$ background (Top-VR), requiring the same selections as for the top pair enriched regions (including the relaxed requirements) and for the W + jets enriched regions (W-VR), requiring the same b-veto and requirements of the selections of this background. For each of the signal selections, the normalisation of these two major backgrounds have been estimated in the two control regions. The background scale factors estimated by the fit have then been applied to the number of Monte Carlo expected events in the validation regions and compared to the observed events. For the top background estimate of some selections, an additional validation region was designed to validate normalisation in the tail of the m_{T} distribution ($m_{\mathrm{T}} > 120\,\mathrm{GeV}$). In this case, the stransverse mass require-

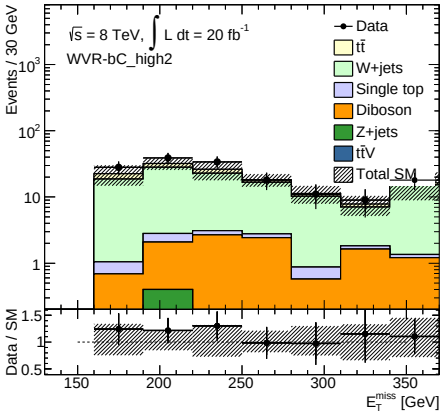

(a) W + jets validation region for bC_high2

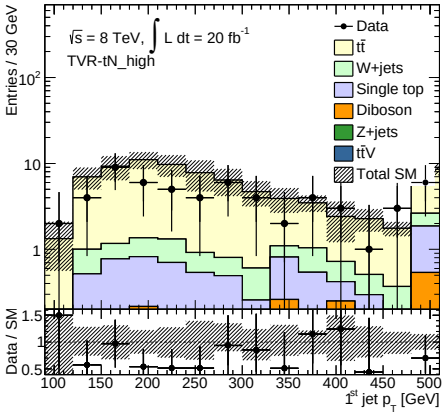

(b) $t\bar{t}$ validation region for tN_high ($90 < m_{\mathrm{T}} < 120$ GeV)

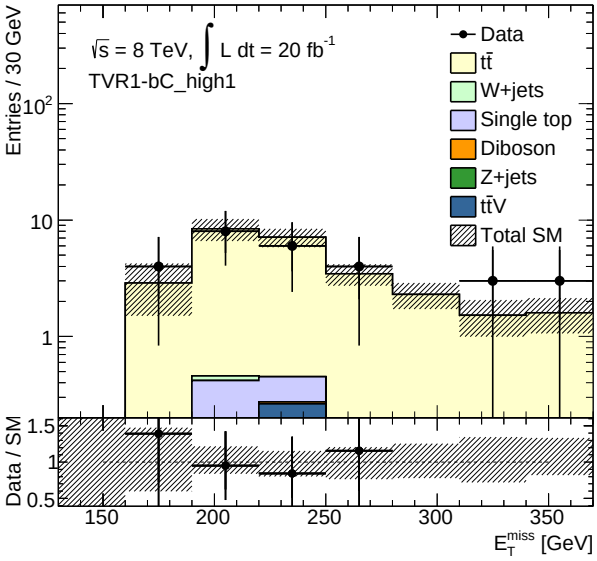

(c) $t\bar{t}$ validation region for bC_high1 ($am_{\mathrm{T2}} < 175$ GeV)

Figure 8.13: *Validation of the Monte Carlo modelling of $t\bar{t}$ and W +* jets *backgrounds. The $t\bar{t}$ and W +* jets *processes are scaled by the factors resulting from the fit for each region.*

	bC_diag	bC_high1	bC_high2	tN_med	tN_high	SR_mix
Top-VR (fit)	865 ± 117	51 ± 13	32.3 ± 6.5	26.7 ± 6.7	79 ± 18	3.3 ± 1.3
Top-VR (data)	925	42	28	16	59	3
Top1-VR (fit)	-	27.3 ± 4.8	12.4 ± 2.5	-	-	-
Top1-VR (data)	-	28	16	-	-	-
W-VR (fit)	722 ± 162	147 ± 36	135 ± 29	24 ± 8	84 ± 24	123 ± 32
W-VR (data)	693	166	157	25	74	117

Table 8.14: *Comparison of the data driven prediction of the major SM backgrounds and the observed experimental yields in dedicated selections.*

ment was inverted in order to guarantee the orthogonality with the signal selections and a low signal contamination:

$$am_{\mathrm{T2}} < 175\,\mathrm{GeV} \tag{8.9}$$

These validation selections will be referred as Top1-VRs. The results of the comparisons show a good agreement between the observed number of events and the prediction in each of the validation regions and are summarised in Table 8.14. The $E_{\mathrm{T}}^{\mathrm{miss}}$ and leading jet p_{T} of one distribution for each type of validation region is shown in Figure 8.13. The $t\bar{t}$ and W + jets distributions in these regions have been derived in the control region and it is possible to observe a good agreement of the predicted yields with the data and the Monte Carlo modelling of the $E_{\mathrm{T}}^{\mathrm{miss}}$ distribution.

8.4.2 Validation of the dileptonic $t\bar{t}$ extra jets radiation

The validity of the background model, and especially $t\bar{t}$ production in the dileptonic channel, is tested in events with exactly two leptons. The following event selection criteria are applied:

- exactly two signal leptons in the combinations ee, $e\mu$ and $\mu\mu$
- the lepton pair is required to be of opposite charge
- $m_{\ell\ell} > 101$ GeV to suppress Z+jets contributions
- at least two jets with $p_T > 25$ GeV and at least one loose b-jet.

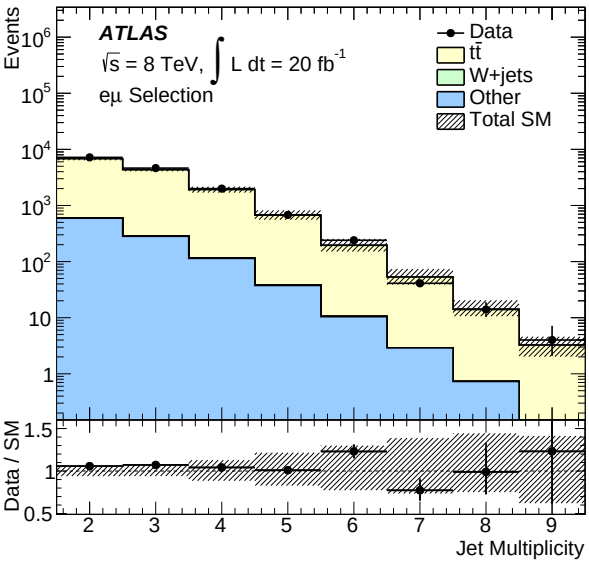

Figure 8.14: *Comparison of the jet multiplicity of dileptonic decaying $t\bar{t}$ events in data and in the Monte Carlo simulation. The shaded bands include only the systematic uncertainties.*

As mentioned before, one of the motivations for these selections is to verify the Monte Carlo modelling of dileptonic $t\bar{t}$ events with extra radiated jets. Therefore one of the most interesting distribution is the jet multiplicity in Figure 8.14, where a good modelling of the number of extra jets produced in association with the top pair is proven.

8.4.3 Validation of the W + jets flavour composition

The b-veto used in the $W^{\pm}$ control region selects events with W plus light flavour jets associate production (~ 60%) with a smaller fraction of W produced in association with charm jets (~ 30%). Conversely in our signal selection this background is represented by 60-80% of W bosons produced in association with heavy flavour jets and the remaining fraction of events are W bosons produced in association with light flavour jets that are incorrectly tagged as b-jets (*mistagged*).

For this reason, a validation region was made for events with W plus heavy flavour jets associate production, in order to verify the accuracy of the normalisation extrapolation from a light flavour dominated control region to a heavy flavour dominated signal region.

A large number of variables have been investigated to define such a validation

region. This is characterised by with reasonable statistics, a dominant contribution of W+b/c events and a reduced contamination of both signal and $t\bar{t}$ and is discussed in detail in Ref. [146]. In general, a high purity of W+b/c events was always achieved at the cost of low number of events. The optimal event selection found in this study is characterised by a relative fraction of $t\bar{t}$, W plus light flavour jets and W plus heavy flavour jets of 34%, 20% and 35% respectively. It relies on an exclusive 3 jets selection (that allows a reasonable $t\bar{t}$ suppression), with transverse momenta of at least 80, 60 and 40 GeV, respectively and at least one loose b-tagged jet. The selection exploits the invariant mass and ΔR between the two jets that are identified by the b-tagging algorithm as the most probable to be b-jets ($m_{bb} < 80$ GeV, $\Delta R_{bb} < 2.5$). These variables are useful because of the correlation that exists between the two extra jets produced in association with the W, a characteristic that is not present in $t\bar{t}$ events. The additional requirements were chosen to enhance the similarity of the kinematic of the selected events with respect to the final selections of this analysis without compromising the statistical power or the background composition of this validation region. Therefore, it was required $E_{\mathrm{T}}^{\mathrm{miss}} > 150$ GeV, $E_{\mathrm{T}}^{\mathrm{miss}}/\sqrt{H_{\mathrm{T}}} > 5$ and $|\Delta\phi(\mathrm{jet}_{1,2}, E_{\mathrm{T}}^{\mathrm{miss}})| > 0.8$ rad. Finally, the transverse mass was required to be between 60 and 90 GeV as in the W + jets enriched selection.

The W + jets contribution is scaled to the W + jets scale factor of the bC_diag signal region, $\mu_W = 0.93$, which is characterised by the same jet multiplicity as this validation region. An expected yield of 171 ± 4 (stat.) ± 20 (syst.) events is obtained, that is well compatible with the observed number of data events of 166. Figure 8.15 proves a good simulation modelling of this background for $E_{\mathrm{T}}^{\mathrm{miss}}$ and the p_{T} of the leptonically decaying W.

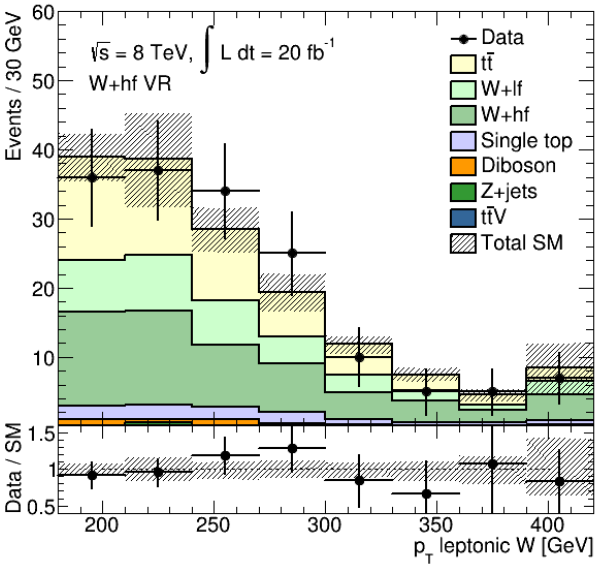

(a) leptonic W p_{T}

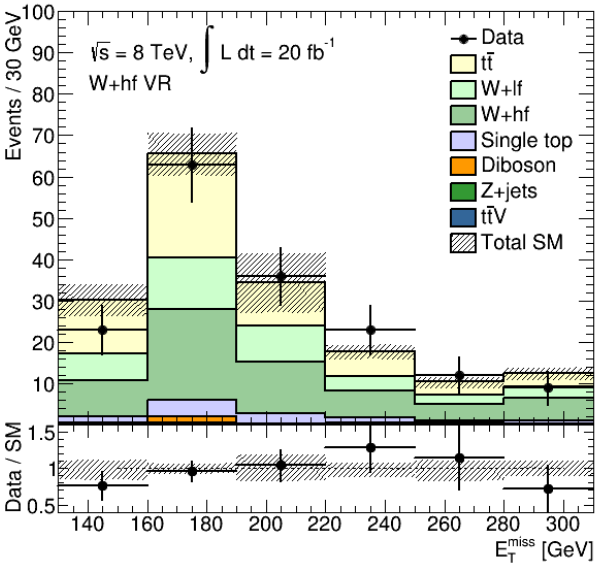

(b) $E_{\mathrm{T}}^{\mathrm{miss}}$

Figure 8.15: *W plus heavy flavour validation region. The W + jets contribution is scaled to $\mu_W = 0.93$. The yellow band includes systematic and statistical uncertainties.*

9 Results and interpretations

The results of the top squark search are extracted by means of a hypothesis test based on a simultaneous likelihood fit of the control and signal regions or the bins of the shape fits as introduced in the previous chapter. Possible sources of systematic uncertainties have been investigated, evaluated and assigned as nuisance parameters in the fit with gaussian constraints. The data yields observed in each signal region are compatible with the SM-only hypothesis, hence the results are interpreted in terms of upper limits on the three top squark decay modes and as limits on the WIMP-nucleon scattering cross section for two hypothesis of contact operators in the context of dark matter Effective Field Theory.

9.1 Discovery test

The results of the top squark search are extracted by means of a hypothesis test based on a simultaneous likelihood fit of the control and signal regions or the bins of the shape fits as described in Ch. 7, Sec. 7.3.2. The systematic uncertainties treated as nuisance parameters in the likelihood fit are described in Section 9.2.2. The first hypothesis test that is performed on the experimental data is the validity of the SM-only hypothesis, also defined as discovery test.

Table 9.1 shows the data yield observed in the six *cut-and-count* and four shape-fit signal regions, the expected number of background events and the p_0 values obtained by the SM-only hypothesis test. In case of the shape fits, the p_0 values are

evaluated separately for each of the most significant bins. Each bin is therefore treated as a separate *cut-and-count* region for the discovery test. The p_0 values are set to 0.5 whenever the number of observed events are below the number of expected events. All p_0 values are $\gtrsim 10\%$, which indicates that the data in all signal regions are compatible with the background-only hypothesis.

Finally, the rightmost columns of Table 9.1 show the upper limits on the number of beyond-the-SM events ($N_{\text{non-SM}}$) and the visible non-SM signal cross section derived from the observation, $\sigma_{\text{vis}} = \sigma_{\text{prod}} \times A \times \epsilon$, where A is the acceptance and ϵ is the reconstruction efficiency. The numbers give the observed and expected 95% CL upper limits for a generic model for which experimental uncertainties are not considered.

Region		Obs.	Exp. bkg.	p_0	$N_{\text{non-SM}}$		σ_{vis} [fb]	
					Obs.	Exp.	Obs.	Exp.
tN_med		12	13 ± 2	≥ 0.5	8.5	9.2	0.4	0.5
tN_high		5	5.0 ± 0.9	≥ 0.5	6.0	6.0	0.3	0.3
bC_diag		493	472 ± 44	0.27	110.6	95.1	5.4	4.7
bC_high1		16	11 ± 1	0.09	13.2	8.5	0.7	0.4
bC_high2		5	4.4 ± 0.7	0.36	6.3	5.7	0.3	0.3
SR_mix		10	7 ± 1	0.13	9.7	7.0	0.5	0.3
tN_diag								
$125 < E_{\text{T}}^{\text{miss}} < 150$ GeV,	$120 < m_{\text{T}} < 140$ GeV	117	136 ± 22	≥ 0.5	42.1	55.7	2.1	2.7
$125 < E_{\text{T}}^{\text{miss}} < 150$ GeV,	$m_{\text{T}} > 140$ GeV	163	152 ± 20	0.35	55.4	47.8	2.7	2.4
$E_{\text{T}}^{\text{miss}} > 150$ GeV,	$120 < m_{\text{T}} < 140$ GeV	101	98 ± 13	0.43	36.1	33.9	1.8	1.7
$E_{\text{T}}^{\text{miss}} > 150$ GeV,	$m_{\text{T}} > 140$ GeV	217	236 ± 29	≥ 0.5	58.7	71.4	2.9	3.5
bC_med								
$175 < am_{\text{T2}} < 250$ GeV,	$90 < m_{\text{T}} < 120$ GeV	10	12 ± 2	≥ 0.5	7.3	8.8	0.4	0.4
$175 < am_{\text{T2}} < 250$ GeV,	$m_{\text{T}} > 120$ GeV	10	7 ± 1	0.10	9.7	7.3	0.5	0.4
$am_{\text{T2}} > 250$ GeV,	$90 < m_{\text{T}} < 120$ GeV	16	21 ± 4	≥ 0.5	9.3	12.3	0.5	0.6
$am_{\text{T2}} > 250$ GeV,	$m_{\text{T}} > 120$ GeV	9	9 ± 2	≥ 0.5	7.7	7.8	0.4	0.4
bC_bulk								
$175 < am_{\text{T2}} < 250$ GeV,	$90 < m_{\text{T}} < 120$ GeV	144	133 ± 22	0.29	36.1	33.9	1.8	1.7
$175 < am_{\text{T2}} < 250$ GeV,	$m_{\text{T}} > 120$ GeV	78	73 ± 8	0.34	58.7	71.4	2.9	3.5
$am_{\text{T2}} > 250$ GeV,	$90 < m_{\text{T}} < 120$ GeV	61	66 ± 6	≥ 0.5	17.5	20.9	0.9	1.0
$am_{\text{T2}} > 250$ GeV,	$m_{\text{T}} > 120$ GeV	29	26 ± 3	0.34	14.8	12.6	0.7	0.6
SR_3body								
$100 < am_{\text{T2}} < 120$ GeV,	$90 < m_{\text{T}} < 120$ GeV	57	68 ± 9	≥ 0.5	7.3	9.9	0.4	0.5
$100 < am_{\text{T2}} < 120$ GeV,	$m_{\text{T}} > 120$ GeV	74	75 ± 11	≥ 0.5	7.9	7.8	0.4	0.4
$am_{\text{T2}} > 120$ GeV,	$90 < m_{\text{T}} < 120$ GeV	160	179 ± 23	≥ 0.5	11.7	14.7	0.6	0.7
$am_{\text{T2}} > 120$ GeV,	$m_{\text{T}} > 120$ GeV	281	306 ± 30	≥ 0.5	55.4	47.8	2.7	2.4

Table 9.1: *Summary of the discovery test results. The first three columns show the data yield observed in the six* cut-and-count *and four shape-fit signal regions, the expected number of background events and the p_0 values of the SM-only hypothesis. The p_0 values of the shape fits are evaluated separately for each of the most significant bins. The last two columns show the upper limits on the number of beyond-the-SM events ($N_{\text{non-SM}}$) and the visible non-SM signal cross section ($\sigma_{\text{vis}} = \sigma_{\text{prod}} \times A \times \epsilon$) derived from the observation. The numbers give the observed and expected 95% CL upper limits for a generic model for which experimental uncertainties are not included.*

9.2 Exclusion limits of top squark production

As no excess in the number of observed events has been found, the results of each signal selection can be interpreted in terms of upper limits for the top squark signal models described in Ch. 1.3.3.

9.2.1 Limits for $\tilde{t} \to b\,\tilde{\chi}^{\pm}$

The first *simplified model* that is considered is:

$$\tilde{t} \to b\,\tilde{\chi}^{\pm} \to b\,W^{\pm}\,\tilde{\chi}^{0}$$

For this decay mode, the acceptance and efficiency for signal models assuming gaugino universality ($m_{\tilde{\chi}^{\pm}} = 2m_{\tilde{\chi}^{0}}$) are shown in Figures 9.1 and 9.2 for bC_high1 *cut-and-count* signal region and one of the most sensitive bins of bC_bulk shape fit. The acceptance is defined as the fraction of signal events which pass the analysis selection performed on generator-level objects, therefore emulating an ideal detector with perfect particle identification and no measurement resolution effects. The efficiency is defined as the ratio between the expected signal rate calculated with simulated data passing all the reconstruction level cuts applied to reconstructed objects, and the signal rate for an ideal detector, yet considering the detector acceptance. The details of the generator-level objects are given in Ref. [115] and acceptance and efficiency plots for the other signal regions can be found in Ref. [9].

The exclusion limits at 95% CL are shown in Figures 9.3, 9.4, 9.5 and 9.6 for each of the chargino mass assumptions presented in Ch. 1.3.3, in the $(m_{\tilde{t}}, m_{\tilde{\chi}^{0}})$ mass plane. In each figure, the red dark line represents the exclusion contour observed in data and the black dashed line indicates the expected exclusion. The yellow band shows the variation of the expected exclusion limit if the signal and background yields are varied, according to their statistical and systematic uncertainties, by $\pm 1\sigma$. All uncertainties, overviewed in the next section, except for the cross section uncertainty on signal are included in the band as well as in the estimate of the observed contour. The dark red dashed line indicates the observed limit varying the signal cross section by $\pm 1\sigma$, where σ is the cross section theoretical uncertainty.

The first figure (Fig. 9.3) spans the $(m_{\tilde{t}}, m_{\tilde{\chi}^{0}})$ parameter space assuming gaugino universality, i.e. $m_{\tilde{\chi}^{\pm}} = 2m_{\tilde{\chi}^{0}}$. Signal models inside the red curve have been excluded at 95% CL. All signal selections presented in this analysis have been combined to obtain this exclusion. The combination was obtained using for the upper limit calculation the result of the signal selection with the best expected limit

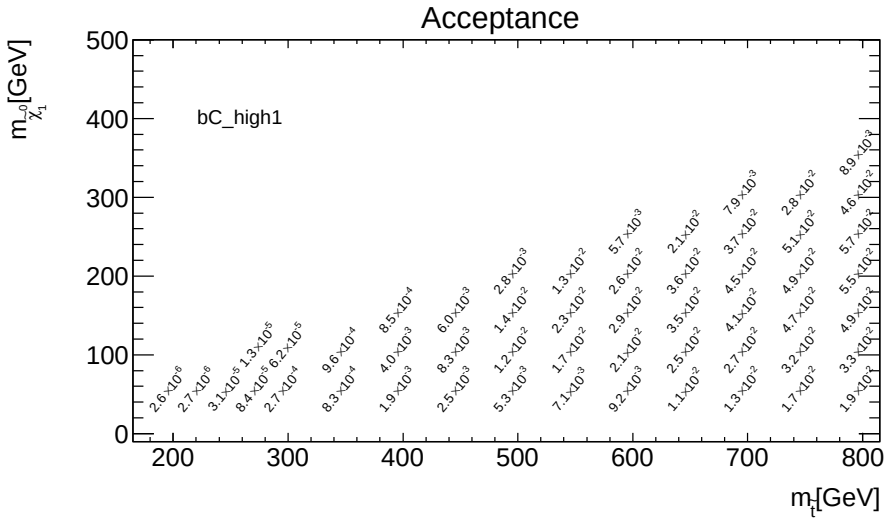

(a) Acceptance of bC_high1

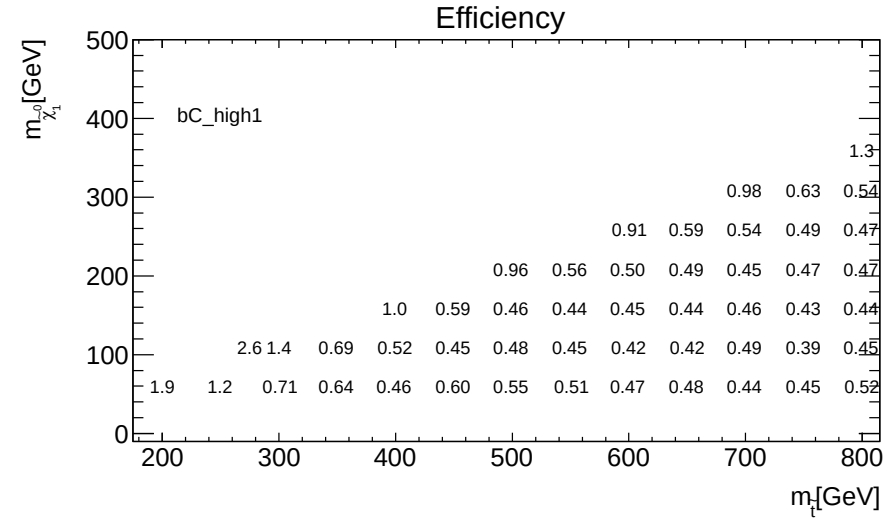

(b) Efficiency of bC_high1

Figure 9.1: *Acceptance and efficiency for $\tilde{t} \to b\,\tilde{\chi}^{\pm}$ signal models, assuming $m_{\tilde{\chi}^{\pm}} = 2m_{\tilde{\chi}^0}$ for the signal selection bC_high1.*

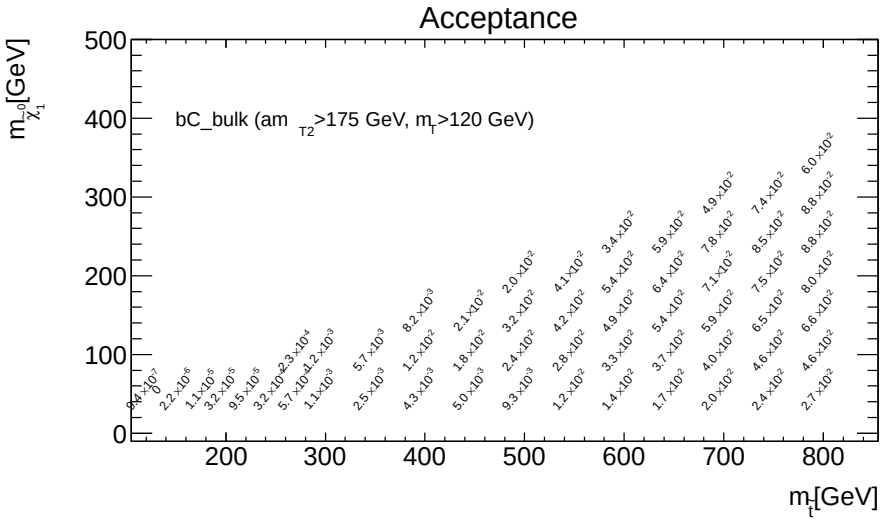

(a) Acceptance of bC_bulk ($am_{\mathrm{T2}} > 250$ GeV, $m_{\mathrm{T}} > 120$ GeV)

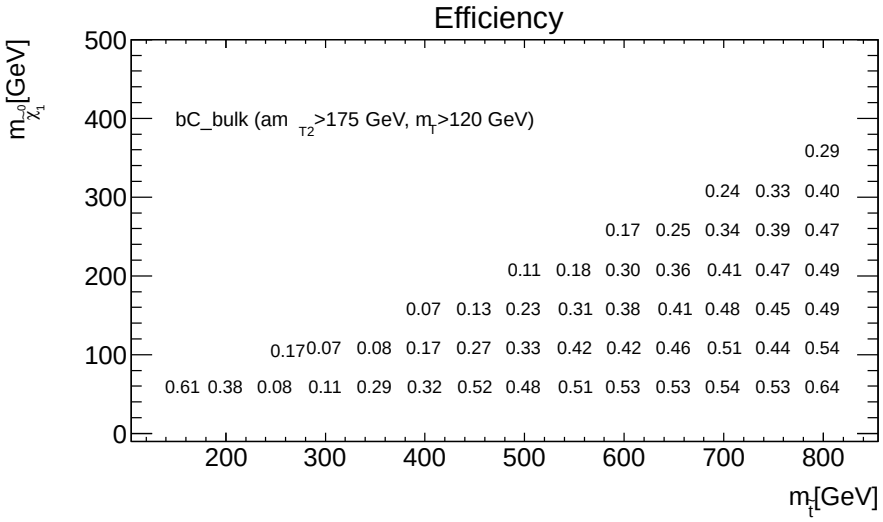

(b) Efficiency of bC_bulk ($am_{\mathrm{T2}} > 250$ GeV, $m_{\mathrm{T}} > 120$ GeV)

Figure 9.2: *Acceptance and efficiency for $\tilde{t} \to b\,\tilde{\chi}^{\pm}$ signal models, assuming $m_{\tilde{\chi}^{\pm}} = 2m_{\tilde{\chi}^{0}}$ for one of the most sensitive bins of bC_bulk shape fit.*

(a) Mapping used in Figures 9.3, 9.6 and 9.5.

Region	Code
bC_bulk	1
bC_diag	2
bC_med	3
bC_high1	4
bC_high2	5

(b) Mapping used in Figure 9.11.

Region	Code
tN_diag	1
tN_med	2
tN_boost	3
SR_3body	4
tN_high	5

Table 9.2: *Mapping of the signal region names and the code used in the exclusion plots. The Figures for which the code is valid are indicated in the sub-caption.*

for each $(m_{\tilde{t}}, m_{\tilde{\chi}^0})$ point. The signal region used for each point is also indicated in the plot, following the mapping shown in Table 9.1(a). The shape fits bC_bulk and bC_med outperform the *cut-and-count* selections bC_high1 and bC_high2. Stop masses up to 500 GeV are excluded in this model, above which the cross section for stop pair production becomes too small for the ATLAS dataset. It is not possible to exclude a small region of the parameter space for $m_{\tilde{t}} \sim m_t$ and $m_{\tilde{\chi}^0} < 70$ GeV. This is due to the large similarity of these events with top pair production. Figure 9.4 shows the excluded $(m_{\tilde{t}}, m_{\tilde{\chi}^0})$ parameter space in the *mass degeneracy* scenario, where $m_{\tilde{t}} - m_{\tilde{\chi}^\pm} = 10$ GeV is assumed. bC_diag is the only region contributing to the sensitivity in this scenario.

If a stop mass of 300 GeV is assumed, a large fraction of $(m_{\tilde{\chi}^\pm}, m_{\tilde{\chi}^0})$ parameter space is well excluded by the analysis as shown in Figure 9.5. The best performing signal regions are indicated also in this case in the plot and follow the mapping in Table 9.1(a). Figure 9.6 shows the excluded models in the $(m_{\tilde{t}}, m_{\tilde{\chi}^0})$ mass plane for a fixed chargino mass. Signal models assuming $m_{\tilde{\chi}^\pm} = 106$ GeV (Fig. 9.6(a)) are characterised by a challenging signature and the systematic uncertainties on the background have a large impact on the results. However, it is important to take into account that the signal selections presented in this analysis were explicitly optimised for signal models assuming gaugino universality (Fig. 9.3) and lower sensitivity is expected in different scenarios. Also in this case, the most challenging parameter range is $m_{\tilde{t}} \sim m_t$ and, in addition, the case of a nearly-massless neutralino. Finally, models with a fixed chargino mass of 150 GeV proved to be well covered by the

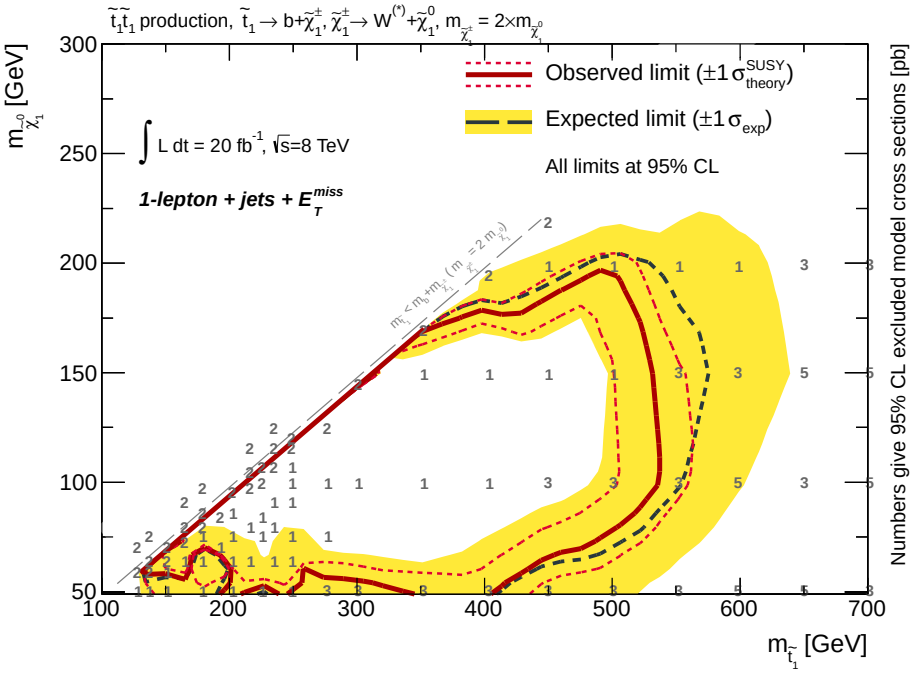

Figure 9.3: *Exclusion limits at* 95% CL *in the* $(m_{\tilde{t}}, m_{\tilde{\chi}^0})$ *mass plane. Signal models inside the dark red contour are excluded and* $m_{\tilde{\chi}^{\pm}} = 2m_{\tilde{\chi}^0}$ *is assumed. The numbers indicate the most sensitive signal region for each point. Mapping is given in Table 9.1(a).*

analysis selections, due to the fact that more of these signal models have similar kinematics to the ones assuming gaugino universality. The excluded models are shown in Figure 9.6(b). Upper limits on the model cross section for each of the top squark signal models discussed so far have been derived and are presented in Appendix A. All results obtained on this decay mode of the top squark can be compared to other searches in ATLAS that exploit two leptons [115] or no leptons [147] in the final state. These results are summarised in Figures 9.7 and 9.8. There is a large complementarity of the parameter space coverage between the various final states. Figure 9.7(a) shows that two leptons final states allow a good sensitivity for compressed top squark signal models up to 450 GeV but have no sensitivity in most of the phase space of this analysis. Similarly the two lepton and no lepton final states have complementary sensitivity among each others and with respect to this analysis for the fixed stop mass parameter space in Figure 9.7(b) and the two

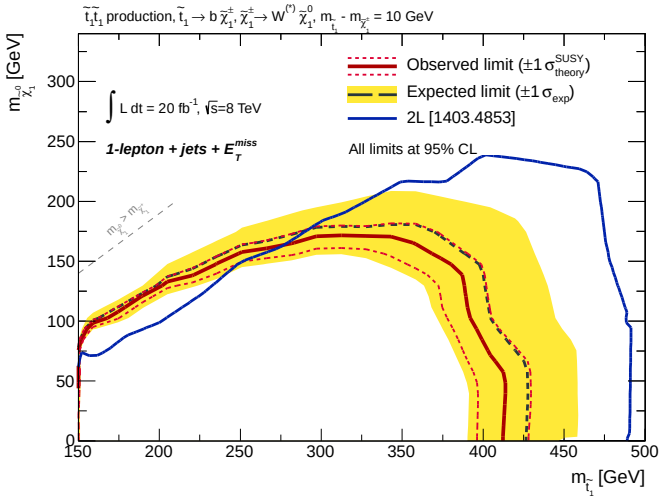

Figure 9.4: *Exclusion limits at* 95% CL *in the* $(m_{\tilde{t}}, m_{\tilde{\chi}^0})$ *mass plane for the scenario in which the stop and the chargino have similar masses* ($m_{\tilde{t}} - m_{\tilde{\chi}^{\pm}} = 10$ GeV). *bC_diag is the only selection contributing to the sensitivity in this scenario. Results are compared with the two leptons final state exclusion limit [115].*

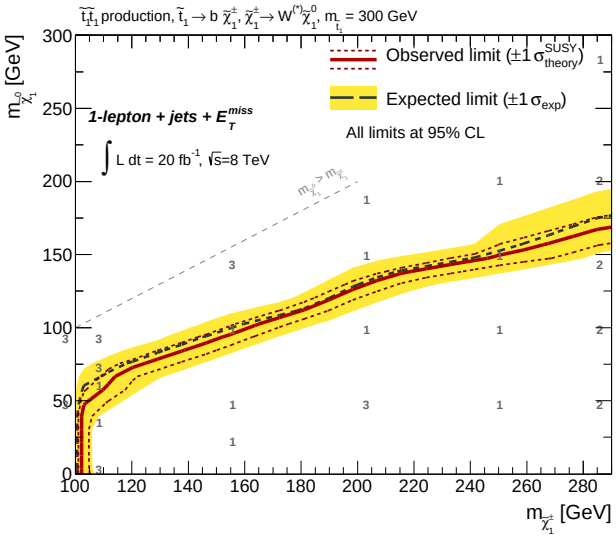

Figure 9.5: *Exclusion limits at* 95% CL *in the* $(m_{\tilde{\chi}^{\pm}}, m_{\tilde{\chi}^0})$ *mass plane. The stop mass is assumed to be* 300 GeV. *Models below the curve are excluded. The numbers indicate the most sensitive signal region for each point. Mapping is given in Table 9.1(a).*

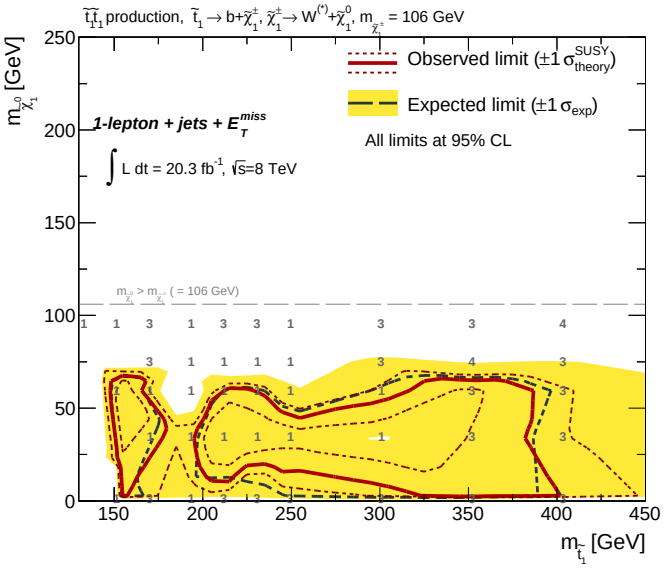

(a) $m_{\tilde{\chi}^{\pm}} = 106$ GeV. Models inside the curve are excluded.

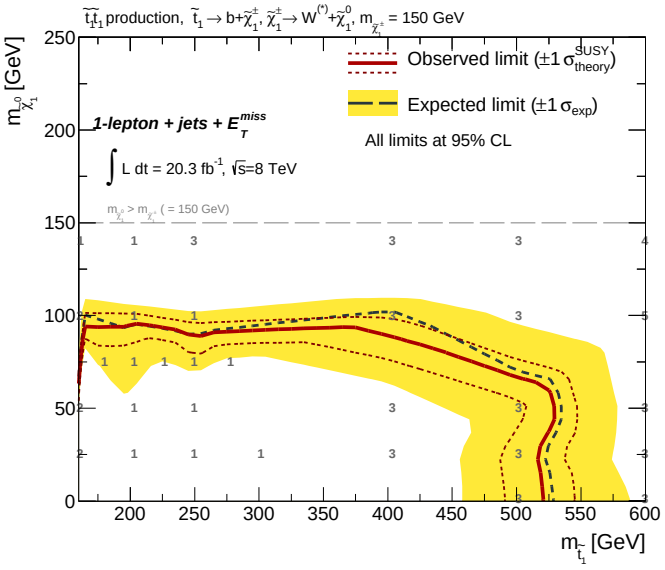

(b) $m_{\tilde{\chi}^{\pm}} = 150$ GeV. Models below the curve are excluded.

Figure 9.6: *Exclusion limits at* 95% CL *in the* $(m_{\tilde{t}}, m_{\tilde{\chi}^0})$ *mass plane. A fixed chargino mass (indicated under each plot) is assumed. The numbers indicate the signal region that is the most sensitive for each point. Mapping between code and signal region is given in Table 9.1(a).*

fixed chargino mass parameter spaces shown in Figures 9.8(a) and 9.8(b). Especially in the case of $m_{\tilde{\chi}^{\pm}} = 150$ GeV the combination of the three analysis is sensitive to and can exclude a large portion of the parameter space.

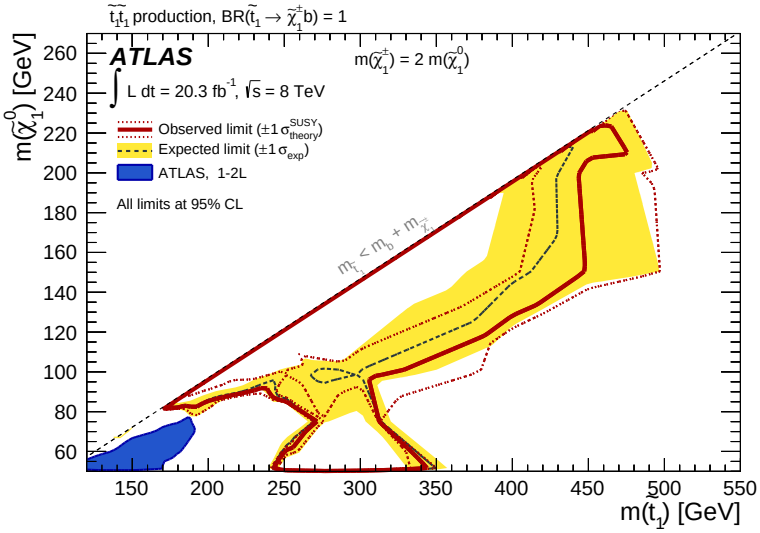

(a) Two leptons final state at 7 (blue area) and 8 TeV (red curve) [115]. Models inside the curves and are excluded.

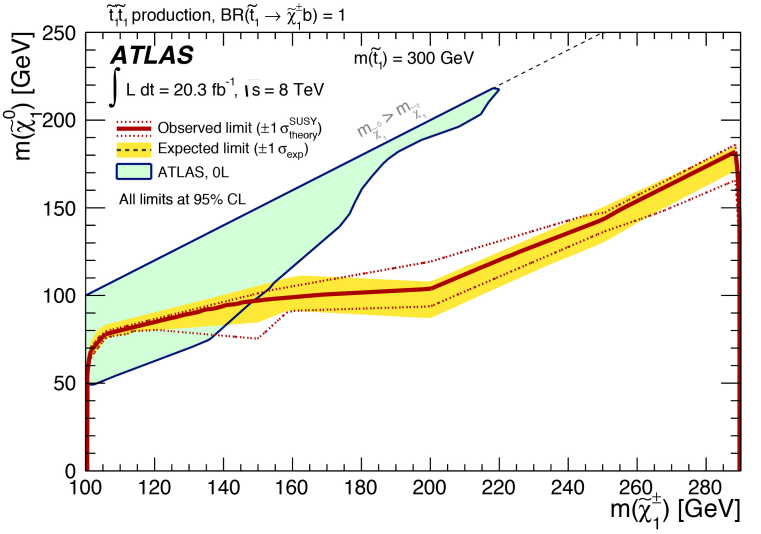

(b) Two [115] leptons (dark red curve) and no leptons and two b-jets [147] (solid azure area). Signal models below the red curves and inside the azure area are excluded.

Figure 9.7: *Exclusion results from ATLAS top squark searches in hadronic and two leptons final states. These searches provide a complementary coverage of parameter space with respect to the results of this analysis. a) is compared to Fig. 9.3, b) is compared to Fig. 9.5.*

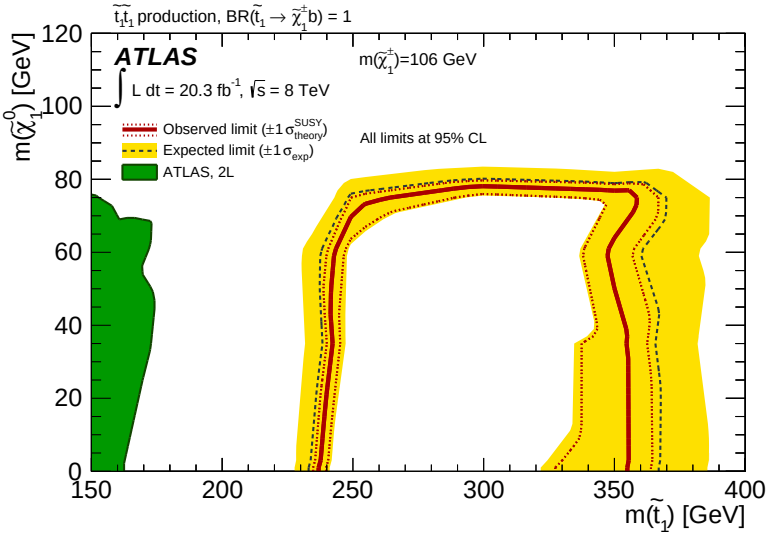

(a) Two leptons final state at 7 (green area) and 8 TeV (red curve) [115]. Models below the curve and inside the dark green area are excluded.

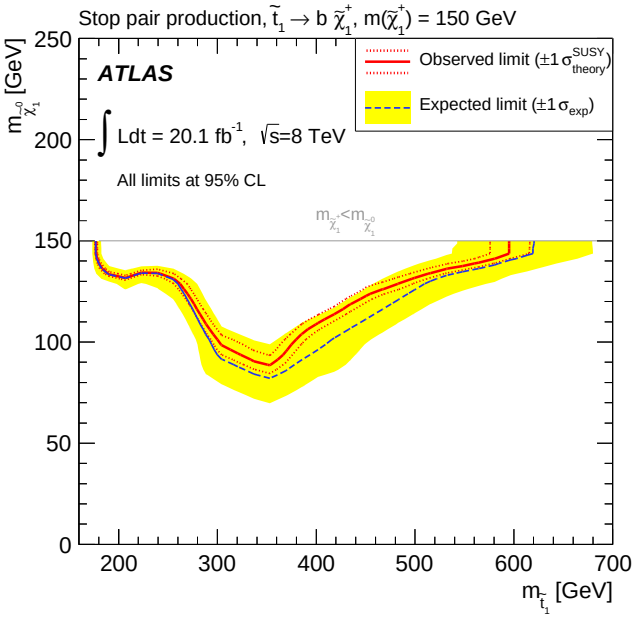

(b) Hadronic final state [147]. Models above the curve are excluded.

Figure 9.8: *Exclusion results from ATLAS top squark searches in hadronic and two leptons final states. 8 TeV analysis are always considered as an improvement to 7 TeV ones. These searches provide a complementary coverage of parameter space with respect to the results of this analysis. a) is compared to Fig. 9.6(a) and b) is compared to Figure 9.6(b).*

9.2.2 Systematic uncertainties of the analysis

For each of the objects that are identified and reconstructed by the ATLAS detector an uncertainty is assigned. These uncertainties are estimated by dedicated calibrations for electrons, muons, jets, b-jets and $E_{\mathrm{T}}^{\mathrm{miss}}$, and have been introduced in Chapter 3. The uncertainties considered in the analysis are described in the following.

a) **Jet Energy Scale and Resolution (JES and JER)** is the dominant uncertainty in this analysis due to the high jet multiplicity requirement of the selections.

b) **B-tagging scale factors** uncertainties are evaluated by propagating in the analysis the systematic uncertainty of the b-tagging calibrations shown in Figure 3.6, Chapter 3.2.2. They are separated into the uncertainty related to the b-jets identification efficiency, the c-jets one and the mistag rate. Also in this case, they represent one of the dominant systematic uncertainty, especially in the selections requiring at least two energetic b-jets.

c) **Multiple interaction and integrated luminosity:** the uncertainty on the pile-up model is evaluated by changing the average number of interactions per bunch crossing in the Monte Carlo simulation by $\pm 10\%$. An uncertainty of 2.8% on the integrated luminosity collected by ATLAS is assigned [83].

d) $E_{\mathrm{T}}^{\mathrm{miss}}$ **Scale and Resolution:** the energy scale calibration and the resolution of the $E_{\mathrm{T}}^{\mathrm{miss}}$ is also varied according to the ATLAS calibration uncertainties. Particularly important in this case is the uncertainty associated to the *soft* term of the $E_{\mathrm{T}}^{\mathrm{miss}}$ calculation, that is the term estimated from topological calorimeter clusters which are not included in any reconstructed object.

e) **Lepton reconstruction:** the uncertainties on the triggering, reconstruction and identification of leptons as well as uncertainties on their momentum scale and resolution have been investigated and found to have a subdominant contribution with respect to the rest of the uncertainties of this analysis.

f) **Tau-veto uncertainties:** the requirement on the BDT used to identify τ leptons described in Sec 7.4.4 is varied by $\pm 10\%$. It corresponds to approximately 3% of uncertainty on the background estimate and it is negligible for signal.

The size of each of the uncertainties just described is used as the width of the gaussian constraint imposed in the likelihood fit to each nuisance parameters used

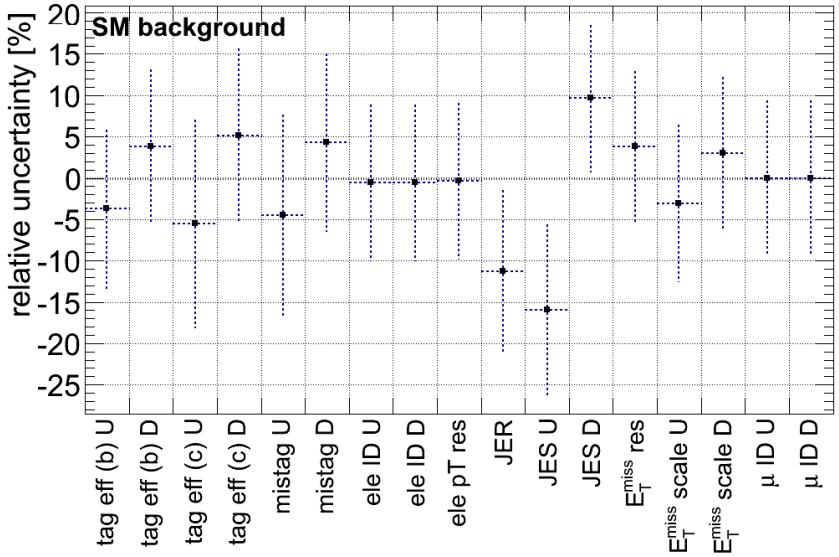

(a) SM background

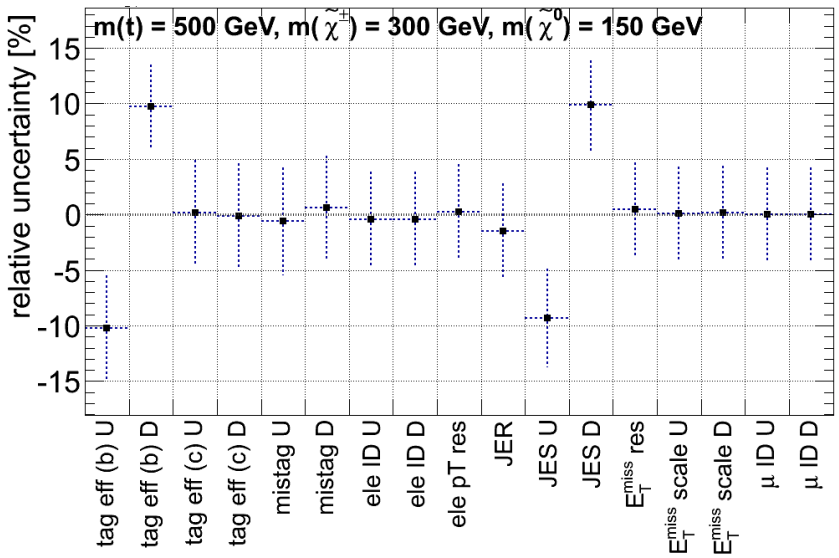

(b) top squark signal

Figure 9.9: *Size of the major detector systematic uncertainties assigned to bC_high2 for the SM background and a benchmark signal model. The error associated to each point represents the statistical uncertainty associated to the systematic uncertainty estimate. U and D in the x-axis label indicate the up and down variation with respect to the nominal yield.*

Uncertainty	$t\bar{t}$ [%]	W+jets [%]	t [%]	$t\bar{t}$+V [%]	dibosons [%]	Z+jets [%]
cross section	N.A.	N.A.	6.8	22	7	50
had. $\oplus$ ISR/FSR	6-20	1-8	5	18	9	-
fac. $\oplus$ ren. scales	< 2	4-20	1-13	< 2	23	-
PDF	< 3	< 3	< 5	< 5	< 6	-
W+heavy flavour	-	28	-	-	-	-
t-$t\bar{t}$ interference	-	-	30	-	-	-

Table 9.3: *Summary of the magnitude of the theoretical systematic uncertainties on all background processes. Ranges indicate the maximum and the minimum size across the signal regions and the shape fit bins. See text for details on evaluation of the different systematics.*

to model each uncertainty. It is shown in Figure 9.9 in terms of percentage variation of the nominal yields of signal and background for a representative signal selection. In the figure, the error associated to each point represent the statistical uncertainty associated to the systematic uncertainty estimate. U and D in the x-axis label indicate the up and down variation with respect to the nominal yield. The first six bins represent the b-tagging uncertainties, then the major uncertainties due to electrons identification and momentum resolution, the jets and $E_{\mathrm{T}}^{\mathrm{miss}}$ related uncertainties and finally the major muon uncertainties are indicated. It is possible to notice that the dominant systematic on the background estimate is due to the JES and JER uncertainties, due to the high jet multiplicity requirement of the analysis. For signal instead, the impact of JES and the impact of b-tagging efficiency have both the same contribution to the systematic uncertainty. This is due to the fact that top squark decays are characterised by more energetic b-jets that the SM background. The calibrations of b-tagging algorithms have access to a limited ensemble of such energetic b-jets and therefore their calibration is estimated with a larger uncertainty.

For each of the SM processes considered in this analysis a number of uncertainties on the simulation have been considered:

a) **Uncertainties on the theoretical cross section calculation** for each SM process are imposed and their values are summarised in Table 9.3. Since the $t\bar{t}$ and W + jets normalisations are already treated as free parameters in the likelihood fit, no additional uncertainty is applied for these processes.

b) **Uncertainty on the hadronisation and showering model:** PYTHIA was com-

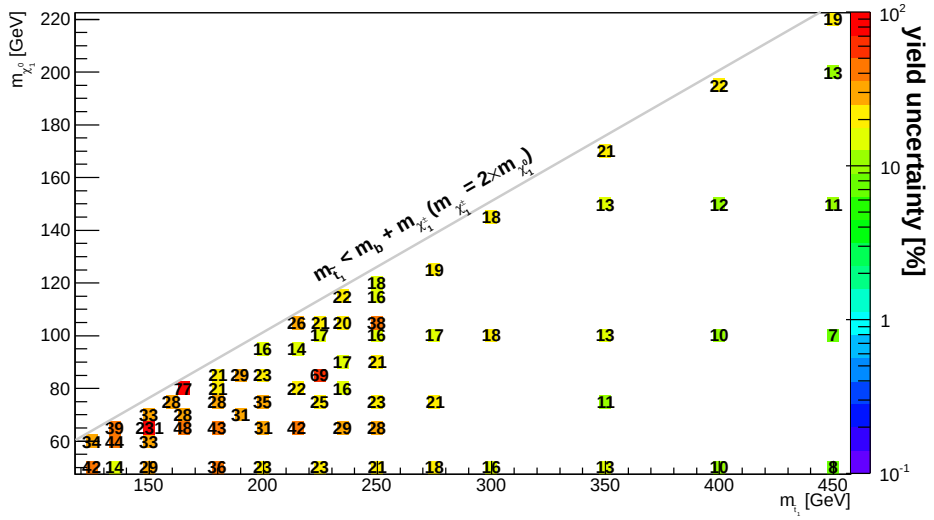

(a) bC_bulk

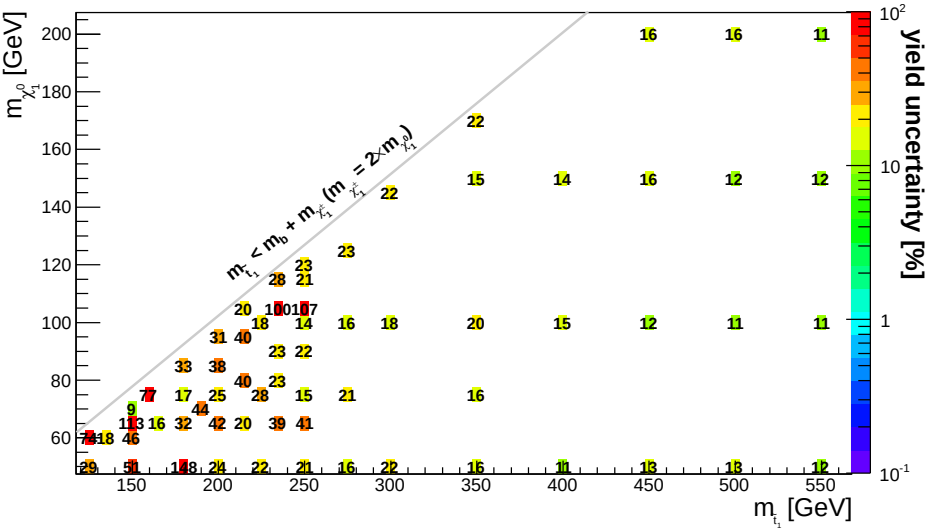

(b) bC_med

Figure 9.10: *Total systematic uncertainty on signal models that assume gaugino universality for the two shape fits. The two highest m_{T} and am_{T2} bins are summed together.*

pared to HERWIG for $t\bar{t}$, $t\bar{t}$+V and single top Monte Carlo samples. For the samples generated and showered with SHERPA, W + jets and dibosons, the scale of the CKKW scheme [148] used to match the NLO matrix element to the parton showering was varied.

c) **Uncertainties on initial (ISR) and final state radiation (FSR)** were evaluated for all processes with dedicated samples generated with an additional amount of ISR/FSR. The highest impact of this uncertainty is observed in bC_diag for $t\bar{t}$ background, due to the fact that these events might rely on extra radiation jets to fulfil the jet multiplicity requirements when no b-jets are found in the final state.

d) **The factorisation and renormalisation scales**[1)] are varied from their nominal value in order to assess these uncertainties. For single top this approach was not possible and the nominal generators (POWHEG and AcerMC) were compared with MC@NLO.

e) **Uncertainties on the PDF** used for the simulation are assessed using the LHC prescription [150] which conservatively compares different results obtained from CTEQ 6.6, MSTW 2008 and NNPDF 2.0 PDF sets.

f) Additional uncertainties were considered for the **heavy flavour component of the** W+jets **background and the single top interference at NLO** with $t\bar{t}$. The former consist of 28% additional uncertainty on the $W^{\pm}$ plus heavy flavour jets component of the W + jets background, due to the fact that the W + jets normalisation is constrained in a region that is dominated by $W^{\pm}$ plus light flavour jets.

The latter regards the NLO Wt-channel single top production, that receives a contribution from LO $t\bar{t}$ production. The calculation of these interference diagrams is meaningless in perturbation theory and the diagrams are therefore removed from the NLO matrix element generation of Wt-channel single top production [151], according to the Diagram Removal (DR) scheme. The uncertainty on this correction procedure is obtained comparing the default removal scheme to an alternative one, Diagram Subtraction (DS), based on a subtrac-

[1)] The factorisation scale μ_F is the scale at which Monte Carlo generators separate (factorize) long-distance from short-distance behaviour in a systematic fashion and perform separate calculations of these different stages (Ref. [149]).

Uncertainty	bC_diag [%]	bC_high1 [%]	bC_high2 [%]
Total	11	33	51
Statistical	4.4	30	48
Systematic	10	12	17
JES	1	1.5	1
JER	5	3	3
$E_{\mathrm{T}}^{\mathrm{miss}}$	2	3	5
b-tagging	5	7	7.5
$t\bar{t}$ model	5	3	2
W + jets model	2	2	2
other bkgs. model	3	7	7

Table 9.4: *Impact of uncertainties on the background estimate, expressed in percentage of the background expected yield, after the likelihood fit for three* cut-and-count *signal regions targeting $\tilde{t} \to b\ \tilde{\chi}^{\pm}$ decay modes. The uncertainty components are obtained from the difference in quadrature between the total uncertainty of the nominal fit and a fit where the systematic in question is disabled by fixing the corresponding nuisance parameter to the nominal value. Individual uncertainties can be correlated and do not necessarily add up quadratically to the total uncertainty.*

tion of the contribution of the interference diagrams. The final uncertainty for this analysis is estimated to be 30%.

The theoretical uncertainties have been estimated for each signal selection and shape fit bin. In Table 9.3 a summary of the magnitude of each uncertainty is given for each of the SM backgrounds. As in the case of the experimental uncertainties, these numbers are assigned as the width of the gaussian constrain of the nuisance parameters of the likelihood fit describing the theoretical uncertainties.

Table 9.4 shows the impact of uncertainties on the background estimate, after the likelihood fit for three *cut-and-count* signal regions targeting $\tilde{t} \to b\ \tilde{\chi}^{\pm}$ decay modes. The uncertainty components are obtained from the difference in quadrature between the total uncertainty of the nominal fit and a fit where the systematic in question is disabled by fixing the corresponding nuisance parameter to the nominal value. Similar uncertainties are also found for each bin of the shape fits.

The uncertainty on the nominal signal cross sections is taken from an envelope of cross section predictions using different PDF sets and factorisation and renor-

malisation scales, as described in Ref. [67]. In the observed exclusion results, this uncertainty is varied separately with respect to the other signal and background uncertainties and indicated in the exclusion plots by a red dashed line.

ISR/FSR uncertainty has also a considerable impact on the signal theoretical uncertainties. It is about 20% for signal models in the compressed scenario for signal regions that select events with high ISR/FSR activity such as bC_diag. It has a negligible impact for all other selections and signal models. The sum of all experimental and theoretical uncertainties (excluded statistical ones) are given in Figure 9.10 for all signal models that assume gaugino universality and for the two shape fits bC_bulk and bC_med. The uncertainties are expressed in percentage of the total signal yield and the two highest m_{T} and am_{T2} bins are summed together.

All the systematic uncertainties discussed in this section also apply to the other interpretations and signal models discussed below.

9.2.3 Exclusion limits for $\tilde{t} \to t\ \tilde{\chi}^0$, $\tilde{t} \to b\ W^{\pm}\ \tilde{\chi}^0$ and asymmetric decay modes

The exclusion limits at 95% CL for the *simplified models*

$\tilde{t} \to t\ \tilde{\chi}^0$

$\tilde{t} \to b\ W^{\pm}\ \tilde{\chi}^0$

are shown in Figure 9.11 and upper limits on the signal cross section are presented in Appendix A. Top squark masses up to 650 GeV are excluded, for different neutralino mass assumptions. The results combine all regions presented in this analysis. As in the case of the previous top squark decay mode, the combination was obtained using the best expected limit for each $(m_{\tilde{t}}, m_{\tilde{\chi}^0})$ point. The signal region used for each point is indicated in the plot, following the mapping shown in Table 9.1(b). As discussed in Section 7.3 an additional selection, tN_boost, that exploits specific techniques to reconstruct highly boosted stops [9] is also included in this result. This particular selection increases the sensitivity of the analysis for stop masses between 600 and 700 GeV, outperforming tN_high. tN_med is the selection with the highest sensitivity for the bulk of the parameter space and tN_diag has the highest sensitivity for $m_{\tilde{t}} - m_{\tilde{\chi}^0} < 250$ GeV. The upper limits on the signal cross section for models where the $\tilde{t}_1$ is a pure $\tilde{t}_L$ and models where it is predominantly a $\tilde{t}_R$ are compared in Figure 9.12. The predominantly $\tilde{t}_R$ mixing composition is the default setting used for all $\tilde{t} \to t\ \tilde{\chi}^0$ scenarios. The weaker $\tilde{t}_L$ model exclusion is mainly due

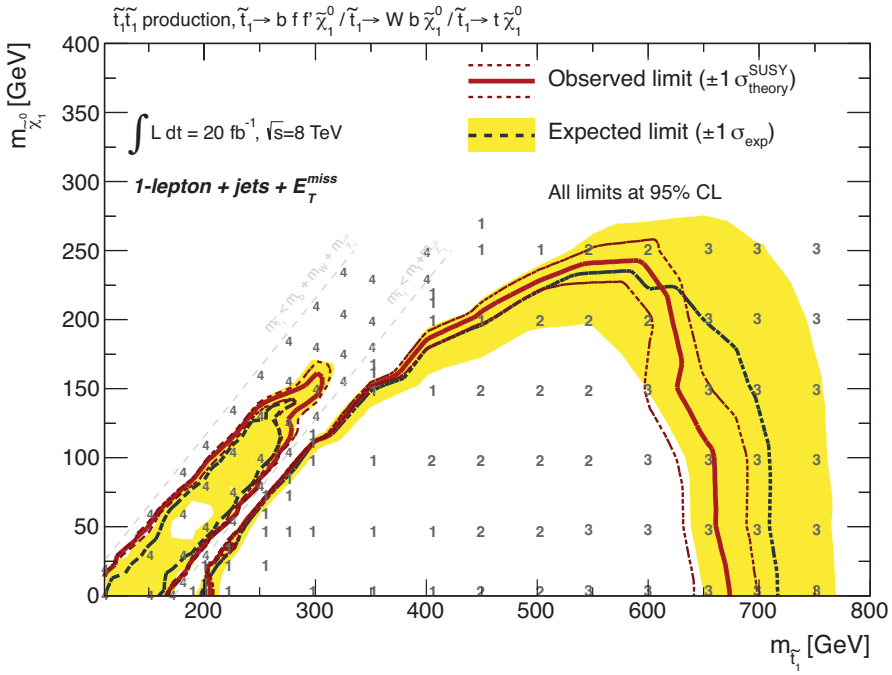

Figure 9.11: *Exclusion limits 95% CL in the $(m_{\tilde{t}}, m_{\tilde{\chi}^0})$ for $\tilde{t} \to t\,\tilde{\chi}^0$ and $\tilde{t} \to b\,W^{\pm}\,\tilde{\chi}^0$ decay modes. The numbers indicate the signal region that is the most sensitive for each point. Mapping between code and signal region is given in Table 9.1(b).*

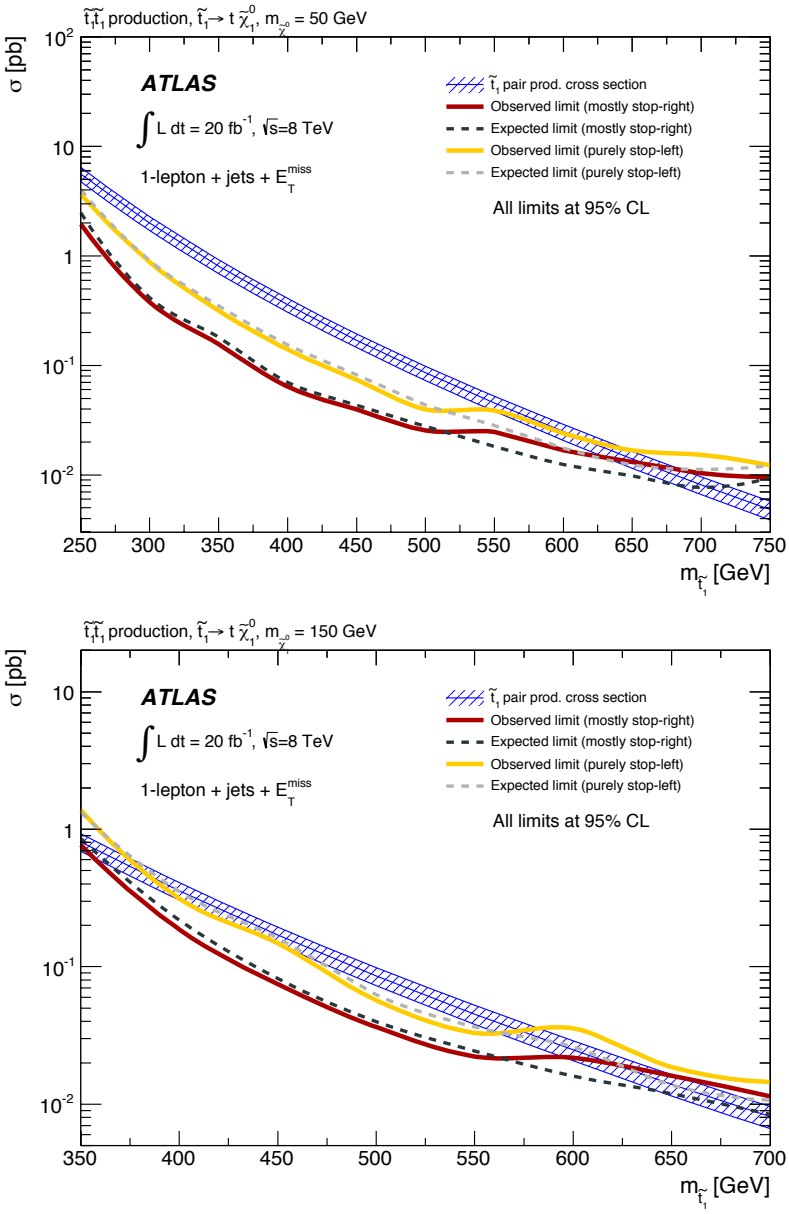

Figure 9.12: *Upper limits on visible cross section (σ_{vis}) for models with $\tilde{t}_1$ being purely $\tilde{t}_L$ and mainly $\tilde{t}_R$. The upper plot assumes $m_{\tilde{\chi}_1^0} = 50$ GeV and the lower plot assumes $m_{\tilde{\chi}_1^0} = 150$ GeV.*

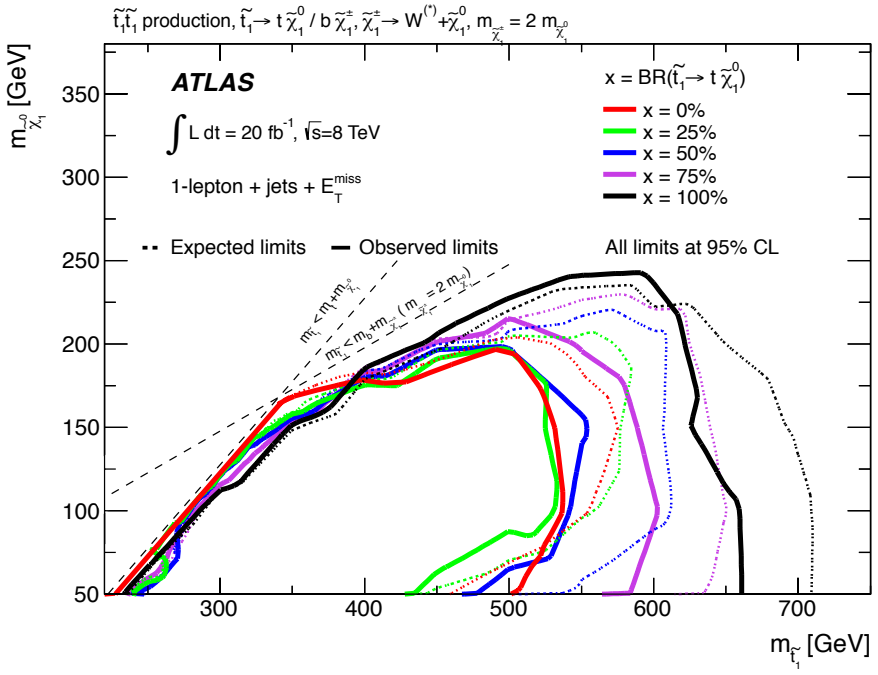

Figure 9.13: *Exclusion limits* 95% CL *in the* $(m_{\tilde{t}}, m_{\tilde{\chi}^0})$ *plane. The two decay modes* $\tilde{t} \to b\,\tilde{\chi}^\pm$ *and* $\tilde{t} \to t\,\tilde{\chi}^0$ *are assumed with a branching ratio of* $(100-x)\%$ *and* $x\%$*, respectively for each line in the plot.* $m_{\tilde{\chi}^\pm} = 2m_{\tilde{\chi}^0}$ *is assumed.*

to the correlation of the top quark polarisation and the boost of the lepton in the top quark decay.

Finally, the results are interpreted in terms of top squark decays where two decay modes are allowed in the same event:

$$\tilde{t} \to t\,\tilde{\chi}^0$$
$$\tilde{t} \to b\,\tilde{\chi}^\pm \to b\,W^\pm\,\tilde{\chi}^0.$$

The results are shown in Figure 9.13 in the $(m_{\tilde{t}}, m_{\tilde{\chi}^0})$ parameter space and gaugino universality is again assumed to fix the chargino mass. Each line in the plot represents the exclusion curve for a different branching ratio in the two decay modes, $x\%$ in $\tilde{t} \to t\,\tilde{\chi}^0$ and $(100-x)\%$ in $\tilde{t} \to b\,\tilde{\chi}^\pm$. Branching ratios of 0-100%, 25-75%, 50-50%, 75-25%, and 100-0% have been tested. The highest sensitivity for the asymmetric mixtures are coming from SR_mix, bC_bulk and bC_med signal regions. This is an

important result since it shows how much the excluded phase space decreases when relaxing the simplified model assumption for $\tilde{t} \to t\,\tilde{\chi}^0$. On the other hand, the pure $\tilde{t} \to b\,\tilde{\chi}^{\pm}$ decay mode curve represents the minimum of the excluded phase space, except in the compressed region. This result can be compared with the ATLAS search for top squarks in all hadronic final states [114], shown in Figure 9.14. Single lepton final states are more powerful to select $\tilde{t} \to b\,\tilde{\chi}^{\pm}$ decays and therefore have higher sensitivity with respect to all hadronic ones, especially in the compressed scenario near the kinematic limit.

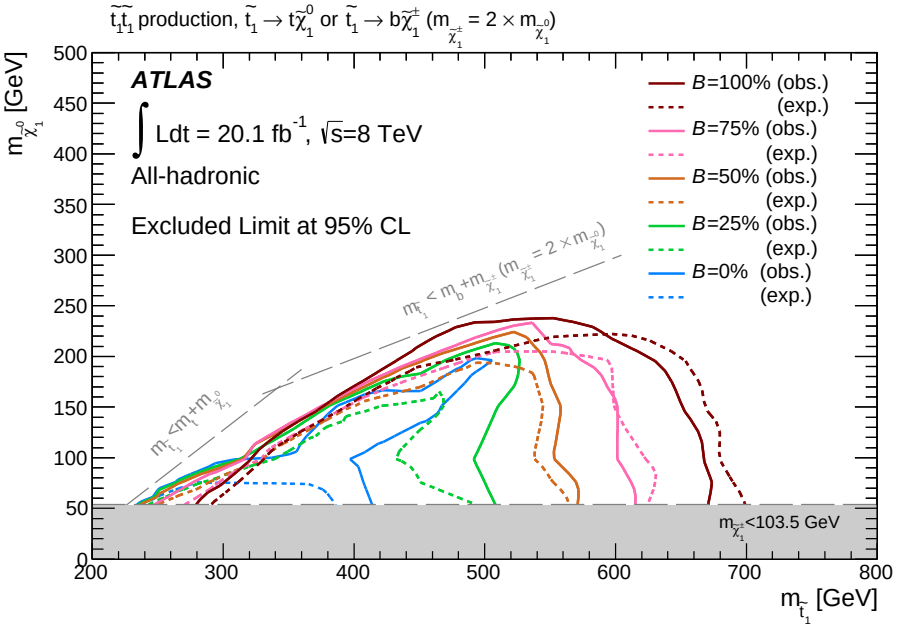

Figure 9.14: *Exclusion contours from Ref. [114] at 95% CL in fully hadronic top/$W^{\pm}$ final states. In this scenario the two decay modes $\tilde{t} \to b\,\tilde{\chi}^{\pm}$ and $\tilde{t} \to t\,\tilde{\chi}^0$ are assumed with a branching ratio of $(1 - B)$ and B, respectively. $m_{\tilde{\chi}^{\pm}} = 2m_{\tilde{\chi}^0}$ is assumed. The grey filled area corresponds to chargino masses below the LEP limit [68]. These results have to be compared with Figure 9.13*

.

9.3 Exclusion limits of Dark Matter production

In Chapter 1 it was highlighted that neutralinos are excellent candidates for WIMP Dark Matter. It was also highlighted that WIMP production associated with heavy flavour quarks, and especially top quarks, is a powerful tool to set constraints on certain contact operators that describe DM interactions with quarks. DM associate production with top quarks ($pp \to t\bar{t}\chi\chi$) has the same final state as the $\tilde{t} \to t\ \tilde{\chi}^0$ decay. Therefore it is reasonable to expect that although the selections of the $\tilde{t} \to t\ \tilde{\chi}^0$ analysis were not optimised for DM signal, they might have some sensitivity to it. All *cut-and-count* selections and shape fits of the stop search were tested for the DM signal models introduced in Ch. 1.4. In particular Dirac and complex scalar DM scalar operators interacting with quarks (D1 and C1) were considered, since they have a dependence on the mass of the quark produced in association with DM. It was found that the DM signal gives rise to a final state that is characterised by $E_{\mathrm{T}}^{\mathrm{miss}}$ values comparable or slightly higher than stop signal models with masses around 500 GeV. The *cut-and-count* signal selection SR_mix was found to have the most optimal cuts for this type of signal and outperformed all the others for all DM mass assumptions and operators. tN_high resulted in too low signal efficiency, being designed for very high top squark masses and tN_med showed a DM signal efficiency very similar to SR_mix but lower background rejection.

The results obtained with SR_mix are compared to a complementary analysis performed in ATLAS that selects fully hadronic final states (no leptons) [10]. This analysis is sensitive to both DM associate production with one or two b-jets, selected by two signal selections, SR1 and SR2, with low jet multiplicity ($\mathcal{N}^{jets} < 5$), and $\chi\chi$+$t\bar{t}$ processes, selected by a high jet multiplicity ($\mathcal{N}^{jets} \geqslant 5$) signal region, SR3. The final background estimates and DM signal yields are shown in Table 9.5 for SR_mix and the three signal selections of Ref. [10].

The cross section upper limit (σ_{excl}) that is obtained for each DM signal model is converted in limits on the inverse effective coupling M_* by the following formula:

$$M_* = \left(\frac{\sigma_{th}}{\sigma_{excl}}\right)^{1/y} [\text{ TeV}] \tag{9.1}$$

where σ_{th} is the NLO production cross section for each process based on a reference value $M_* = 1$ TeV and y is equal to 6 for Dirac scalar DM plus quarks (D1) and 4 for complex scalar DM plus quarks (C1). Subsequently, M_* is converted into a WIMP-nucleon cross section (see Ch. 1.4). The 95% CL exclusion curves on M_* as a function

	SR1	SR2	SR3	SR_mix
Observed data	440	264	107	10
Total SM	385 ± 45	245 ± 31	95.6 ± 13.4	7.2 ± 1.0
Dirac scalar operator (D1)				
m_χ = 10 GeV	10.4 ± 2.4	50 ± 15	29 ± 10	35 ± 12
m_χ = 50 GeV	9.0 ± 2.4	48 ± 17	27 ± 10	35 ± 13
m_χ = 100 GeV	8.3 ± 2.3	32 ± 12	11.8 ± 5.0	28 ± 11
m_χ = 200 GeV	6.0 ± 1.9	18.4 ± 8.9	12.3 ± 6.7	16.5 ± 8.8
Complex scalar operator (C1)				
m_χ = 10 GeV	166 ± 22	608 ± 104	642 ± 141	507 ± 101
m_χ = 50 GeV	140 ± 20	723 ± 130	414 ± 94	397 ± 83
m_χ = 100 GeV	94 ± 14	450 ± 90	392 ± 95	243 ± 55
m_χ = 200 GeV	28.2 ± 6.2	151 ± 40	95 ± 28	106 ± 29

Table 9.5: *Final yields for different* DM *masses m_χ for the three hadronic signal regions of Ref. [10] (SR1, SR2, SR3) and SR_mix of the top squark search. The signal yields correspond to a mediator mass M_Ψ = 1 TeV and a scale factor of 10^6 and $6 \cdot 10^6$ is applied for D1 and C1, respectively. The observed number of data events and the expected SM background including systematic and statistical uncertainties are also indicated for each region.*

of the DM masses are given in Figures 9.15 and 9.16 for the two operators. Effective masses M_* below the curve are excluded. In each Figure, SR_mix is compared to the hadronic selection with the best sensitivity (SR3) and it is possible to notice that, despite the fact that SR_mix was not optimised for this search, it has a greater sensitivity than the hadronic analysis. This is due to the fact that the $t\bar{t}$ semi-leptonic decays provide a much cleaner signature compared to the fully hadronic channel. The four signal regions are completely orthogonal and can be combined to improve the final result. The combined exclusion curves at 95% CL for DM-nucleon scattering cross section are given in Figure 9.17, for operators D1 and C1. Values above the curve are excluded and the results are compared with limits obtained by the ATLAS mono-jet analysis using the 7 TeV data set and the exclusion limits (at 90% CL) recently set by the LUX and Super-CDMS collaborations. The exclusion limits resulting from this analysis are currently the world strongest constraints on scalar coupling Dark Matter for operators involving heavy quarks.

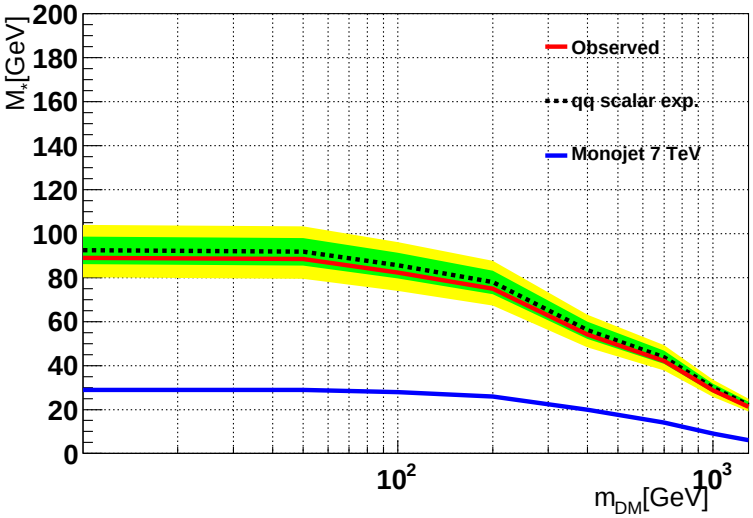

(a) SR3

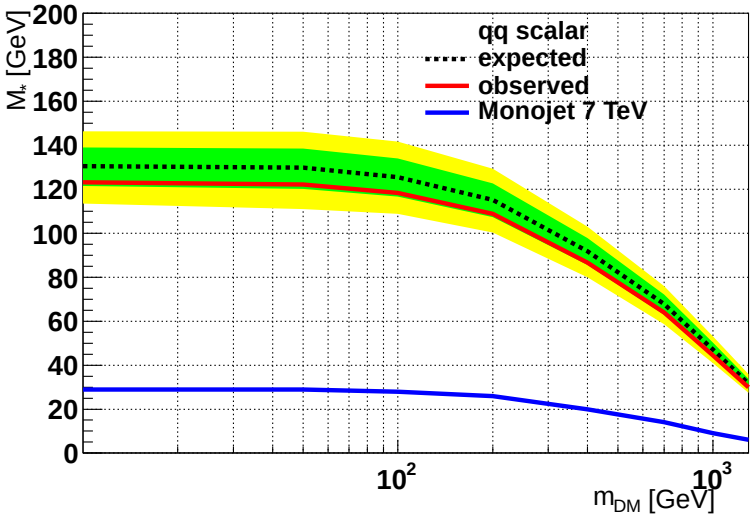

(b) SR_mix

Figure 9.15: *Exclusion curves at* 95% *CL for the effective mass* M_* *for the Dirac scalar contact operator D1.* M_* *values below the curve are excluded. The expected limits are given by the dashed line, observed in red and the green and yellow bands indicted the* $\pm 1, 2\ \sigma$ *uncertainties. In blue are the results of the ATLAS* 7 *TeV mono-jet analysis [152]*

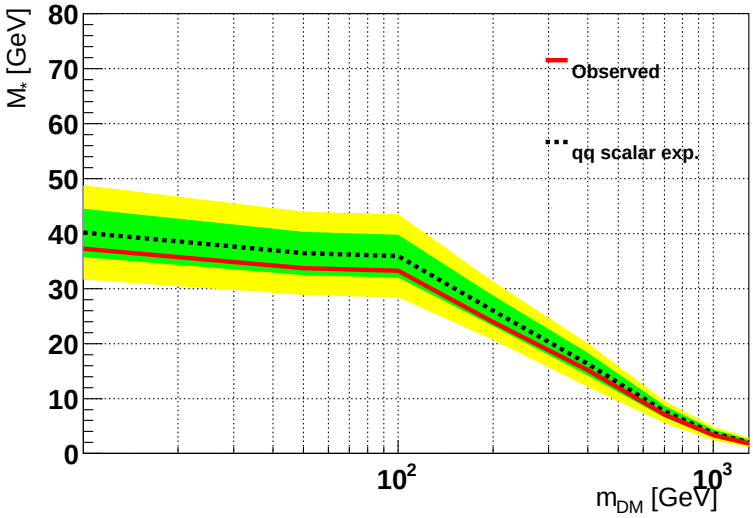

(a) SR3

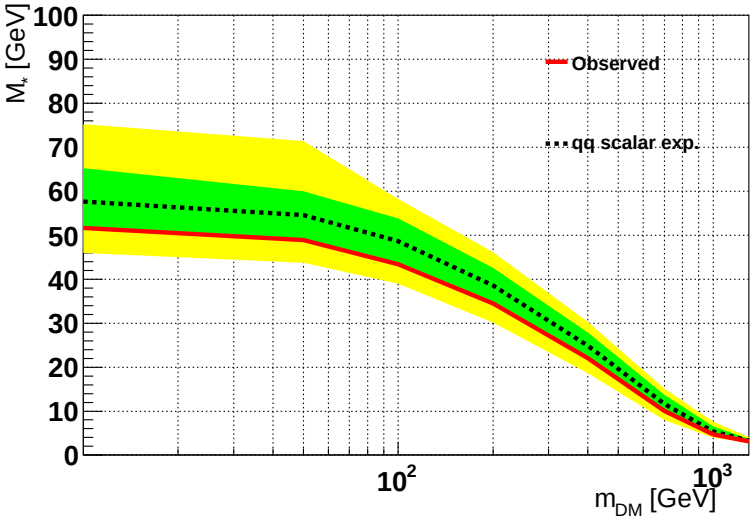

(b) SR_mix

Figure 9.16: *Exclusion curves at* 95% CL *for the effective mass* M_* *for the complex scalar contact operator C1.* M_* *values below the curve are excluded. The expected limits is given by the dashed line, observed in red and the green and yellow bands indicate the* $\pm 1, 2\ \sigma$ *uncertainties.*

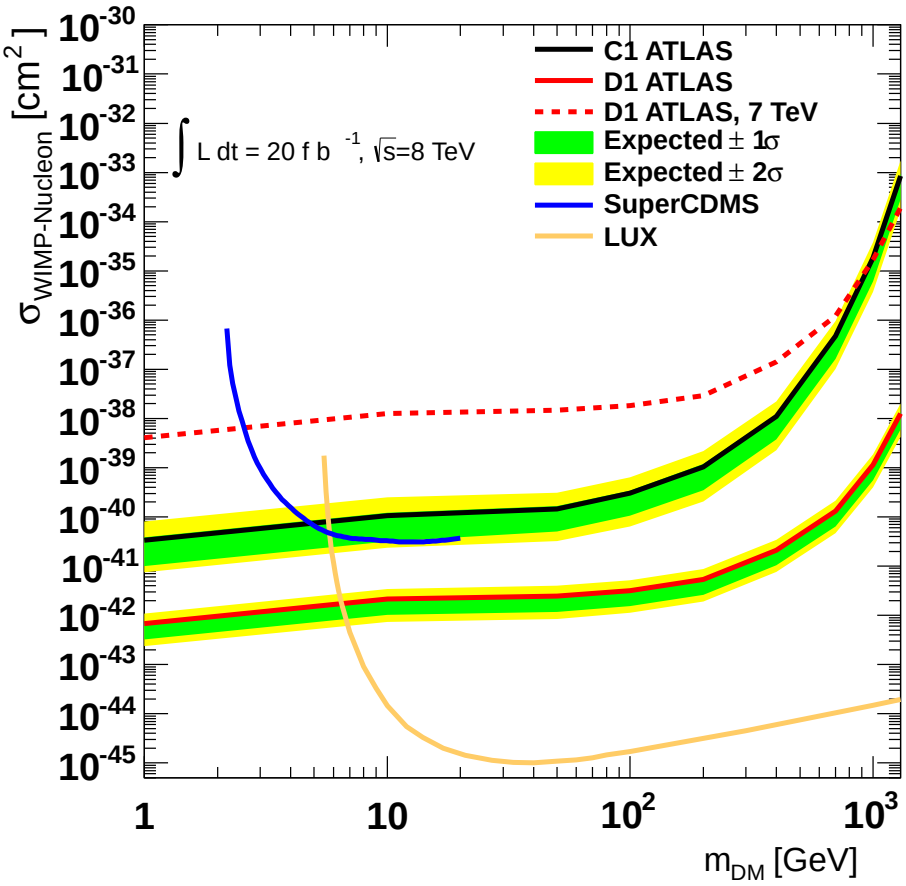

Figure 9.17: *Exclusion curves at 95% CL for DM-nucleon scattering cross section for operators D1 and C1. The results are compared with 90% CL exclusion curves from the Super-CDMS and the LUX Collaborations and values above the curves are excluded.*

9.4 Conclusions and perspectives

A search for direct production of top squark pairs in final states with one isolated lepton, jets, and missing transverse momentum was presented. Proton-proton collision data from the full 2012 data taking period were analysed, corresponding to an integrated luminosity of $20\,\text{fb}^{-1}$ collected at $\sqrt{s} = 8$ TeV by the ATLAS detector at the LHC. Three decay modes of the top squark were addressed exploiting six *cut-and-count* signal regions and four shape fits:

a) $\tilde{t} \to b\,\tilde{\chi}^{\pm} \to b\,W^{\pm}\,\tilde{\chi}^{0}$ (with on/off-shell W)

b) $\tilde{t} \to t\,\tilde{\chi}^{0}$

c) $\tilde{t} \to b\,W^{\pm}\,\tilde{\chi}^{0}$ (via off-shell top)

Each of the decay modes was assumed to have 100% branching ratio and investigated separately. Additionally, signal models where the first two decay modes were allowed at the same time in different mixtures were investigated. The data event counts observed in all selections were found to be compatible with the expected SM background, therefore the results were interpreted in terms of upper limits for different assumptions of stop, chargino and neutralino masses. A large portion of parameter space is excluded at 95% CL. It was shown that this excluded region decreases if the $\tilde{t} \to t\,\tilde{\chi}^{0}$ decay is considered with a branching ratio different from 100%. This is not the case for the pure $\tilde{t} \to b\,\tilde{\chi}^{\pm}$ scenario assuming gaugino universality, that represents the minimum of the excluded parameter space, with the exception of the very challenging signal models of the compressed scenario $m_{\tilde{t}} \sim m_{\tilde{\chi}^{0}}$. If the stop is assumed to decay via off-shell tops in $\tilde{t} \to b\,W^{\pm}\,\tilde{\chi}^{0}$, masses up to 250 GeV are excluded.

In case the chargino is too heavy to be produced via stop decays, there are still many signal models in the $(m_{\tilde{t}}, m_{\tilde{\chi}^{0}})$ plane that are still completely out of reach from the current ATLAS sensitivity. These signal models are characterised by either too small production cross sections (i.e. high stop mass values) or small mass difference between the stop and the neutralino, that gives rise to signatures that are more difficult to select. These difficult scenarios and high top squark masses ($\gtrsim 700$ GeV) will be probed with the LHC *Run II*, since the increased centre-of-mass energy of 13 TeV will provide a larger amount of stop pairs produced.

However, as mentioned in the first chapter of this thesis, *naturalness* arguments favour a light chargino. This scenario results in a more challenging signature and a

much smaller fraction of the parameter space in the $(m_{\tilde{t}}, m_{\tilde{\chi}^{\pm}}, m_{\tilde{\chi}^{0}})$ tridimensional space is excluded. The higher stop pair production cross section at $\sqrt{s}$ = 13 TeV will be paramount to discover the top squark if this scenario is realised.

Finally, it is important to turn the effort of searches toward more complex (and realistic) scenarios in which SUSY can present itself. More attention in the next run needs to be devoted to compressed scenarios, higgsino-like chargino assumptions, longer stop decay chains involving heavier charginos and neutralinos. A powerful tool to achieve this goal will be the so called *phenomenological* MSSM (pMSSM). These models extract and define combinations of the SUSY parameters, and therefore the mass hierarchy of SUSY particles and their decay, such that they satisfy experimental constraints such as the Higgs mass, the universe relic density measured by WMAP and guarantee a small amount of fine tuning.

Bibliography

[1] S. L. Glashow, J. Iliopoulos, and L. Maiani. "Weak Interactions with Lepton-Hadron Symmetry". In *Phys. Rev. D* 2 (7 Oct. 1970), pp. 1285–1292. DOI: 10.1103/PhysRevD.2.1285.

[2] S. Weinberg. "A Model of Leptons". In *Phys. Rev. Lett.* 19 (21 Nov. 1967), pp. 1264–1266. DOI: 10.1103/PhysRevLett.19.1264.

[3] A. Salam. *Weak and Electromagnetic Interactions*. Originally printed in *Svartholm: Elementary Particle Theory, Proceedings Of The Nobel Symposium Held 1968 At Lerum, Sweden*, Stockholm 1968, 367-377.

[4] S. Glashow. "Partial Symmetries of Weak Interactions". In *Nucl. Phys.* 22 (1961), pp. 579–588. DOI: 10.1016/0029-5582(61)90469-2.

[5] ATLAS Collaboration. "Observation of a new particle in the search for the Standard Model Higgs boson with the ATLAS detector at the LHC". In *Phys. Lett.* B716 (2012), pp. 1–29. DOI: 10.1016/j.physletb.2012.08.020. arXiv:1207.7214 [hep-ex].

[6] CMS Collaboration. "Observation of a new boson at a mass of 125 GeV with the CMS experiment at the LHC". In *Phys. Lett.* B716 (2012), pp. 30–61. DOI: 10.1016/j.physletb.2012.08.021. arXiv:1207.7235 [hep-ex].

[7] Y. Gershtein et al. *Working Group Report: New Particles, Forces, and Dimensions*. 2013. arXiv:1311.0299 [hep-ex].

[8] ATLAS Collaboration. "Performance of b-Jet Identification in the ATLAS Experiment". 2014. in preparation, to be submitted to JINST.

[9] ATLAS Collaboration. *Search for top squark pair production in final states with one isolated lepton, jets, and missing transverse momentum in $\sqrt{s}$ = 8 TeV pp collisions with the ATLAS detector*. 2014. arXiv:1407.0583 [hep-ex].

[10] ATLAS Collaboration. “Search for Dark Matter in Events with Heavy Quarks and Missing Transverse Momentum in *pp* collisions with the ATLAS detector at the LHC”. 2014. in preparation, to be submitted to PRL.

[11] P. W. Higgs. “Broken Symmetries and the Masses of Gauge Bosons”. In *Phys. Rev. Lett.* 13 (16 Oct. 1964), pp. 508–509. DOI: 10.1103/PhysRevLett.13.508.

[12] F. Englert and R. Brout. “Broken Symmetry and the Mass of Gauge Vector Mesons”. In *Phys. Rev. Lett.* 13 (9 Aug. 1964), pp. 321–323. DOI: 10.1103/PhysRevLett.13.321.

[13] G. S. Guralnik, C. R. Hagen, and T. W. B. Kibble. “Global Conservation Laws and Massless Particles”. In *Phys. Rev. Lett.* 13 (20 Nov. 1964), pp. 585–587. DOI: 10.1103/PhysRevLett.13.585.

[14] B. Fuks. *Supersymmetry - When Theory Inspires Experimental Searches*. 2014. arXiv:1401.6277 [hep-ph].

[15] ATLAS Collaboration. “Measurements of Higgs boson production and couplings in diboson final states with the ATLAS detector at the LHC”. In *Phys. Lett.* B726 (2013), pp. 88–119. DOI: 10.1016/j.physletb.2013.08.010. arXiv:1307.1427 [hep-ex].

[16] H. Miyazawa. “Baryon Number Changing Currents”. In *Prog. Theor. Phys.* 36 (6) (1966), pp. 1266–1276. DOI: 10.1143/PTP.36.1266.

[17] P. Ramond. “Dual Theory for Free Fermions”. In *Phys. Rev.* D3 (1971), pp. 2415–2418. DOI: 10.1103/PhysRevD.3.2415.

[18] Y. A. Gol'fand and E. P. Likhtman. “Extension of the Algebra of Poincare Group Generators and Violation of p Invariance”. In *JETP Lett.* 13 (1971), pp. 323–326.

[19] A. Neveu and J. H. Schwarz. “Factorizable dual model of pions”. In *Nucl. Phys.* B31 (1971), pp. 86–112. DOI: 10.1016/0550-3213(71)90448-2.

[20] A. Neveu and J. H. Schwarz. “Quark Model of Dual Pions”. In *Phys. Rev.* D4 (1971), pp. 1109–1111. DOI: 10.1103/PhysRevD.4.1109.

[21] J. Gervais and B. Sakita. “Field theory interpretation of supergauges in dual models”. In *Nucl. Phys.* B34 (1971), pp. 632–639. DOI: 10.1016/0550-3213(71)90351-8.

[22] D. V. Volkov and V. P. Akulov. “Is the Neutrino a Goldstone Particle?” In *Phys. Lett.* B46 (1973), pp. 109–110. DOI: 10.1016/0370-2693(73)90490-5.

[23] J. Wess and B. Zumino. “A Lagrangian Model Invariant Under Supergauge Transformations”. In *Phys. Lett.* B49 (1974), p. 52. DOI: 10.1016/0370-2693(74)90578-4.

[24] J. Wess and B. Zumino. “Supergauge Transformations in Four-Dimensions”. In *Nucl. Phys.* B70 (1974), pp. 39–50. DOI: 10.1016/0550-3213(74)90355-1.

[25] S. Coleman and J. Mandula. “All Possible Symmetries of the S-Matrix”. In *Phys. Rev.* 159 (5 July 1967), pp. 1251–1256. DOI: 10.1103/PhysRev.159.1251.

[26] R. Haag, J. Lopuszanski, and M. Sohnius. “All possible generators of supersymmetries of the S-matrix”. In *Nucl. Phys. B* 88.2 (1975), pp. 257 –274. ISSN: 0550-3213. DOI: 10.1016/0550-3213(75)90279-5.

[27] S. Dimopoulos, S. Raby, and F. Wilczek. “Supersymmetry and the Scale of Unification”. In *Phys. Rev.* D24 (1981), pp. 1681–1683. DOI: 10.1103/PhysRevD.24.1681.

[28] N. Sakai. “Naturalness in Supersymmetric Guts”. In *Zeit. Phys.* C11 (1981), p. 153. DOI: 10.1007/BF01573998.

[29] L. E. Ibanez and G. G. Ross. “Low-Energy Predictions in Supersymmetric Grand Unified Theories”. In *Phys. Lett.* B105 (1981), p. 439. DOI: 10.1016/0370-2693(81)91200-4.

[30] M. B. Einhorn and D. R. T. Jones. “The Weak Mixing Angle and Unification Mass in Supersymmetric SU(5)”. In *Nucl. Phys.* B196 (1982), p. 475. DOI: 10.1016/0550-3213(82)90502-8.

[31] W. J. Marciano and G. Senjanovic. “Predictions of Supersymmetric Grand Unified Theories”. In *Phys. Rev.* D25 (1982), p. 3092. DOI: 10.1103/PhysRevD.25.3092.

[32] C. Giunti, C. W. Kim, and U. Lee. “Running coupling constants and grand unification models”. In *Mod. Phys. Lett.* A6 (1991), pp. 1745–1755. DOI: 10.1142/S0217732391001883.

[33] J. Ellis, S. Kelley, and D. Nanopoulos. “Probing the desert using gauge coupling unification”. In *Phys. Lett.* B260 (1991), pp. 131–137. DOI: 10.1016/0370-2693(91)90980-5.

[34] U. Amaldi, W. de Boer, and H. Furstenau. “Comparison of grand unified theories with electroweak and strong coupling constants measured at LEP”. In *Phys. Lett.* B260 (1991), pp. 447–455. DOI: 10.1016/0370-2693(91)91641-8.

[35] P. Langacker and M.-X. Luo. “Implications of precision electroweak experiments for $M(t)$, $\rho(0)$, $\sin^2\theta_W$ and grand unification”. In *Phys. Rev.* D44 (1991), pp. 817–822. DOI: 10.1103/PhysRevD.44.817.

[36] A. H. Chamseddine, R. Arnowitt, and N. Pran. “Locally Supersymmetric Grand Unification”. In *Phys. Rev. Lett.* 49 (14), pp. 970–974. DOI: 10.1103/PhysRevLett.49.970.

[37] R. Barbieri, S. Ferrara, and C. A. Savoy. “Gauge Models with Spontaneously Broken Local Supersymmetry”. In *Phys. Lett.* B119 (1982), p. 343. DOI: 10.1016/0370-2693(82)90685-2.

[38] L. E. Ibanez. “Locally Supersymmetric SU(5) Grand Unification”. In *Phys. Lett.* B118 (1982), p. 73. DOI: 10.1016/0370-2693(82)90604-9.

[39] L. J. Hall, J. D. Lykken, and S. Weinberg. “Supergravity as the Messenger of Supersymmetry Breaking”. In *Phys. Rev.* D27 (1983), pp. 2359–2378. DOI: 10.1103/PhysRevD.27.2359.

[40] N. Ohta. “Grand Unified Theories Based on Local Supersymmetry”. In *Prog. Theor. Phys.* 70 (1983), p. 542. DOI: 10.1143/PTP.70.542.

[41] G. L. Kane, C. F. Kolda, L. Roszkowski, and J. D. Wells. “Study of constrained minimal supersymmetry”. In *Phys. Rev.* D49 (1994), pp. 6173–6210. DOI: 10.1103/PhysRevD.49.6173.

[42] H. Goldberg. “Constraint on the photino mass from cosmology”. In *Phys. Rev. Lett.* 50 (1983), p. 1419. DOI: 10.1103/PhysRevLett.50.1419.

[43] J. Ellis, J. Hagelin, D. Nanopoulos, K. Olive, and M. Srednicki. “Supersymmetric relics from the big bang”. In *Nucl. Phys.* B238 (1984), pp. 453–476. DOI: 10.1016/0550-3213(84)90461-9.

[44] J. Beringer et al. *Particle Data Group*. Vol. D86, 010001. 2012.

[45] S. P. Martin. *A Supersymmetry primer*. 1997. arXiv:hep-ph/9709356 [hep-ph].

[46] M. Drees, R. Godbole, and P. Roy. *Theory and Phenomenology of Sparticles*. 2005. ISBN: 978-981-02-3739-4.

[47] S. Dawson. *SUSY and such*. 1997. arXiv:hep-ph/9612229 [hep-ph].

[48] S. Dimopoulos and D. W. Sutter. "The Supersymmetric flavor problem". In *Nucl. Phys.* B452 (1995), pp. 496–512. DOI: 10.1016/0550-3213(95)00421-N. arXiv:hep-ph/9504415 [hep-ph].

[49] H1 and ZEUS Collaboration. "Combined Measurement and QCD Analysis of the Inclusive e+- p Scattering Cross Sections at HERA". In *JHEP* 1001 (2010), p. 109. DOI: 10.1007/JHEP01(2010)109. arXiv:0911.0884 [hep-ex].

[50] H1 Collaboration. "Measurement of inclusive jet production in deep-inelastic scattering at high Q**2 and determination of the strong coupling". In *Phys. Lett.* B653 (2007), pp. 134–144. DOI: 10.1016/j.physletb.2007.07.050. arXiv:0706.3722 [hep-ex].

[51] ZEUS Collaboration. "Inclusive-jet and dijet cross-sections in deep inelastic scattering at HERA". In *Nucl. Phys.* B765 (2007), pp. 1–30. DOI: 10.1016/j.nuclphysb.2006.09.018. arXiv:hep-ex/0608048 [hep-ex].

[52] ZEUS Collaboration. "Inclusive jet cross-sections in the Breit frame in neutral current deep inelastic scattering at HERA and determination of alpha(s)". In *Phys. Lett.* B547 (2002), pp. 164–180. DOI: 10.1016/S0370-2693(02)02763-6. arXiv:hep-ex/0208037 [hep-ex].

[53] D0 Collaboration. "Measurement of the inclusive jet cross-section in $p\bar{p}$ collisions at $s^{1/2}$ =1.96-TeV". In *Phys. Rev. Lett.* 101 (2008), p. 062001. DOI: 10.1103/PhysRevLett.101.062001. arXiv:0802.2400 [hep-ex].

[54] CDF Collaboration. "Measurement of the Inclusive Jet Cross Section using the k_T algorithm in $p\bar{p}$ Collisions at$\sqrt{s}$ = 1.96 TeV with the CDF II Detector". In *Phys. Rev.* D75 (2007), p. 092006. DOI: 10.1103/PhysRevD.75.119901,10.1103/PhysRevD.75.092006. arXiv:hep-ex/0701051 [hep-ex].

[55] V. Gribov and L. Lipatov. "Deep inelastic e p scattering in perturbation theory". In *Sov. J. Nucl. Phys.* 15 (1972), pp. 438–450.

[56] V. Gribov and L. Lipatov. "e+ e- pair annihilation and deep inelastic e p scattering in perturbation theory". In *Sov. J. Nucl. Phys.* 15 (1972), pp. 675–684.

[57] L. Lipatov. "The parton model and perturbation theory". In *Sov. J. Nucl. Phys.* 20 (1975), pp. 94–102.

[58] G. Altarelli and G. Parisi. "Asymptotic Freedom in Parton Language". In *Nucl. Phys.* B126 (1977), p. 298. DOI: 10.1016/0550-3213(77)90384-4.

[59] Y. L. Dokshitzer. "Calculation of the Structure Functions for Deep Inelastic Scattering and e+ e- Annihilation by Perturbation Theory in Quantum Chromodynamics." In *Sov. Phys. JETP* 46 (1977), pp. 641–653.

[60] W. Beenakker, M. Kramer, T. Plehn, M. Spira, and P. Zerwas. "Stop production at hadron colliders". In *Nucl. Phys.* B515 (1998), pp. 3–14. DOI: 10.1016/S0550-3213(98)00014-5. arXiv:hep-ph/9710451 [hep-ph].

[61] W. Beenakker, R. Hopker, M. Spira, and P. Zerwas. "Squark and gluino production at hadron colliders". In *Nucl. Phys.* B492 (1997), pp. 51–103. DOI: 10.1016/S0550-3213(97)80027-2. eprint: hep-ph/9610490 (hep-ph).

[62] ATLAS Collaboration. *Search for squarks and gluinos with the ATLAS detector in final states with jets and missing transverse momentum and 20.3 fb^{-1} of $\sqrt{s}$ = 8 TeV proton-proton collision data*. May 2013. eprint: ATLAS-CONF-2013-047. URL: https://cds.cern.ch/record/1547563/.

[63] W. Beenakker, M. Kramer, T. Plehn, M. Spira, and P. Zerwas. "Stop production at hadron colliders". In *Nucl. Phys.* B515 (1998), pp. 3–14. DOI: 10.1016/S0550-3213(98)00014-5. eprint: hep-ph/9710451 (hep-ph).

[64] ATLAS Collaboration. *Search for pair-produced top squarks decaying into a charm quark and the lightest neutralinos with 20.3 fb^{-1} of pp collisions at $\sqrt{s}$ = 8 TeV with the ATLAS detector at the LHC*. July 2013. eprint: ATLAS-CONF-2013-068. URL: https://cds.cern.ch/record/1562880?ln=en.

[65] W. Beenakker, S. Brensing, M. Kramer, A. Kulesza, E. Laenen, and I. Niessen. "Supersymmetric top and bottom squark production at hadron colliders". In *JHEP.* 1008 (2010), p. 098. eprint: arXiv:1006.4771[hep-ph].

[66] W. Beenakker, S. Brensing, M. Kramer, A. Kulesza, E. Laenen, et al. "Squark and gluino hadroproduction". In *Int. J. Mod. Phys.* A26 (2011), pp. 2637–2664. DOI: 10.1142/S0217751X11053560. arXiv:1105.1110 [hep-ph].

[67] M. Kramer, A. Kulesza, R. van der Leeuw, M. Mangano, S. Padhi, et al. "Supersymmetry production cross sections in pp collisions at $\sqrt{s}$ = 7 TeV". In (2012). arXiv:1206.2892 [hep-ph].

[68] G. Abbiendi et al. "Search for chargino and neutralino production at $\sqrt{s}$ = 192 GeV to 209 GeV at LEP". In *Eur. Phys. J.* C35 (2004), pp. 1–20. DOI: 10.1140/epjc/s2004-01758-8. arXiv:hep-ex/0401026 [hep-ex].

[69] J.H. Oort. “The force exerted by the stellar system in the direction perpendicular to the galactic plane and some related problems”. In *Bulletin of the Astronomical Institutes of the Netherlands* 6 (1932), p. 249.

[70] F. Zwicky. “Die Rotverschiebung von extragalaktischen Nebeln”. In *Helvetica Physica Acta* 6 (1933), pp. 110–127.

[71] M. Bradac et al. “Revealing the properties of dark matter in the merging cluster MACSJ0025.4-1222”. In (2008). arXiv:0806.2320 [astro-ph].

[72] WMAP Collaboration. “Seven-Year Wilkinson Microwave Anisotropy Probe (WMAP) Observations: Cosmological Interpretation”. In *Astrophys. J. Suppl.* 192 (2011), p. 18. DOI: 10.1088/0067-0049/192/2/18. arXiv:1001.4538 [astro-ph.CO].

[73] Plank Collaboration. *Planck 2013 results. XVI. Cosmological parameters*. 2013. arXiv:1303.5076 [astro-ph.CO].

[74] C. Aalseth et al. *Search for An Annual Modulation in Three Years of CoGeNT Dark Matter Detector Data*. 2014. arXiv:1401.3295 [astro-ph.CO].

[75] R. Bernabei et al. “New results from DAMA/LIBRA”. In *Eur. Phys. J.* C67 (2010), pp. 39–49. DOI: 10.1140/epjc/s10052-010-1303-9. arXiv:1002.1028 [astro-ph.GA].

[76] J. Goodman et al. “Constraints on Dark Matter from Colliders”. In *Phys. Rev.* D82 (2010), p. 116010. DOI: 10.1103/PhysRevD.82.116010. arXiv:1008.1783 [hep-ph].

[77] M. Beltran, D. Hooper, E. W. Kolb, Z. A. Krusberg, and T. M. Tait. “Maverick dark matter at colliders”. In *JHEP* 1009 (2010), p. 037. DOI: 10.1007/JHEP09(2010)037. arXiv:1002.4137 [hep-ph].

[78] N. Zhou, D. Berge, and D. Whiteson. “Mono-everything: combined limits on dark matter production at colliders from multiple final states”. In *Phys. Rev.* D87.9 (2013), p. 095013. DOI: 10.1103/PhysRevD.87.095013. arXiv:1302.3619 [hep-ex].

[79] G. Artoni, T. Lin, B. Penning, G. Sciolla, and A. Venturini. *Prospects for collider searches for dark matter with heavy quarks*. 2013. arXiv:1307.7834 [hep-ex].

[80] G. Busoni, A. De Simone, E. Morgante, and A. Riotto. "On the Validity of the Effective Field Theory for Dark Matter Searches at the LHC". In *Phys. Lett.* B728 (2014), pp. 412–421. DOI: 10.1016/j.physletb.2013.11.069. arXiv:1307.2253 [hep-ph].

[81] O. S. Bruning, P. Collier, P. Lebrun, S. Myers, R. Ostojic, J. Poole, and P. Proudlock. *LHC Design Report*. 2004. eprint: CERN-2004-003. URL: https://cds.cern.ch/record/782076?ln=en.

[82] L. Evans and P. Bryant. "LHC Machine". In *JINST* 3 (2008), S08001. DOI: doi:10.1088/1748-0221/3/08/S08001.

[83] ATLAS Collaboration. "Improved luminosity determination in pp collisions at $\sqrt{s} = 7$ TeV using the ATLAS detector at the LHC". In *Eur. Phys. J.* C73 (2013), p. 2518. DOI: 10.1140/epjc/s10052-013-2518-3. arXiv:1302.4393 [hep-ex].

[84] *ATLAS Luminosity Public Page*. URL: https://twiki.cern.ch/twiki/bin/view/AtlasPublic/LuminosityPublicResults\#Data_Taking_Efficiency_and_Pileu.

[85] ATLAS Collaboration. "ATLAS Experiment at the CERN Large Hadron Collider". In *JINST* 3 (2008), S08003. DOI: 10.1088/1748-0221/3/08/S08003.

[86] A. Salvucci. *Measurement of muon momentum resolution of the ATLAS detector*. 2011. arXiv:1201.4704.

[87] *Preliminary results on the muon reconstruction efficiency, momentum resolution, and momentum scale in ATLAS 2012 pp collision data*. Aug. 2013. eprint: ATLAS-CONF-2013-088. URL: https://cds.cern.ch/record/1580207.

[88] ATLAS Collaboration. *ATLAS liquid Argon calorimeter: Technical design report*. eprint: CERN-LHCC-96-41. URL: https://cds.cern.ch/record/331061?ln=en.

[89] ATLAS Collaboration. *ATLAS tile calorimeter: Technical design report*. eprint: CERN-LHCC-96-42. URL: https://cds.cern.ch/record/331062?ln=en.

[90] ATLAS Collaboration. *ATLAS muon spectrometer : Technical Design Report*. 1997. eprint: CERN-LHCC-97-022. URL: https://cds.cern.ch/record/331068.

[91] ATLAS collaboration. *Global χ^2 approach to the alignment of the ATLAS silicon tracking detectors*. 2005. eprint: ATL-INDET-PUB-2005-002. URL: https://cdsweb.cern.ch/record/835270.

[92] R. Hartel. *Iterative local Chi2 alignment approach for the ATLAS SCT detector*. 2005. eprint: MPP-2005-174. URL: https://www.mpp.mpg.de/english/research/experimental/atlas/sct/thesen/index.html?action=search&language=en&mpi=MPP-2005-174.

[93] ATLAS Collaboration. *Alignment of the ATLAS Inner Detector Tracking System with 2010 LHC proton-proton collisions at $\sqrt{s}$ = 7 TeV*. 2011. eprint: ATLAS-CONF-2011-012. URL: http://cdsweb.cern.ch/record/1334582.

[94] *ATLAS ID Aligment Public Plots*. URL: http://atlas.web.cern.ch/Atlas/GROUPS/PHYSICS/IDTRACKING/PublicPlots/ATL-COM-PHYS-2012-500/.

[95] ATLAS Collaboration. "Operation and performance of the ATLAS semiconductor tracker". In (2014). arXiv:1404.7473 [hep-ex].

[96] *ATLAS SCT public page*. URL: https://twiki.cern.ch/twiki/bin/view/AtlasPublic/SCTPublicResults.

[97] A. Chilingarov. *Generation current temperature scaling*. Jan. 2013. eprint: PH-EP-Tech-Note-2013-001. URL: https://cds.cern.ch/record/1511886?ln=en.

[98] Ferrari, A. and Sala, P. R. and Fassó, A. and Ranft, J. *FLUKA: A multi-particle transport code (program version 2005)*. Geneva, 2005.

[99] ATLAS Collaboration. "Electron performance measurements with the ATLAS detector using the 2010 LHC proton-proton collision data". In *Eur. Phys. J. C* 72.3 (2012), pp. 1–46. ISSN: 1434-6044. DOI: 10.1140/epjc/s10052-012-1909-1.

[100] W. Lampl, S. Laplace, D. Lelas, P. Loch, H. Ma, S. Menke, S. Rajagopalan, D. Rousseau, S. Snyder, and G. Unal. *Calorimeter Clustering Algorithms: Description and Performance*. eprint: ATL-LARG-PUB-2008-002.ATL-COM-LARG-2008-003. URL: https://cds.cern.ch/record/1099735?ln=en.

[101] R. Nicolaidou, L. Chevalier, S. Hassani, J. F. Laporte, E. L. Menedeu, and A. Ouraou. "Muon identification procedure for the ATLAS detector at the LHC using Muonboy reconstruction package and tests of its performance using cosmic rays and single beam data". In *Journal of Physics: Conference Series* 219.3 (2010), p. 032052.

[102] *ATLAS Muon public page*. URL: https://atlas.web.cern.ch/Atlas/GROUPS/PHYSICS/MUON/PublicPlots/2013/ATL-COM-PHYS-2013-340/index.html.

[103] M. Cacciari, G. P. Salam, and G. Soyez. "The anti kt jet clustering algorithm". In *JHEP* 0804 (2008), p. 063. DOI: 10.1088/1126-6708/2008/04/063. arXiv:0802.1189.

[104] ATLAS Collaboration. "Jet energy measurement with the ATLAS detector in proton-proton collisions at $\sqrt{s}$ = 7 TeV". In *Eur. Phys. J. C* 73 (2013), p. 2304. arXiv:1112.6426v1.

[105] ATLAS Collaboration. *Jet energy measurement and its systematic uncertainty in proton--proton collisions at $\sqrt{s}$ = 7 TeV with the ATLAS detector*. 2014. arXiv:1406.0076 [hep-ex].

[106] *ATLAS Jet Calibrations public page*. URL: https://twiki.cern.ch/twiki/bin/view/AtlasPublic/JetEtmissApproved2013JESUncertainty.

[107] ATLAS Collaboration. *Expected performance of the ATLAS experiment: detector,trigger and physics*. 2009. arXiv:0901.0512v4.

[108] ATLAS Collaboration. *Calibration of the performance of b-tagging for c and light-flavour jets in the 2012 ATLAS data*. July 2014. eprint: ATLAS-CONF-2014-046. URL: https://cds.cern.ch/record/1741020?ln=en.

[109] ATLAS Collaboration. *Calibration of b-tagging using dileptonic top pair events in a combinatorial likelihood approach with the ATLAS experiment*. Feb. 2014. eprint: ATLAS-CONF-2014-004. URL: https://cds.cern.ch/record/1664335?ln=en.

[110] T. Sjostrand, S. Mrenna, and P. Z. Skands. "PYTHIA 6.4 Physics and Manual". In *JHEP* 0605 (2006), p. 026. DOI: 10.1088/1126-6708/2006/05/026.

[111] ATLAS Collaboration. *The simulation principle and performance of the ATLAS fast calorimeter simulation FastCaloSim*. 2010. eprint: ATL-PHYS-PUB-2010-013. URL: https://cds.cern.ch/record/1300517.

[112] S. Agostinelli et al. "GEANT4: A simulation toolkit". In *Nucl. Instrum. Meth.* A506 (2003), pp. 250–303. DOI: 10.1016/S0168-9002(03)01368-8.

[113] P. Z. Skands. "Tuning Monte Carlo generators: The Perugia tunes". In *Phys. Rev. D* 82 (7 Oct. 2010), p. 074018. DOI: 10.1103/PhysRevD.82.074018.

[114] ATLAS Collaboration. *Search for direct pair production of the top squark in all-hadronic final states in proton-proton collisions at $\sqrt{s}$ = 8 TeV with the ATLAS detector*. 2014. arXiv:1406.1122 [hep-ex].

[115] ATLAS Collaboration. "Search for direct top-squark pair production in final states with two leptons in pp collisions at $\sqrt{s}$=8 TeV with the ATLAS detector". In (2014). arXiv:1403.4853 [hep-ex].

[116] J. Alwall, M. Herquet, F. Maltoni, O. Mattelaer, and T. Stelzer. "MadGraph 5 : Going Beyond". In *JHEP* 1106 (2011), p. 128. DOI: 10.1007/JHEP06(2011)128. arXiv:1106.0522 [hep-ph].

[117] D. Stump, J. Huston, J. Pumplin, K. Tung, H.-L. Lai, S. Kuhlmann, and J. F. Owens. "Inclusive jet production, parton distributions, and the search for new physics". In *JHEP* 2003.10 (2003), p. 046.

[118] M. Bahr, S. Gieseke, M. Gigg, D. Grellscheid, K. Hamilton, et al. "Herwig++ Physics and Manual". In *Eur. Phys. J.* C58 (2008), pp. 639–707. DOI: 10.1140/epjc/s10052-008-0798-9. arXiv:0803.0883 [hep-ph].

[119] *ATLAS SM public page*. URL: https://twiki.cern.ch/twiki/bin/view/AtlasPublic/StandardModelPublicResults.

[120] ATLAS Collaboration, CDF Collaboration, CMS Collaboration, D0 Collaboration. *First combination of Tevatron and LHC measurements of the top-quark mass*. Mar. 2014. eprint: arXiv:1403.4427.ATLAS-CONF-2014-008.CDF-NOTE-11071.CMS-PAS-TOP-13-014.D0-NOTE-6416.

[121] M. Czakon and A. Mitov. "NNLO corrections to top pair production at hadron colliders: the quark-gluon reaction". In *JHEP* 1 (2013), pp. 1–19. DOI: 10.1007/JHEP01(2013)080.

[122] M. Czakon and A. Mitov. *Top++: a program for the calculation of the top-pair cross-section at hadron colliders*. arXiv:1112.5675[hep-ph]. URL: http://arxiv.org/abs/1112.5675.

[123] M. Cacciari, M. Czakon, M. Mangano, A. Mitov, and P. Nason. "Top-pair production at hadron colliders with next-to-next-to-leading logarithmic soft-gluon resummation". In *Phys. Lett. B* 710.4–5 (2012), pp. 612 –622. ISSN: 0370-2693. DOI: http://dx.doi.org/10.1016/j.physletb.2012.03.013.

[124] N. Kidonakis. "Next-to-next-to-leading-order collinear and soft gluon corrections for t-channel single top quark production". In *Phys. Rev. D* 83 (9 May 2011), p. 091503. DOI: 10.1103/PhysRevD.83.091503.

[125] N. Kidonakis. “Two-loop soft anomalous dimensions for single top quark associated production with a W^- or a H^-”. In *Phys. Rev. D* 82 (5 Sept. 2010), p. 054018. DOI: 10.1103/PhysRevD.82.054018.

[126] N. Kidonakis. “Next-to-next-to-leading logarithm resummation for s-channel single top quark production”. In *Phys. Rev. D* 81 (5 Mar. 2010), p. 054028. DOI: 10.1103/PhysRevD.81.054028.

[127] P. Nason. “A new method for combining NLO QCD with shower Monte Carlo algorithms”. In *JHEP* 2004.11 (2004), p. 040.

[128] S. Frixione, P. Nason, and C. Oleari. “Matching NLO QCD computations with parton shower simulations: the POWHEG method”. In *JHEP* 2007.11 (2007), p. 70.

[129] H.-L. Lai, M. Guzzi, J. Huston, Z. Li, P. M. Nadolsky, J. Pumplin, and C.-P. Yuan. “New parton distributions for collider physics”. In *Phys. Rev. D* 82 (7 Oct. 2010), p. 074024. DOI: 10.1103/PhysRevD.82.074024.

[130] B. P. Kersevan and E. Richter-Was. “The Monte Carlo event generator AcerMC versions 2.0 to 3.8 with interfaces to {PYTHIA} 6.4, {HERWIG} 6.5 and {ARIADNE} 4.1”. In *Computer Physics Communications* 184.3 (2013), pp. 919 –985. ISSN: 0010-4655. DOI: http://dx.doi.org/10.1016/j.cpc.2012.10.032.

[131] ATLAS Collaboration. “Measurements of top quark pair relative differential cross-sections with ATLAS in pp collisions at $\sqrt{s}$ = 7 TeV”. In *Eur. Phys. J.* C73 (2013), p. 2261. DOI: 10.1140/epjc/s10052-012-2261-1. arXiv:1207.5644 [hep-ex].

[132] ATLAS Collaboration. “Study of jets produced in association with a W boson in pp collisions at $\sqrt{s}$ = 7 TeV with the ATLAS detector”. In *Phys. Rev. D* 85 (9 May 2012), p. 092002. DOI: 10.1103/PhysRevD.85.092002.

[133] J. Butterworth, E. Dobson, U. Klein, B. Mellado Garcia, T. Nunnemann, J. Qian, D. Rebuzzi, and R. Tanaka. *Single Boson and Diboson Production Cross Sections in pp Collisions at sqrts=7 TeV*. Aug. 2010. eprint: ATL-COM-PHYS-2010-695. URL: https://cds.cern.ch/record/1287902.

[134] ATLAS Collaboration. “Measurement of the cross-section for W boson production in association with b-jets in pp collisions at $\sqrt{s}$ = 7 TeV with the ATLAS detector”. In *JHEP* 2013.6 (2013), p. 84. DOI: 10.1007/JHEP06(2013)084.

[135] ATLAS Collaboration. *Measurement of the production of a W boson in association with a charm hadron in pp collisions at sqrt(s)=7 TeV*. 2013. eprint: ATLAS-CONF-2013-045. URL: https://cds.cern.ch/record/1546800.

[136] T. Gleisberg, S. Höche, F. Krauss, M. Schönherr, S. Schumann, F. Siegert, and J. Winter. "Event generation with SHERPA 1.1". In *JHEP* 2009.02 (2009), p. 007.

[137] M. Garzelli, A. Kardos, C. Papadopoulos, and Z. Trócsányi. "$t\bar{t}W^{\pm}$+$t\bar{t}Z$ hadroproduction at NLO accuracy in QCD with Parton Shower and Hadronization effects". In *JHEP* 2012.11 (2012), pp. 1–21. DOI: 10.1007/JHEP11(2012)056.

[138] J. Alwall, M. Herquet, F. Maltoni, O. Mattelaer, and T. Stelzer. "MadGraph 5: going beyond". In *JHEP* 2011.6 (2011), pp. 1–40. DOI: 10.1007/JHEP06(2011)128.

[139] A. L. Read. "Presentation of search results: the CL s technique". In *Journal of Physics G: Nuclear and Particle Physics* 28.10 (2002), p. 2693.

[140] G. Cowan, K. Cranmer, E. Gross, and O. Vitells. "Asymptotic formulae for likelihood-based tests of new physics". In *Eur. Phys. J.* C71 (2011), p. 1554. DOI: 10.1140/epjc/s10052-011-1554-0. arXiv:1007.1727 [physics.data-an].

[141] B. Nachman and C. G. Lester. "Significance Variables". In *Phys. Rev.* D88 (2013), p. 075013. DOI: 10.1103/PhysRevD.88.075013. arXiv:1303.7009 [hep-ph].

[142] ATLAS Collaboration. *Identification of the Hadronic Decays of Tau Leptons in 2012 Data with the ATLAS Detector*. eprint: ATLAS-CONF-2013-064. URL: https://cds.cern.ch/record/1562839.

[143] C. Lester and D. Summers. "Measuring masses of semiinvisibly decaying particles pair produced at hadron colliders". In *Phys. Lett.* B463 (1999), pp. 99–103. DOI: 10.1016/S0370-2693(99)00945-4. arXiv:hep-ph/9906349 [hep-ph].

[144] M. L. Graesser and J. Shelton. "Hunting Asymmetric Stops". In *Phys. Rev. Lett.* 111 (2013), p. 121802. DOI: 10.1103/PhysRevLett.111.121802. arXiv:1212.4495 [hep-ph].

[145] ATLAS Collaboration. *Search for direct top squark pair production in final states with one isolated lepton, jets, and missing transverse momentum in $sqrts = 8$,TeV pp collisions using 21 fb^{-1} of ATLAS data*. Mar. 2013. eprint: ATLAS-CONF-2013-037. URL: https://cds.cern.ch/record/1532431?ln=en.

[146] Paolo Radaelli. "W+heavy flavour and W+light flavour background suppression for stop searches". Bachelor thesis. Universiteit van Amsterdam, 2013.

[147] ATLAS Collaboration. "Search for direct third-generation squark pair production in final states with missing transverse momentum and two b-jets in $\sqrt{s}$ = 8 TeV pp collisions with the ATLAS detector". In *JHEP* 1310 (2013), p. 189. DOI: 10.1007/JHEP10(2013)189. arXiv:1308.2631 [hep-ex].

[148] S. Hoeche, F. Krauss, N. Lavesson, L. Lonnblad, M. Mangano, et al. *Matching parton showers and matrix elements*. 2006. arXiv:hep-ph/0602031 [hep-ph].

[149] J. C. Collins, D. E. Soper, and G. F. Sterman. "Factorization of Hard Processes in QCD". In *Adv. Ser. Direct. High Energy Phys.* 5 (1988), pp. 1–91. arXiv:hep-ph/0409313 [hep-ph].

[150] M. Botje, J. Butterworth, A. Cooper-Sarkar, A. de Roeck, J. Feltesse, et al. "The PDF4LHC Working Group Interim Recommendations". In (2011). arXiv:1101.0538 [hep-ph].

[151] S. Frixione, E. Laenen, P. Motylinski, B. R. Webber, and C. D. White. "Single-top hadroproduction in association with a W boson". In *JHEP* 0807 (2008), p. 029. DOI: 10.1088/1126-6708/2008/07/029. arXiv:0805.3067 [hep-ph].

[152] ATLAS Collaboration. "Search for dark matter candidates and large extra dimensions in events with a jet and missing transverse momentum with the ATLAS detector". In *JHEP* 1304 (2013), p. 075. DOI: 10.1007/JHEP04(2013)075. arXiv:1210.4491 [hep-ex].

A Upper limits on top squark signal cross section

Upper limits on the signal cross section for all top squark signal models discussed in Chapter 9 are presented.

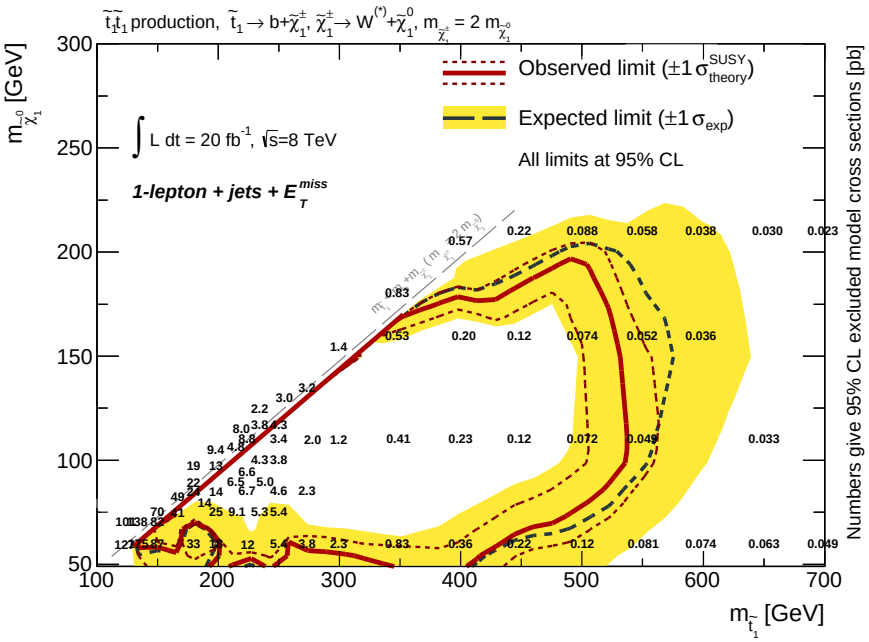

Figure A.1: *Upper limits on the model cross-section in units of* pb *for* $\tilde{t} \to b\ \tilde{\chi}^{\pm} \to b\ W^{\pm}\ \tilde{\chi}^0$ *assuming* $m_{\tilde{\chi}^{\pm}} = 2m_{\tilde{\chi}^0}$. *The numbers are displayed* 10 GeV *higher for better visibility.*

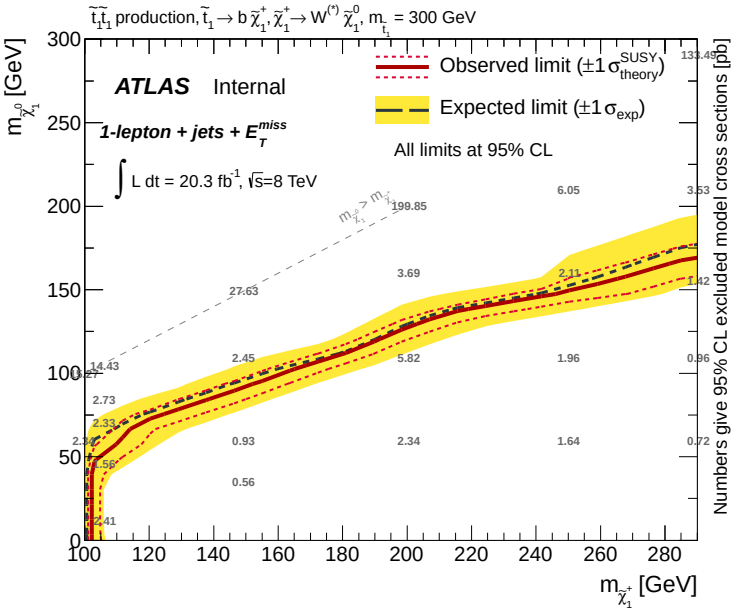

(a) $m_{\tilde{t}}$ = 300 GeV

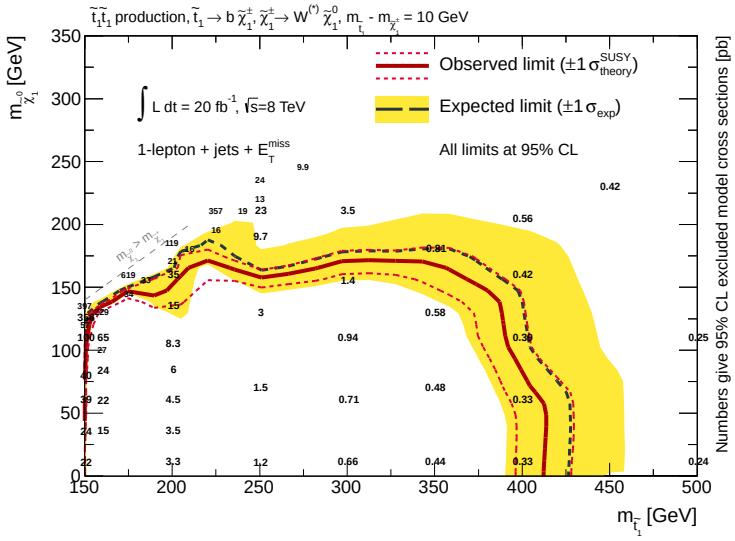

(b) $m_{\tilde{t}} - m_{\tilde{\chi}^\pm}$ = 10 GeV

Figure A.2: *Upper limits on the model cross-section in units of* pb *for* $\tilde{t} \to b\,\tilde{\chi}^\pm \to b\,W^\pm\,\tilde{\chi}^0$ *decay modes. Assumptions on the stop, chargino and neutralino masses are indicated below each figure.*

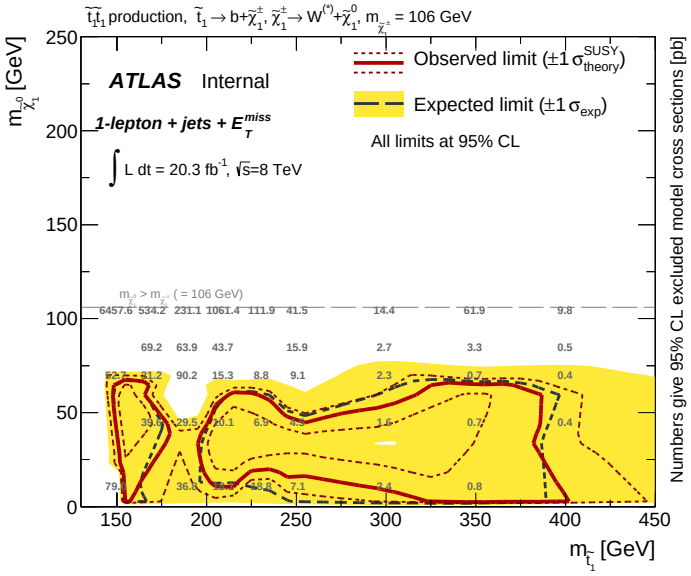

(a) $m_{\tilde{\chi}^{\pm}}$ = 106 GeV

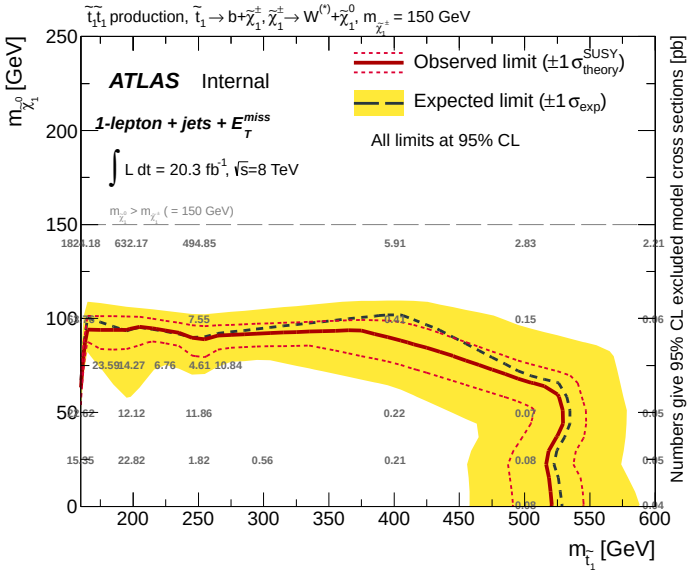

(b) $m_{\tilde{\chi}^{\pm}}$ = 150 GeV

Figure A.3: *Upper limits on the model cross-section in units of* pb *for* $\tilde{t} \to b\ \tilde{\chi}^{\pm} \to b\ W^{\pm}\ \tilde{\chi}^0$ *decay modes. Assumptions on the stop, chargino and neutralino masses are indicated below each figure.*

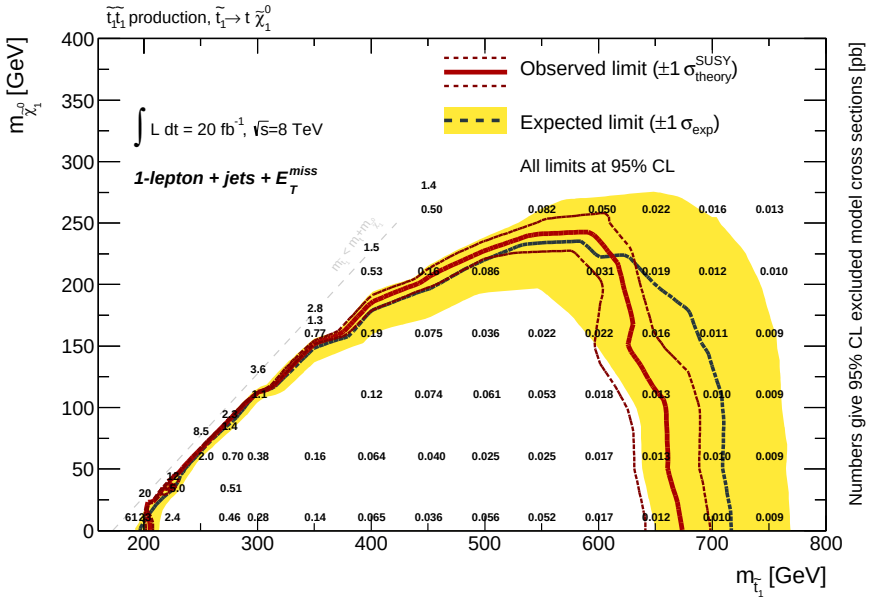

(a) $\tilde{t} \to t\,\tilde{\chi}^0$

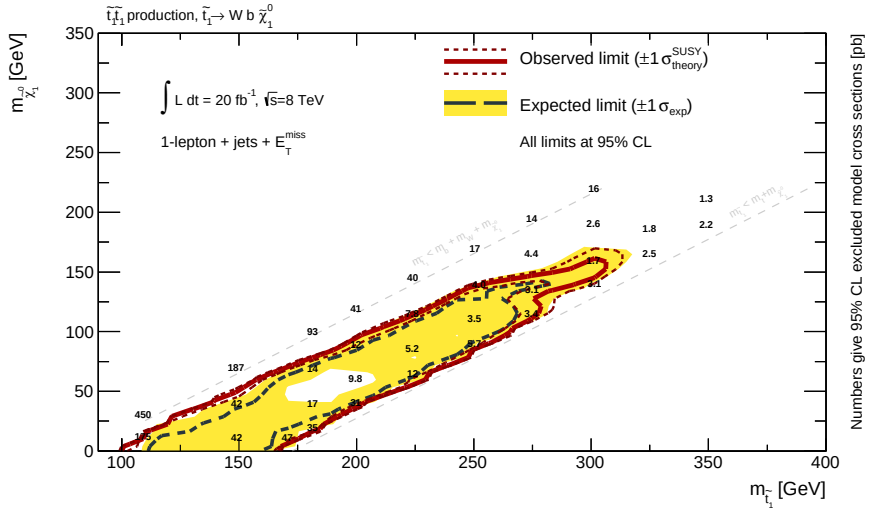

(b) $\tilde{t} \to b\,W^{\pm}\,\tilde{\chi}^0$

Figure A.4: *Upper limits on the model cross-section in units of* pb *for the top squark decay modes indicated below each figure. The numbers are displayed* 10 GeV *higher for better visibility.*

B Acronyms

AcerMC Acer Monte Carlo generator; A Leading Order Monte Carlo generator dedicated to specific SM processes simulation such as single top t-channel production.

ALICE A Large Ion Collider Experiment; One of the detectors recording collisions at the LHC, with main focus on Heavy Ions physics.

ATLAS A Toroidal LHC ApparatuS; One of the detectors recording collisions at the LHC

ATLFAST-II ATLAS Fast Simulation tool v2; Tool dedicated to the simulation of the ATLAS detector geometry based on the Geant4 toolkit [112]. In this package a *fast* simulation of the ATLAS calorimeter is implemented, which relies on the parameterisations of the longitudinal and lateral energy profiles. The rest of the detector, including the tracking system is fully simulated. In this way the simulation time is reduced by one order of magnitude.

BDT Boosted Decision Tree; Multivariate analysis method based on a decision support tool that uses a tree-like graph or model of decisions.

BSM Beyond the Standard Model

CaloTag Calorimeter Tagged; Category of muons that combine an Inner Detector to a calorimeter energy deposit.

CB Combined; Category of muons that combine information of the Inner Detector and the Muon Spectrometer.

CERN Conseil Europèen pour la Recherche Nucléaire; European research organisation whose purpose is to operate the world's largest particle physics laboratory.

CL Confidence Level; measure of the reliability of an estimate. In the specific of this thesis it represents the reliability of a signal model exclusion limit and is chosen to be 95%.

CMS Compact Muon Solenoid; One of the detectors recording collisions at the LHC.

CSC Cathode Strip Chamber; Precision chambers of the muon spectrometer.

DM Dark Matter

DGLAP Dokshitzer–Gribov–Lipatov–Altarelli–Parisi

DoF Degrees of Freedom

DR Diagram Removal; Scheme to correct the Wt-channel single top production for the interference with $t\bar{t}$.

DS Diagram Subtraction; Scheme to correct the Wt-channel single top production for the interference with $t\bar{t}$.

EFT Effective Field Theory

EM Electromagnetic

EM+JES Electromagnetic + Jet Energy Scale; Jet calibration scheme used in 2011.

FCal Forward Calorimeter; Calorimeter that provides both hadronic and electromagnetic calorimetry coverage for pseudorapidities between 3 and 4.9.

FSR final state radiation

GUT Grand Unification Theories

HEC Hadronic End-cap Calorimeter; End-cap component of the hadronic calorimeter.

HERWIG A Leading Order, general purpose Monte Carlo generator able to simulate hard scattering of processes, showering and hadronization.

ID Inner Detector; Tracking system of the ATLAS detector.

IP3D b-tagger based on 3 dimensional information on the track impact parameter.

IP Impact Parameter

ISR initial state radiation

JetProb Jet Probability b-tagging algorithm.

JES Jet Energy Scale

JER Jet Energy Resolution

LEP Large Electron-Positron; Electron-positron collider at CERN operating from 1989 until 2000.

LCG LHC Computing Grid

LCW Local Calibration Weighting

LCW+JES Local Calibration Weighting + Jet Energy Scale; Jet calibration scheme used in 2012.

LHC Large Hadron Collider; Proton-proton collider facility situated at CERN in Geneva, Switzerland

LHCb LHCb experiment; One of the detectors recording collisions at the LHC, with main focus on B hadrons physics.

LO Leading Order

MADGRAPH A Leading Order general purpose matrix element Monte Carlo generator. It needs to be interfaced to other generators such as HERWIG or PYTHIA for the parton showering simulation.

MC@NLO Monte Carlo at Next to Leading Order; A Next-to-Leading Order matrix element Monte Carlo generator, that needs to be interfaced to other generators such as HERWIG or PYTHIA for the parton showering simulation.

MDT Monitored Drift Tube; Precision chambers of the muon spectrometer.

MS Muon Spectrometer

MSSM Minimal Supersymmetric Standard Model

MV1 Multi Variate based b-tagging algorithm.

NLO Next-to-Leading Order

NLL Next-to-Leading Logarithm

PDF Parton Distribution Function; Momentum distribution functions of the partons within the proton.

PID Particle Identification

POWHEG Positive Weight Hardest Emission Generator; A Next-to-Leading Order matrix element Monte Carlo generator. It can be interfaced to PYTHIA or HERWIG for the hadronization and showering of the events.

PSB Proton Synchrotron Booster; First stage of the injector chain at the LHC.

PS Proton Synchrotron; Second stage of the injector chain at the LHC.

PV Primary Vertex; Primary interaction vertex of a bunch crossing. It is identified as the vertex reconstructed by tracks with the highest squared-sum momentum ($\sum_{tracks} p_{\mathrm{T}}^2$).

PYTHIA A Leading Order, general purpose Monte Carlo generator able to simulate hard scattering of processes with two incoming and two outgoing particles. It also generates the parton showering and hadronization of these events.

RPC Resistive Plate Chamber; Triggering chambers of the muon spectrometer.

SCT Semi-Conductor Tracker; Silicon strip based detector of the ATLAS experiment tracking system.

SHERPA Simulation of High Energy Reactions of PArticles; A Leading Order matrix element Monte Carlo generator suited to generate processes with multi-partons in the final state. It can perform the showering and the hadronization of these events as well.

SM Standard Model

SPS Super Proton Synchrotron; Third stage of the injector chain at the LHC. Protons are accelerated up to 450 GeV and then injected into the LHC.

ST Segment Tagged; Category of muons that combine an Inner Detector track with an Muon Spectrometer hit.

SUSY Supersymmetry

SV Secondary Vertex

SV1 Secondary Vertex b-tagging algorithm.

TGC Thin Gap Chamber; Triggering chambers of the muon spectrometer.

TRT Transition Radiation Tracker; Straw-tube based tracking system of the ATLAS detector, specialised in measuring transition radiation photons.

WIMP Weakly Interacting Massive Particle

Summary

The Standard Model and beyond

In the last century high energy physics has made incredible steps forward toward the comprehension of the nature of our universe, its matter content and the interactions of that matter. The SM provides a cogent description of all known subatomic particles and their quantum interactions (strong, weak and electromagnetic). The SM predictive power has been tested to unprecedented precision, with the recent discovery of a Higgs boson by the LHC experiments completing the last piece of the particles puzzle. Despite its success, the SM is not considered to be the conclusive theory of elementary particles due to its inability to explain a number of open questions about our universe, such as the nature of Dark Matter and Dark Energy that compose 96% of the universe content or the relation of gravity with the other three interactions. These and many more open questions about nature call for theories that extend the the SM.

Among these theories, Supersymmetry is one of the most compelling ideas. It is grounded on a generalisation of space-time transformations linking fermions and bosons and it predicts the existence of a supersymmetric partner for every known particle with half a unit of spin difference, but otherwise with the same properties and quantum numbers. Supersymmetry is one of the main focuses of the research program at the LHC experiments.

The LHC and the ATLAS experiment during Run I

The Large Hadron Collider (LHC) is currently the most powerful proton-proton collider in the world and it is located at CERN near Geneva in Switzerland. The first Run of data-taking lasted from 2010 to 2012. The A Toroidal LHC ApparatuS (ATLAS) experiment is one of four experiments recording the collisions delivered by the LHC.

This thesis is based on the data recorded by ATLAS during Run I, which correspond to a total integrated luminosity of pp collisions of 5 and 20 fb^{-1} at a centre-of-mass energy of 7 and 8 TeV, respectively.

The ATLAS detector is often denoted as a *general purpose* experiment, with the aim to express that behind its design lies the purpose of performing a large variety of very different measurements with the data collected in the next twenty years of data taking.

For this reason, it is of utmost importance to ensure that the detector reaches, and if possible outperforms, its design requirements.
This can be summarised in three different key points of action:

(a) Guarantee that the detector efficiently records high quality data.

(b) Increase the understanding of the detector in order to improve the performance and achieve a precise simulation description;

(c) Evaluate the time evolution of the detector's performance, both in the long and in the short term, to ensure the detector's health throughout the experiment lifetime.

A section of this thesis is focused on two examples of performance monitoring and improvement, namely the alignment of the inner tracker, which was achieved with a precision of the order of $10\,\mu$m and the monitoring of one of its sub detectors, the SCT, which achieved data taking efficiencies of 99.9%, 99.6% and 99.1% in 2010, 2011 and 2012 respectively [95].

Calibration of bottom-quark jets identification algorithms

In 2011, the main focus of the ATLAS experiment has been not only to probe for the first time physics at the energy frontier, but also to improve the understanding and calibration of the detector and the tuning and validation of the Monte Carlo simulation used to model the SM (and new physics) processes.

A large number of measurements and new physics searches performed in ATLAS rely on the identification of jets originating from b-quarks, which is performed by means of dedicated *b-tagging* algorithms. The aim of the first analysis presented in this thesis is to investigate the reliability of the Monte Carlo simulation in describing the quantities exploited directly and indirectly by these b-tagging algorithms. This is achieved by studying a b-jet enriched sample from fully reconstructed $\mathrm{B}^{\pm} \to \mathrm{J}/\psi\,\mathrm{K}^{\pm}$

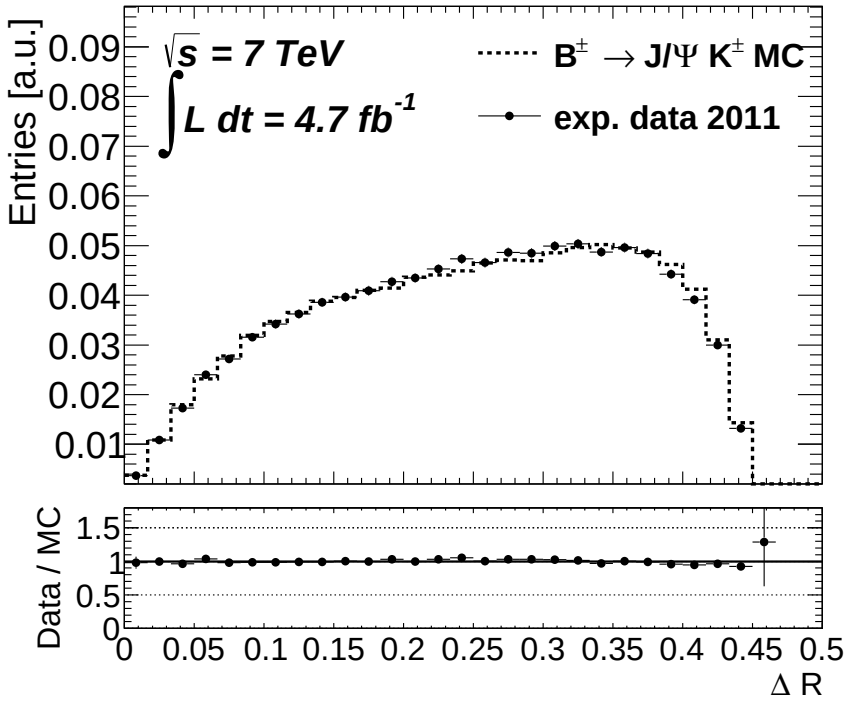

Summary, Figure 1: *Angular distance between the hadronization tracks of the jet and the jet axis.*

decays. The study is based on the 5 fb^{-1} of data collected in 2011 at centre-of-mass energy of $\sqrt{s}$ = 7 TeV and it was driven by the need of understanding the calibration factors of the b-tagging algorithms needed to match the simulation to the experimental data. B-jets properties and the performance of the tagging algorithms are studied in data and compared to the Monte Carlo simulation. The majority of the observables are found to be well described by the simulation and the b-tagging performance has been found to be in agreement to the Monte Carlo at the few percent level. Fig. 1 compares the angular distance between the hadronization tracks in a b-jet and the jet axis[1)]. The solid line represents the distribution from the Monte Carlo simulation that is compared to the same distribution from data (indicated with points). The points in the lower panel of the figure show the ratio between the

[1)] defined as $\Delta R(\text{jet}, \text{trk}) = \sqrt{(\phi_{\text{jet}} - \phi_{\text{trk}})^2 + (\eta_{\text{jet}} - \eta_{\text{trk}})^2)}$

data and the Monte Carlo simulation. The two distributions agree at a few percent level, proving a good modelling of the b-jets hadronization track topology by the simulation. The distributions of the transverse and longitudinal impact parameters of hadronization tracks have shown instead up to 20% disagreement between the data and the Monte Carlo simulation.

Search for scalar top-quarks and Dark Matter

The dataset collected by ATLAS in 2012 is four times bigger than the one in 2011 and the higher centre-of-mass energy results in a higher production cross section for one of the most intriguing particles predicted by Supersymmetry: a scalar top quark (top squark).

The SUSY analysis presented in this thesis is a search for top squarks in final states with one isolated lepton, b-jets and missing transverse momentum. Since R-parity is assumed to be conserved, top squarks are always produced in pairs. Of all the possible top squark decay modes, three are considered:

a) $\tilde{t} \to t\,\tilde{\chi}^0$ (with subsequent decay $t \to W\,b$)

b) $\tilde{t} \to b\,\tilde{\chi}^{\pm} \to b\,W^{\pm}\,\tilde{\chi}^0$ (with $W^{\pm} \to \ell\nu$ or $W^{\pm} \to \bar{q}q'$)

c) $\tilde{t} \to b\,W^{\pm}\,\tilde{\chi}^0$ (via off-shell top and $W^{\pm} \to \ell\nu/\bar{q}q'$)

The neutralino ($\tilde{\chi}^0$) is assumed to be the lightest supersymmetric particle and due to the conservation of R-parity it is stable and escapes the detector without interacting. The masses of the top squark and the other supersymmetric particles in the decay chain (charginos and neutralinos) are unknown.

In order to achieve a good sensitivity for the three top squark decay modes and the widest range of assumptions for $m_{\tilde{t}}, m_{\tilde{\chi}^{\pm}}, m_{\tilde{\chi}^0}$ we exploit two different strategies to define the signal enriched regions:

- Selections defined by requirements on a number of quantities with high discrimination power between signal and background. The final discrimination is achieved by counting and comparing the number of signal and background events passing all requirements, and therefore these selections are called *cut-and-count* selections.

- A simultaneous likelihood fit of multi-bin selections (*shape fits*). The binning is defined in the two most discriminating quantities and allows to exploit the

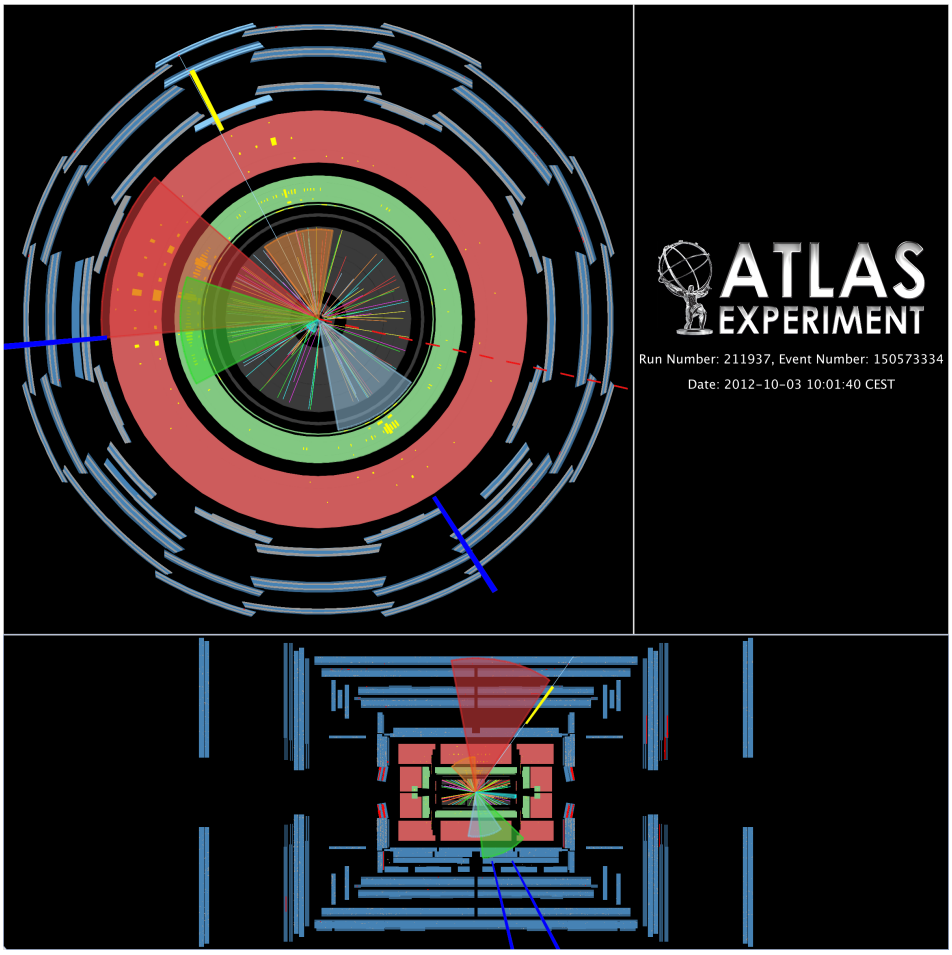

Summary, Figure 2: *Event display of a* $\tilde{t} \to b\,\tilde{\chi}^{\pm}$ *candidate event. This event has a* $E_{\mathrm{T}}^{\mathrm{miss}}$ *value of* 609 GeV *(red dashed line). It has four jets of transverse momenta of* $424, 199, 130$ *and* 99 *GeV, respectively. Jets are indicated as cones with area proportional to the jet transverse momentum. The second and the third most energetic jets are identified as* b*-jets using the MV1* b*-tagging algorithm (blue lines). One muon is identified in the event and it has a transverse momentum of* 51 GeV *(yellow line). Tracks with transverse momentum of at least* 0.5 GeV *are shown in the inner tracker.*

difference in shape between the background and the signal in order to increase the discriminating potential.

A total of seven *cut-and-count* selections and four *shape fit* selections are defined for this analysis.

A $\tilde{t} \to b\,\tilde{\chi}^{\pm}$ candidate event display is shown in Fig. 2. This event has a $E_{\mathrm{T}}^{\mathrm{miss}}$ value of 609 GeV, indicated with a red dashed line in the figure. It has four selected jets of transverse momenta of $424, 199, 130$ and 99 GeV, respectively. Jets are indicated as cones and the area of the cone is proportional to the jet transverse momentum. The second and the third most energetic jets are identified as b-jets using the MV1 b-tagging algorithm (blue lines). One muon is identified in the event and it has a transverse momentum of 51 GeV (yellow line).

The data yield observed in each signal region are compatible with the SM-only hypothesis, hence the results have been interpreted in terms of upper limits on the

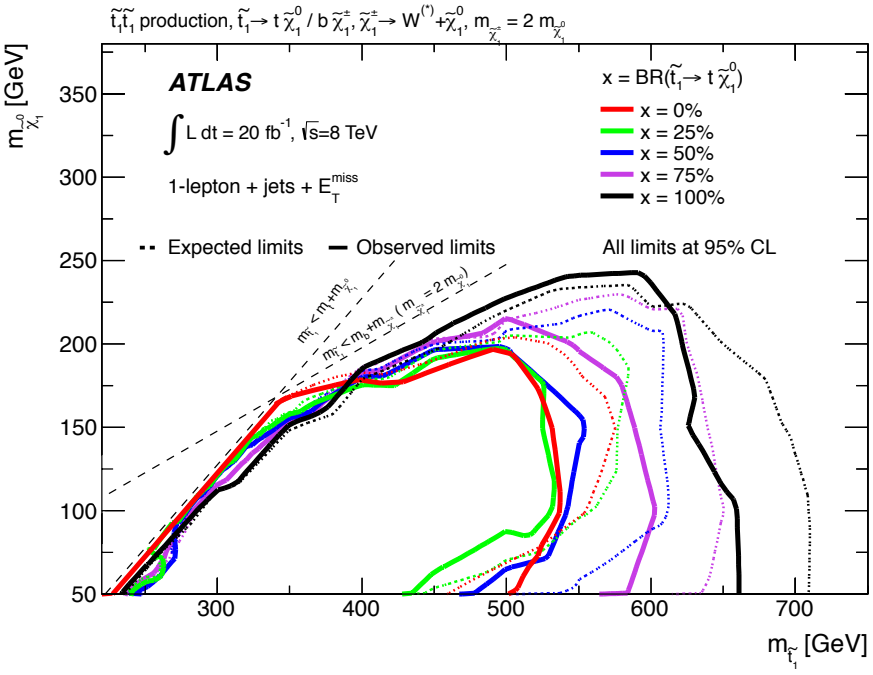

Summary, Figure 3: *Exclusion limits 95% CL in the $(m_{\tilde{t}}, m_{\tilde{\chi}^0})$ plane. The two decay modes $\tilde{t} \to b\,\tilde{\chi}^{\pm}$ and $\tilde{t} \to t\,\tilde{\chi}^0$ are assumed with a branching ratio of $(100 - x)\%$ and $x\%$, respectively for each line in the plot. $m_{\tilde{\chi}^{\pm}} = 2m_{\tilde{\chi}^0}$ is assumed.*

three top squark decay modes.

Fig. 3 shows the result in the $(m_{\tilde{t}}, m_{\tilde{\chi}^0})$ mass plane obtained for models where two decay modes of the top squark are allowed in the same event. Each line in the plot represents the exclusion curve for a different branching ratio in the two decay modes, $x\%$ in $\tilde{t} \to t\ \tilde{\chi}^0$ and $(100 - x)\%$ in $\tilde{t} \to b\ \tilde{\chi}^{\pm} \to b\ W^{\pm}\ \tilde{\chi}^0$. $(m_{\tilde{t}}, m_{\tilde{\chi}^0})$ mass assumptions inside the solid line have been excluded at 95% CL. Dashed lines indicate the expected exclusion contours. Branching ratios of 0-100%, 25-75%, 50-50%, 75-25%, and 100-0% have been tested. All signal selections presented in this analysis have been combined to obtain this exclusion. The combination was obtained by selecting a-priori the signal region with the best expected limit for each $(m_{\tilde{t}}, m_{\tilde{\chi}^0})$ point. Top squark masses between 290 and 530 GeV are excluded for all branching ratios in the case of a neutralino mass of 100 GeV.

Neutralinos are excellent candidates for WIMP Dark Matter. In the context of an Effective Field Theory description of DM [76, 77], certain Lagrangian operators describing the contact interaction between DM particles and quarks are proportional to the quark masses, being therefore possibly enhanced for bottom and top quarks. The results of the top squark analysis were interpreted in terms of DM associate production with top quarks ($pp \to t\bar{t}\chi\chi$), that has the same final state as the $\tilde{t} \to t\ \tilde{\chi}^0$ decay. The combined exclusion curves at 95% CL for the DM-nucleon scattering cross section are given in Figure 4, for contact operators D1 (Dirac scalar DM) and C1 (complex scalar DM). Values above the curve are excluded. The results are compared with limits obtained by the ATLAS mono-jet analysis using the 7 TeV data set and the exclusion limits (at 90% CL) recently set by the LUX and Super-CDMS collaborations. Assuming a DM mass of 1 GeV, DM-nucleon scattering cross sections above $3 \cdot 10^{-41}\,\mathrm{cm}^2$ and $7 \cdot 10^{-43}\,\mathrm{cm}^2$ are excluded for complex scalar and Dirac DM contact operators, respectively. The exclusion limits resulting from this analysis are currently the world strongest constraints on scalar coupling of Dark Matter for operators involving heavy quarks.

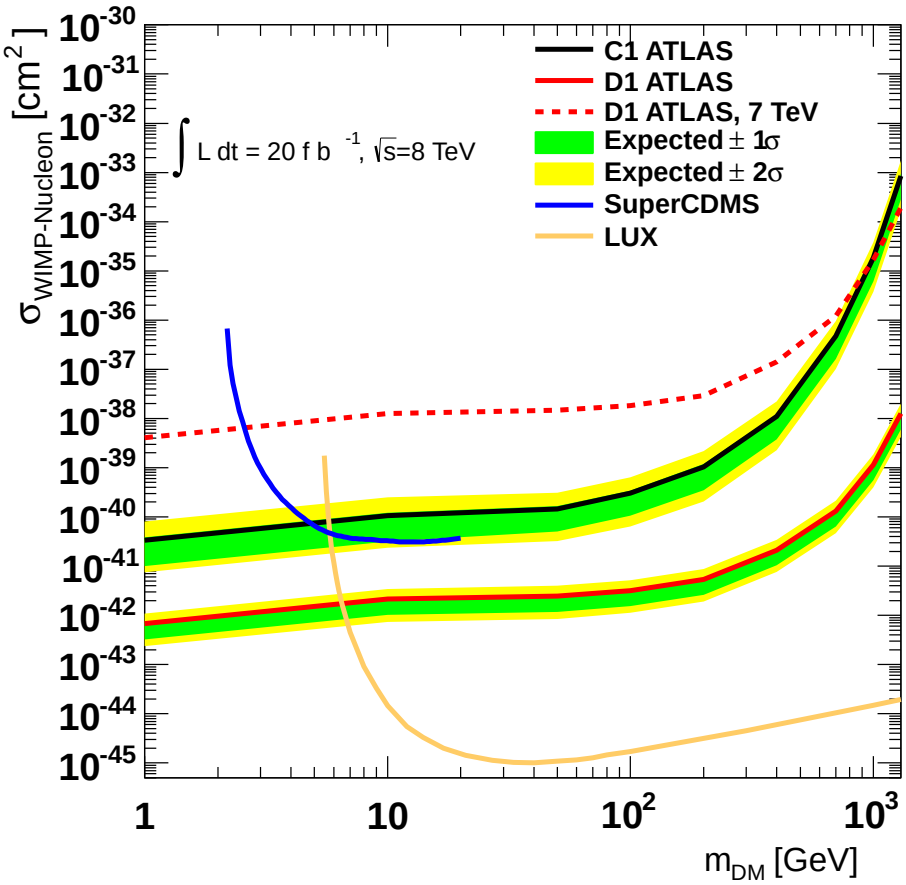

Summary, Figure 4: *Exclusion curves at 95% CL for DM-nucleon scattering cross section for operators D1 and C1. The results are compared with 90% CL exclusion curves from the Super-CDMS and the LUX Collaborations and values above the curves are excluded.*

Samenvatting

Het Standaard Model en verder

In de vorige eeuw heeft de hoge energie fysica ongelooflijke stappen gemaakt in ons begrip van de aard van het heelal, de materiële inhoud ervan en de interacties van die materie. Het Standard Model (SM) levert een overtuigende beschrijving van alle bekende subatomaire deeltjes en hun quantum interacties via de sterke, zwakke en elektromagnetische wisselwerkingen. De voorspellende kracht van het SM is tot op ongekende nauwkeurigheid getest, inclusief de recente ontdekking van het higgs-deeltje door de Large Hadron Collider (LHC)-experimenten waarmee het laatste stukje van de deeltjespuzzel is gelegd. Ondanks zijn succes wordt het SM niet als een complete theorie van elementaire deeltjes gezien doordat het een aantal vragen over ons heelal open laat, zoals de aard van donkere materie en donkere energie die 96% van de inhoud van het universum uitmaken, en de relatie van de zwaartekracht met de andere drie interacties. Deze en nog veel meer open vragen over de natuur roepen op tot theorieën die het SM uitbreiden.

Een van deze theorieën, Supersymmetry is een van de meest veelbelovende ideeën voor een dergelijke uitbreiding. Het is gebaseerd op een generalisatie van de ruimte-tijd transformaties die fermionen en bosonen koppelen, en het voorspelt het bestaan van een supersymmetrische partner voor elk bekend deeltje met een verschil in spin van een halve eenheid, terwijl de andere eigenschappen en quantum getallen hetzelfde blijven. Supersymmetry is een van de belangrijkste aandachtspunten van het onderzoeksprogramma van de LHC experimenten.

De LHC en het ATLAS-experiment tijdens Run I

De Large Hadron Collider (LHC)is momenteel de meest krachtige proton-proton versneller ter wereld en het is gelegen op CERN bij Genève in Zwitserland. De eerste

periode waarin de LHC in bedrijf was (Run I) duurde van 2010 tot 2012. Het A Toroidal LHC ApparatuS (ATLAS) experiment is een van vier experimenten die gegevens verzamelt van de door de LHC geleverde botsingen. Dit proefschrift is gebaseerd op de door ATLAS tijdens Run I verzamelde data overeenkomend met een totale geïntegreerde luminositeit van pp botsingen van respectievelijk 5 en 20 fb^{-1} met een zwaartepuntsenergie van 7 en 8 TeV.

De ATLAS detector wordt vaak aangeduid als een *multifunctioneel* experiment; het ontwerp van de detector is zodanig dat het een grote verscheidenheid aan zeer verschillende metingen kan verrichten op de in de komende twintig jaar te verzamelen data.

Daarom is het van groot belang dat de detector de gestelde ontwerpeisen bereikt, en indien mogelijk zelfs beter presteert.
Dit kan in drie verschillende actiepunten worden samengevat:

(a) Garandeer dat de detector efficiënt gegevens registreert met hoge kwaliteit.

(b) Verhoog het begrip van de detector zodat de prestaties kunnen worden verbeterd en een nauwkeurige simulatie van de detector kan worden gemaakt;

(c) Evalueer de tijdevolutie van de prestaties van de detector, zowel op de lange als op de korte termijn, zodat de goede status van de detector gedurende het hele experiment kan worden gegarandeerd.

Een deel van dit proefschrift richt zich op twee voorbeelden van prestatiemonitoring en verbetering, namelijk voor de *inner tracker*, de binnenste detector die de sporen van geladen deeltjes meet. Na uitlijning bereikt de inner tracker een nauwkeurigheid in de orde van $10\,\mu$m. De controle van een van de sub-detectoren, de Semi-Conductor Tracker (SCT), laat zien dat in het verzamelen van botsingsdata een efficiëntie van respectievelijk 99,9%, 99,6% en 99,1% in 2010, 2011 en 2012 bereikt wordt [95].

Kalibratie van bottom-quark jet identificatie algoritmes

In 2011 was de belangrijkste focus van het ATLAS experiment niet alleen om voor het eerst fysica bij de allerhoogste energiën te doen, maar ook om verbeteringen aan te brengen in het begrip en de kalibratie van de detector, en aan de afstemming en de validatie van de Monte Carlo simulaties die gebruikt worden om SM (en nieuwe fysica) processen na te bootsen.

Een groot aantal metingen en de speurtochten naar nieuwe fysica die worden gedaan in ATLAS vertrouwen op de identificatie van jets afkomstig van b-quarks,

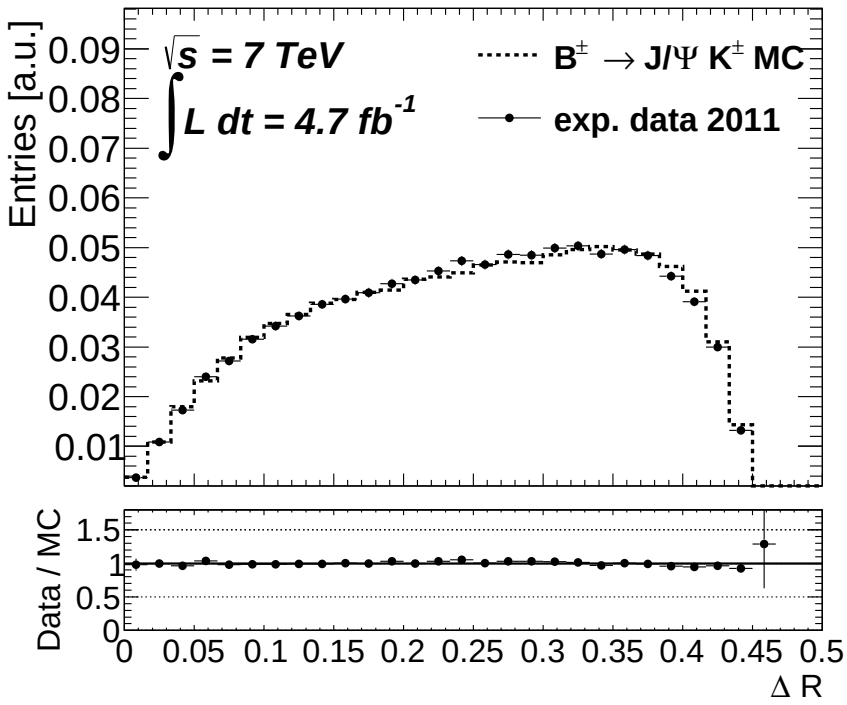

Samenvatting, Figuur 1: *Hoekafstand tussen de sporen van geladen deeltjes die ontstaan in de hadronisatie van een jet en de jet as.*

die wordt uitgevoerd door middel van toegewijde b-*tagging* algoritmes. Het doel van de eerste analyse gepresenteerd in dit proefschrift is om de betrouwbaarheid van de Monte Carlo simulaties bij het beschrijven van de directe en indirecte resultaten door deze b-tagging algoritmes te onderzoeken. Dit wordt bereikt door het bestuderen van een verzameling van volledig gereconstrueerde $\mathrm{B}^{\pm} \to \mathrm{J}/\psi\ \mathrm{K}^{\pm}$ vervallen. Het onderzoek is gebaseerd op de $5\ \mathrm{fb}^{-1}$ van gegevens verzameld in 2011 bij een zwaartepuntsenergie van $\sqrt{s}$ = 7 TeV, en het werd gedreven door de noodzaak om de factoren die een rol spelen bij de kalibratie van de b-tagging algoritmes en die nodig zijn om de simulatie overeen te laten komen met de experimentele gegevens beter te begrijpen. De eigenschappen van de b-jets en de prestaties van de tagging algoritmes zijn bestudeerd in data en vergeleken met de Monte Carlo simulatie. De meeste observabelen blijken goed te worden beschreven door de simulatie en de b-tagging prestaties in data blijken in overeenstemming te zijn met de Monte Carlo

binnen een paar procent. Figuur 1 toont de hoekafstand tussen de sporen van geladen deeltjes die ontstaan in de hadronisatie van een b-jet en de jet-as[2)]. De ononderbroken lijn geeft de verdeling aan voor de Monte Carlo simulatie, en die wordt vergeleken met dezelfde verdeling voor data, aangegeven met punten. De punten in het onderste deel van de figuur tonen de verhouding tussen de data en de Monte Carlo simulatie. De twee distributies komen op een niveau van een paar procent overeen, waaruit blijkt dat de hadronisatie topologie van de geladen deeltjes in de b-jets goed gemodelleerd is door de simulatie. De verdelingen van de transversale en longitudinale impact parameters van de hadronisatie deeltjes blijken daarentegen in data en Monte Carlo simulatie tot 20 % niet overeen te komen.

Zoeken naar scalaire top-quarks en Dark Matter

De in 2012 door ATLAS verzamelde dataset is vier keer groter dan die in 2011 en de hogere zwaartepuntsenergie resulteert in een hogere productie werkzame doorsnede voor een van de meest intrigerende deeltjes voorspeld door Supersymmetry: het scalaire top quark (top squark).

De Supersymmetry (SUSY) analyse gepresenteerd in dit proefschrift is een speurtocht naar top squarks in gevallen waarbij de eindtoestand een geïsoleerd lepton, b-jets en missende transversale impuls bevatten. Aangezien R-pariteit wordt verondersteld geconserveerd te zijn worden top squarks altijd geproduceerd in paren. Van alle mogelijke top squark vervalswijzen worden er drie beschouwd:

a) $\tilde{t} \to t\,\tilde{\chi}^0$ (met daaropvolgende verval $t \to W\,b$)

b) $\tilde{t} \to b\,\tilde{\chi}^\pm \to b\,W^\pm\,\tilde{\chi}^0$ (met $W^\pm \to \ell\nu$ or $W^\pm \to \bar{q}q'$)

c) $\tilde{t} \to b\,W^\pm\,\tilde{\chi}^0$ (via off-shell top en $W^\pm \to \ell\nu/\bar{q}q'$)

De neutralino ($\tilde{\chi}^0$) wordt verondersteld het lichtste supersymmetrische deeltje te zijn, en als gevolg van het behoud van de R-pariteit is het stabiel en ontsnapt het de detector zonder interacties. De massa's van de top squark en van de andere supersymmetrische deeltjes in de vervalsketen (chargino's en neutralino's) zijn onbekend.

Om een goede gevoeligheid voor de drie top squark vervalswijzen te verkrijgen en om het breedste scala aan aannames voor $m_{\tilde{t}}, m_{\tilde{\chi}^\pm}, m_{\tilde{\chi}^0}$ te bereiken worden twee verschillende strategiën bekeken om selecties verrijkt in SUSY signaal te definiëren:

[2)] gedefinieerd als $\Delta R(\text{jet}, \text{trk}) = \sqrt{(\phi_{\text{jet}} - \phi_{\text{trk}})^2 + (\eta_{\text{jet}} - \eta_{\text{trk}})^2)}$

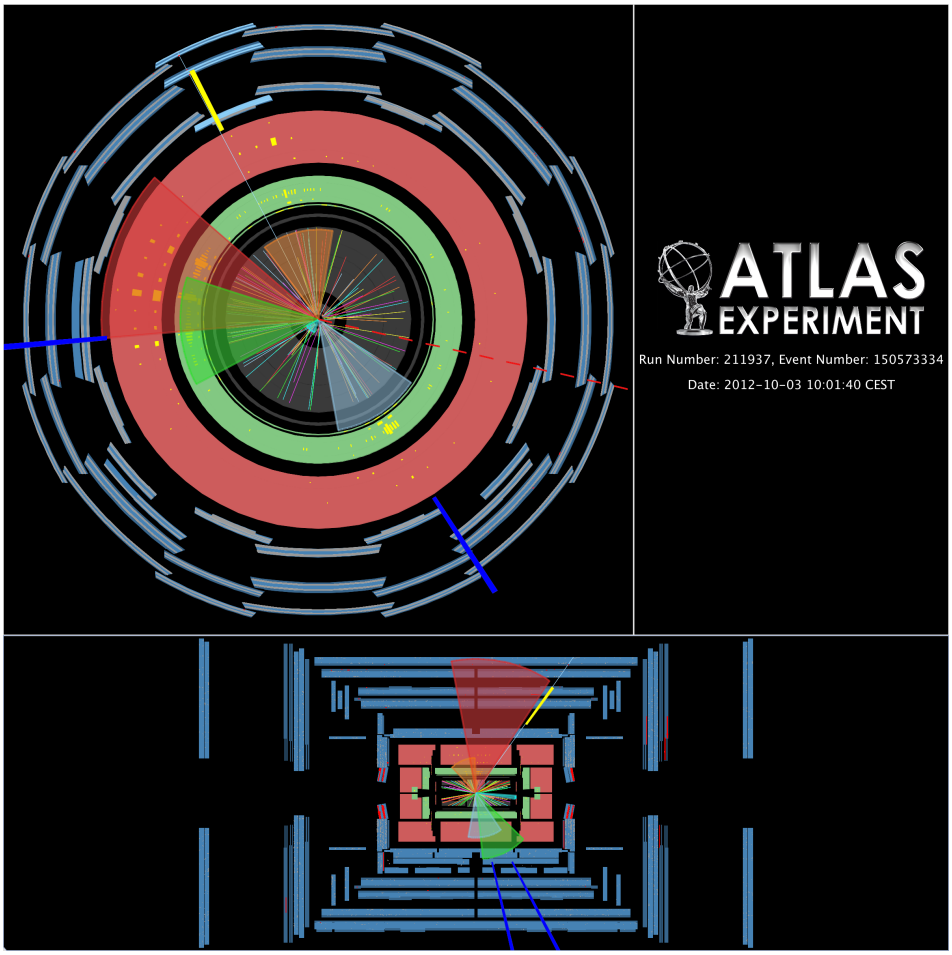

Samenvatting, Figuur 2: *Grafische weergave van een* $\tilde{t} \to b\,\tilde{\chi}^{\pm}$ *kandidaat gebeurtenis. Deze gebeurtenis heeft een missende transversale impuls van* 609 GeV *(rode stippellijn). Hij heeft vier jets met transversale impuls van respectievelijk* $424, 199, 130$ *en* 99 *GeV. Jets worden aangeduid als kegels met een oppervlakte evenredig met de jet transversale impuls. De tweede en de derde meest energieke jets zijn geïdentificeerd als* b*-jets met behulp van het* MV1 b*-tagging algoritme (blauwe lijnen). Een muon is geïdentificeerd in het event en het heeft een transversale impuls van* 51 GeV *(gele lijn). Sporen met een transversale impuls van minstens* $0,5$ GeV *worden getoond in de inner tracker.*

- Selecties gedefinieerd door snedes te maken in een aantal variabelen die het signaal van de achtergrond goed kunnen scheiden. De uiteindelijke separatie wordt bereikt door het tellen en het vergelijken van het aantal signaal en achtergrond gebeurtenissen die aan alle eisen voldoen. Daarom worden deze selecties *cut-and-count* selecties genoemd.

- Een gelijktijdige waarschijnlijkheidsfit aan multi-bin selecties (*vorm fits*). De binning is gedefinieerd in de twee meest discriminerende variabelen en bekijkt het verschil in vorm tussen de distributies van die variabelen in de achtergrond en in het signaal om het onderscheidend vermogen te verhogen.

Een totaal van zeven *cut-and-count* selecties en vier *vorm fits* zijn gedefinieerd voor deze analyse.

Een grafische weergave van een $\tilde{t} \to b\ \tilde{\chi}^{\pm}$ kandidaat gebeurtenis is getoond in

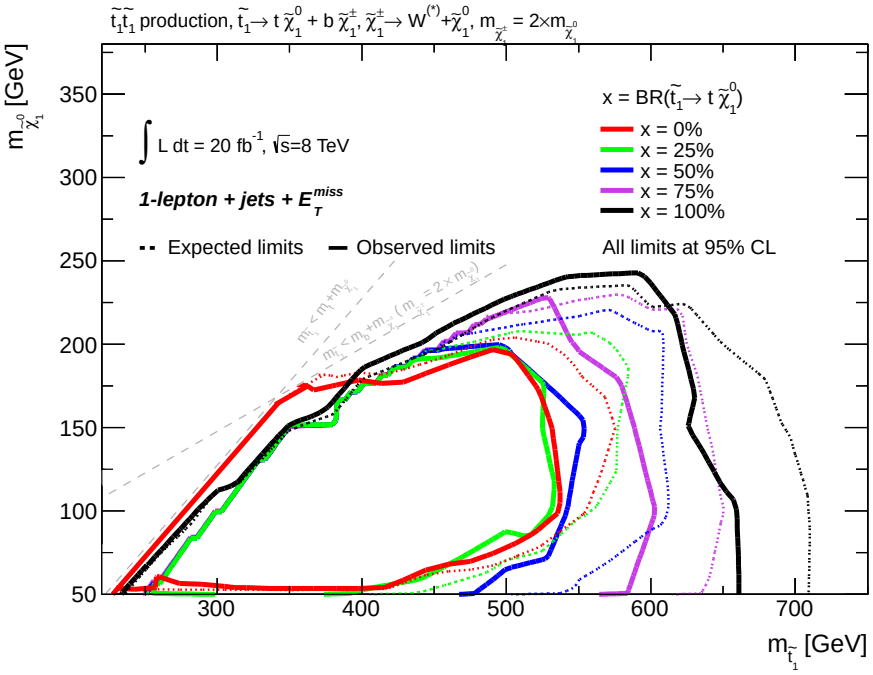

Samenvatting, Figuur 3: *Uitsluiting limieten op* 95% CL *in het* $(m_{\tilde{t}}, m_{\tilde{\chi}^0})$ *vlak. De twee vervalswijzen* $\tilde{t} \to b\ \tilde{\chi}^{\pm}$ *en* $\tilde{t} \to t\ \tilde{\chi}^0$ *worden verondersteld met een fractie van respectievelijk* $(100 - x)\%$ *en* $x\%$*, voor elke lijn in de plot.* $m_{\tilde{\chi}^{\pm}} = 2m_{\ nino}$ *wordt aangenomen.*

figuur 2. Deze gebeurtenis heeft een missende transversale impuls van 609 GeV, aangegeven met een rode stippellijn in de figuur. Hij heeft vier geselecteerde jets met een transversale impuls van respectievelijk $424, 199, 130$ en 99 GeV. Jets worden aangeduid als kegels en het oppervlak van de kegel is evenredig met de transversale impuls van de jet. De tweede en de derde meest energieke jets zijn geïdentificeerd als b-jets met behulp van het MV1 b-tagging algoritme (blauwe lijnen). Een muon is geïdentificeerd in de gebeurtenis met een transversale impuls van 51 GeV (gele lijn).

De hoeveelheid geobserveerde gebeurtenissen in data na toepassing van alle selecties komt overeen met de hypothese dat alleen het SM bijdraagt, en er zijn geen aanwijzingen voor top squarks. Derhalve zijn de resultaten geïnterpreteerd in termen van bovengrenzen op top squark productie, aannemende de drie bestudeerde top squark vervalswijzen.

Figuur 3 toont het resultaat in het $(m_{\tilde{t}}, m_{\tilde{\chi}^0})$ massa vlak verkregen voor modellen waarin twee verschillende vervalswijzen van de top squark in dezelfde gebeurtenis zijn toegestaan. Elke lijn in de grafiek stelt de uitsluiting curve voor voor een gegeven fractie van de twee vervalswijzen, $x\%$ in $\tilde{t} \to t\,\tilde{\chi}^0$ en $(100{-}x)\%$ in $\tilde{t} \to b\,\tilde{\chi}^{\pm} \to b\,W^{\pm}\,\tilde{\chi}^0$. $(m_{\ stop}, m_{\tilde{\chi}^0})$ massa veronderstellingen binnen de ononderbroken lijnen zijn uitgesloten op 95 % CL. Onderbroken lijnen geven de verwachte uitsluitingen op basis van alleen simulaties. Vertakking verhoudingen van 0-100 %, 25-75 %, 50-50 %, 75-25 % en 100-0 % zijn getest. Voor de uitsluitingen zijn alle signaal selecties die in deze analyse zijn gepresenteerd gecombineerd. De combinatie werd verkregen door a-priori de selectie te kiezen met de beste verwachte limiet voor elk $(m_{\tilde{t}}, m_{\tilde{\chi}^0})$ punt. Top squark massa's tussen de 290 en 530 GeV zijn uitgesloten voor alle combinaties van vervalswijzen in het geval van een neutralino massa van 100 GeV.

Neutralinos zijn uitstekende kandidaten voor Weakly Interacting Massive Particle (WIMP) Dark Matter. In het kader van een Effectieve Velden Theorie beschrijving van DM [76, 77], zijn bepaalde Lagrangiaan operatoren die de contact interacties tussen DM deeltjes en quarks beschrijven evenredig met de quark massa's, waardoor interacties tussen DM en bottom en top quarks mogelijk versterkt zijn. De resultaten van de top squark analyse zijn geïnterpreteerd in termen van DM deeltjes productie samen met top quarks ($pp \to t\bar{t}\chi\chi$), dat dezelfde eindtoestand heeft als $\tilde{t} \to t\,\tilde{\chi}^0$ verval. De gecombineerde uitsluiting curves op 95% CL voor de werkzame doorsnede voor DM-nucleon verstrooiing zijn aangegeven in figuur 4, voor contact operatoren D1 (Dirac scalaire DM) en C1 (complex scalaire DM). Waarden boven de curves zijn uitgesloten. De resultaten zijn vergeleken met limieten verkregen door de ATLAS mono-jet analyse op basis van de 7 TeV dataset en met de

uitsluiting limieten (90 % CL) die onlangs door de LUX en Super-CDMS samenwerkingen zijn bepaald. Uitgaande van een DM massa van 1 GeV, DM-nucleon verstrooiings werkzame doorsnedes boven de $3 \cdot 10^{-41}\,\mathrm{cm}^2$ en $7 \cdot 10^{-43}\,\mathrm{cm}^2$ zijn uitgesloten voor respectievelijk complex scalaire and Dirac DM contact operatoren. De uitsluitings grenzen die voortvloeien uit deze analyse zijn de sterkste beperkingen op scalaire Dark Matter koppelingen ter wereld voor operatoren met zware quarks.

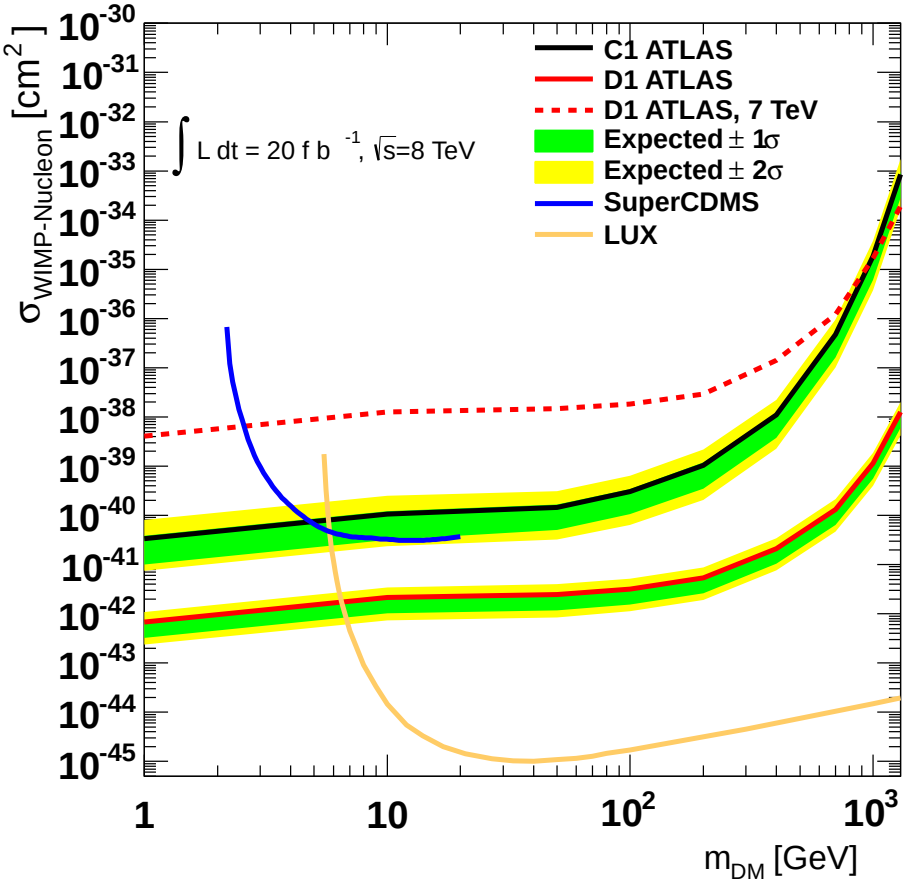

Samenvatting, Figuur 4: *Uitsluitings curves op* 95% CL *voor de werkzame doorsnede voor* DM*-nucleon verstrooiing voor operatoren D1 en C1. De resultaten worden vergeleken met 90 %* CL *uitsluiting curves van de Super-CDMS en de LUX samenwerkingen en waarden boven de curves zijn uitgesloten.*

Acknowledgements

At the end of this four year journey I would like to thank the many people without whom this thesis would not have been possible. Although there are too many persons to mention by name, there are some that I would like to explicitly thank. First and above all I would like to thank my promoter and supervisor, Paul de Jong and my co-promoter and advisor Auke-Pieter Colijn. They have guided and constantly supported me through my PhD, teaching me how to be a physicist and a researcher.

Many more people, both at Nikhef and at CERN have given an invaluable contribution to my intellectual growth and to my work through discussions, advices and collaborations. From my first months as a PhD I would like to mention Martijn Gosselink for introducing me to the world of the ATLAS Software and the *b-tagging group* conveners, Sara Strandberg, Fabrizio Parodi and Frank Filthaut for their guide and advice in my first analysis in ATLAS.

I would like to thank the people of the *SCT Operations group* for enjoyable and interesting days and nights spent together monitoring the detector. My hearty thanks to Saverio D'Auria, Steve McMahon, Dave Robinson, Nick Barlow, Gaetano Barone, Alex Kastanas and Adrian Vogel. I would like to express my gratitude to Carolina Deluca for teaching me how to perform a search from the beginning to the end and to all the members of the *stop1L team* for two years spent together looking for the stop. My gratitude in particular to Kilian Rosbach for the many many hours spent together debugging the code. As this analysis would not have been possible without the Nikhef CPU cluster, I owe my gratitude to Ronald Starink, Jeff Templon and Hurng-Chun Lee for their help and patience with me and my jobs.

Finally, my biggest thanks to the friends that have endured my presence, my anxiety and my complains in these four years. The list is too long to name everyone among the colleagues in the ATLAS, LHCb, Theory, ANTARES and R&D groups at Nikhef and the Italo-Spanish(-German) community at CERN: I thank you all nonethe-

less! A particular recognition to the people with whom I shared a house or an office in these years: Julian, Dennis, Duc, Pieter, Pierfrancesco and Joern, Carolina, Marija, Rogier, Afroditi, Ingrid, Stefan and Lydia and my thanks for fruitful and interesting discussions at any time of the day or of the night.

My last and biggest thanks to my paranymphs, Duc Bao Ta and Francesco Zappon, for their support and friendship from the very beginning to the end of this journey.

Priscilla Pani
Amsterdam, 2014